

UNIVERSITY OF BELGRADE
FACULTY OF MECHANICAL ENGINEERING



Abdussalam Yousef Solob

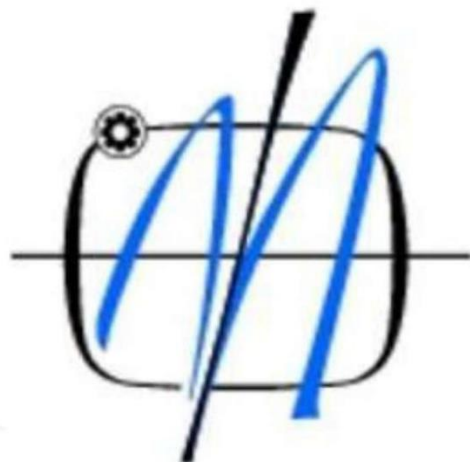
**FATIGUE LIFE ANALYSIS OF DAMAGED LIGHT AIRCRAFT
WING-FUSELAGE FITTING**

Doctoral Dissertation

Belgrade, 2021.

УНИВЕРЗИТЕТ У БЕОГРАДУ

МАШИНСКИ ФАКУЛТЕТ



Абдусалам Јусеф Солоб

**АНАЛИЗА ВЕКА ПОД ЗАМОРОМ ОШТЕЋЕНОГ ОКОВА ВЕЗЕ
КРИЛО ТРУП ЛАКЕ ЛЕТЕЛИЦЕ**

докторска дисертација

Београд, 2021.

SUPERVISOR:

Dr Aleksandar Grbović, redovni profesor,
Univerzitet u Beogradu, Mašinski fakultet

.....

BOARD OF COMMISSION

Dr Aleksandar Sedmak, redovni profesor,
Univerzitet u Beogradu, Mašinski fakultet

.....

Dr Gordana Kastratović, redovni profesor,
Univerzitet u Beogradu, Saobraćajni fakultet

.....

Data of defence

ACKNOWLEDGMENT

Thanks to Allah.

I would like to express my full thanks to my supervisor full Prof. Aleksandar Grbovic, for his offers, continuous support to the thesis guides, and revision of my research.

I would like to thank full Prof. Aleksandar Sedmak, full Prof. Gordana Kastratovic, and full Prof. Bojan Babic to teach me and their help during my Ph.D. study.

I would also like to extend my gratitude to the Mechanical Engineering faculty staff at Belgrade University.

I would like to thanks my job in Libya for financial supports.

I would like to thank any who helped me with this thesis.

Finally, my deep appreciation is addressed to whole my family Parents, wife, daughters, and sons for their patience and supporting me during the period of my study

Dedication

To my family

To my parents

To my friends

Abstract

Pin-loaded attachment lugs are the most responsible for wing-to-fuselage load transfer during the flight and, therefore, their structural integrity is crucial for overall aircraft safety. The potential failure of the wing-fuselage attachment lug would almost certainly result in wing loss and, subsequently, loss of life. As a result, special attention must be devoted to the fatigue design of these parts. Since lugs are the most heavily loaded components, their load-bearing capacity must be checked in accordance with recommendations defined by aviation regulations. During the service, the highest stresses are expected to occur in the region around the attachment lug's hole; thus, potential fatigue damage could occur and spread in this area. To prevent this, materials used in the wing-fuselage attachment manufacturing are expensive high strength fatigue-resistant alloyed steels and according to Federal Aviation Administration (FAA) regulations these attachments are not the subject of experimental verifications since they are designed as safe-life components.

However, some recent events in commercial aviation indicate that damages in the wing-fuselage attachment might occur quite unexpectedly. Cracks were found on the pickle forks (parts of the wing-fuselage attachment of Boeing 737NG jets) with less time in service than meets the threshold for mandatory inspections. The cracking issue has led many airlines to check their airplanes and it's reported that approximately 50 jets have been grounded worldwide in a search of a solution for this problem. Thus, numerical investigation of this kind of attachment is absolutely justified since the evaluation of aircraft safety is of the highest importance.

The research presented in this thesis was based on three main steps: i) analytical evaluation of loads acting on the wing of the light aerobatic aircraft during the flight, ii) experimental analysis of real aerobatic aircraft wing under presumed loads, and iii) numerical evaluation – based on the use of the extended finite element method (XFEM) and finite element method (FEM) – of stress intensity factors (SIFs) in the case of fatigue crack occurrence in the wing-fuselage attachment lug (SIF values are the most important for fatigue life estimation). All three steps are connected since the results of one step are used in others with the ultimate goal: to achieve the best design of lugs which will significantly increase the fatigue life of damaged lug and prevent catastrophic consequences.

Experimental analysis of full-scale wing was carried out for the purpose of numerical model verification. Comparisons of deformations measured and deformations calculated in FE simulations of aircraft wing deflection under load showed very good agreement, also confirming that loads acting on the wing-fuselage attachment lug were accurately evaluated in the analytical step. The detailed analysis has shown that the total maximum axial force transferred to lug by pin would be $P_{ax,max} = 208,830.7$ N, whereas the maximum transverse force would be $P_{tr,max} = 20,177.3$ N.

Then, to demonstrate how dangerous the crack appearance could be and to estimate the residual strength and fatigue life of the cracked component, a finite element model of the actual attachment lug was made, and analyses were carried out using the maximum forces. It was assumed that due to very high stress both the corner crack and through crack may appear in the lug, i.e. that there is a possibility of damage presence which does not spread throughout the whole thickness of the lug and a possibility of the appearance of damage through the whole thickness. The idea was to compare the growth of the corner crack with the growth of the through crack, both located at the same position, and then to assess the risk of losing the integrity of wing-fuselage attachment once the crack has occurred. The calculated number of cycles to complete failure (obtained with the help of Paris law and using XFEM in Abaqus) was – as expected – low, confirming the fact that the actual attachment lugs must be redesigned using a fail-safe approach.

The assessment of obtained values of a number of cycles in XFEM analysis might be a problem since the experimental data are missing; thus, classical FEM was used to evaluate the number of cycles

obtained by XFEM. The same geometry was imported into Ansys Workbench and the simulation based on the use of Unstructured Mesh Method (UMM) and Separating Morphing and Adaptive Remeshing Technology (SMART) was carried out, achieving very similar results. Differences in calculated mean values of SIFs are not significant (XFEM results are somewhat higher), while the evaluated number of cycles in Ansys is close to the number obtained using XFEM. It is important to point out that – unlike the XFEM where the same mesh is used through the whole simulation – mesh around the crack front in Ansys changes and adapts with every growth step for the purpose of better capturing the field values around the crack front nodes.

Finally, after completing the above-mentioned three steps, in the final phase of work alternative designs of the wing-fuselage attachment were analyzed with the goal of achieving longer fatigue life of the damaged lug (fail-safe approach). Several geometrical parameters have been changed during the redesign process with a predefined target: increase of the number of cycles until complete failure. The new proposed design of lug brings increased mass (but not a significant increase when compared to the mass of whole attachment), but significantly improved fatigue life which reduces the possibility of lug failure before the crack is observed in regular maintenance inspections.

Key words: XFEM, Fatigue crack growth, Wing-fuselage attachment lug, Light aerobatic aircraft

Scientific field: Mechanical Engineering

Scientific subfield: Aerospace Engineering

UDK number: 629.735:621.791.05: 539.42(043.3)

Сажетак

Ушке окова са носећом осовиницом најодговорније су за пренос оптерећења са крила на труп током лета, па је њихов структурни интегритет кључан за укупну безбедност летелице. Потенцијални лом ушки окова везе крило-труп скоро сигурно би резултирао губитком крила и, последично, губитком живота путника. Због тога се посебна пажња мора посветити пројектовању ових елемената са аспекта лома услед замора. С обзиром да су ушке најоптерећенији делови окова, њихова носивост се мора проверити у складу са препорукама дефинисаним ваздухопловним прописима. Очекује се да ће током радног века доћи до појаве великих напрезања у области око отвора ушки; стога би се у овом подручју могле појавити и проширити прслине као резултат замора материјала. Да би се то спречило, материјали који се користе у производњи окова везе крило-труп јесу легирани челици високе чврстоће отпорни на замор и према прописима Федералне управе за ваздухопловство (ФАА) окови нису предмет експерименталних провера јер се пројектују као тзв. *safe-life* компоненте на којима током века није дозвољена појава било каквог оштећења.

Међутим, неки недавни догађаји у комерцијалном ваздухопловству указују на то да би оштећења на вези крило-труп могла настати сасвим неочекивано. Откривене су прслине на тзв. носећим виљушкама (деловима везе крило-труп трупа авиона Boeing 737NG) пре времена предвиђеног за обавезни преглед овог склопа. Проблем уочених прслина навео је многе авио компаније да провере своје авионе и око 50 млазних летелица приземљено је широм света у потрази за решењем проблема. Стога је нумеричко истраживање ове врсте везе апсолутно оправдано јер је процена безбедности кључних делова авиона од највећег значаја за сигурност летелице и путника.

Истраживање представљено у овој тези засновано је на три основна корака: 1) аналитичкој процени оптерећења која делују на крило лаког акробатског авиона током лета, 2) експерименталној анализи реалног крила акробатског авиона изложеног претпостављеним оптерећењима, и 3) нумеричкој процени – заснованој на употреби проширене методе коначних елемената (ПМКЕ) и методе коначних елемената (МКЕ) – фактора интензитета напона (ФИН) у случају појаве заморне прслине на ушкама окова везе крило-труп (правилно израчунате вредности ФИН-а најважније су за добру процену века елемента изложеног замору). Ова три корака су повезана јер се резултати из једног користе у другом с јасним циљем: остварити најбољи дизајн ушки који ће значајно повећати њихов век под замором кад се појави прслина и тиме спречити катастрофалне последице.

У циљу верификације нумеричког модела извршена је експериментална анализа крила у пуној величини. Поређења измерених деформација и израчунатих деформација у МКЕ симулацијама угиба крила авиона под оптерећењем, показала су веома добро слагање, потврђујући да су оптерећења која делују на ушку окова везе крило-труп добро процењена у аналитичком кораку. Детаљна анализа је показала да би укупна максимална аксијална сила пренета на ушку преко осовинице била $P_{ax,max} = 208,830.7 \text{ N}$, док би максимална трансверзална сила била $P_{tr,max} = 20,177.3 \text{ N}$.

Затим, како би се проучило колико би појава прслине могла бити опасна и како би се проценила преостала чврстоћа и век трајања под замором оштећене компоненте, направљен је модел коначних елемената ушке окова и спроведене су анализе коришћењем максимални вредности сила. Претпостављено је да се због врло великог напрезања на ушки могу појавити и угаона и продорна прслина, односно да постоји могућност појаве оштећења које не иде по целој дебљини ушке и могућност појаве оштећења по целој дебљини. Идеја је била да се упореди раст угаоне прслине са растом продорне (дубинске) прслине, обе смештене на истој позицији, а затим да се процени ризик од губитка интегритета окова везе када дође до појаве оштећења. Израчунати број циклуса до потпуног лома (добијен помоћу Парисовог закона коришћењем ПМКЕ у Abaqus-у) био је очекивано низак, што потврђује чињеницу да се пројектоване ушке окова морају

редизајнирати коришћењем тзв. *fail-safe* приступа који дозвољава појаву и раст прслине до одређене дужине.

Процена добијеног броја циклуса коришћењем ПМКЕ може представљати проблем јер не постоје експериментални подаци о расту прслина на оковима; стога је класична МКЕ коришћена за процену броја циклуса добијених у Abaqus-у. Иста геометрија је увезена у Ansys Workbench и извршена је нумеричка симулација заснована на коришћењу методе неструктуриране мреже (МНМ) и SMART технологије инкорпориране у Ansys Workbench: добијени су врло слични резултати онима из Abaqus-а. Разлике у израчунатим средњим вредностима ФИН-ова нису биле значајне (вредности добијене коришћењем ПМКЕ су нешто више), док је процењени број циклуса у Ansys-у близу броја циклуса добијеног у Abaqus-у. Важно је истаћи да се – за разлику од ПМКЕ где се иста мрежа користи током целе симулације – мрежа око фронта прслине у Ansys-у мења и прилагођава са сваком кораком раста у сврху бољег „хватања“ вредности поља око чворова мреже у близини фронта прслине.

Коначно, након што су завршена сва три корака, у завршној фази рада анализирани су алтернативни облици ушке окова везе крило-труп са циљем да се постигне дужи век трајања оштећене ушке коришћењем *fail-safe* приступа. Неколико геометријских параметара је варирано током процеса редизајна са унапред дефинисаним циљем: повећати број циклуса до потпуног лома услед замора. Нови предложени дизајн ушке доноси повећану масу (али не и значајно повећану у поређењу са масом читавог окова), али и значајно побољшан век под замором што смањује могућност потпуног лома ушки пре него што се оштећење примети у редовним прегледима као делу одржавања летелице.

Кључне речи: ПМКЕ, Раст заморне прслине, Ушка окова везе крило-труп, Лак акробарски авион

Научна област: Област техничких наука, машинство

Ужа научна област: Ваздухопловство

УДК број: 629.735:621.791.05: 539.42(043.3)

Nomenclature

L_T	Horizontal tail lift (N)
L_W	Wing Lift (N)
M_{AC}	Mean aerodynamic centre
x_{AC}	Position of aerodynamic centre (m)
$x_{C.G}$	Position of centre of gravity (m)
$x_{C.G\ nom}$	Position nominal of centre of gravity (m)
FT	Transversal forces due to aerodynamic loading (N)
MF	Bending moment due to aerodynamic loading (N)
X_{cp}	Positions of center of pressure (m)
Fr	Equivalent concentrated forces (N)
Fr_t	Total Equivalent concentrated forces (N)
M_f	Equivalent concentrated moment (Nm)
M_{rf}	Total Equivalent concentrated moment (Nm)
q	Aerodynamic load per unit length (N/m)
P	local pressure (N/m ²)
S_E	Area of elliptic wing (m ²)
$CE(y)$	Local chord of equivalent elliptic wing (m ²)
c_{SE}	Chord of equivalent elliptic wing at plane of symmetry (m)
$Z(y)$	Local upward force (N)
$L(y)$	Local lift force (N)
\bar{m}	Mass of the wing per unit span (N/m))
$MT(Y)$	Local torsion moment (N.m)
$Ma(Y)$	Aerodynamic moment about aerodynamic center (Nm)
$X_o (N)$	Main spar reaction in X direction (N)
$Y_o (N)$	Main spar reaction in Y direction (N)
$Z_o (N)$	Main spar reaction in Z direction (N)
$Y_l (N)$	Main spar reaction in Y direction (N)
$Z_l (N)$	Main spar reaction in Z direction (N)
m_F	Mass of fuel (kg)
m_w	mass of the half empty wing (kg)
\vec{G}	Gravity force (m/s ²)
C_f	Friction coefficient
α_n	Root section incidence angle (deg)
α_w	Induced angle from the wing in tail region (downwash angle) v(deg)
α	Angle of attack (deg)
AR	Aspect ratio
b	Wing span (m)
c	Wing Chord (m)
C_L	Lift coefficient of the airplane
C_D	Drag coefficient of the airplane
CG	Airplane center of gravity
C_{Mac}	Moment coefficient about aerodynamic center
g	Gravity acceleration $g = 9.81(m/s)^2$
MS	Margin of safety
n	Load factor

n_1	Airplane positive maneuvering limit load factor
n_2	Air plane negative maneuvering limit load factor
n_3	Load factor on wheels
ρ	Air density (kg/m^3)
S_w	Wing area (m^2)
$S.f$	Factor of safety
V	Airspeed (m/s)
V_A	Design maneuvering speed (m/s)
V_C	Design cruising speed (m/s)
V_D	Design diving speed (m/s)
V_{DF}	Design flap speed (m/s)
V_{NE}	Never exceed speed (m/s)
V_S	Stalling speed (flaps retracted) (m/s)
V_{SF}	Stalling speed (flaps full extended) (m/s)
a	Crack length (m)
a_0	Initial crack length (m)
E	Young's modulus
F	Applied force (N)
K	Stress intensity factor ($MPa\ mm^{0.5}$)
K_I	Mode-I stress intensity factor ($MPa\ mm^{0.5}$)
K_{II}	Mode-II stress intensity factor ($MPa\ mm^{0.5}$)
K_{III}	Mode-III stress intensity factor ($MPa\ mm^{0.5}$)
K_{eff}	Effective stress intensity factor ($MPa\ mm^{0.5}$)
ν	Poisson's ratio
c	Constant (in Paris equation)
m	Constant (in Paris equation)
da/dN	Fatigue crack growth rate (mm/Cycle)
ΔK	Stress intensity factors range
R	Stress ratio
N	Number of cycles
X_{Gw}	Wing c.g in x direction (m)
X_{Gw}	Wing c.g in y direction (m)
X_{Gw}	Wing c.g in z direction (m)
X_{GF}	Fuel c.g in x direction (m)
X_{GF}	Fuel c.g in y direction (m)
X_{GF}	Fuel c.g in z direction (m)

Abbreviations

EASA	European Aviation Safety Agency
FAR	Federal Aviation Regulations
SIF(s)	Stress Intensity Factor
XFEM	Extended Finite Element Method.
LEFM	Linear Elastic Fracture Mechanics
CTOD	Crack Tip Opening Displacement
FEM	Finite Element Method
BEM	Boundary Elements Method
GFEM	Generalized Finite Element Method
DEM	The Displacement Extrapolation Method

SN	Stress Level Versus Number of Cycles (curve)
VCCT	Virtual Crack Closure Technique
GDC	Generalized Form Displacement Correlation Method
MCCI	Modified Crack Closure Integral
PUM	Partition of Unity Method
DOF	Degrees of freedom
UMM	Unstructured Mesh Method
PUFEM	Partition of unity finite element method

Table of Contents

1	INTRODUCTION.....	2
1.1	Background and Motivation	2
1.2	Literature review.....	2
1.3	Objective and thesis organization.....	7
1.3.1	Objective	7
1.3.2	Thesis organization	7
➤	In the fourth chapter Numerical Determination of Loading of Wing-Fuselage Fitting "Based on the data obtained in previous chapter in this chapter the determination of the wing- fuselage attachment load was carried out."	8
2	Linear-Elastic Fracture Mechanics.....	10
2.1	Fracture Mechanics and Fatigue	10
2.2	Stress Concentration	10
2.3	Analytical calculations	11
2.3.1	Stress Intensity Factors	13
2.3.2	Fracture modes.....	14
I.	Mode I.....	14
II.	Mode II	14
III.	Mode III.....	15
IV.	Mixed mode	15
2.3.3	The Energy Release Rate.....	15
2.3.4	J-integral.....	15
2.3.5	Fatigue Crack Propagation.....	16
2.3.6	Description of the fatigue phenomenon	17
2.3.7	Fatigue crack growth regions.....	19
2.3.8	Crack growth.....	19
2.3.9	Crack closure.....	23
2.3.10	Effect of Residual Stresses on Crack Propagation.....	24
3	DETERMINATION OF LOADS ACTING ON THE WING and PIN-LUG WING ATTACHMENT	27
3.1	Equilibrium equations:	27
3.2	DETERMINATION OF LOADS ACTING ON THE WING and PIN-LUG WING ATTACHMENT.....	27
3.2.1	C.G. at D_0.23	28
3.2.2	C.G. at D_0.28	29

3.2.3	Case D Loads	29
3.2.4	Case A.....	31
3.2.5	Case E.....	33
3.2.6	Case G	35
3.2.7	Overview of defined cases Table 3.1.....	36
3.3	Approximate span-wise distribution of aerodynamic load	37
3.4	Loading of wing	40
3.5	Analysis of the wing structure using finite element method.....	40
3.6	Load distribution along the chord	43
3.7	Flap and aileron loading	45
3.8	Inertial loading (constant chord) Case D_0.23	46
3.8.1	Moment due to aerodynamic loading:	47
3.8.2	Distributed loading due to inertial loading in case <i>D_023</i>	47
3.8.3	Distributed loading due to inertial loading in case <i>E_023</i>	48
3.9	Finite element model of the wing structure.....	50
3.10	RESULTS OF FINITE ELEMENT ANALYSIS	53
4	Numerical Determination of Loading of Wing-Fuselage Fitting	57
4.1	Loads on wing	57
4.1.1	Input data	58
4.1.2	Load cases	59
4.1.3	Deflection of Elevator to Balance Airplane	62
4.1.4	Summary of Aerodynamic Parameters.....	62
4.2	Reactions of Supports (Internal forces and moments):	64
4.3	Characteristic point coordinates.....	64
4.4	Equilibrium of forces:	64
4.5	External forces.....	65
4.5.1	Lift force.....	65
4.5.2	Drag force	65
4.5.3	Gravity force.....	67
4.6	Design fuel load.....	67
4.7	External Moments	69
4.7.1	Moment due to Lift force:	69
4.7.2	Moment due to Drag force:	71
4.7.3	Moment due to Gravity forces:.....	71
4.7.4	Equilibrium of Moments:	71

4.7.5	Load Distribution over Wing.....	72
4.7.6	Overview of Maximum Loading Cases	74
4.8	Fittings Analysis	75
4.9	Main Spar.....	75
4.9.1	Applied Load Cases	76
4.9.2	Axial load analysis.....	77
4.9.3	Transverse load analysis.....	82
5	NUMERICAL CRACK PROPAGATION ANALYSIS	85
5.1	Introduction	85
5.2	Finite element method (FEM)	85
5.2.1	The effect of the mesh	86
5.3	Extended Finite Element Method (XFEM).....	86
5.3.1	Introduction.....	86
5.3.2	Partition of unity	87
5.3.3	Enrichment functions	89
5.3.4	The Heaviside function	89
5.3.5	Asymptotic near-tip field functions.....	90
5.3.6	Level set method for modelling discontinuities	91
5.3.7	Numerical integration and convergence	93
5.3.8	XFEM implementation in ABAQUS	94
5.3.9	Improved Finite Element Method	94
5.3.10	Finite Element Analysis of the Wing-fuselage Attachment Lug.....	95
5.3.11	XFEM analysis of the crack growth in the lug.....	97
5.3.12	XFEM simulation of the corner crack growth	98
5.3.13	XFEM simulation of the through crack growth.....	100
5.3.14	Improved FEM analysis of the crack propagation in the lug	102
6	EXPERIMENTAL VERIFICATION of NUMERICALLY OBTAINED LOAD	106
6.1	Test setup.....	110
6.2	Determination of loads for critical case D and whiffle-tree system dimensions.....	111
6.3	Wing test loading and obtained displacements at the wing tip	118
7	OPTIMIZATION of THE WING-FUSELAGE ATTACHMENT LUG	121
7.1	Model number 1: Original lug with increased thickness.....	123
7.2	Model number 2: Two-parameter optimization of lug	126
7.3	Model number 3: Three-parameter optimization of lug	129

7.4	Model number 4: Different combination of three parameters.....	133
7.5	Comparison of results	135
8	CONCLUSION.....	138
	References	141

List of Figure

Figure 1.1 Light aircraft wing-fuselage attachment (circled) with two pairs of lugs	3
Figure 2.1 A prototype of a notched part (strip with central hole)	10
Figure 2.2 An elliptical hole with stress concentration.....	11
Figure 2.3 Hole shape and its effect on Kt	12
Figure 2.4 Factors of different phases of the fatigue life.	13
Figure 2.5 Three types of cracks are shown by Photo-elastic picture.....	13
Figure 2.6 The three basic crack loading types in Mode I, Mode II, and Mode III of fracture mechanics	14
Figure 2.7 Counter clockwise loop around the crack tip with a clockwise loop	16
Figure 2.8 Fatigue loading vs number of cycles	17
Figure 2.9 Stress vs. number of cycles curves for low-carbon steel 1045 and AA 2014	17
Figure 2.10 Ewing & Humfrey showed crack surface in 1903.....	18
Figure 2.11 Linear correlation between crack growth rate da/dN and stress intensity factor K on a log-log scale (Paris' Law)	18
Figure 2.12 The rate of crack growth in different regions	19
Figure 2.13 (a)Crack length vs number of cycles, and (b) $\log da/dn$ vs $\log dK$	20
Figure 2.14 Mean stress effect on fatigue crack for Aluminium alloys.....	21
Figure 2.15 Constant amplitude fatigue crack growth under small yielding conditions	23
Figure 2.16 Elber's principle of crack closure theory.....	24
Figure 2.17 The reverse plastic zone forms during periodic loading [48].....	25
Figure 3.1 Forces acting during symmetric equilibrium manoeuvre.....	27
Figure 3.2 Variations of a position of the centre of gravity	28
Figure 3.3 Span-wise distribution of aerodynamic loading	38
Figure 3.4 Shear forces due to aerodynamic loading.....	39
Figure 3.5 Bending moment due to aerodynamic loading	39

Figure 3.6 Chord wise distribution of p for A023 and D023 cases	40
Figure 3.7 Numbers of points i x and y directions at which the forces are applied.....	42
Figure 3.8 Numbers of applied forces at nodes on lower side of ribs	42
Figure 3.9 Ribs Positions and numbers.....	42
Figure 3.10 Stringer with an effective thickness of skin.....	43
Figure 3.11 Functions for chord-wise load distribution.....	45
Figure 3.12 Actual chord-wise pressure distributions at positions of ribs Case D0.23	45
Figure 3.13 Distributions of applied equivalent forces at nodes of ribs Case D0.23.....	45
Figure 3.14 Actual and assumed distributed loads over flap and aileron for D_023 load case.....	46
Figure 3.15 Shear forces due to inertial loading of the wing.....	48
Figure 3.16 Span-wise distribution of bending moment due to inertial loading.....	48
Figure 3.17 Transversal forces due to inertial loading of wing	49
Figure 3.18 Span-wise distribution of bending moment due to inertial loading.....	50
Figure 3.19 Wing structure – without skin	50
Figure 3.20 Finite element model of the wing structure – with skin	51
Figure 3.21 Finite element model of the wing structure – without skin	51
Figure 3.22 Example of applied aerodynamic loads: CASE 023	52
Figure 3.23 Case E_0.23: Loading of wing structure $J = 1.0$ applied at ribs.....	52
Figure 3.24 Fittings and constrained displacements of wing.....	53
Figure 3.25 Deformed and undeformed configuration of wing structure for CASE D_023 $J=1.0$ (maximum displacement at the tip of the wing is 63.3 mm)	53
Figure 3.26 Deformed and undeformed configuration of wing structure for CASE D_0.23 $J=1.55$ (maximum displacement at the tip of the wing is 98.1 mm)	54
Figure 3.27 CASE D_0.23 $J=1.0$ total displacements, maximum displacement 35.9 mm.....	54
Figure 3.28 CASE D_0.23 $J=1.55$ Total displacements, maximum displacement 55.6 mm.....	55
Figure 4.1 Airplane geometry (all dimensions in mm).....	57
Figure 4.2 Loads and reactions	58

Figure 4.3 Definition of horizontal tail angle of attack.....	61
Figure 4.4 Friction Coefficient.....	66
Figure 4.5 Form Factor	67
Figure 4.6 (a) Double Shear; (b) Multiple Shear or Finger Type	75
Figure 4.7 Connections Points in the Fitting of Main Spar	76
Figure 4.8 Applied load cases for axial and transverse.....	77
Figure 4.9 Lug tension and shear-tear out failures.....	77
Figure 4.10. Axial Loading	78
Figure 4.11 Axial Loading	79
Figure 4.12 Pin Moment Arm for Determination of Bending Moment.....	80
Figure 4.13 Peaking Factor for Pin Bending.....	81
Figure 4.14 Failure mode of transverse load.....	82
Figure 4.15 Transverse Loading K_t	83
Figure 5.1 The cut and patch procedure of generating singular elements around a crack tip.....	85
Figure 5.2 Comparison of a crack path in FEM (left) and XFEM (right).....	87
Figure 5.3 Partition of unity of a circle with four functions	88
Figure 5.4 Evaluation of Heaviside function	90
Figure 5.5 The Enriched nodes in extended finite element method. [73].....	91
Figure 5.6 Construction of level set functions normal function for $\phi(x)$ and tangential function, $\psi(x)$	92
Figure 5.7 Picture of normal level set function of $\psi(x)$ for (a) 2D contour of $\psi(x)$ and (b) 3D contour of $\psi(x)$	92
Figure 5.8 Sub-triangulation of elements cut by a fracture.....	93
Figure 5.9 The dimensions of wing-fuselage attachment lugs used in the analysis	95
Figure 5.10 The stress distribution (a) in wing-fuselage attachment, (b) around the lower lug hole	96
Figure 5.11. The lug dimensions and forces necessary for evaluation of σ_t, max	96
Figure 5.12 The lug model used for XFEM analysis of crack growth.....	97

Figure 5.13 (a) Initial penny-shaped crack in hexahedral mesh, and (b) crack after 6th step of propagation	98
Figure 5.14 (a) Initial penny-shaped crack in tetrahedral mesh, and (b) crack after 6th step of propagation	98
Figure 5.15. Number of cycles vs crack depth for hexahedral and tetrahedral mesh	100
Figure 5.16 (a) Initial through crack, and (b) through crack after 9th step of propagation	101
Figure 5.17 Von Mises stresses after 9th step of through crack growth	102
Figure 5.18 Von Mises stresses after “opening” of through crack in Ansys simulation	103
Figure 5.19 Von Mises stresses and the crack shape at the end of propagation (magnified view)	103
Figure 5.20 The mean K_I values calculated for the through crack growth using XFEM and FEM	104
Figure 5.21 Crack depth vs number of cycles graphs obtained using XFEM and FEM	104
Figure 6.1 Prototype of the wing used in experiments	106
Figure 6.2 Completely functional flap and aileron	107
Figure 6.3 Rib number 11 and pins (circled) used to connect the central spar to steel plate.....	107
Figure 6.4 Steel plate (circled) with holes used to fix the wing and hold it in a horizontal position ...	108
Figure 6.5 Test bench consisting of 6 I-beams carries the wing prototype during experiments	108
Figure 6.6 Strain gauges used to monitor deflections and strains on the upper surface of the wing	109
Figure 6.7 Strain gauges used to monitor deflections and strains on the lower surface of the wing	109
Figure 6.8 Data from Catman software exported to MS Excel.....	109
Figure 6.9 Scheme of the whiffle-tree for wing structure testing	110
Figure 6.10 Hydraulic jack (with force transducer) used to apply loads on the wing	111
Figure 6.11 Designed whiffle-tree system for wing structure testing (CATIA drawing).....	111
Figure 6.12 Load ($L - W$) distribution along the span.....	113
Figure 6.13 Moment distribution along the span	113
Figure 6.14 Moment calculated at ribs’ positions (orange squares) vs moment distribution	114
Figure 6.15 Screenshot of MS Excel file used to design the whiffle-tree	115
Figure 6.16 Forces, moments, and dimensions of the whiffle-tree.....	115

Figure 6.17 Whiffle-tree is not introducing the force on the 11 th rib.....	116
Figure 6.18 Test assembly for the light aerobatic aircraft wing	117
Figure 6.19 Test assembly for the light aerobatic aircraft wing (view from the other side).....	117
Figure 6.20 Graph of displacements at the wingtip	119
Figure 7.1 Finite element mesh used in optimization	121
Figure 7.2 SIF values along crack front after 1 st step of propagation (original lug).....	122
Figure 7.3 SIF values after 15 th step of propagation (total crack extension 7.37 mm).....	122
Figure 7.4 Crack length vs Number of cycles for original lug ($N_{max}=515$).....	123
Figure 7.5 Thickness of lug was varied by adding material perpendicularly to the highlighted face ..	123
Figure 7.6 Stress intensity factor (SIF) values along crack front after 1 st step of propagation.....	124
Figure 7.7 SIF values after 20 th step of propagation (total crack extension 6.84 mm).....	125
Figure 7.8 Maximum <i>KI</i> after crack opening for different lug thicknesses.....	125
Figure 7.9 Crack length vs Number of cycles for lug with thickness 17mm ($N_{max}=1085$)	126
Figure 7.10 Thickness of lug was varied along with the radius of the surface (highlighted)	126
Figure 7.11 Maximum <i>KI</i> (column D) and lug mass (column E) after crack opening.....	127
Figure 7.12 Response surface for different thicknesses and radii of lug	127
Figure 7.13 SIF values along crack front after 1 st step of propagation.....	128
Figure 7.14 SIF values after 14 th step of propagation (total crack extension 6.75 mm).....	128
Figure 7.15 SIF values after 23 rd step of propagation (total crack extension 10.89 mm).....	129
Figure 7.16 Crack length vs Number of cycles for lug with $t=17\text{mm}$ and $r=19\text{mm}$ ($N_{max}=1933$)	129
Figure 7.17 Thickness was varied by adding/removing material perpendicularly to the highlighted face	130
Figure 7.18 Radii of highlighted surfaces were varied	130
Figure 7.19 Initial crack position was kept constant with respect to the yellow surface.....	131
Figure 7.20 Generated design points with selected parameters ($r_1=14.5\text{mm}$, $r_2=7.5\text{mm}$, $t=17\text{mm}$)	131
Figure 7.21 SIF values along crack front after 1 st step of propagation.....	132

Figure 7.22 SIF values after 15th step of propagation (total crack extension 7.03 mm) 132

Figure 7.23 Crack length vs Number of cycles for three-parameter lug model 1 ($N_{max}=786$) 133

Figure 7.24 Generated design points with selected parameters ($r_1=19\text{mm}$, $r_2=7.5\text{mm}$, $t=12\text{mm}$) 134

Figure 7.25 SIF values along crack front after 1st step of propagation 134

Figure 7.26 SIF values after 15th step of propagation (total crack extension 7.09 mm) 134

Figure 7.27 Crack length vs Number of cycles for three-parameter lug model 2 ($N_{max}=824$) 135

Figure 7.28 Crack length vs Number of cycles for all five lug models (max extension 7mm) 136

List of Table

Table 3.1 Summary of defined cases	36
Table 3.2 Load cases at $y = 0$	40
Table 3.3 Results of Loads for Case D_0.23 for Transversal Forces and Bending Moments	41
Table 3.4 Results of Loads for Case E_0.23 for Transversal Forces and Bending Moments	41
Table 3.5 Load distribution of forces and pressure case D0.23.....	43
Table 3.6 Load distribution of forces and pressure case E0.23	43
Table 3.7 Load cases for Ribs	46
Table 3.8 Results of Inertial Loads case D_0.23	47
Table 3.9 Results of Inertial Loads case E_0.23	49
Table 4.1 Load cases data	59
Table 4.2 Aerodynamic Parameters at Envelope Point A ($\delta_F = 0^\circ$, $\delta_A = 0^\circ$, $n = 6.0$, $V = 66.87m/s$)	62
Table 4.3 Aerodynamic Parameters at Envelope Point D ($\delta_F = 0^\circ$, $\delta_A = 0^\circ$, $n = 6.0$, $V = 107.22 m/s$) ..	63
Table 4.4 Aerodynamic Parameters at Envelope Point E ($\delta_F = 0^\circ$, $\delta_A = 0^\circ$, $n = -3.0$, $V = 107.22 m/s$) .	63
Table 4.5 Aerodynamic Parameters at Envelope Point G ($\delta_F = 0^\circ$, $\delta_A = 0^\circ$, $n = -3.0$, $V = 42.25 m/s$) ...	63
Table 4.6 Aerodynamic Parameters at Envelope Point AA+ ($\delta_F = 0^\circ$, $\delta_A = 15^\circ$, $n = 4.0$, $V = 66.87m/s$)	64
Table 4.7 Aerodynamic Parameters at Envelope Point AA- ($\delta_F = 0^\circ$, $\delta_A = -23^\circ$, $n = 4.0$, $V = 66.87m/s$)	64
Table 4.8 Aerodynamic Parameters at Envelope Point DA+ ($\delta_F = 0^\circ$, $\delta_A = 5.0^\circ$, $n = 4.0$, $V = 107.22m/s$)	64
Table 4.9 Aerodynamic Parameters at Envelope Point DA- ($\delta_F = 0^\circ$, $\delta_A = -7.7^\circ$, $n = 4.0$, $V = 107.22m/s$)	64
Table 4.10 Aerodynamic Parameters at Envelope Point AF ($\delta_F = 30^\circ$, $\delta_A = 0.0^\circ$, $n = 2.0$, $V = 33.5m/s$)	64
Table 4.11 Aerodynamic Parameters at Envelope Point AFA+ ($\delta_F = 30^\circ$, $\delta_A = 15^\circ$, $n = 2.0$, $V = 33.5m/s$)	64
Table 4.12 Aerodynamic Parameters at Envelope Point AFA- ($\delta_F = 30^\circ$, $\delta_A = -23^\circ$, $n = 2.0$, $V = 33.5m/s$)	64
Table 4.13 Aerodynamic Parameters at Envelope Point DFA+ ($\delta_F = 30^\circ$, $\delta_A = 5.0^\circ$, $n = 2.0$, $V = 49.14m/s$)	64

Table 4.14 Aerodynamic Parameters at Envelope Point DFA- ($\delta_F = 30^\circ$, $\delta_A = -7.7^\circ$, $n = 2.0$, $V=49.14m/s$)	64
Table 4.15 Aerodynamic Parameters at Envelope Point AH ($\delta_F = 0^\circ$, $\delta_A = 0.0^\circ$, $n = 1.0$, $V=66.87m/s$)	64
Table 4.16 Aerodynamic Parameters at Envelope Point DH ($\delta_F = 0^\circ$, $\delta_A = 0.0^\circ$, $n = 1.0$, $V=102.22m/s$)	64
Table 4.17 Fuel Weight Effect Case A	68
Table 4.18 Fuel Weight Effect Case D	68
Table 4.19 Fuel Weight Effect Case E	69
Table 4.20 Fuel Weight Effect Case G	69
Table 4.21 Support Reactions at case A, at point A, ($\delta_F = 0^\circ$, $\delta_A = 0^\circ$, $n = 6.0$, $V = 67.12 m /s$)	73
Table 4.22 Support Reactions at case D, at point D, ($\delta_F = 0^\circ$, $\delta_A = 0^\circ$, $n = 6.0$, $V = 107.22m /s$)	73
Table 4.23 Support Reactions at case E, at point E, ($\delta_F = 0^\circ$, $\delta_A = 0^\circ$, $n = -3.0$, $V = 107.22m /s$)	73
Table 4.24 Support Reactions at case G, at point G, ($\delta_F = 0^\circ$, $\delta_A = 0^\circ$, $n = -3.0$, $V = 46.65m /s$)	74
Table 4.25 Maximum Loading Cases	74
Table 4.26 The reaction used for the lug analysis	76
Table 5.1 SIF values calculated for corner crack growth in the lug model with hexahedral mesh	99
Table 5.2 SIF values calculated for corner crack growth in the lug model with tetrahedral mesh	99
Table 5.3 SIF values calculated for through crack growth in the lug model with hexahedral mesh	101
Table 6.1 Load and moment distribution along the span for case D, $n=6$ (without fuel)	112
Table 6.2 Calculated loads and moments at ribs	114
Table 6.3 Force and moment at each rib for the whiffle-tree configuration shown in Figure 6.16 Forces, moments, and dimensions of the whiffle-tree	115
Table 6.4 Values of forces and displacements measured at 10 wing locations	118
Table 6.5 Values of forces and displacement measured by sensors S10 and S11	119
Table 7.1 Values of maximum SIFs after crack opening for different thicknesses	124
Table 7.2 Comparison of properties for five lug models	136

CHAPTER 1

INTRODUCTION

1 INTRODUCTION

1.1 Background and Motivation

The wing spar is connected to the supporting elements of the aircraft fuselage through specially designed elements-aircraft fittings. In most cases, to the main frame of the fuselage. All loads from the wing are transmitted to the main frame and through the wing-fuselage fitting.

It is needless to point out the extreme importance of the accurate design of this fitting: its fatigue damage leads to an immediate separation of the wing from the fuselage and a consequent loss of aircraft. During the flight, fatigue cracks appear on the parts of the wing exposed to tensile stresses. These cracks are monitored, and certain measures are taken when they reach a critical length, but their appearance is not tolerated in the wing-fuselage fittings. This is also the reason why the cracks growth in these has not been studied so far and why the experimental tests of the remaining fatigue life of the damaged fitting were not required from the manufacturer.

This, of course, does not mean that fatigue cracks did not appear and that they cannot appear in practice: a few recent cases, which only by sheer luck did not turn into tragedies, confirm this. Namely, in November 2019, the appearance of fatigue cracks on the wing-fuselage fitting for two Boeing 737 NG aircraft was reported by the Indonesian Airline Lion Air. These cracks were accidentally discovered before their regular inspection [1].

After that, over 50 aircraft of this type were landed around the world to determine the condition of their wing-fuselage fitting (Ryanair discovered 3 cracked wing-fuselage fitting in its fleet) [2]. The institutions of the international aviation authorities in charge of aircraft safety are now widely considering the introduction of mandatory fatigue tests for damaged fittings to estimate their remaining fatigue life.

By redesigning the wing-fuselage attachment, it is possible to extend the life even in the event of damage, but this will not change the long-adopted approach (safe-life) in their design. The intention is to increase the aircraft's safety and guarantee it even in the event of unforeseen damage. Of course, the question arises about the size of the "safe" damage to the fitting, i.e., the crack size that will not lead to its failure.

The answer to this question can be given most precisely by experiments that are often time-consuming and expensive. As a suitable alternative to the experimental verification of a newly designed (or modified) fitting, numerical modelling is imposed. Over the years, many numerical techniques, such as the finite element method (FEM), the boundary element method (BEM), the mesh less process, and the extended finite element method (XFEM), have been presented to simulate fracture mechanics problems, such as fatigue crack growth.

By using XFEM, a conformal mesh is not required, which makes modelling of variable discontinuities or crack growth significantly simplified. On the other hand, by applying the Unstructured Mesh Method (UMM), FEM has been improved by enabling alteration of the finite element mesh only in the immediate vicinity of the crack, which considerably simplifies the modelling of crack propagation with this method as well.

1.2 Literature review

Pin-loaded attachment lugs (Figure 1.1) are the most responsible for wing-to-fuselage load transfer during the flight and, therefore, their structural integrity is crucial for overall aircraft safety. The potential failure of the wing-fuselage attachment lug would almost certainly result in wing loss and, subsequently, loss of life.

As a result, these parts have to be carefully designed as far as fatigue is concerned. The load-bearing capacity of the lugs must be checked following recommendations defined by the aviation regulations since they are the most heavily loaded components.

During the service, the highest stresses are likely to occur in the region around the attachment lug's hole; thus, potential fatigue damage could occur and spread in this area. In order to avoid this, materials used in the wing-fuselage attachment manufacturing are expensive high strength fatigue-resistant alloyed steels.

Lugs are redesigned and optimised regularly to reduce costs while maintaining required safety, but new shape must be approved before manufacturing.

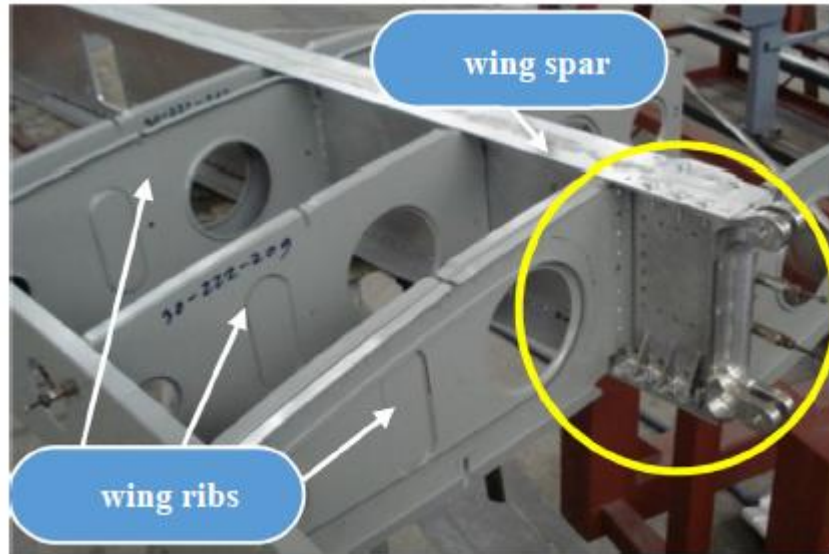


Figure 1.1 Light aircraft wing-fuselage attachment (circled) with two pairs of lugs

Many researchers have made great efforts to analyse the fatigue behaviour of different types of aircraft attachment lugs and fittings.

Many researchers concentrated their efforts on analysing the fatigue behaviour of the various types of aircraft attachment lugs and fittings.

S. Barter et al. (1994) [3]. Inspected two F/A-18 trailing-edge flap (TEF) hinge lugs, and large cracks were found to be present. These cracks were found in different regions around the monoball bearing hole, and they were similar. The surfaces of both hinge lug bearing holes indicated extensive pitting corrosion and, in one case, extensive fretting, while the fracture surfaces revealed clear proof of fatigue. They concluded that the crack growth rate was approximately 10 times quicker than the rate evaluated by the manufacturer, and it is likely to be accelerated by the corrosive environment. Therefore, the contributing factor in unexpected failure was corrosion fatigue. They suggested that performing a combined photography and laboratory investigation can find the reason for a failure and improve inspection methods to avoid future disastrous failures. Fractography offered the possible crack growth rate, which showed that non-destructive investigation (NDI) are needed frequently and sensitively. A new NDI procedure allowed for the detection of smaller cracks.

A three-dimensional boundary element method (BEM) and the J-integral were used by R.

Rigby and M. H. Aliabadi (1997) [4]. Used the BEM and mixed-mode J-integral to investigate crack behaviour in attachment lugs. Stress intensity factors for both single and two-quarter elliptical cracks were obtained for several crack length ratios and radius ratios. To evaluate the stress intensity factors for cracks at attachment lugs. Also, they used the BEM and mixed-mode J-integral to investigate crack

behavior in attachment lugs. Stress intensity factors for both single and two-quarter elliptical cracks were obtained for several crack length ratios and radius ratios.

C.R.F. Azevedo et al. (2002) [5]. Studied the failure of an aircraft landing gear; the failure was caused by the fracture of the outer cylinder lug. The results revealed clear evidence of both stable and unstable crack propagation caused by the orientation of the microstructure adjacent to the free surface. Moreover, the corrosion cavities located in a critical area and the severe loads absorbed by the outer cylinder during the landing procedure may be the reason for this failure.

Jong-Ho Kimu Honget et al. (2003) [6]. This research conducted by stress intensity factors for cracks passing through the thickness initiated from lug holes was compared using the weight function method, the boundary element method (BEM), interpolating the Brussat solution. The authors found that the prediction of fatigue crack growth based on the numerical stress intensity factor was quite similar to the experimental expectation. Also, it was found that the fatigue life of an attachment lug decreases as the clipping level increases because the clipping of high load cycles reduces the delay effect.

Katarina Maksimović et al. (2004) [7]. Suggested analytical and numerical methods for estimating fatigue crack growth life and calculating stress intensity factors for cracks at the attachment lugs. The stress intensity factor results obtained from finite element numerical methods were in good agreement with the analytical results for the damaged lugs. The presented analytical methods satisfy the requirements for damage tolerance analyses of lugs-type joints.

Lucjan Witek (2006) [8]. Analyze the failure of a wing-fuselage connector for an agricultural aircraft. The careful observation indicated that the original crack surface was covered with corrosion products; therefore, the failure had a combined fatigue and corrosion character. A method of nonlinear finite element was employed to analyse the stress state of the connector during the operating condition. The wing lug failure occurred due to the high-stress areas in the wing lug region. The results were then included in the total fatigue life (S-N) and crack initiation (e-N) analyses conducted for the load time history corresponding to 10 minutes of light operation. Visual inspection revealed a typical fatigue fracture with impact marks. The crack growth was accelerated by the corrosion which covered the crack original surface. It was clear that the extreme stress in the critical area of the lug was the main reason for premature fatigue failure. Based on his study, he advised redesigning the wing-fuselage connector for better fatigue durability.

A. Lanciotti et al. (2006) [9]. Examined two different specimens experimentally.

The first specimen was tested using constant amplitude loading to validate the fatigue crack growth rate data contained in NASGRO 4 software which is used for Damage Tolerance evaluations. This specimen was also tested under variable amplitude loading to validate crack growth models used in this study. The second specimen was tested using both constant and variable amplitude loading fatigue tests, a lug-fork joint designed as the actual joints present on the aircraft. They observed a higher crack propagation rate in the lug surface direction than in the lug thickness direction, in contrast to what was observed previously in the literature. Moreover, they observed that the crack shapes were not concerning variable amplitude loading or residual stress field produced during bushing installation. Also, they observed that fatigue life is increased more than five times when ForceMate bushings are used, compared to the shrink fit bushings.

Huan and Moan (2007) [10]. Presented the fatigue life to failure is evaluated through the crack growth concept. The behaviour of fatigue of the damaged lug is investigated to consider the effect of the lug head. The failure analysis results compared with the relevant experimental results show that the developed model can be used for a reliable estimate of the fatigue strength of the pin-loaded lug with crack through-the-thickness of a hole.

L. Allegrucci et al. in (2009) [11]. Examined a lever reverse of the canopy balancing system of an MB339 CD aircraft. The lever reverse forged a 7075-T6 aluminium alloy, was broken into two parts during a pre-flight inspection. Visual observation showed the failure of the lever reverse resulted from high-cycle fatigue caused by the application of an abnormal force due to an over length of the actuator

lugs. The corrosion pit also aggravated the fatigue. Visual observation indicated that an over the length of the actuator lugs caused a severe force on the lever reverse, resulting in high-cycle fatigue failure. A corrosion pit also boosted the fatigue.

Li-Ming Wu and et al. (2011) [12]. Built a finite element model of a straight attachment lug subjected to an oblique loading less than 45° using ANSYS software, a boundary condition of cosine pin-bearing pressure is assigned at the lug hole. By studying the influence of some dimensionless parameters such as crack length, radius ratio, and pin-load angle (β) on the SIFs values. The SIF expression for the straight attachment lug with a single through-the-thickness crack is determined and validated, which can be used to calculate the stress intensity factor's amplitude (ΔK). The fatigue crack growth model is established, and the fatigue crack growth behaviour of 30CrMnSiA straight attachment lugs was investigated analytically and experimentally.

N. Antoni and F. Gaisne (2011) [13]. Suggested analytical models for bush fitting and pin-loading condition, leading to an entire calculation of the stress distribution in the lug. Their results were verified by comparing them with that obtained from finite element numerical simulations, which show the validity of the adopted assumptions, such as geometric axisymmetry. The main phenomena of friction pin deformation and local plastic effects under pin-loading are considered to enhance the models. Based on stress or strain approaches, analytical fatigue models have been derived by considering a fatigue lifetime calculation of connecting lugs.

S. Mikheevskiy et al. (2012) [14]. Calculated stress intensity factor using the weight function method; this factor is essential for analysing fatigue crack growth. Also, they have determined the rate of load shedding by computing the amount of the load transferred through the cracked ligament with the help of the finite element method. Simulations of the fatigue crack growth under two-variable amplitude loading spectra have been conducted using the UniGrow fatigue crack growth model. They compared their computed results with experimental data to prove the ability of the UniGrow model to precisely predict fatigue crack growth behaviour of two-dimensional planar cracks under a complex stress field. Moreover, they have indicated that the relatively accurate prediction of fatigue lives of cracked bodies subjected to complex variable amplitude service loading spectra can be attained using appropriate 'memory rules' and the two-parameter driving force. The significance of the load shedding in lugs has been estimated by accounting to reduce the resultant load in the cracked cross-section. They also concluded that eliminating this in the fatigue crack growth analysis could result in a high underestimation of the life of fatigue crack growth.

Boljanović and Maksimović (2013) [15]. They proposed a computational model to assess the residual strength of a damaged lug subjected to cyclic loading. A crack through-the-thickness situation was theoretically studied by using fracture mechanics based on numerical and analytical models.

Mookaiya et al. (2013) [16]. Proposed a computational model used to analyse crack growth in the attachment lugs with single quarter-elliptical crack and those with single through-the-thickness crack. The proposed model also addresses the fatigue life estimation, the stress analysis and the crack path simulations. The commercial software ANSYS and quarter-point (Q-P) finite element were used to analyse the stress around the crack tip and estimate the stress intensity factor.

Naderi and Iyyer (2015) [17]. Used a three-dimensional finite element method (FEM) and extended finite element method (XFEM) available in ABAQUS to calculate the stress intensity factor (SIF) in straight lugs of Aluminium 7075-T6. Also, they estimated the crack growth and fatigue life of single through-thickness and single quarter elliptical corner cracks in the attachment lug. They have compared their results with the available experimental data for two different load ratios equal to 0.1 and 0.5. They concluded that the results of the SIF obtained from the XFEM indicate that the estimated fatigue life was significantly affected by the introduction of different loading boundary conditions.

Slobodanka Boljanović et al. (2017) [18]. They have developed a calculation procedure for evaluating the strength of a pin-loaded lug with a crack through the thickness. Cyclic loading with either constant

amplitude or an overload is applied to the lug. The constructed procedure considers both the calculation of the stress intensity factor and the assessment of the residual strength. The stresses are addressed through both analytical and numerical approaches. The fatigue life up to failure is calculated using Walker's two-parameter driving force model and the Wheeler retardation model for constant amplitude cyclic loads and overloads, respectively. The suggested crack growth procedure is evaluated by comparing the computed results with the experimental data available in the literature. A good agreement between the different results implies that the developed procedure offers a reliable estimation of the strength for a pin-loaded lug with a crack passing through the thickness under cyclic load. Besides, such a procedure is carried out to examine the differences between the residual fatigue life under constant amplitude loads and that under overloads. Finally, they analysed the effect of the width, the diameter of a hole and the thickness on the lug strength.

Abraham J. Pulickal et al. (2017) [19]. They considered the design of a Wing-Fuselage Lug attachment for a transport aircraft with a mid-wing configuration. They observed that the maximum elongation was at the spar only, and the maximum stresses were at the rivet holes that are close to the lugs. They also found that the best material that can be used for this design is Aluminium AA 2024 as it has a factor of safety of 2.15. They concluded that the material properties affect strains but not on stresses in FE calculations (linear elastic conditions). The calculated fatigue life obtained the maximum allowable working period of the designed wing-fuselage lug attachment.

Sumanth M H and Ayyappa T (2018) [20]. Study the wing-fuselage lug attachment bracket employed the finite element approach. This study was performed in two cases. In the first case, steel alloy AISI 4340 and aluminium alloy 2024 T351 were used, whereas in the second case, titanium alloy Ti 6Al 4V and aluminium alloy 7075 T6 were used. Several iterations were performed for a mesh-independent value for a maximum stress result. The materials utilized in the second case have better properties than those used in the first case in the aircraft industry. Comparing the total weight of the brackets used in the first and second cases were 36.187 kg and 24.435 kg, respectively. Therefore, materials used in the second case are better and could be used for bracket fabrication. As previously mentioned, several numerical techniques have been proposed to simulate fracture mechanics problems, such as fatigue crack growth.

Sedmak (2018) [21]. Provided an overview of the state of the art of computational fracture mechanics, beginning with initial efforts and going as far as recent achievements. Discussion of some problems of specific aspects of elastic-plastic and linear elastic fracture mechanics has been presented. These problems include static loading, which its numerical simulation is not an easy task because of complex geometries, material nonlinearity, and heterogeneity. This complexity becomes more serious, especially if crack growth is included. Thus, micromechanical modelling of elastic-plastic crack growth is proposed as a novel and promising approach to address some of the gaps in traditional approaches. In addition to static loading, some other important practical issues are addressed, such as fatigue crack growth, with the remaining service life at the focus of the study, utilizing empirical laws for crack growth rates. Numerical simulation of fatigue crack growth is a challenging problem because of both the complex processes of material damage and the lack of a strong theoretical basis for defining them. Therefore, the combination of the theoretical, experimental and numerical approach is presented here to provide a reliable and efficient estimate of the service life under fatigue loading. This study showed that most current methods, such as extended finite element methods (XFEM) and improved finite element methods (FEM), have shown remarkable progress in a very short time and that they have been successfully used in various research [22], [23], [24], [17], [25], [26], [27]. Still, it has also shown that their potential is not yet fully appreciated.

James C Sobotka et al. (2019) [28]. They have proposed a new SIF solution for tapered lugs and oblique loads. These solutions offer driving force estimates for fatigue and fracture across the elliptical quarter-corner cracks and cracks under pin load. These solutions also include a wide range of geometries based on comments received from the industry partners. The powerful novel methods employed in their study

can easily be extended to build new reliable SIF solutions for other complex combinations of cracked geometries and loads. For example, SIF solutions address other important features of lug-pin connections.

K. Shridhar et al. (2019) [29]. They have used MSC Patran/Nastran to study the stress distribution for a **pin-loaded lug and** detect the maximum tensile stress location, which is likely to be a region of developing fatigue cracks. Finally, they came up with some remarks; such as, increasing radius ratio reduces stress concentration factor, the largest stress concentration occurs at the location perpendicular to the loading direction which, indicates exponential decline as we move further towards the lug edge, the stress intensity factor (SIF) values are more critical for smaller radius ratios that indicate a significant change for smaller variations in crack length. The maximum number of cycles to failure increases as the radius ratio increases, and a higher fatigue crack growth rate occurs in lugs with smaller radius ratios.

1.3 Objective and thesis organization

1.3.1 Objective

The mentioned studies and research activities undoubtedly have significant scientific and engineering contribution. Most of them were case studies in which analytical and finite and boundary element based numerical methods were used to determine the causes of cracks appearing in the first place and then their growth. They did not deal with the fatigue life assessment of the damaged fitting part nor its optimization.

Based on the previously mentioned, the main goal of the research conducted within the thesis was to determine the fatigue behaviour of the real damaged wing-fuselage fitting of a light aircraft by using the newest numerical methods, namely improved finite element methods (FEM) and extended finite element methods (XFEM). It is expected that the dissertation will contribute to further upgrading of the design of integral aircraft elements, in the sense that based on its results, verified numerical models, and adopted methodology, it will be possible to efficiently and accurately determine how resistant a newly designed (or modified) structure is and how long its remaining life is under the effects of various fatigue loads.

In accordance, with the mentioned research goal, in this thesis, special attention was paid to the determination of the load that is transferred from the wing spar to the wing-fuselage attachment lug by using analytical methods and CFD analysis, then experimental verification of the numerical model of the wing and, finally, numerical analysis of fatigue behaviour (FEM and XFEM).

Based on the conclusions about the fatigue life of the damaged fitting, guidelines for improving its fatigue characteristics will be defined, both through a suggestion to change the geometry (while preserving or even reducing the weight of the fitting) and through a material suggestion that would allow longer fatigue life than that obtained by using numerical methods. These methods will also be used to estimate the fatigue life of the improved wing-fuselage fitting.

1.3.2 Thesis organization

The thesis comprises e chapters.

- Background of the thesis topic, literature review, and the thesis objectives and content were presented in **the first chapter**.
- In **the second chapter** theoretical background necessary for thesis research is presented: concepts of linear-elastic fracture mechanics (LEFM), fatigue crack growth propagation and fatigue life determination.
- In **the third chapter** the determination of the load that is transferred from the wing spar to the wing-fuselage attachment lug was carried out by using analytical methods and CFD analysis.

- In **the fourth chapter** Numerical Determination of Loading of Wing-Fuselage Fitting "Based on the data obtained in previous chapter in this chapter the determination of the wing-fuselage attachment load was carried out."
- In **the fifth chapter** XFEM and improved FEM (implemented in software packages *Ansys Workbench* and *Morfeo for Abaqus*) were employed for necessary stress-deformation analyses of the damaged wing-fuselage fitting and numerical simulation of the crack growth propagation and fatigue life assessment.
- Experimental verification of the numerically calculated stresses and deformations obtained in the third chapter was presented in **the sixth chapter**.
- Optimization of the wing-fuselage attachment lug, together with the numerical analysis of its fatigue behavior with mentioned methods, and comparison of fatigue lives of original and optimized attachment lug, were conducted in **the seventh chapter**.
- Finally, in **the eighth chapter**, the conclusions and guidelines for further research, together with the thesis's achieved contributions, are given.

CHAPTER 2
LINEAR ELASTIC FRACTURE MECHANICS and
FATIGUE

2 Linear-Elastic Fracture Mechanics

2.1 Fracture Mechanics and Fatigue

Fracture mechanics is a scientific and engineering discipline dealing with the study of mechanical phenomena, such as stress distribution, in materials with geometrical discontinuities, namely cracks. Fracture mechanics uses two different approaches to describe the behaviour of cracked structures. The first is linear-elastic fracture mechanics (LEFM), and the second is elastoplastic fracture mechanics (EPFM). LEFM represent an analytical approach to fracture by linking the stress distribution in the vicinity of the crack tip/front to other parameters such as the nominal applied stress and the geometry and orientation of the crack.

Linear elastic fracture mechanics (LEFM) can be applied only as long as the nonlinear material deformation domain is restricted to a small zone surrounding the crack tip. But, for many materials, LEFM cannot be used for fracture characterization. In those cases, an alternative fracture mechanics model is required, and that is EPFM. EPFM applies to materials that exhibit time-independent, nonlinear behaviour (i.e., plastic deformation) [30].

2.2 Stress Concentration

Stress concentration factors, K_t , can be determined by theoretical formulas, testing or computational methods. The index near K stands for theoretical because it is determined recurring to the elastic theory. Usually, theoretical modes of obtaining K_t are through the Elastic Theory, and the computational ones are through the Finite Element Method. It is possible to get K_t through testing as well by using photo-elasticity or strain gauges. This parameter is also very important for crack initiation and propagation, as a crack is normally formed due to stress concentration on the micro crack's tip. As so, designers should try to avoid stress concentration on the components to prevent fatigue.

Additionally, geometrically similar components have the same K_t , but different stress gradients will be found in the two components. This occurs because the stress concentration factor is a dimensionless parameter. Consequently, the biggest components will have higher areas and volumes where there will be highly stressed material, thus contributing to an increase in fatigue effects. This is known as the fatigue size effect. Stress concentration around fastener holes is one of the most critical aspects leading to fatigue in aircraft. As so, its comprehension and determination are of great importance.

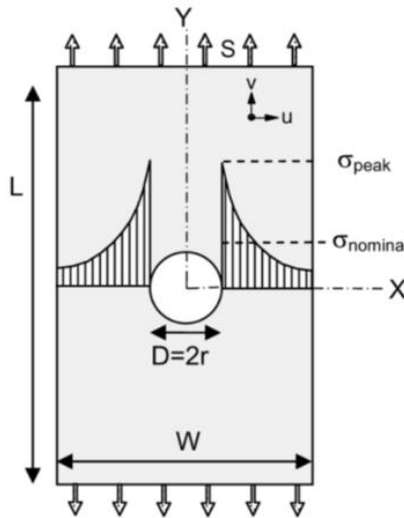


Figure 2.1 A prototype of a notched part (strip with central hole)

Geometrical notches such as holes cannot be avoided. The notches are causing an inhomogeneous stress distribution, as shown in Figure 2.1.

The theoretical stress concentration factor, K_t , is defined as the ratio between the peak stress, the stress concentration point (the root of the notch) and the nominal stress present if a stress concentration did not occur.

$$K_t = \frac{\sigma_{peak}}{\sigma_{normal}} \quad (2.1)$$

The stress concentration is depending on the geometry of the notch configuration. Reducing stress concentrations as much as possible is required to avoid fatigue problems. The present section is dedicated to various aspects of stress concentrations and the effect of the geometry on K_t . This is one of the fundamental issues of designing a fatigue-resistant structure. Problems discussed in the present section covers definitions of stress concentration factors, calculations and estimations of K_t -values, stress gradients, aspects related to size and shape effects, superposition of notches and methods to determine K_t -values.

2.3 Analytical calculations

As shown in Figure 2.2, the displacement functions $u(x,y)$ and $v(x,y)$ has to be found for a two-dimensional problem. The strains follow these functions, and the stresses are linked to the strains by Hooke's law. Then the problem is solved. The tensile strains, $\epsilon_x(x,y)$ and $\epsilon_y(x,y)$, and the shear strain $\gamma_{xy}(x,y)$ must satisfy the compatibility equation. The stresses σ_x , σ_y and τ_{xy} are linked to the strains by three equations representing Hooke's law, including the elastic constants of the material.

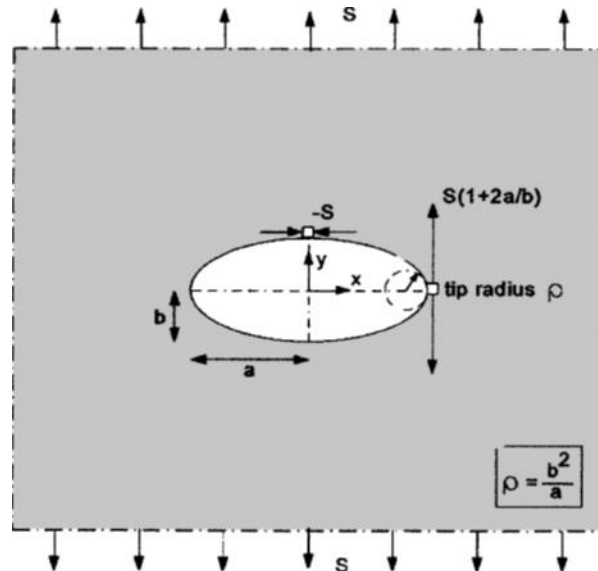


Figure 2.2 An elliptical hole with stress concentration.

The Airy stress function ϕ leads to a biharmonic equation. The problem then is to find a function ϕ that satisfies this equation. The solution will still contain unknown constants, which should follow the boundary conditions. These conditions are essential for solving a particular problem. For the tensile strip with a central hole in Figure 2.1, the boundary conditions are:

1. At the upper and lower edge: $\sigma_y = S$, $\sigma_x = 0$, $\tau_{xy} = 0$.
2. At the side edges ($x = \pm W/2$): $\sigma_x = 0$, $\tau_{xy} = 0$.

3. At the edge of the hole: the stress perpendicular to the hole edge, and the shear stress is zero. An exact analytical solution for the simple case of Figure 2.1, a strip with a hole, is not available, but accurate numerical approximations were obtained. However, for an infinite sheet with an elliptical hole, the exact solution was obtained [31].

This problem is known as a classical problem in the theory of Elasticity [32]. It is not a simple problem. Elliptical coordinates and complex functions are used to arrive at the solution, which then provides the stress distribution in the entire plate. The results illustrate several interesting features of stress distributions around the hole. The tangential stresses along the edge of the hole are of great interest. The maximum stress, σ_{peak} , occurs at the end of the main axis ($x=a, y=0$), see Figure 2.2. The semi-axes of the elliptical hole are a and b , respectively. The tip radius at the end of the major axis follows from $\rho = \frac{b^2}{a}$. The equations for the peak stress and K_t are simple:

$$\sigma_{peak} = S \left(1 + 2 \frac{a}{b} \right) = S \left(1 + 2 \sqrt{\frac{a}{\rho}} \right) \quad (2.2)$$

$$K_t = \frac{\sigma_{peak}}{\sigma_{normal}} = 1 + 2 \frac{a}{b} = 1 + 2 \sqrt{\frac{a}{\rho}} \quad (2.3)$$

The last equation indicates that a small notch root radius ρ will give a high K_t . A significant radius results in a low K_t value, illustrated in Figure 2.3.

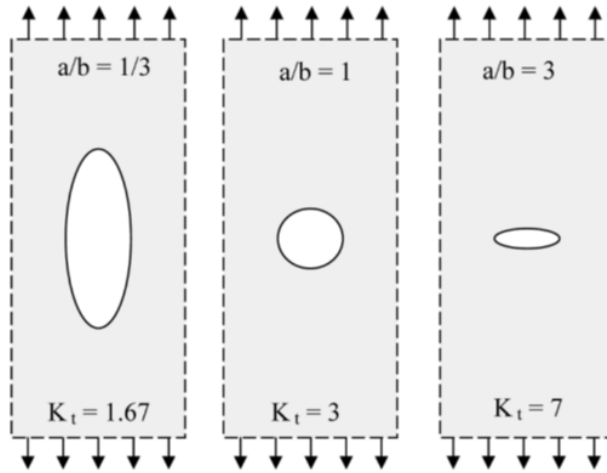


Figure 2.3 Hole shape and its effect on K_t

Using large radii in notched components is to reduce the stress concentration. A circular hole is a particular case obtained from an ellipse with equal axes; $a = b$. The K_t -value according to Equation (2.3) is equal to 3. The K_t -value will be somewhat lower because the component has a finite width. In practice, fatigue cracks have indeed frequently occurred in structures at open holes.

The tangential stress at the end of the vertical axis ($y = b, x = 0$) in Figure 2.2 is compressive stress, equal to the tensile stress applied to the infinite plate. This result is valid for all ellipses and a circular hole (see Figure 2.3). Along the edge of the hole, starting from a to the top of hole b , the tangential stress changes from $+3S$ to $-S$, following the equation:

$$\sigma_\varphi = S(1 + 2 \cos 2\varphi) \quad (2.4)$$

The value of the tangential stress must go through zero ($\sigma_\varphi = 0$) which occurs at $\varphi = 60^\circ$.

2.3.1 Stress Intensity Factors

If the notch root radius ρ is reduced to a minimal value, the stress concentration factor K_t tends to approach infinity. In that case, the notch becomes crack. So, the K_t -value is no longer a meaningful concept to indicate the severity of the stress distribution around the crack tip. A new concept to describe the stress distribution around the crack tip is called stress intensity factor K . This concept was originally developed through the work of [33] Irwin. The stress intensity factor K is the fracture mechanics parameter, and it describes the stress distribution around crack tips. The crack initiation life is highly dependent on the K_t -value. The crack initiation period is followed by the fatigue crack growth period, see Figure 2.4.

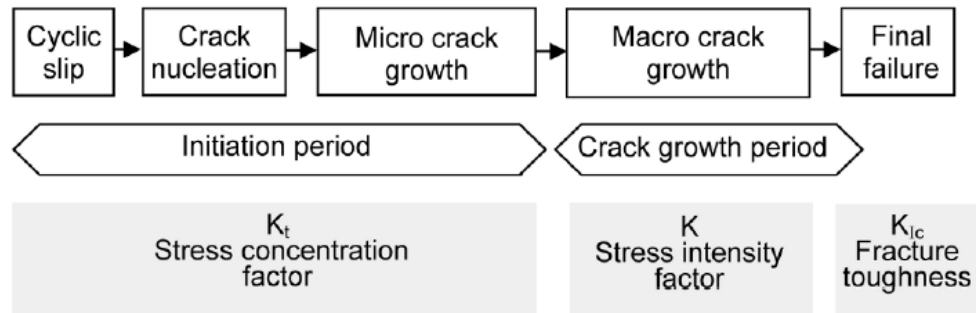


Figure 2.4 Factors of different phases of the fatigue life.

The application of the stress intensity factor to present fatigue crack tip data and predict fatigue crack growth is referred to as “linear elastic fracture mechanics”.

The stress concentration factor K_t is given by Equation:

$$K_t = 1 + 2\frac{a}{b} = 1 + 2\sqrt{a/\rho} \quad (2.5)$$

with the tip radius $\rho = b^2/a$. The elliptical hole becomes a crack by decreasing the minor axis b to zero. If $b = 0$ the hole is a crack with a tip radius $\rho = 0$, stress concentration factor is $K_t = \infty$, regardless of the semi-crack length. This result is not valid. However, the stress distribution around the tip of a crack shows a characteristic picture; this is illustrated in Figure 2.5 by photo-elastic results of a specimen with three cracks loaded in tension.

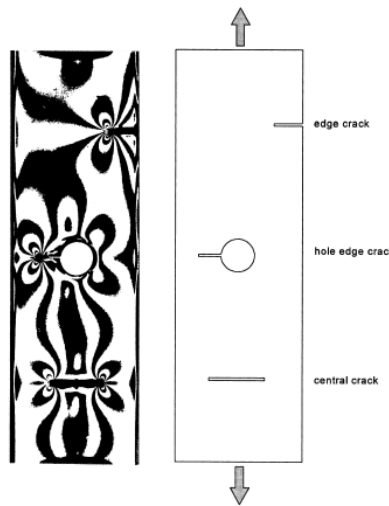


Figure 2.5 Three types of cracks are shown by Photo-elastic picture

Note the similar butterfly pattern at each crack tip. Similar isochromatic pictures occur at the tips of the three cracks, which suggest similar stress distributions at the crack tips. The “intensity” of the crack tip stress distribution is depending on the stress intensity factor K , which can be written as:

$$K = \beta S \sqrt{\pi a} \quad (2.6)$$

In this equation, S is the remote loading stress, a is the crack length, and β is a dimensionless factor depending on the specimen's geometry or structural component. The important feature is that stress distribution around the tip of the crack can be fully described as a linear function of the stress intensity factor K . The concept of the stress intensity factor is presented in this chapter. First, different cracks are listed, followed by more details about stress intensity factors for several geometries. Some basic aspects of the stress analysis of cracked configurations are addressed, including differences between plane stress and plane strain situations, crack tip plasticity and determination of K factors. The basic principle of the application of K factors to fatigue crack growth is considered.

2.3.2 Fracture modes

I. Mode I

Mode I (Figure 2.6-MODE I) encompasses all normal stresses that cause the crack to open, i.e., the crack edges to be removed symmetrically with respect to the crack plane. A pure state of mode I stress thus always exists when there is a symmetrical force flow path with respect to the crack plane. For example, this is the case in tensile-loaded and bending-loaded components when the crack grows perpendicular to the normal stress. Since extended fatigue crack growth occurs under the influence of normal stress, fatigue cracks whose loading direction does not change in the cracking process are generally in a state of mode I loading.

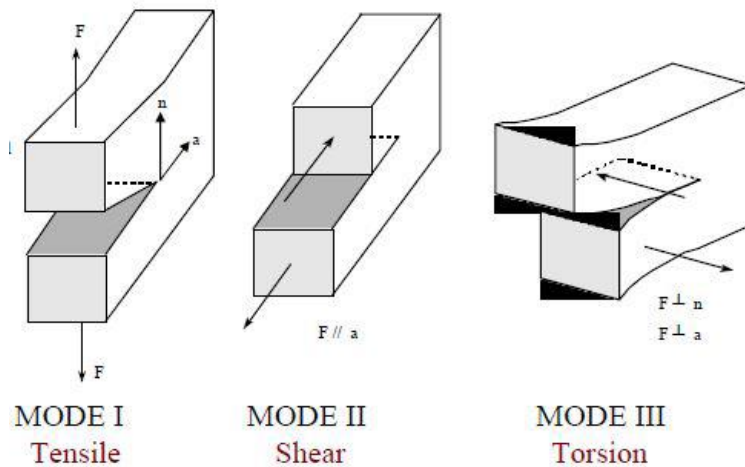


Figure 2.6 The three basic crack loading types in Mode I, Mode II, and Mode III of fracture mechanics

II. Mode II

This loading mode (Figure 2.6-MODE II) is associated with all shear stresses that engender opposed sliding of the crack surfaces in the direction of the crack. This is the case, for example, in components that are subjected to plane shear loading, either globally or locally.

III. Mode III

This loading mode (Figure 2.6-MODE III) corresponds to the non-plane shear stress state, which causes the crack surfaces to move against each other at a right angle to the crack direction, i.e., in the direction of the crack front. Mode III loading can be encountered, for example, in torsional loaded shafts when the crack is found in a plane that is perpendicular to the shaft axis.

IV. Mixed mode

The basic crack loading types described above can also appear in a combination called mixed-mode loading. It is a plane mixed-mode situation when, for example, mode I and mode II are superimposed. Mixed-mode loading can be recognized, among other ways, by its asymmetrical force flow distribution with respect to the crack. If all three crack loading mode types are superimposed, it is referred to as a general or spatial mixed mode state. For example, this is associated with surface cracks, internal cracks, or edge cracks lying at an angle to the loading direction within the component or on the component surface, or cracks in multiaxially loaded component [34].

2.3.3 The Energy Release Rate

This method is known as energy balance. The energy release rate G is defined by the energy necessary to make the crack fronts extending the crack length by a unit length [35]:

$$G = - \frac{dW_{pot}}{da} \quad (2.7)$$

Where:

$W_{pot} = W_{\varepsilon} - W_{ext}$ (W_{ext} is the work of external forces, and W_{ε} is the strain energy of structure). The energy release rate G corresponds to the decrease in the total potential energy W_{pot} of the cracked body.

The relation between G to the stress intensity factors is given by:

$$G = \frac{(K_I^2 + K_{II}^2)}{E'} + \frac{K_{III}^2}{2\mu} \quad (2.8)$$

Where:

$E' = E$ for plane stress, and $E' = E/(1 - \nu^2)$ for plane strain. μ is the shear modulus.

2.3.4 J-integral

J-integral is a parameter to deal with the Non-linear fracture problem. J-integral is based on the concept of conservation of energy. It is less dependent on the crack tip, which means there is no need to do the special treatment on the mesh around the crack tip. The J-integral equation is given by: [35], [36]. This means there is no need to do the special treatment on the mesh around the crack tip. The J-integral equation is given by:

$$J = \int_{\Gamma} \left(W dx_2 - T_i \frac{\partial u_i}{\partial x_i} \right) ds \quad (2.9)$$

Where:

W is the strain energy density, T_i is the traction vector, u_i is the displacement vector, and ds is an element of arc along the integration contour (see Figure 2.7).

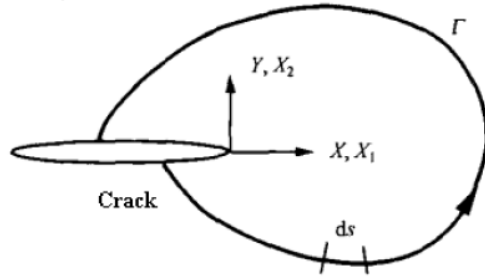


Figure 2.7 Counter clockwise loop around the crack tip with a clockwise loop

In the LEFM method, the stress and displacement components at the crack tip are known as functions relative to the crack tip. But for a multi-mode loading, they have been used by the SIF K_I , K_{II} and K_{III} . The integration path is usually required to be only a circle around the crack tip; this can be done because the J-integral is path-independent. The J-integral is related to the SIF. In Mode I, the J-integral is equivalent to the energy release rate G . This means that J-integral can be used in the crack growth criteria of LEFM as a replacement for K and G [35], [36].

$$\text{Plane stress } J = \frac{1}{E} K_I^2 \quad (2.10)$$

$$\text{Plane strain } J = \frac{(1 - \nu^2)}{E} K_I^2 \quad (2.11)$$

2.3.5 Fatigue Crack Propagation

Fatigue is a process of local strength reduction. The phenomenon is often referred to as a process of damage accumulation in a material undergoing fluctuating loading, which occurs in engineering materials such as metallic alloys, polymers and composites. Different parameters are used to define the mechanical fatigue process that occurs when a structure is subjected to repeated loads, like cyclic load, stress intensity, and crack growth rate. The maximum load is P_{max} , the minimum load P_{min} [kN], and the ratio between the minimum and maximum load is (P_{min}/P_{max}) is called the load ratio R , which is often used to measure the mean stress. Crack growth rate da/dN is the crack increment da per loading cycle increment dN . The stress intensity factor K [$MPa\sqrt{m}$], working on the crack tip, is calculated from the applied load P and actual crack length and direction in a construction. The maximum stress intensity is K_{max} , the minimum K_{min} , and the difference between both is ΔK , see Figure 2.8. Fluctuating loads can lead to fluctuating local high stresses, and small microscopic cracks may appear. Once a crack exists in a structure, it will tend to grow under cyclic loading. Even if the maximum of the cyclic load on construction is below the material's elastic limit, fatigue may lead to failure. Fatigue is progressive in which the damage develops slowly in the early stages and near the end of a structure's life, and it accelerates very quickly towards failure.

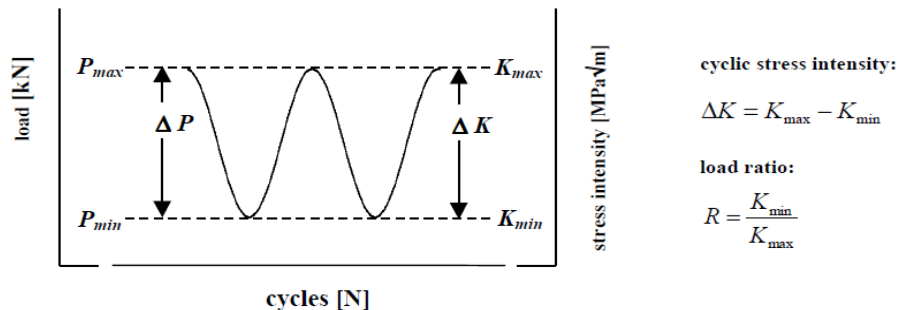


Figure 2.8 Fatigue loading vs number of cycles

However, details of the fatigue process may differ between materials. The fatigue process can be defined generally as [37] “The process of the cycle-by-cycle accumulation of local damage in a material undergoing fluctuating stresses and strains.”

2.3.6 Description of the fatigue phenomenon

Fatigue of metallic in structures has been studied since the beginning of the 19th century. Railroads, bridges, steam engines: a whole gamut of new structures and machines was developed, made of steel in the Industrial Revolution. Many of them were exposed to cyclic stresses during service life, and many of them failed; the origin of failure was unknown until Albert [38] made the first report about failure caused by fatigue in 1829. He observed the failure of iron mine-hoist chains caused by repeated small loads. Ten years later, in 1839, Poncelet, a professor of mechanics at the école d'application, Metz, introduced the term fatigue in his lectures. Rankine [39] recognized the importance of stress concentration in 1843. He noted that fracture occurs near sharp corners. However, until then, the phenomenon was described qualitatively only.

Wöhler made a major step in 1860. Wöhler, a railroad engineer, started performing systematic experimental research on railroad axles. He observed that steel would rupture at stress below the elastic limit if cyclic stress were applied. However, there was a critical value of cyclic stress, the fatigue limit, below which failure would not occur. He found a way to visualize “time to failure” for specific materials. the stress amplitude σ is plotted as a function of the number of cyc` to failure In the S-N-curve approach (see Figure 2.10) [40] [36].

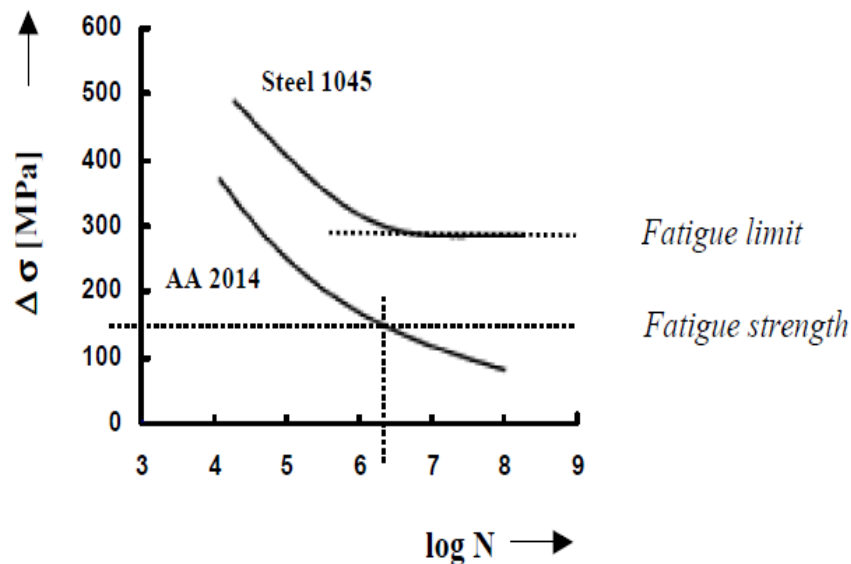


Figure 2.9 Stress vs. number of cycles curves for low-carbon steel 1045 and AA 2014

A logarithmic scale is used for the horizontal axis, while the stress is plotted using either a linear or logarithmic scale. **Fatigue limit:** the stress below which a material can be stressed cyclically for an infinite number of times without failure. **Fatigue strength:** the stress at which failure occurs for a given number of cycles.

The first crack surface investigations were made by Ewing [41] in 1903. He showed the nature of fatigue cracks using a microscope, see Figure 2.10.

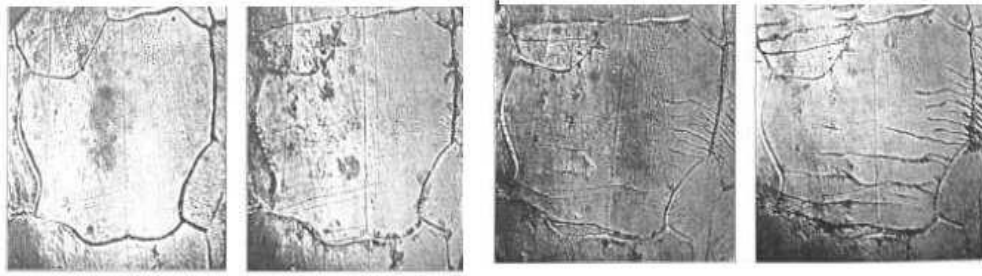


Figure 2.10 Ewing & Humfrey showed crack surface in 1903

Around 1920, Griffith investigated the discrepancy between a material's theoretical strength and the actual value, sometimes 1000 times less than the predicted value. He discovered that many microscopic cracks and/or other imperfections exist in every material. He assumed that these small cracks lowered the overall strength. Because of the applied load, high-stress concentrations are expected near these small cracks, which magnify the stresses at the crack tip. These cracks will grow more quickly, causing the material to fail long before reaching its theoretical strength. Any voids, corners, or hollow areas in the internal area of the material also result in stress concentrations. Mostly fracture will begin in one of these areas simply because of this phenomenon [42].

After 1960: Paris and Elber have made an important push to understand Paris, and Elber made the fatigue process. In 1961, Paris found a more or less linear correlation on double logarithmic scales between crack growth rate da/dN and cyclic stress intensity factor ΔK for some part of the fatigue curve (See Figure 2.11) [43]. This well-known Paris' law reads:

$$\frac{da}{dN} = C(\Delta K)^n \quad (2.12)$$

Where: $\Delta K = K_{max} - K_{min}$ and C and m are experimentally determined scaling constants. Paris' law will be discussed in more detail in the next section.

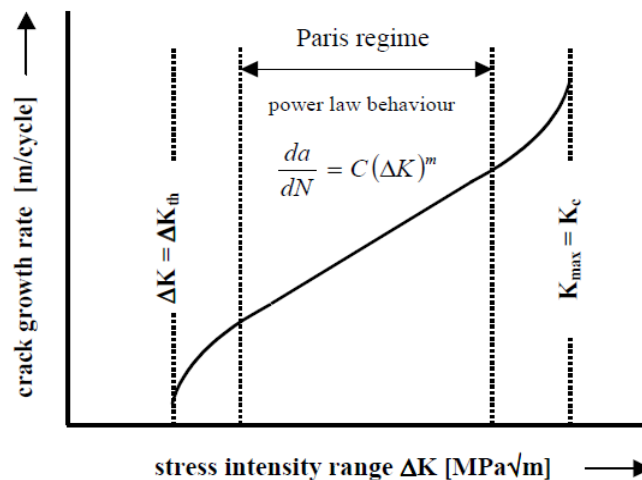


Figure 2.11 Linear correlation between crack growth rate da/dN and stress intensity factor K on a log-log scale (Paris' Law)

2.3.7 Fatigue crack growth regions

Fatigue crack propagation, referred to as stage II in Figure 2.12, represents a large portion of the fatigue life of many materials and engineering structures. Accurate prediction of the fatigue crack propagation stage is of utmost importance for determining the fatigue life. The main objective of the fatigue crack propagation may be presented in this form: "Determine the number of the cycles N_c required for a crack to grow, from a certain initial crack size a_0 to the maximum allowable crack size a_c , and the form of this increase $a = a(N)$, where the crack size a corresponds to N loading cycles.

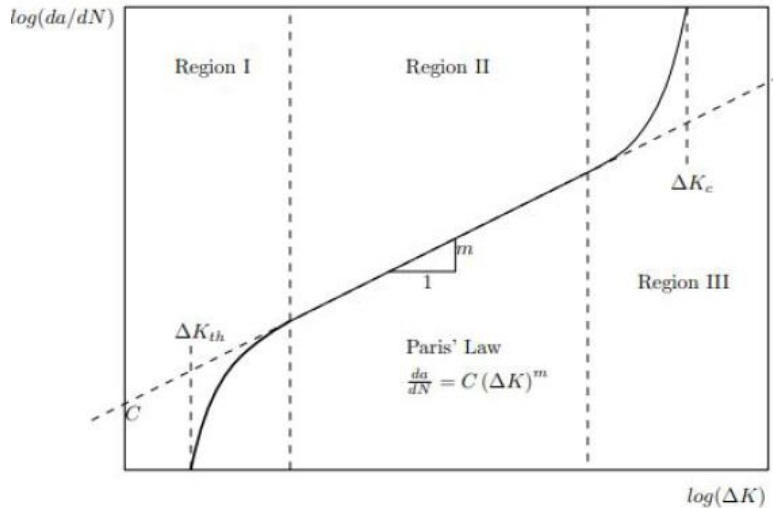


Figure 2.12 The rate of crack growth in different regions

As shown in Figure 2.13, fatigue crack growth results cover a range of K -values and crack growth rates. It does not give indications about crack growth rates outside this range. More extensive experiments have shown that two vertical asymptotes occur in a da/dN - ΔK graph (see Figure 2.12). The left asymptote at $K = K_{th}$ indicates that K -values below this threshold level are too low to cause crack growth. The other asymptote at the right-hand side occurs for a K cycle with $K_{max} = K_c$. It means that K_{max} reaches a critical value which leads to complete failure of the specimen. If da/dN is plotted as a function of K on a double log scale, the function $da/dN = fR(K)$ is supposed to cover three different parts, indicated by I, II, and III [44]. The corresponding ΔK -regions are referred to as:

- Stage I - the threshold K -region: transition to a finite crack growth rate from no propagation below a threshold value of ΔK .
- Stage II - the Paris- K -region: "power law" dependence of crack growth rate on ΔK .
- Stage III - the stable tearing crack growth region: acceleration of growth rate with ΔK , approaching catastrophic fracture.

2.3.8 Crack growth

The data on fatigue crack propagation is obtained from pre-cracked specimens subjected to fluctuating loads, and the change in crack size as a function of loading cycles is reported. The size of the crack is proportional to the number of loading cycles for various load amplitudes. The stress intensity factor is used as a correlation parameter. Typically, experimental results are plotted as a $\log(K)$ versus $\log(da/dN)$ graph. K denotes the range of the stress intensity factor, and da/dN denotes the crack propagation rate. Typically, the load is sinusoidal in shape and has a constant amplitude and frequency. To define the variance in the stress intensity factor during a loading period, two of the four parameters K_{max} , K_{min} , $R = K_{min} / K_{max}$, or $R = K_{max} - K_{min}$, are required.

Figure 2.12 illustrates a standard plot of the characteristic sigmoidal of a $\log(K)$ - $\log(da/dN)$ fatigue crack growth rate curve. Three distinct regions may be identified. In area I, da/dN quickly decreases to a minimal value. There is a threshold value for the stress strength factor range K_{th} for certain materials, indicating that no crack propagation occurs when $K < K_{th}$, ultimately resulting in catastrophic failure.

The experimental results show that the fatigue crack growth rate curve is proportional to the ratio R and that as R increases, the curve shifts toward higher da/dN values. Cyclic stresses caused by constant or variable amplitude loading can be represented using two of a variety of alternative parameters. Cyclic stresses with constant amplitude are characterized by three parameters: mean stress (σ_m), stress amplitude (σ_a) and a frequency (ω, ν). The frequency does not have to be defined to convey information about the severity of the stresses. Only two parameters are necessary to accurately describe the stresses generated by a constant amplitude loading period.

Other parameters, such as the minimum stress (σ_{min}) and the maximum stress (σ_{max}), can describe the stresses completely. Additionally, the stress range, $\Delta\sigma = \sigma_{max} - \sigma_{min}$, can be used in conjunction with any of the others, except a . Additionally, another parameter is frequently more convenient. This is referred to as the stress ratio R , which is defined as $R = \min/\max$.

One of the above parameters can be replaced by the load ratio R to define the cyclic load. Any of the following combinations fully describe the stresses in a constant amplitude loading: $\Delta\sigma$ and R , σ_{min} and R , σ_{max} and R , σ_a and R , and σ_m and R . The case of $R=0$ defines the condition in which the stress always rises from, and returns to 0. When $R = -1$, the stress cycles around zero as a mean, called fully reversed loading.

To study the parameters that affect fatigue crack growth, a through-thickness crack is considered a wide plate subjected to remote stressing that varies cyclically between the constant minimum and maximum values. The stress range is defined as $\Delta\sigma = \sigma_{max} - \sigma_{min}$.

The fatigue crack growth rate is defined as the crack extension, Δa , during a small number of cycles, ΔN , the propagation rate is $\Delta a / \Delta N$, which in the limit can be written as the differential da/dn . It has been found experimentally that provided the stress ratio $R = \sigma_{min} / \sigma_{max}$ is the same then ΔK correlates fatigue crack growth rates in specimens with different stress ranges and crack lengths and also correlates crack growth rates in specimens of different geometry. This correlation is presented in

Figure 2.13

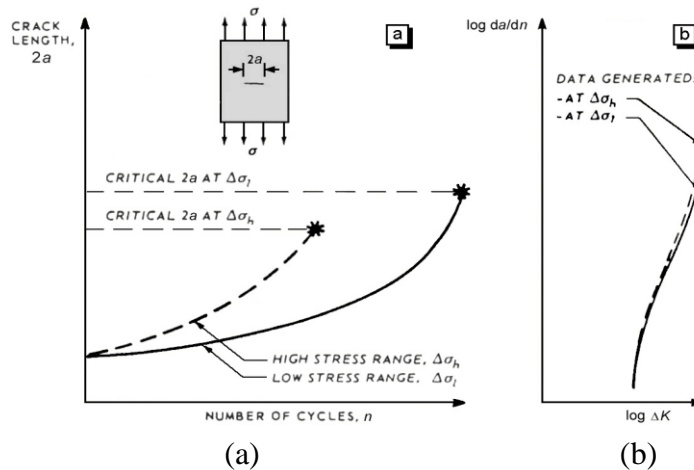


Figure 2.13 (a) Crack length vs number of cycles, and (b) $\log da/dn$ vs $\log dK$

The data obtained with a high-stress range, $\Delta\sigma_{\text{high}}$, commence at relatively high values of da/dN and ΔK . The data for a low-stress range, $\Delta\sigma_{\text{low}}$, commence at lower values of da/dN and ΔK but reach the same high values as in the high-stress range case.

Furthermore, the stress ratio R can have a significant influence on the crack growth behaviour. In other words, besides the stress intensity factor range, ΔK , there is an influence of the relative values of K_{max} and K_{min} since $R = \sigma_{\text{min}} / \sigma_{\text{max}} = K_{\text{max}} / K_{\text{min}}$. This is presented in Figure 2.12 The rate of crack growth in different regions shows that crack growth rates at the same stress intensity range ΔK values are generally higher when load ratio R increases. It is important to note that the effect of the load ratio R has proved to be from the bibliography strongly material dependent [45] [36].

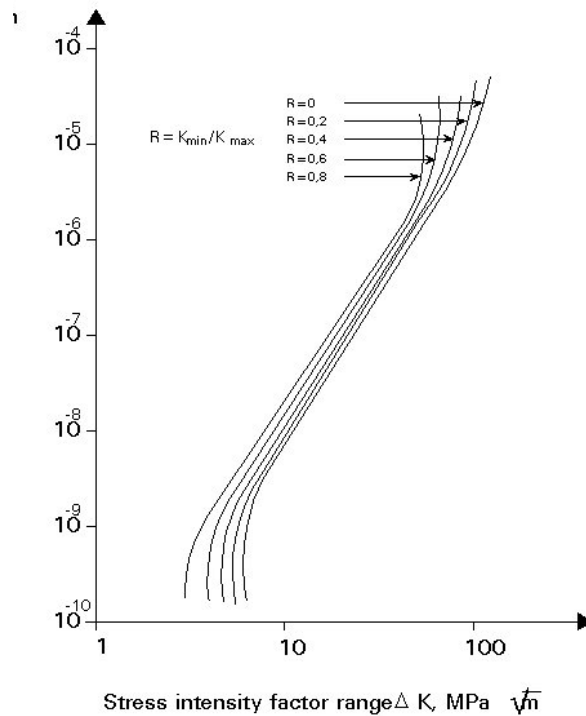


Figure 2.14 Mean stress effect on fatigue crack for Aluminium alloys

Several different quantitative continuum mechanics models of fatigue crack propagation have been proposed in the literature. All these models lead to relations based mainly on experimental data correlations. They relate da/dN to such variables as the external load, the crack length, the geometry, and the material properties. As previously mentioned, one of the most widely used fatigue crack propagation laws proposed by Paris and Erdogan is usually referred to in the literature as the "Paris law". It has the form:

$$\frac{da}{dN} = C(\Delta K)^m \quad (2.13)$$

Where $\Delta K = K_{\text{max}} - K_{\text{min}}$, with K_{max} and K_{min} referring to the maximum and minimum values of the stress intensity factor in the load cycle. The constant C and m are determined empirically from a $\log(\Delta K) - \log(da/dN)$ plot. The value of m is usually taken equal to 4 for aluminium alloys, resulting in the so-called "4th power law", while the coefficient C is assumed to be a material constant. Paris Law relation represents a linear relationship between $\log(\Delta K)$ and $\log(da/dN)$ and is used to describe the fatigue crack propagation. Experimental data are well predicted using the Paris Law equation for specific geometrical configurations and loading conditions. The effect of a mean stress, loading, and specimen

geometry is included in the constant C. "Paris law" has been widely used to predict the fatigue crack propagation life of engineering components.

The crack growth mechanism shows that a fatigue crack grows by a small amount in every load cycle. Growth is the geometrical consequence of slip and cracks tip blunting. Re-sharpening of the crack tip upon unloading sets the stage for growth in the next cycle. It can be concluded from this mechanism that the crack growth per cycle, Δa , will be larger if the maximum stress in the cycle is higher (more opening) and if the minimum stress is lower (more re-sharpening). The local stresses at the crack tip can be described in terms of the stress intensity factor K, where $K = \beta \sigma \sqrt{\pi a}$. If σ is the nominal applied stress. In a cycle, the applied stress varies from σ_{\min} to σ_{\max} over range ΔK . Therefore, the local stresses vary by the following equation:

$$\Delta K = \beta \Delta \sigma \sqrt{\pi a} \quad (2.14)$$

An amount of crack growth is defined as Δa in one cycle, which is expressed in m/cycle. If growth were measured over, e.g. $\Delta N = 10000$ cycles, the average growth per cycle would be $\Delta a / \Delta N$, the crack propagation rate. In the limit where $N \rightarrow 1$, this rate can be expressed as the differential da/dN . When a structural component is subjected to fatigue loading, a dominant crack reaches a critical size under the peak load during the last cycle leading to catastrophic failure. The basic objective of the fatigue crack propagation simulation is the determination of the crack size, a , as a function of the number of cycles, N . Thus, the fatigue crack propagation life N_p is obtained. When the type of the applied load and the expression of the stress intensity factor is known, the application of one of the foregoing fatigue laws enables a realistic calculation of the fatigue crack propagation life of the component. For example, consider a plane fatigue crack of the length $2a_0$ in a plane subjected to a uniform stress σ perpendicular to the plane of the crack. The stress intensity factor K is given by:

$$K = f(a) \sigma \sqrt{\pi a} \quad (2.15)$$

Where $f(a)$ is a geometry-dependent function. Integrating the fatigue crack propagation law expressed by equation 2.12 gives:

$$N - N_0 = \int_a^{a_0} \frac{da}{C(\Delta K)^m} \quad (2.16)$$

where N_0 is the number of load cycles corresponding to the half crack length a_0 . Introducing the stress intensity factor range ΔK , where K is given from equation 2.13, into the previous equation results in:

$$N - N_0 = \int_a^{a_0} \frac{da}{C[f(a)\Delta\sigma\sqrt{\pi a}]^m} \quad (2.17)$$

Assuming that the function $f(a)$ is equal to its initial value $f(a_0)$ so that $\Delta K = \Delta K_0 \sqrt{a/a_0}$, where $\Delta K_0 = f(a_0)\Delta\sigma\sqrt{\pi a_0}$, so, the previous equation gives:

$$N - N_0 = \frac{2a_0}{(m-2)C(\Delta K_0)^m} \left[1 - \left(\frac{a_0}{a}\right)^{\frac{m}{2}-1} \right] \quad (2.18)$$

Form #2. Unstable crack propagation occurs when $K_{max} = K_{IC} = f(a)\sigma_{max}\sqrt{\pi a}$. From which the critical crack length a_0 is obtained. Then, the equation 2.15 for $a = a_0$ gives the fatigue crack propagation life $N_p = N_c - N_0$. Usually, since $f(a)$ varies with the crack length a , the integration of the previous equation cannot be performed directly, but only through numerical methods.

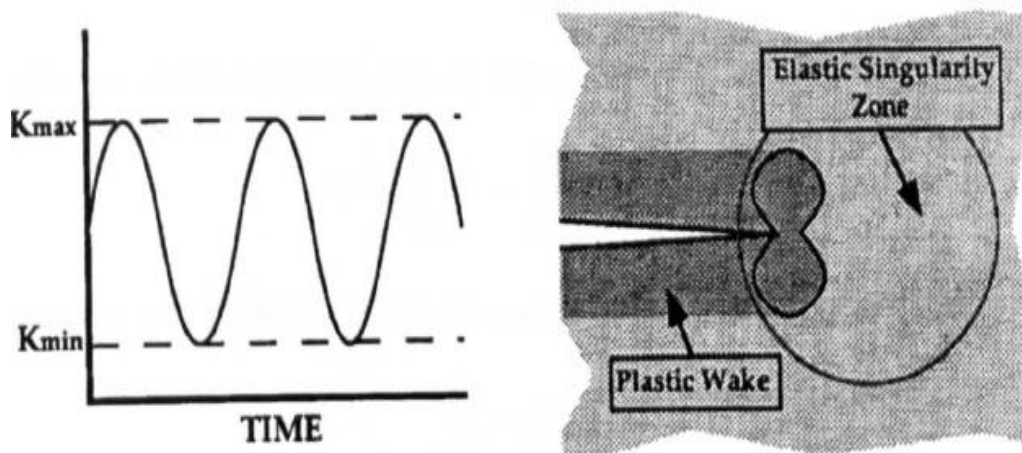


Figure 2.15 Constant amplitude fatigue crack growth under small yielding conditions

Since 1960 Paris, et al. [43], [46] and [36] confirmed the application of fracture mechanics to fatigue problems, and it has become almost routine. The techniques for investigating fatigue under constant amplitude loading at small-scale yielding conditions are fairly well established. Still, several uncertainties remain. The concept of similitude, when it applies, provides the theoretical basis for fracture mechanics. Similitude implies that the crack tip conditions are uniquely defined by a single loading parameter such as the stress intensity factor. Consider a growing crack in the presence of constant amplitude cyclic stress intensity

Figure 2.15. Behind the plastic zone, which is developed at the crack tip, a plastic wake is formed. When it is small, the plastic zone is embedded in an elastic singularity zone. In that case, the conditions at the crack tip are uniquely defined by the current K value, and K_{min} and K_{max} describe the crack growth rate. For the similitude assumption to be valid, the crack tip of the growing crack needs to be sufficiently far from its initial position, and external boundaries should be remote.

Soon after the Paris law gained wide acceptance as a predictor of fatigue crack growth, many researchers realized that this simple expression was not universally applicable. As Figure 2.12 illustrates, a log-log plot of da/dN versus ΔK is sigmoidal rather than linear when crack growth data are obtained over a sufficiently wide range. Also, the fatigue crack growth rate shows a dependence on the R ratio, especially at both extremes of the crack growth curve. A discovery by Elber [47] provided at least a partial explanation for both the fatigue threshold and R ratio effect.

2.3.9 Crack closure

Paris' law is generally accepted for a wide range of different materials; however, the physical meaning is limited. The primary issue at that time was how to explain stress ratio effects. In 1970 Elber published a famous article titled "Fatigue Crack Closure under Cyclic Tension" [47]. In this article, he assumed crack closure to be the cause of stress ratio-effects. He meant contact of the crack surfaces by crack closure at a load above the minimum load. Elber assumed that, when crack closure occurs, the effective cyclic stress intensity range ΔK_{eff} that works on the crack tip is lower than the expected or applied ΔK -range, see Figure 2.16. The crack growth rate is no longer a result of the total ΔK magnitude but only of its part.

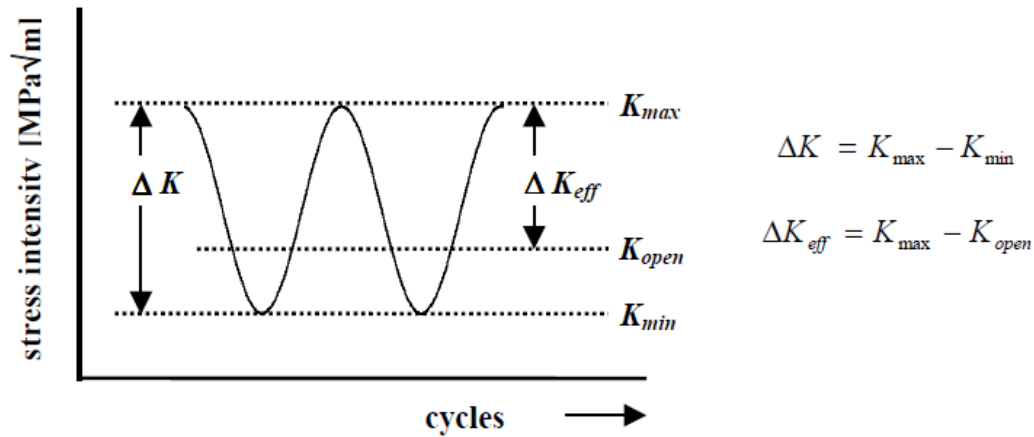


Figure 2.16 Elber's principle of crack closure theory

When a specimen is cyclically loaded at K_{max} and K_{min} , the crack faces are in contact below K_{op} , the stress intensity at which the crack opens. Elber assumed that the portion of the cycle that is below K_{op} does not contribute to fatigue crack growth. Since the definition of the effective stress intensity range is $\Delta K_{eff} = K_{max} - K_{op}$. A modified version of equation 2.11 proposed:

$$\frac{da}{dN} = C(\Delta K_{eff})^m \quad (2.19)$$

Crack closure occurs as a consequence of crack tip plasticity. At the tip of a growing fatigue crack, each loading cycle generates a monotonic plastic zone during increased loading and a much smaller reversed plastic zone during unloading. Approximately the reversed plastic zone size is one-quarter of the size of the monotonic plastic zone. Due to this, there is a residual plastic deformation consisting of monotonically stretched material. As the crack grows, the residual plastic deformation forms a wake of monotonically stretched material along the crack edges. Because the residual deformation results from tensile loading, the material in the crack edges are elongated normal to the crack surfaces and have to be accommodated by the surrounding elastically stressed material, this is no problem as long as the crack is open. Since then, the crack edges will show a displacement normal to the crack surfaces. However, as the fatigue load decreases, the crack will tend to close during unloading, and the residual deformation becomes important.

2.3.10 Effect of Residual Stresses on Crack Propagation

Our knowledge of the correlation between residual stress and fatigue strength is perplexed because:

- The fatigue strength depends significantly on the condition of the surface. Such major factors overshadow the effect of residual stress as weld geometry and surface irregularities.
- A fatigue crack may initiate in a region containing tensile residual stresses. The rate of crack growth may be amplified due to the presence of tensile residual stresses. However, when the crack grows and enters regions containing compressive residual stresses, the crack growth rate may be reduced. As a result, it is questionable whether or not the total effect of residual stresses on the overall crack growth is significant.
- When residual stresses are altered by heat treatment such as peening, the metallurgical and mechanical properties of the metal are also changed. A schematic presentation of the stress field behind and in front of a crack tip under cyclic loading without welding residual stresses is illustrated in Figure 2.17.

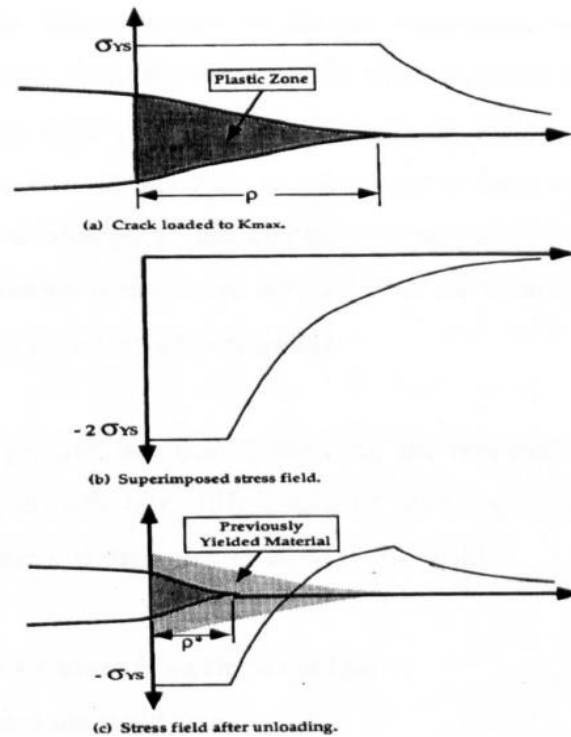


Figure 2.17 The reverse plastic zone forms during periodic loading [48].

How residual stresses affect the plastic zone shown in Figure 2.17 and the fatigue strength of a welded structure is still a matter of debate. Some researchers had reported that the fatigue strength increased when specimens had compressive residual stresses, especially on the specimen surfaces; others believe that residual stresses have only a negligible effect on the fatigue strength of the weld elements. It has been suggested that in a good weld, residual stresses can be ignored. Also, it has been recommended that geometry affects fatigue behaviour much more than residual stresses. But, others researchers feel that there is significant evidence that residual stresses affect fatigue strength. Munse [49] summarizes as follows:

"Based on the available data, it is believed that the effects of residual stresses may differ from one instance to another, depending upon the materials and geometry analyzed parts, the state of stress, the scale of applied stress, the type of stress cycle, and perhaps other factors. Many of the investigations designed to evaluate the effects of residual stress have included tests of members that have been subjected to different stress relief heat treatments. The changes in fatigue behaviour resulting from these heat treatments, in some cases, have been negligible. In contrast, in other investigations, the various stress-relief treatments have increased fatigue strength by as much as twenty percent. Since it is impossible to carry out heat treatment for stress relief without altering the metallurgical and mechanical properties of weldment, the question always arises as to whether benefits are derived from the reduction of residual stresses or the improved properties in other respects."

CHAPTER 3
DETERMINATION OF LOADS ACTING ON THE
WING and PIN-LUG WING ATTACHMENT

3 DETERMINATION OF LOADS ACTING ON THE WING and PIN-LUG WING ATTACHMENT

"In order to conduct the fatigue life analysis of the wing-fuselage fitting, it was necessary to determine the appropriate wing loads. To do that, all necessary aerodynamic parameters were calculated for all the load cases, in accordance with EASA CS 23 requirements. Based on these aerodynamic parameters the corresponding forces and moments that are acting on the wing were obtained (including weight of the aircraft and fuel), and the critical load cases were determined and the analysis of the wing structure using finite element method was carried out. These calculations are presented in this chapter."

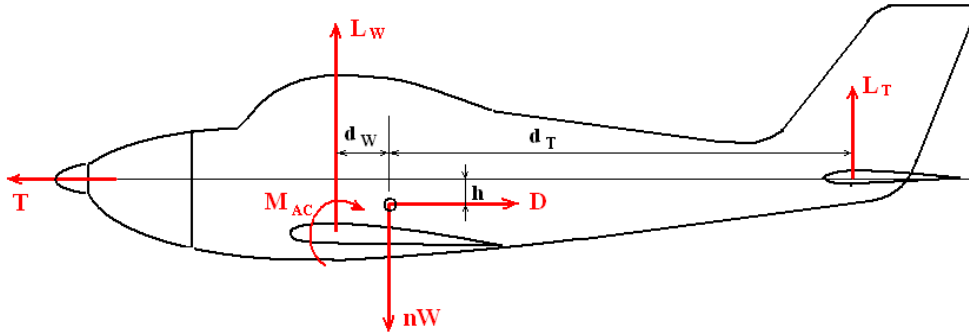


Figure 3.1 Forces acting during symmetric equilibrium manoeuvre

3.1 Equilibrium equations:

$$L_w + L_T - nW = 0 \quad (3.1)$$

$$T - D = 0 \quad (3.2)$$

$$M_{AC} + L_w \cdot d_w - L_T \cdot d_T - T \cdot h = 0 \quad (3.3)$$

Assuming that thrust and drag are in-line, then $h = 0$ so the drag or thrust are not involved in the moment equation for vertical loads, lift forces may be solved directly a

$$M_{AC} + L_w \cdot d_w - L_T \cdot d_T = 0 \quad (3.4)$$

$$L_T = \frac{M_{AC} + nW \cdot d_w}{d_w + d_T} \quad (3.5)$$

3.2 DETERMINATION OF LOADS ACTING ON THE WING and PIN-LUG WING ATTACHMENT

$$L_W = nW - L_T \quad (3.6)$$

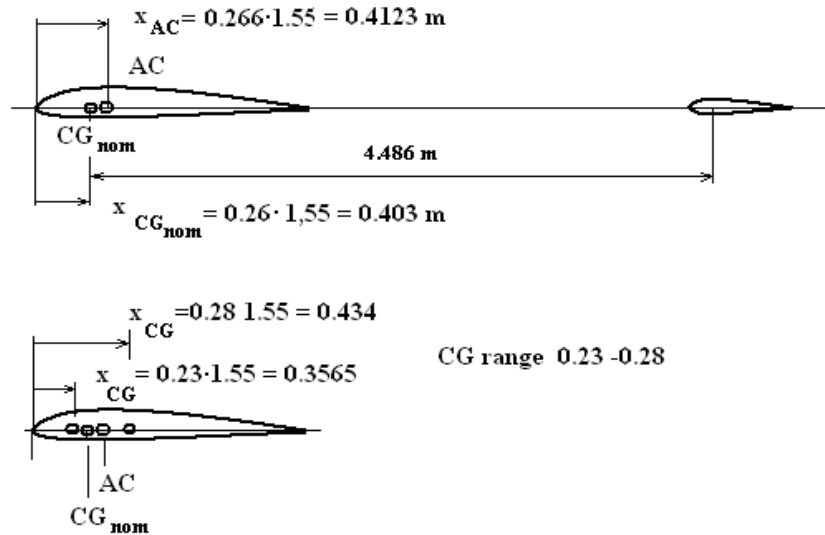


Figure 3.2 Variations of a position of the centre of gravity

$$W = mg \quad (3.7)$$

$$M = \frac{1}{2} \cdot \rho \cdot V \cdot S_W \cdot C_M \cdot \bar{c} \quad (3.8)$$

3.2.1 C.G. at D_0.23

$$d_W = x_{0.23} - x_{0.266} \quad (3.9)$$

$$d_W = 0.0558 \text{ m}$$

$$d_T = x_{WE} + x_{0.26} - x_{0.23} \quad (3.10)$$

$$d_T = 4.4532 \text{ m}$$

$$d_w + d_T = 4.4762 \text{ mm} \quad (3.11)$$

$$L_T = \frac{M_{AC} + nW \cdot d_W}{d_w + d_T} \quad (3.12)$$

$$L_W = nW - L_T \quad (3.13)$$

$$C_L = \frac{L_W}{\frac{1}{2} \cdot \rho \cdot V_D^2 \cdot S_W} \quad (3.14)$$

3.2.2 C.G. at D_0.28

$$d_W = x_{0.28} - x_{0.266} = 0.217 \text{ m} \quad (3.15)$$

$$d_T = x_{WE} + x_{0.26} - x_{0.28} = 4.455 \text{ m} \quad (3.16)$$

$$d_w + d_T = 4.4767 \text{ m} \quad (3.17)$$

$$L_T = \frac{M_{ACD} + nW \cdot d_W}{d_w + d_T} \quad (3.18)$$

$$L_T = \frac{M_{AC} + nW \cdot d_W}{d_w + d_T} \quad (3.19)$$

$$L_T = \frac{M_{ACA} + nW \cdot d_W}{d_w + d_T} \quad (3.20)$$

As L_W, L_T and nW changes their directions, while M_{AC} don't, and the previously obtained equations will be changed

$$L_T = \frac{M_{AC} - nW \cdot d_W}{d_w + d_T} \quad (3.21)$$

3.2.3 Case D Loads

$$m = 920 \text{ Kg} , W = mg = 9022.12 \text{ N}$$

$$n = 6 , nW = 54132.71 \text{ N}$$

$$V_D = 107.06 \text{ m/s} , \rho = 1.225 \text{ Kg/m}^3 , S_W = 15.027 \text{ m}^2 , \bar{c} = 1.55 \text{ m} , C_{MAC} = -0.066$$

$$x_{WE} = 4.486 \text{ m}$$

$$M_{ACD} = \frac{1}{2} \cdot \rho \cdot V_D^2 \cdot S_W \cdot C_{MAC} \cdot \bar{c} \quad (3.22)$$

$$M_{ACD} = -10792.16 \text{ N} \cdot \text{m} \quad (3.23)$$

a. C.G. at D_0.23

$$d_W = x_{0.23} - x_{0.266} \quad (3.24)$$

$$d_W = -0.0558 \text{ m} \quad (3.25)$$

$$d_T = x_{WE} + x_{0.26} - x_{0.23} \quad (3.26)$$

$$d_T = 4.4532 \text{ m} \quad (3.27)$$

$$d_w + d_T = 4.4762 \text{ m} \quad (3.28)$$

$$L_T = \frac{M_{AC} + nW \cdot d_W}{d_w + d_T} \quad (3.29)$$

$$L_T = -3085.48 \text{ N} \quad (3.30)$$

$$L_W = nW - L_T \quad (3.31)$$

$$L_W = 57218.20 \text{ N} \quad (3.32)$$

$$C_L = \frac{L_W}{\frac{1}{2} \cdot \rho \cdot V_D^2 \cdot S_W} \quad (3.33)$$

$$C_L = 0.5424 \quad (3.34)$$

b. C.G. at D_0.28

$$d_W = x_{0.28} - x_{0.266} \quad (3.35)$$

$$d_W = 0.0217 \text{ m} \quad (3.36)$$

$$d_T = x_{WE} + x_{0.26} - x_{0.28} \quad (3.37)$$

$$d_T = 4.455 \text{ m} \quad (3.38)$$

$$d_W + d_T = 4.4767 \text{ m} \quad (3.39)$$

$$L_T = \frac{M_{ACD} + nW \cdot d_W}{d_W + d_T} \quad (3.40)$$

$$L_T = -2148.34 \text{ N} \quad (3.41)$$

$$L_W = nW - L_T \quad (3.42)$$

$$L_W = 56281.05 \text{ N} \quad (3.43)$$

$$C_L = \frac{L_W}{\frac{1}{2} \cdot \rho \cdot V_D^2 \cdot S_W} \quad (3.44)$$

$$C_L = 0.5335 \quad (3.45)$$

3.2.4 Case A

$$m = 920 \text{ Kg}, W = mg = 9022.12 \text{ N}$$

$$n = 6, nW = 54132.71 \text{ N}$$

$$V_A = 66.905 \text{ m/s}, \rho = 1.225 \text{ Kg/m}^3, S_W = 15.027 \text{ m}^2, \bar{c} = 1.55 \text{ m}, C_{MAC} = -0.0663$$

$$M_{ACA} = \frac{1}{2} \cdot \rho \cdot V_A^2 \cdot S_W \cdot C_{MAC} \cdot \bar{c} \quad (3.46)$$

$$M_{ACA} = -4214.74 \text{ Nm} \quad (3.47)$$

a. C.G. at A_0.23

$$d_W = x_{0.23} - x_{0.266} \quad (3.48)$$

$$d_W = -0.0558 \text{ m} \quad (3.49)$$

$$d_T = x_{WE} + x_{0.26} - x_{0.23} \quad (3.50)$$

$$d_T = 4.4532 \text{ m} \quad (3.51)$$

$$d_w + d_T = 4.4762 \text{ m} \quad (3.52)$$

$$L_T = \frac{M_{AC} + nW \cdot d_w}{d_w + d_T} \quad (3.53)$$

$$L_T = -1616.22 \text{ N} \quad (3.54)$$

$$L_W = nW - L_T \quad (3.55)$$

$$L_W = 55748.93 \text{ N} \quad (3.56)$$

$$C_L = \frac{L_W}{\frac{1}{2} \cdot \rho \cdot V_A^2 \cdot S_W} \quad (3.57)$$

$$C_L = 1.3531 \quad (3.58)$$

b. C.G. at A_{0.28}

$$d_W = x_{0.28} - x_{0.266} \quad (3.59)$$

$$d_W = 0.0217 \text{ m} \quad (3.60)$$

$$d_T = x_{WE} + x_{0.26} - x_{0.28} \quad (3.61)$$

$$d_T = 4.455 \text{ m} \quad (3.62)$$

$$d_w + d_T = 4.4767 \text{ m} \quad (3.63)$$

$$L_T = \frac{M_{ACA} + nW \cdot d_w}{d_w + d_T} \quad (3.64)$$

$$L_T = -679.08 \text{ N} \quad (3.65)$$

$$L_W = nW - L_T \quad (3.66)$$

$$L_W = 54811.79 \text{ N} \quad (3.67)$$

$$C_L = \frac{L_W}{\frac{1}{2} \cdot \rho \cdot V_A^2 \cdot S_W} \quad (3.68)$$

$$C_L = 1.330 \quad (3.69)$$

3.2.5 Case E

$$m = 920 \text{ Kg}, W = mg = 9022.12 \text{ N}, n = 3, nW = 27066.355 \text{ N}$$

$$V_E = 107.06 \text{ m/s}, \rho = 1.225 \text{ Kg/m}^3, S_W = 15.027 \text{ m}^2, \bar{c} = 1.55 \text{ m}, C_{MAC} = -0.0663$$

$$M_{ACE} = \frac{1}{2} \cdot \rho \cdot V_G^2 \cdot S_W \cdot C_{MAC} \cdot \bar{c} \quad (3.70)$$

$$M_{ACE} = -10792.16 \text{ Nm} \quad (3.71)$$

As L_W, L_T and nW changes their directions, while M_{AC} don't, and the previously obtained equations will be changed.

a. C.G. at E_0.23

$$d_W = x_{0.23} - x_{0.266} \quad (3.72)$$

$$d_W = -0.0558 \text{ m} \quad (3.73)$$

$$d_T = x_{WE} + x_{0.26} - x_{0.23} \quad (3.74)$$

$$d_T = 4.4532 \text{ m} \quad (3.75)$$

$$d_w + d_T = 4.4762 \text{ m} \quad (3.76)$$

$$L_T = \frac{M_{ACE} + nW \cdot d_W}{d_w + d_T} \quad (3.77)$$

$$L_T = -2748.41 \text{ N} \quad (3.78)$$

$$L_W = nW - L_T \quad (3.79)$$

$$L_W = 29814.765 \text{ N} \quad (3.80)$$

$$C_L = \frac{L_W}{\frac{1}{2} \cdot \rho \cdot V_E^2 \cdot S_W} \quad (3.81)$$

$$C_L = 0.2826 \quad (3.82)$$

b. C.G. at E_0.28

$$d_W = x_{0.28} - x_{0.266} \quad (3.83)$$

$$d_W = 0.0217 \text{ m} \quad (3.84)$$

$$d_T = x_{WE} + x_{0.26} - x_{0.28} \quad (3.85)$$

$$d_T = 4.455 \text{ m} \quad (3.86)$$

$$d_w + d_T = 4.4767 \text{ m} \quad (3.87)$$

$$L_T = \frac{M_{AC} - nW \cdot d_W}{d_w + d_T} \quad (3.88)$$

$$L_T = -2541.94 \text{ N} \quad (3.89)$$

$$L_W = nW - L_T \quad (3.90)$$

$$L_W = 29608.295 \text{ N} \quad (3.91)$$

$$C_L = \frac{L_W}{\frac{1}{2} \cdot \rho \cdot V_E^2 \cdot S_W} \quad (3.92)$$

$$C_L = 0.2806 \quad (3.93)$$

3.2.6 Case G

$m = 920 \text{ Kg}$, $W = mg = 9022.12 \text{ N}$, $n = 3$, $nW = 27066.355 \text{ NV}_G = 66.905 \text{ m/s}$, $\rho = 1.225 \text{ Kg/m}^3$, $S_W = 15.027 \text{ m}^2$, $\bar{c} = 1.55 \text{ m}$, $C_{MAC} = -0.066$

$$M_{ACG} = \frac{1}{2} \cdot \rho \cdot V_G^2 \cdot S_W \cdot C_{MAC} \cdot \bar{c} \quad (3.94)$$

$$M_{ACG} = -4214.74 \text{ Nm} \quad (3.95)$$

a. C.G. at G_0.23

$$d_W = x_{0.23} - x_{0.266} \quad (3.96)$$

$$d_W = -0.0558 \text{ m} \quad (3.97)$$

$$d_T = x_{WE} + x_{0.26} - x_{0.23} \quad (3.98)$$

$$d_T = 4.4532 \text{ m} \quad (3.99)$$

$$d_w + d_T = 4.4762 \text{ m} \quad (3.100)$$

$$L_T = \frac{M_{ACG} + nW \cdot d_W}{d_w + d_T} \quad (3.101)$$

$$L_T = -1278.996 \text{ N} \quad (3.102)$$

$$L_W = nW - L_T \quad (3.103)$$

$$L_W = 28345.351 \text{ N} \quad (3.104)$$

$$C_L = \frac{L_W}{\frac{1}{2} \cdot \rho \cdot V_G^2 \cdot S_W} \quad (3.105)$$

$$C_L = 0.6880 \quad (3.106)$$

b. C.G. at G_0.28

$$d_W = x_{0.28} - x_{0.266} \quad (3.107)$$

$$d_W = 0.0217m \quad (3.108)$$

$$d_T = 4.486 + x_{0.26} - x_{0.28} \quad (3.109)$$

$$d_T = 4.455m \quad (3.110)$$

$$d_w + d_T = 4.4767m \quad (3.111)$$

$$L_T = \frac{M_{AC} - nW \cdot d_W}{d_w + d_T} \quad (3.112)$$

$$L_T = -1072.683 \quad (3.113)$$

$$L_W = nW - L_T \quad (3.114)$$

$$L_W = 28139.038N \quad (3.115)$$

$$C_L = \frac{L_W}{\frac{1}{2} \rho V_A^2 S_W} \quad (3.116)$$

$$C_L = 0.6830 \quad (3.117)$$

3.2.7 Overview of defined cases Table 3.1

Table 3.1 Summary of defined cases

<i>Case</i>	<i>n</i>	<i>V (m/s)</i>	<i>P_d (N/m²)</i>	<i>L_T (N)</i>	<i>L_T (m)</i>	<i>L_W (m)</i>	<i>C_L</i>
A_023	6	66.90	2741.311	-1616.08	-3085.480	55748.930	1.353
A_028	6	66.90	2741.311	-10792.16	-2148.340	54811.789	1.330
D_023	6	107.06	7020.379	-4214.74	-1616.220	57218.199	0.542
D_028	6	107.06	7020.379	-4214.74	-679.080	56281.051	0.533
E_023	3	107.06	7020.379	-10792.16	-2748.410	29814.766	0.283
E_028	3	107.06	7020.379	-10792.16	-2541.940	29608.295	0.281
G_023	3	66.90	2741.721	-4214.74	-1278.996	28345.352	0.688
G_028	3	66.90	2741.721	-4214.74	-1072.683	28139.037	0.683

3.3 Approximate span-wise distribution of aerodynamic load

Schrenk examined experimental results for many untwisted wing plan forms and devised. The approximate rule that distribution of the additional lift (lift associated with the chord distribution without twist) is nearly proportional at every point to the ordinate that lies halfway between the elliptical and actual chord distribution for the same total area and span. For the untwisted wing, the basic lift equal to zero.

The area of the real wing is:

$$S = \int_{-b/2}^{b/2} c(y) \cdot dy \quad (3.118)$$

While the area of the elliptic wing is:

$$S_E = \frac{\pi}{4} \cdot c_{SE} \cdot b \quad (3.119)$$

As the area of real wing and equivalent elliptic one are equals, so c_{SE} -chord of the equivalent elliptic wing at the plane of symmetry is $c_{SE} = \frac{4 \cdot S}{\pi b}$, where b – is span (equal for both wings)

The local chord of the equivalent elliptic wing is:

$$c_E(y) = c_{SE} \cdot \sqrt{1 - \left(\frac{y}{b/2}\right)^2} \quad (3.120)$$

Lift equation is written as:

$$L = \int_{-\frac{b}{2}}^{\frac{b}{2}} p(y) \cdot c(y) \cdot dy \quad (3.121)$$

Where local pressure is defined as:

$$p = \left(\frac{N}{m^2}\right) = k \cdot \frac{1}{2} \left[1 + \frac{c_{SE}}{c(y)} \sqrt{1 - \left(\frac{y}{b/2}\right)^2}\right] \quad (3.122)$$

and factor of proportionality: $k = \frac{L}{S'}$

So we find:

$$p\left(\frac{N}{m^2}\right) = \frac{1}{2} \left[1 + \frac{c_{SE}}{c(y)} \sqrt{1 - \left(\frac{y}{b/2}\right)^2}\right] \cdot \frac{L}{S'} \quad (3.123)$$

Schrenk's approximate span wise distributed aerodynamic load is:

$$q_A\left(\frac{N}{m}\right) = \frac{1}{2} \left[c(y) + c_{SE} \sqrt{1 - \left(\frac{y}{b/2}\right)^2} \right] \cdot \frac{L}{S'} \quad (3.124)$$

Aerodynamic Load:

A Fortran Code WING_LOADING is used to calculate aerodynamic load and the results can be found in Appendix A

Aerodynamic Loads

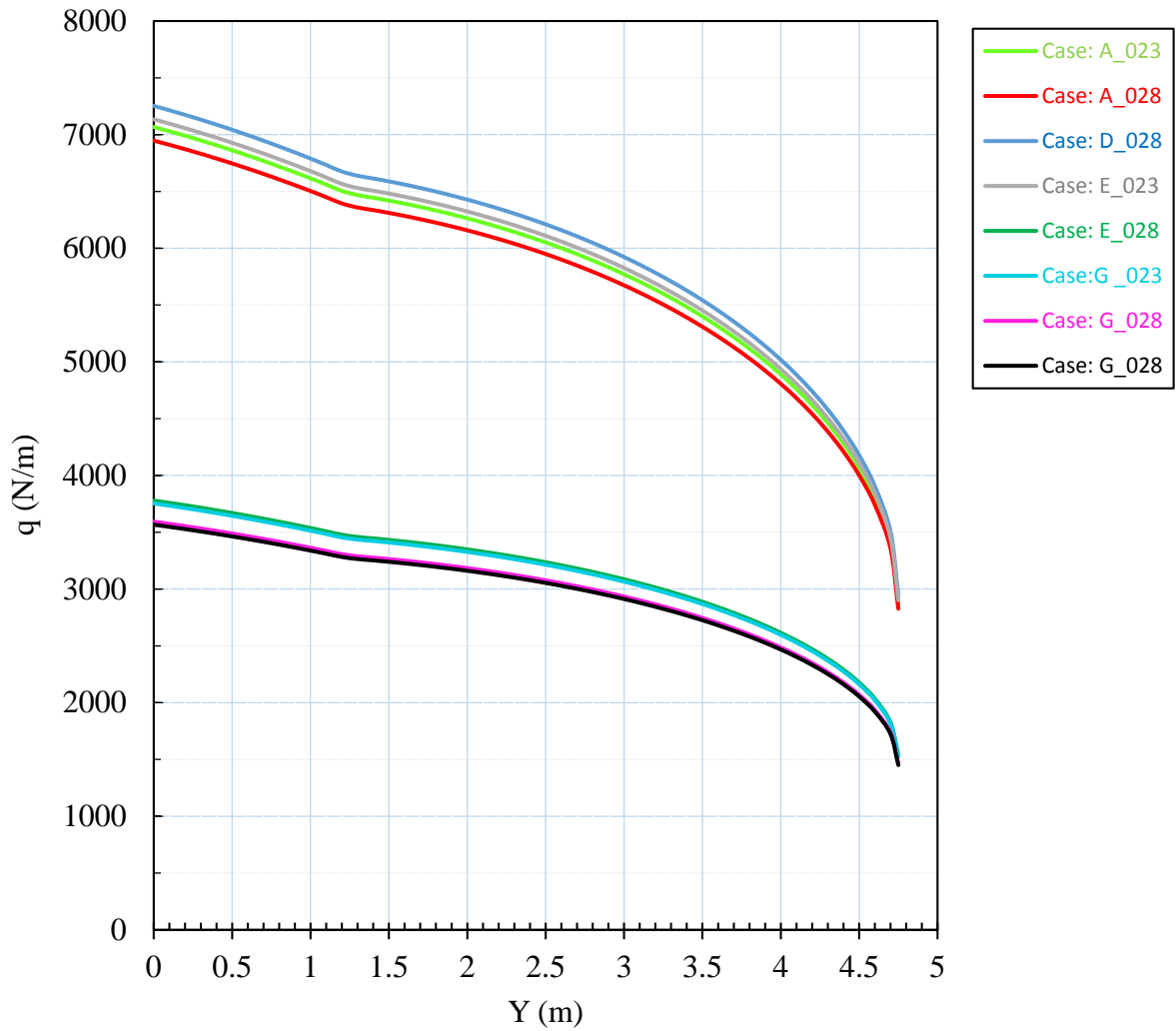


Figure 3.3 Span-wise distribution of aerodynamic loading

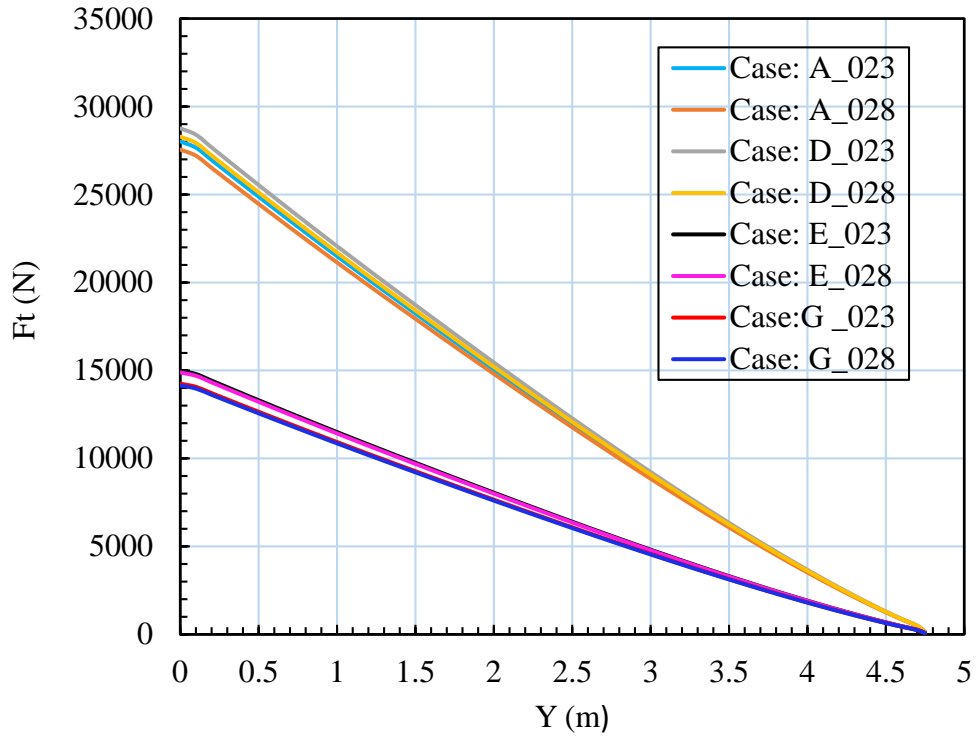


Figure 3.4 Shear forces due to aerodynamic loading

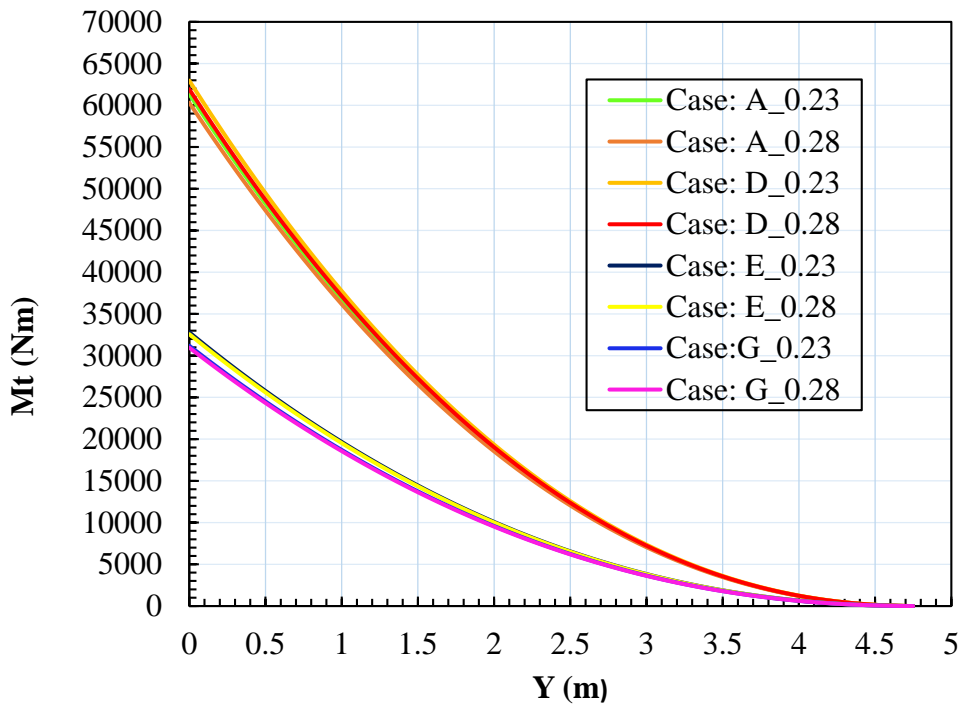


Figure 3.5 Bending moment due to aerodynamic loading

3.4 Loading of wing

Table 3.2 Load cases at $y = 0$

<i>Case</i>	<i>Y (m)</i>	<i>q (N/m)</i>	<i>FT (N)</i>	<i>MF (Nm)</i>
A_0.23	0	7066.73	28023.35	61340.898
A_0.28	0	6947.93	27552.28	60309.77
D_0.23	0	7252.97	28761.91	62957.566
D_0.28	0	7134.18	28290.82	61926.41
E_0.23	0	3779.32	14987.01	32805.383
E_0.28	0	3753.14	14883.22	32578.203
G_0.23	0	3593.05	14248.37	31188.576
G_0.28	0	3566.9	14144.67	30961.568

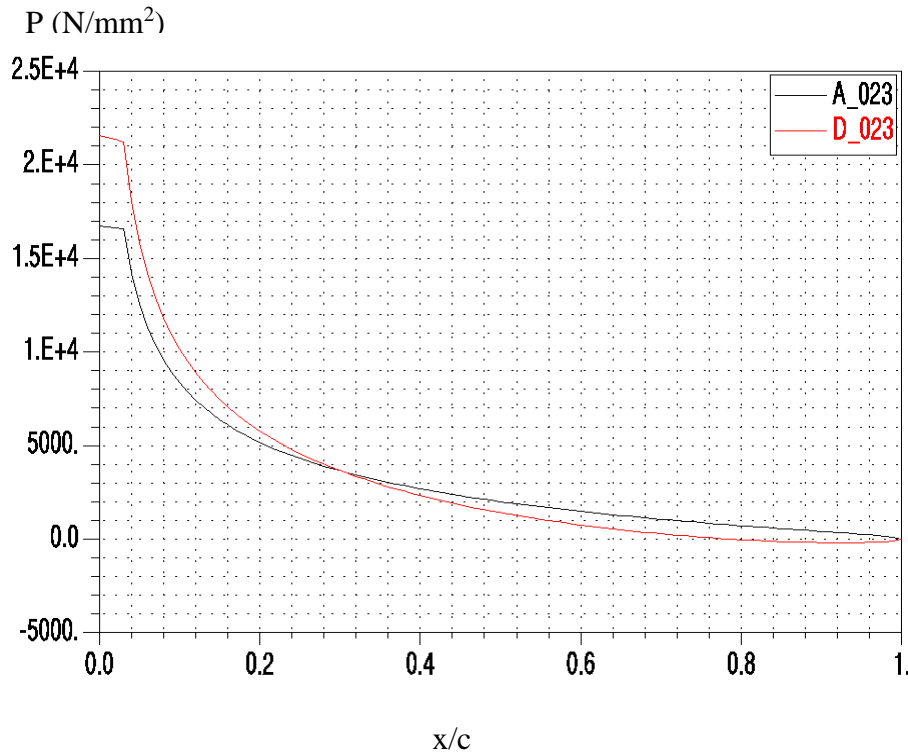


Figure 3.6 Chord wise distribution of p for A023 and D023 cases

3.5 Analysis of the wing structure using finite element method

For these two cases, the distributed pressure loading is recalculated in equivalent systems of forces distributed along each rib.

These forces are distributed over the ribs of the wing. The bending moments at positions of ribs cross-sections are equal to moments of distributed pressure loading. The moments of systems of forces and moments of distributed pressure loading about the wing's leading edge are similar too.

The transversal forces and bending moments for a case of distributed pressure loading and loading of concentrated forces on ribs.

Table 3.3 Results of Loads for Case D_0.23 for Transversal Forces and Bending Moments

Case: D_023					
Y (m)	Distributed pressure loading		Equivalent concentrated forces.		
	Ft (N)	Mf (Nm)	Fr (N)	Frt (N)	Mrf (Nm)
0	28761.9	62957.566	0	28399.4	62957.566
0.08	28471.8	60685.621	1150.51	28399.4	60685.621
0.337	26696.5	53682.66	1791.9	27248.9	53682.66
0.593	24883.4	47165.68	1943.93	25457	47165.68
0.884	22860.6	40323.383	2213.92	23513	40323.383
1.24	20446.6	32740.896	2346.85	21299.1	32740.896
1.596	18088.3	25993.887	2269.9	18952.3	25993.887
1.922	15960.7	20555.436	2095.28	16682.4	20555.436
2.247	13876.3	15814.63	2046.53	14587.1	15814.63
2.573	11830	11726.408	1990.7	12540.6	11726.408
2.895	9861.32	8329.353	1994.26	10549.9	8329.353
3.23	7880.97	5463.226	1915.81	8555.6	5463.226
3.565	5982.19	3238.893	1814.33	6639.8	3238.893
3.899	4187.69	1627.189	1752.12	4825.46	1627.189
4.235	2512.09	594.546	1243.98	3073.35	594.546
4.56	1055.8	92.727	1829.37	829.369	0

Table 3.4 Results of Loads for Case E_0.23 for Transversal Forces and Bending Moments

Case: E_023					
Y (m)	Distributed pressure loading		Equivalent concentrated forces		
	Ft (N)	Mf (Nm)	Fr (N)	Frt (N)	Mrf (Nm)
0	14987	32805.383	0	14798.1	32805.383
0.08	14835.8	31621.535	599.517	14798.1	31621.535
0.337	13910.8	27972.502	933.646	14198.6	27972.502
0.593	12966	24576.682	1012.94	13264.9	24576.682
0.884	11912	21011.355	1153.65	12252	21011.355
1.24	10654.1	17060.344	1222.85	11098.3	17060.344
1.596	9425.29	13544.67	1182.79	9875.49	13544.67
1.922	8316.67	10710.849	1091.79	8692.7	10710.849
2.247	7230.54	8240.551	1066.4	7600.92	8240.551
2.573	6164.26	6110.296	1037.29	6534.52	6110.296
2.895	5138.45	4340.188	1044.14	5497.23	4340.188
3.233	4097.51	2835.044	997.215	4453.09	2835.044
3.565	3117.15	1687.694	941.461	3455.87	1687.694
3.899	2182.09	847.881	912.978	2514.41	847.881
4.235	1308.98	309.8	648.202	1601.43	309.8
4.56	550.145	48.318	953.231	953.231	0

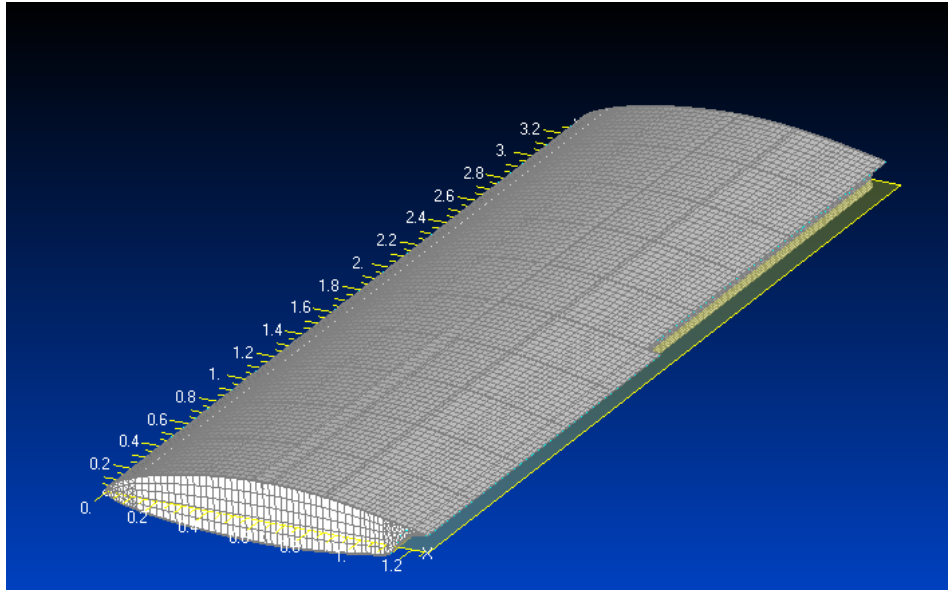


Figure 3.7 Numbers of points i x and y directions at which the forces are applied

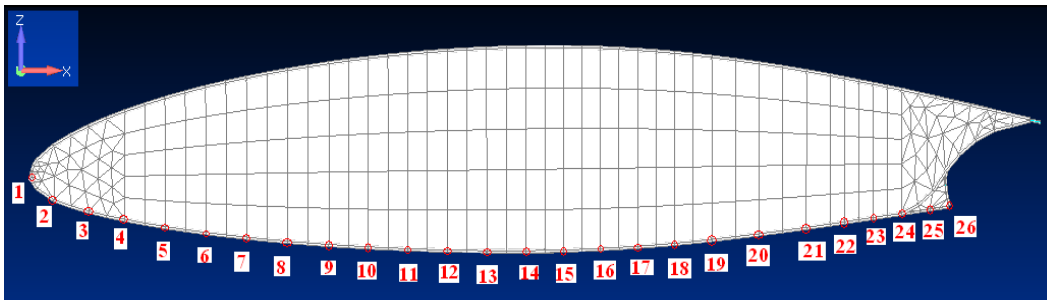


Figure 3.8 Numbers of applied forces at nodes on lower side of ribs

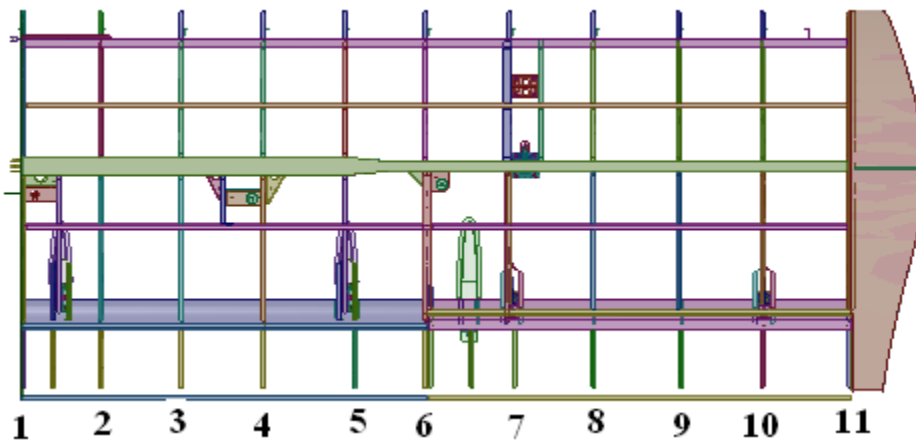


Figure 3.9 Ribs Positions and numbers

3.6 Load distribution along the chord

Distributed load $P(x)$ per m^2 , along the cord c of the airfoil at a distance y from the plane of symmetry:

PROGRAM WING_FORCES

Table 3.7 Load cases distribution of forces and pressure

Table 3.5 Load distribution of forces and pressure case D0.23

Table 3.6 Load distribution of forces and pressure case E0.23

$$P(x) = q \cdot [C_L \cdot f_L(\theta) + \bar{C} \cdot f_M(\theta) + \beta \cdot f_\beta(\theta, \phi)] \quad (3.125)$$

q – Dynamical pressure.

β -angle of aileron or flap deflection.

C_L - Local lift coefficient due to angle of attack α and angle β of aileron or flap deflection.

$$C_L = C_{L(\beta=0)} + \frac{dC_L}{d\beta} \cdot \beta \quad (3.126)$$

\bar{C}_M -coefficient of the moment without deflection of aileron or flap, which corresponds to the angle of attack α for case $C_{L(\beta=0)}$.

This moment coefficient is related to the point at $x = 0.28 \cdot c$

$$\bar{C}_M = C_{M(\beta=0)} - 0.28 \cdot C_{L(\beta=0)} \quad (3.127)$$

$C_{M(\beta=0)}$ —moment coefficient related to the point at the leading edge of an airfoil.

$C_L \cdot f_L(\theta)$ -function of load distribution for straight-line airfoil at the angle of attack α
(Without deflection of aileron or flap) having:

$$C_L = C_{L(\beta=0)} + \frac{dC_L}{d\beta} \cdot \beta \quad (3.128)$$

$\bar{C}f_M(\theta)$ -function of load distribution for the parabolic airfoil, with lift equal to zero and curvature, is such that the coefficient of the moment at $x = 0.28 \cdot c$ is exactly \bar{C}

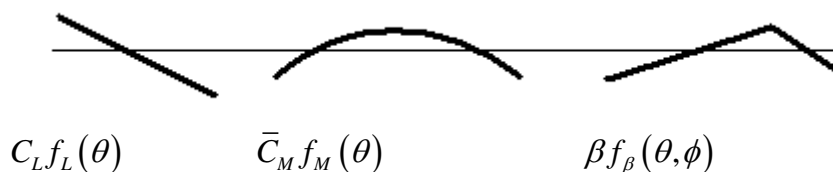


Figure 3.10 Stringer with an effective thickness of skin

$\beta f_\beta(\theta, \phi)$ -function of load distribution of straight-line airfoil with deflected aileron or flap for angle β , and with lift equal to zero.

$$\theta = \arccos\left(1 - \frac{2x}{c}\right) \quad (3.129)$$

$$\phi = \arccos\left(\frac{2c_{a,f}}{c} - 1\right) \quad (3.130)$$

Curve-1

$$f_L(\theta) = 0.716 \cdot \cot g\left(\frac{\theta}{2}\right) \quad (3.131)$$

Curve-2

$$f_M(\theta) = 5.8 \cdot \sin(\theta) - 3.26 \cdot \cot g\left(\frac{\theta}{2}\right) \quad (3.132)$$

Curve-3

$$f_\beta(\theta, \phi) = 1.3 \cdot \log\left(\frac{1 - \cos(\theta + \phi)}{1 - \cos(\theta - \phi)}\right) + (0.024 - 1.273 \cdot \sin(\phi)) \cdot \cot g\left(\frac{\theta}{2}\right) \quad (3.133)$$

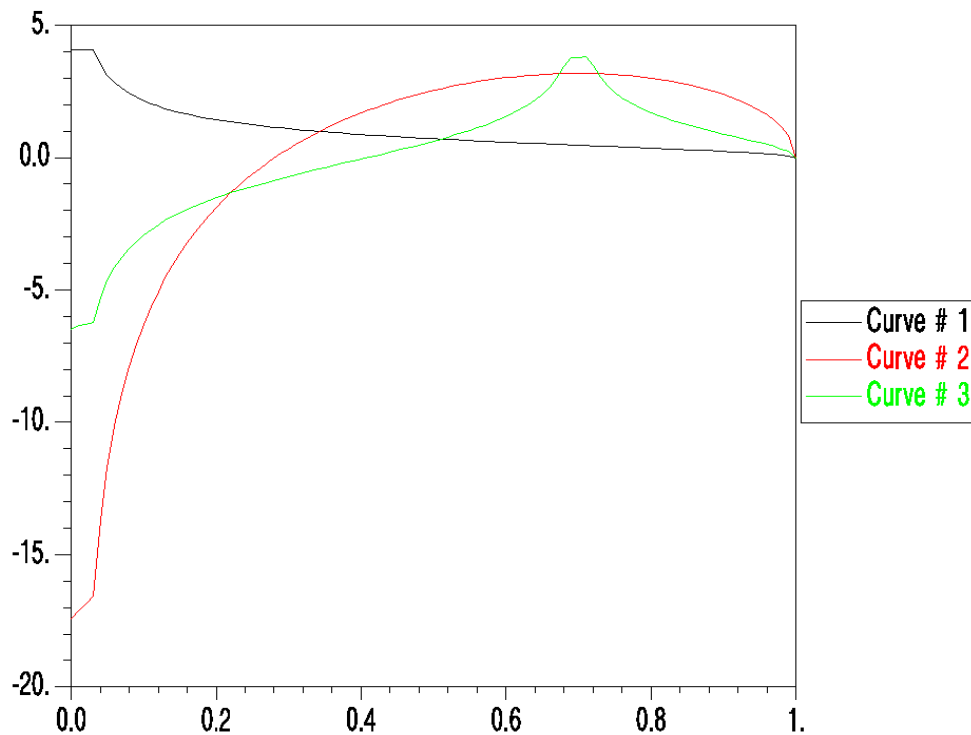


Figure 3.11 Functions for chord-wise load distribution

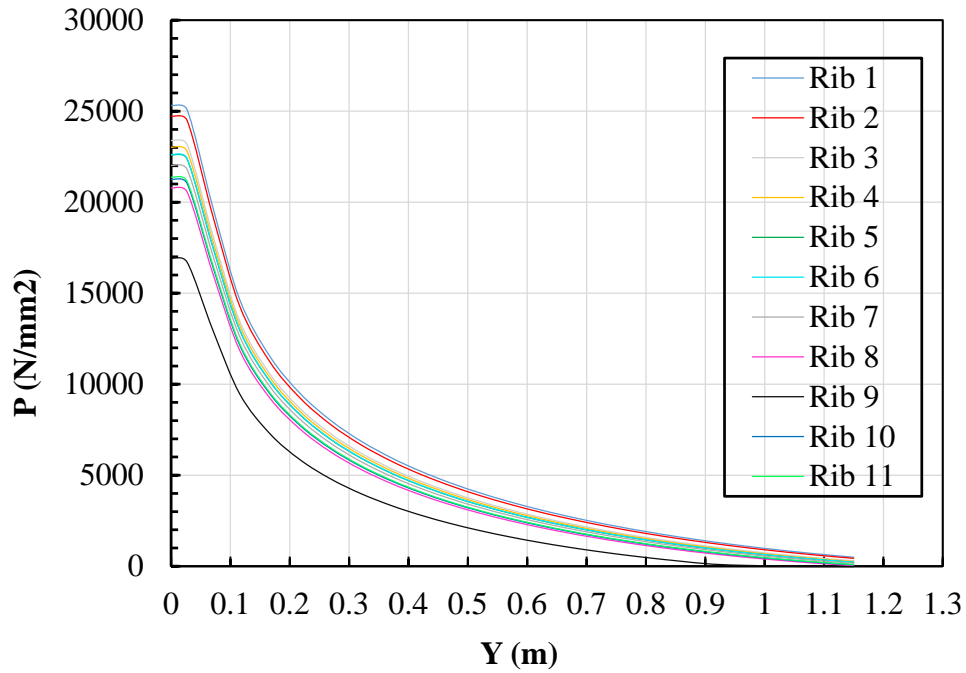


Figure 3.12 Actual chord-wise pressure distributions at positions of ribs Case D0.23

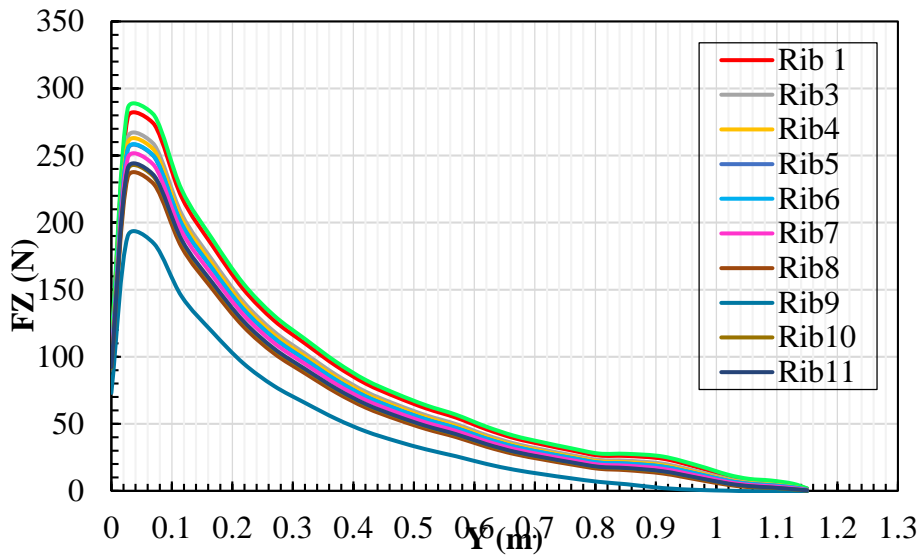


Figure 3.13 Distributions of applied equivalent forces at nodes of ribs Case D0.23

3.7 Flap and aileron loading

Pressure on point 26 at the end of the rib is the pressure at the leading edge of the flap or aileron.

Position of flap ribs equals positions of (1,2,3,4,5 and 6) wing ribs, while positions of aileron ribs are equal to positions of 6,7,8,9,10 and 11 wing ribs.

Instead of lightly curvilinear, it is assumed that chord-wise distributions of pressure over flap and aileron are linear (triangle shape). Chords of aileron and flaps approximatively are 0.4 m, and the distance between their ribs approximatively is 0.32 m, so the distributed loading is $a = 0.4 m$.

$$q = \frac{1}{2} \cdot a \cdot p \text{ (N/m)} \tag{3.134}$$

Table 3.7 Load cases for Ribs

Rib	y (m)	p (N/m ²)	q (N/m)
1	1.240	497.046	99.4092
2	1.596	436.415	87.283
3	1.922	298.809	59.7618
4	2.247	260.396	52.0792
5	2.573	216.398	43.2796
6	2.895	219.205	43.841
7	3.230	157.382	31.4764
8	3.565	77.421	15.4842
9	3.899	28.392	5.6784
10	4.235	72.026	14.4052
11	4.560	89.269	17.8538

Instead of lightly parabolic span-wise load distribution over aileron and flap, the linear ones are assumed.

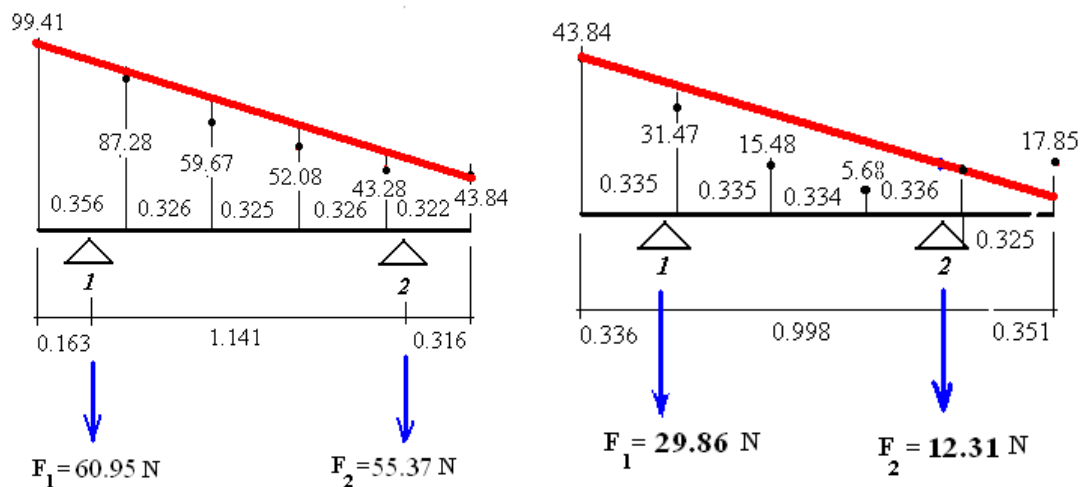


Figure 3.14 Actual and assumed distributed loads over flap and aileron for D_{023} load case.

3.8 Inertial loading (constant chord) Case D_0.23

Mass of the complete wing: 50.142 kg

Mass of the wing without flap and aileron: 42.181 kg

Position of c.g $x = 623$ mm, $y = 1561$ mm
 Mass per unit span of wing:

3.8.1 Moment due to aerodynamic loading:

$$M_{x(y=1.40)}^A = 29599.908 \text{ (Nm)}$$

Mass of wing structure: $M = 50.142$ (kg)

Mass per unit length of the wing

$$(y - y_{start}) = 3.32 \text{ m}$$

$$M = \frac{M}{(y - y_{start})} \tag{3.135}$$

$$M = 15.1 \text{ (kg/m)} \tag{3.136}$$

3.8.2 Distributed loading due to inertial loading in case D_{023}

Inertial loading data:

Mass of the complete wing: 50.142 kg

Position of c.g. $x = 734$ mm, $y = 1575$ mm

Mass of the wing without flap and aileron: 42.181 kg

Position of c.g $x = 623$ mm, $y = 1561$ mm

Mass per unit span of wing: $42.181/(4.56-1.24) = 42.181/3.32 = 12.705$ kg/m

Distributed inertial loading in D flight case: $n=6$

$$q_1^l = m \cdot g \cdot n \tag{3.137}$$

$$q_i^n = 747.561 \text{ (N/m)}$$

Table 3.8 Results of Inertial Loads case $D_{0.23}$

Rib	y (m)	p (N/m ²)	q (N/m)	FT (N)	Mf (Nm)
1	1.24	497.046	99.409	2481.926	4119.997
2	1.596	436.415	87.283	2215.792	3283.803
3	1.922	298.809	59.672	1972.084	2601.179
4	2.247	260.396	52.079	1729.125	1999.733
5	2.573	216.398	43.28	1485.418	1475.762
6	2.895	219.205	43.841	1244.701	1036.213
7	3.23	157.382	31.476	994.265	661.186
8	3.565	77.421	15.484	743.830	370.055
9	3.899	28.392	5.678	494.142	163.314
10	4.235	72.026	14.405	242.959	39.481
11	4.56	89.269	17.854	0.000	0.000

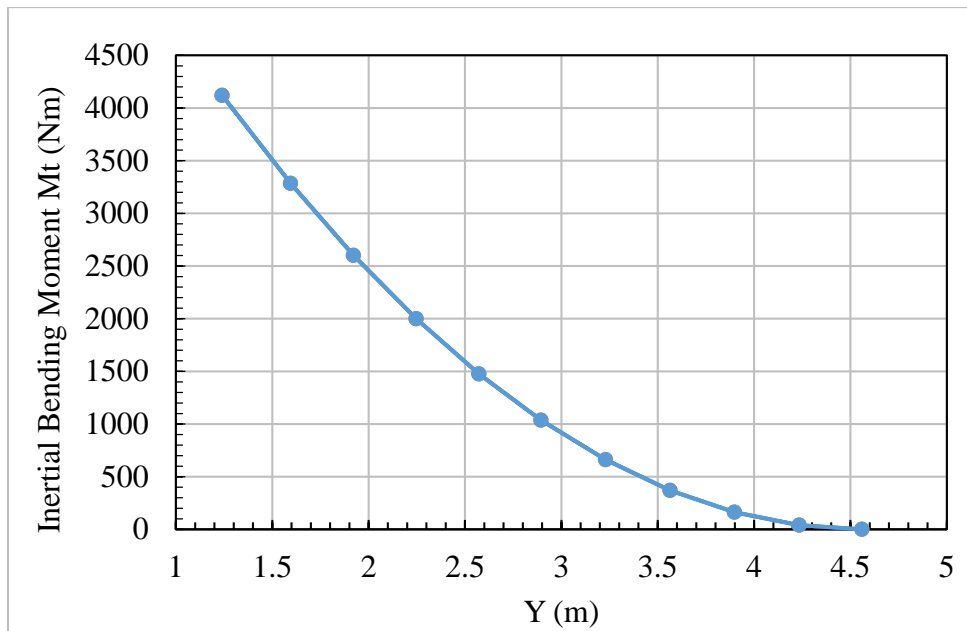


Figure 3.15 Shear forces due to inertial loading of the wing

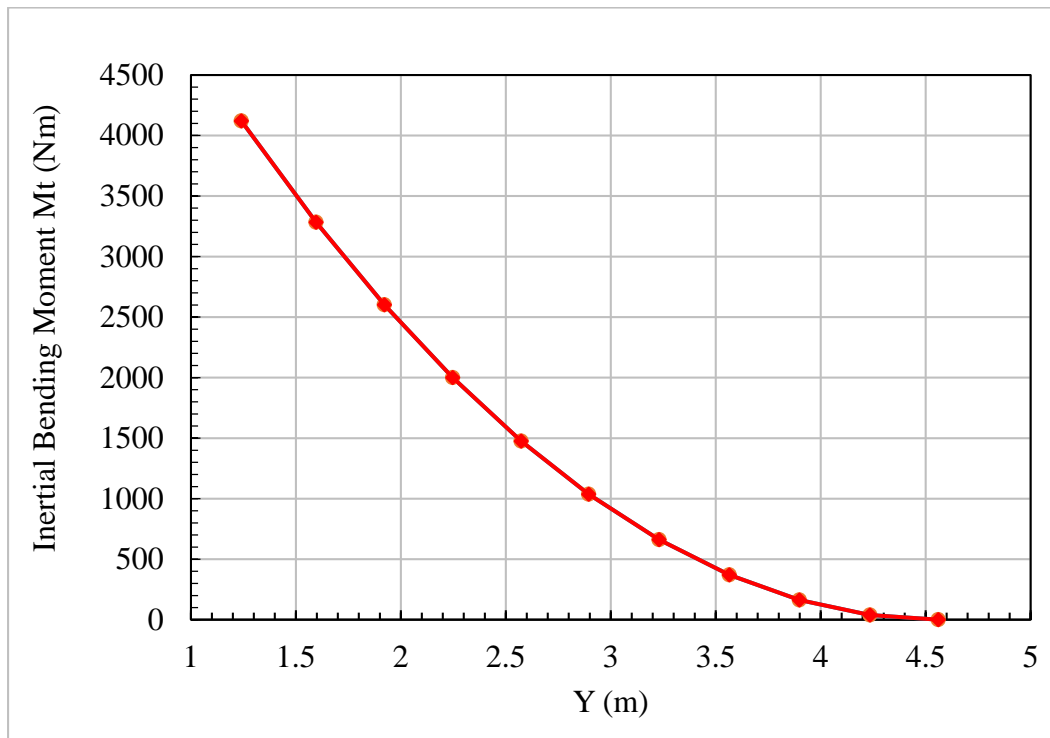


Figure 3.16 Span-wise distribution of bending moment due to inertial loading

3.8.3 Distributed loading due to inertial loading in case *E_023*

$$q_1^l = m \cdot g \cdot n \tag{3.138}$$

$$q_l^n = 373.780 \text{ (N/m)}$$

Table 3.9 Results of Inertial Loads case **E_0.23**

Rib	y (m)	q (N)	Ft (N)	Mf (Nm)
1	1.24	373.784	1240.963	2059.998
2	1.596	373.784	1107.896	1641.902
3	1.922	373.784	986.042	1300.590
4	2.247	373.784	864.562	999.866
5	2.573	373.784	742.709	737.881
6	2.895	373.784	622.350	518.107
7	3.23	373.784	497.133	330.593
8	3.565	373.784	371.915	185.028
9	3.899	373.784	247.071	81.657
10	4.235	373.784	121.480	19.740
11	4.56	373.784	0.000	0.000

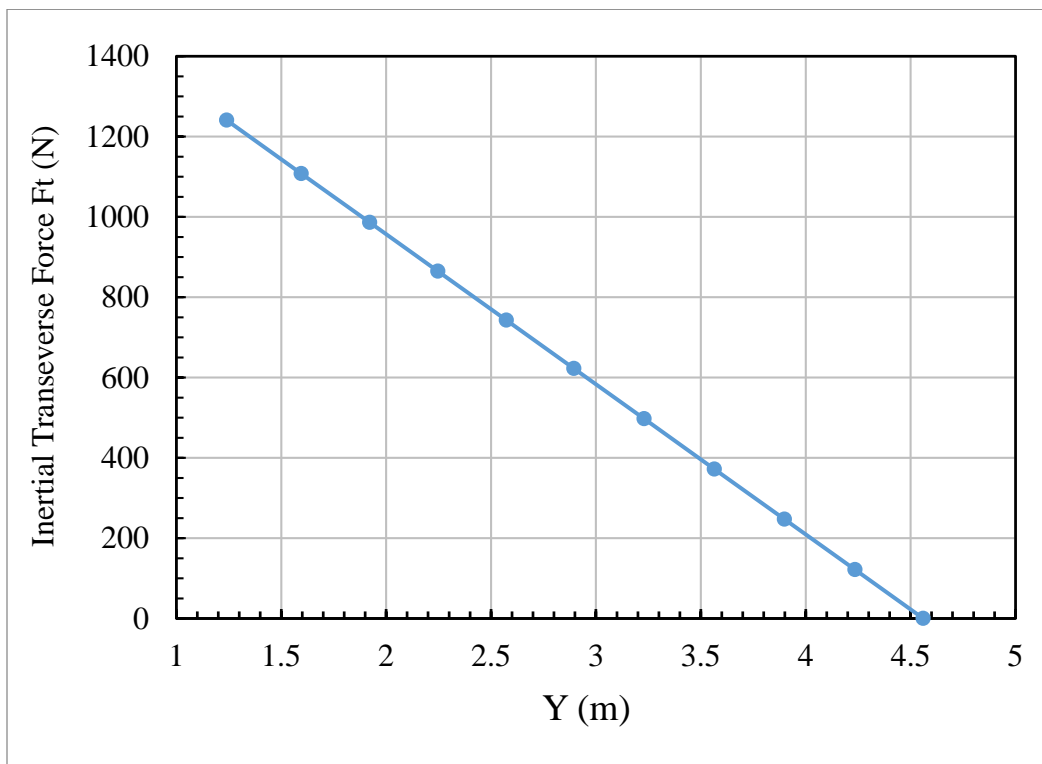


Figure 3.17 Transversal forces due to inertial loading of wing

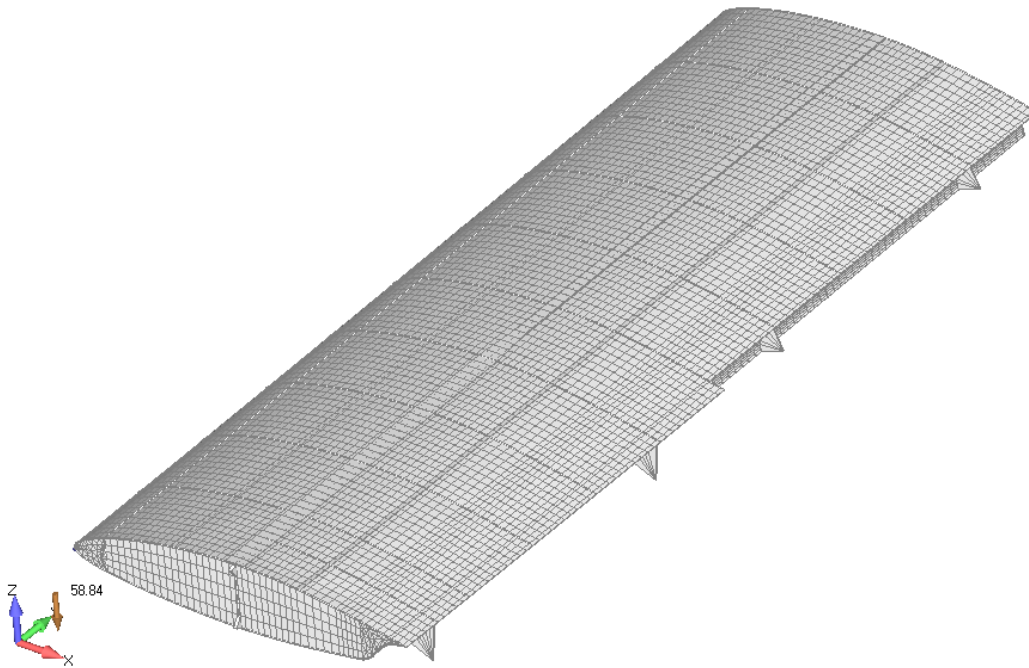


Figure 3.20 Finite element model of the wing structure – with skin

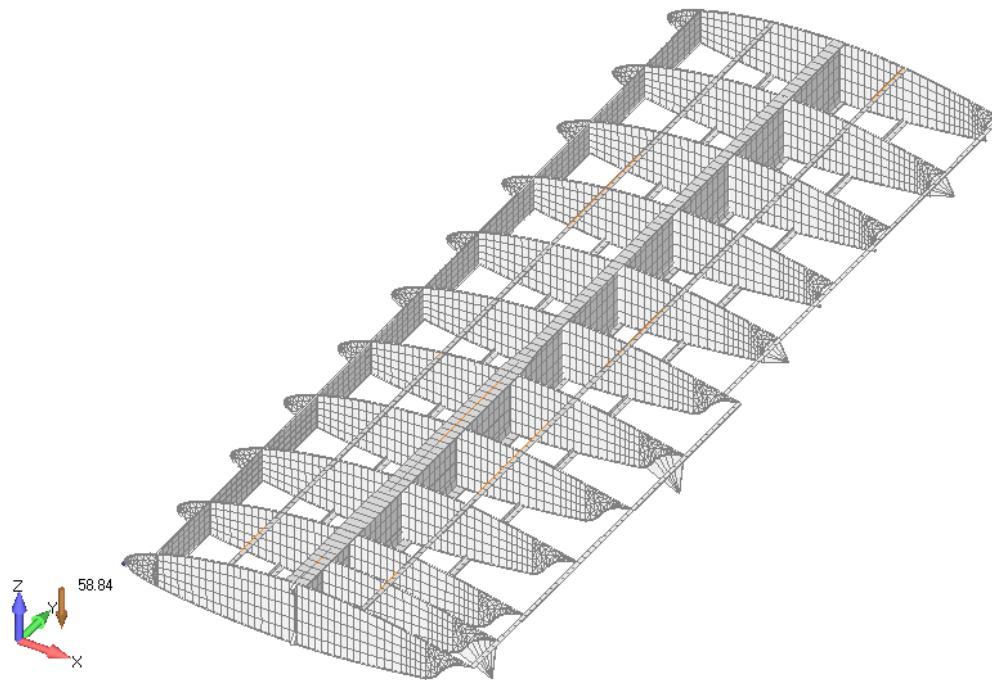


Figure 3.21 Finite element model of the wing structure – without skin

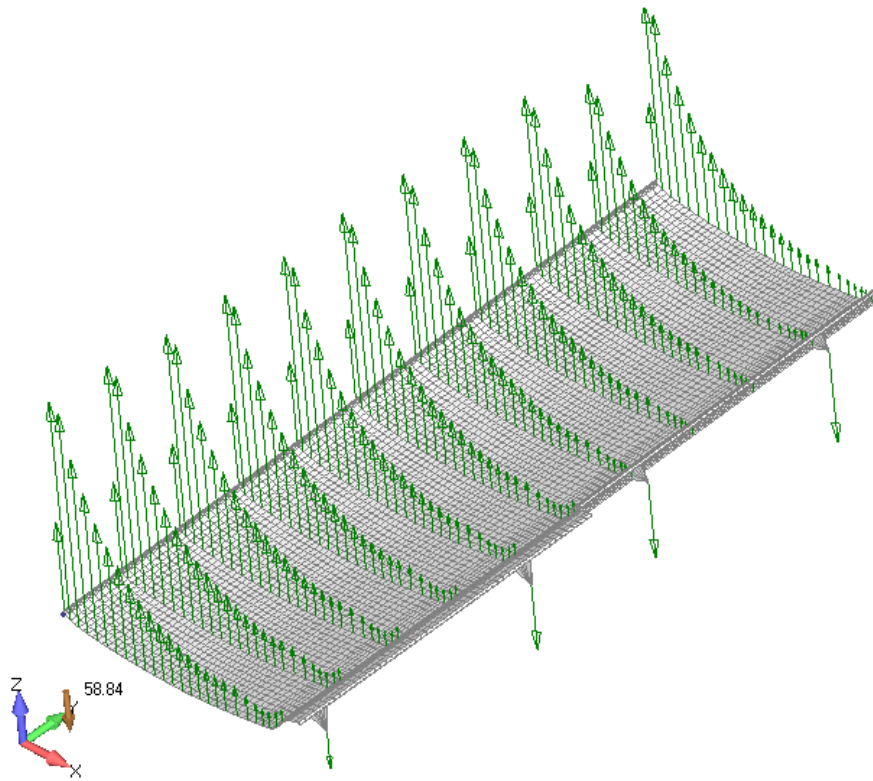


Figure 3.22 Example of applied aerodynamic loads: CASE 023

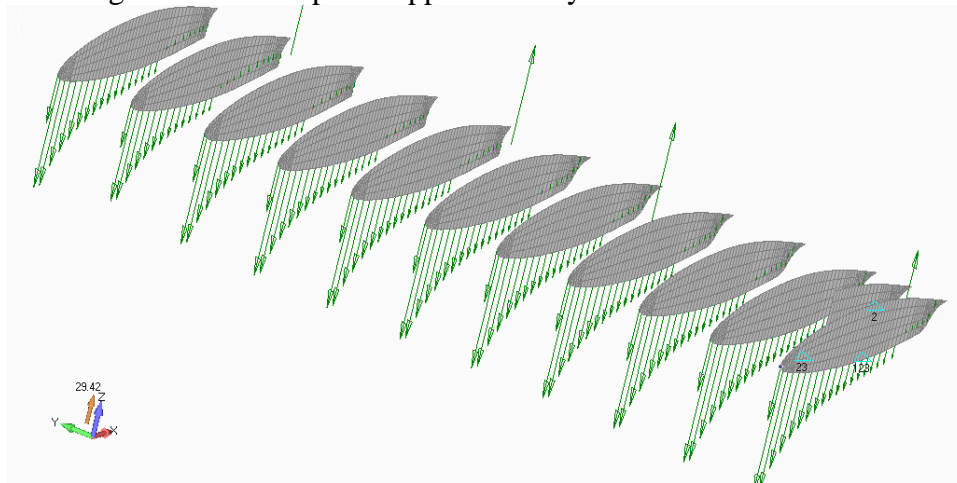


Figure 3.23 Case E_0.23: Loading of wing structure $J = 1.0$ applied at ribs

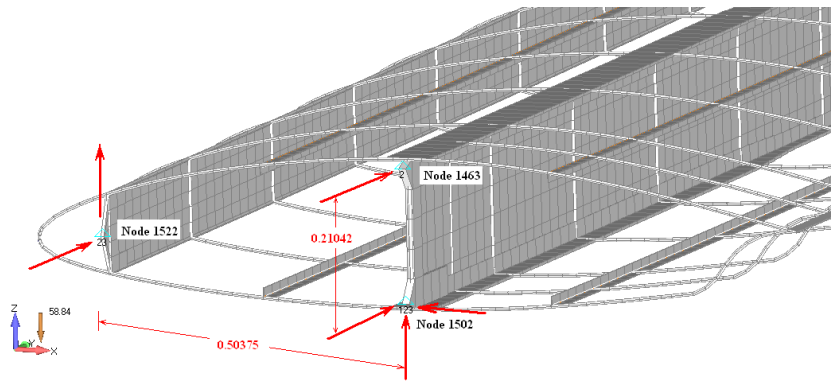


Figure 3.24 Fittings and constrained displacements of wing

3.10 RESULTS OF FINITE ELEMENT ANALYSIS

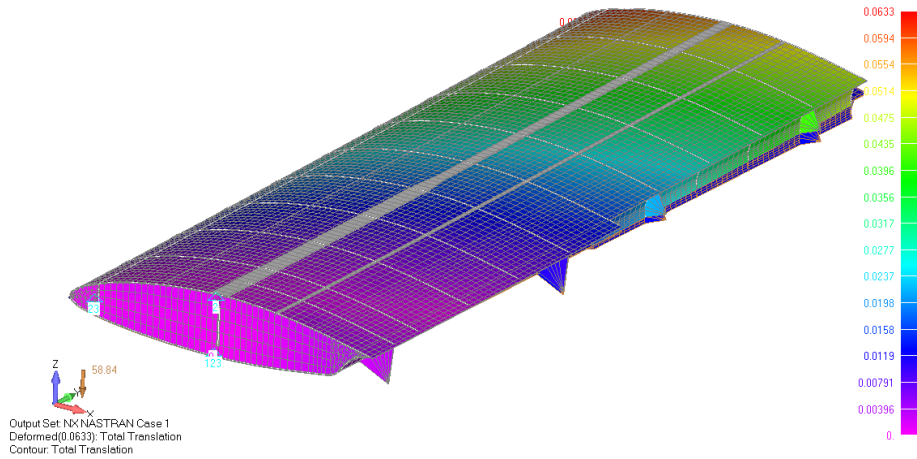


Figure 3.25 Deformed and undeformed configuration of wing structure for CASE D_023 J=1.0 (maximum displacement at the tip of the wing is 63.3 mm)

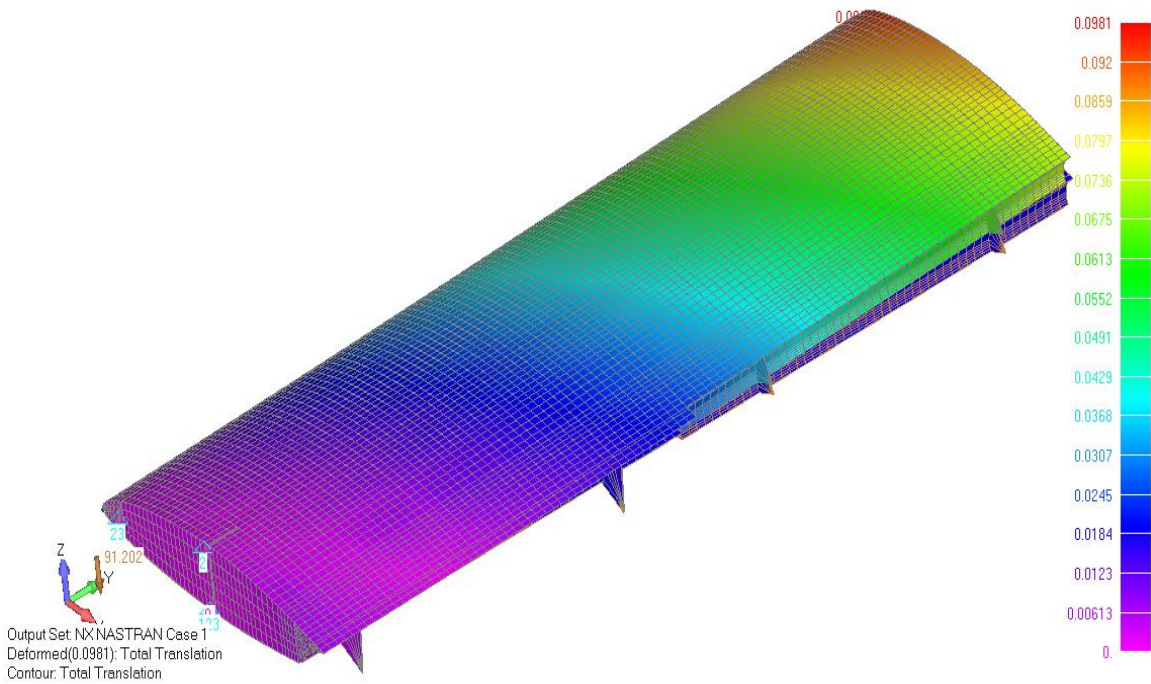


Figure 3.26 Deformed and undeformed configuration of wing structure for CASE D_0.23 J=1.55 (maximum displacement at the tip of the wing is 98.1 mm)

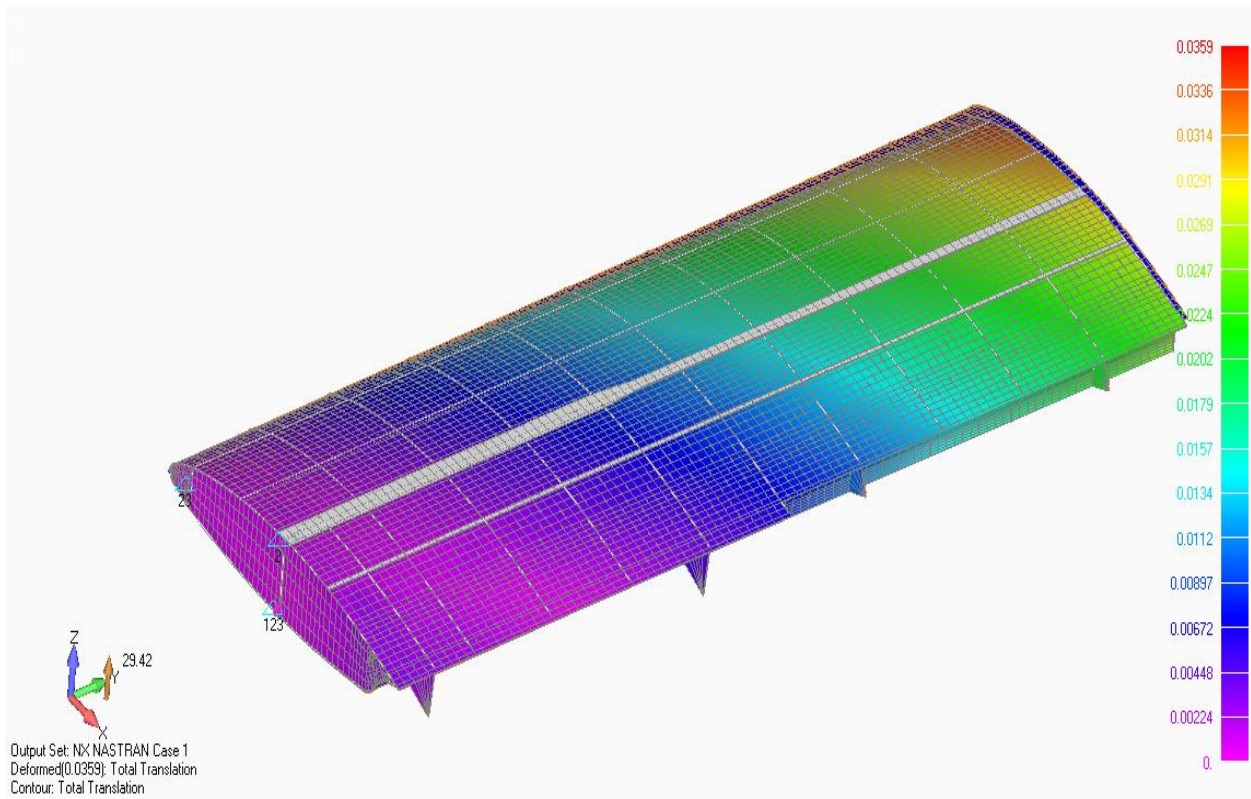


Figure 3.27 CASE D_0.23 J=1.0 total displacements, maximum displacement 35.9 mm

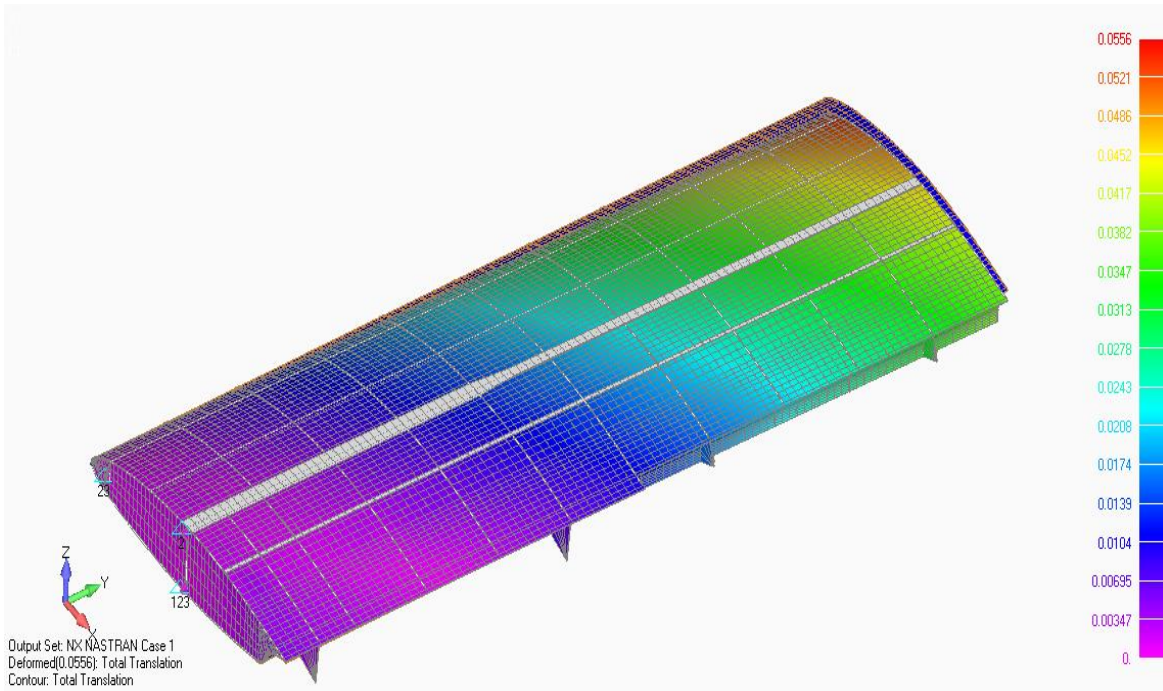


Figure 3.28 CASE D_0.23 $J=1.55$ Total displacements, maximum displacement 55.6 mm

CHAPTER 4
NUMERICAL DETERMINATION of LOADING of
WING-FUSELAGE FITTING

4 Numerical Determination of Loading of Wing-Fuselage Fitting

"Based on the data obtained in previous chapter in this chapter the determination of the wing-fuselage attachment load was carried out."

4.1 Loads on wing

Calculations performed in this chapter are done following the requirements in EASA CS 23 [50]. Loads on the wing are calculated by the small program that utilizes the Anderson method to calculate span-wise load distribution. Deflection of elevators determined for each flying condition to maintain the equilibrium of moments acting on the airplane. Loads on the wing and reactions of the supports are presented schematically in

Figure 4.2. It is assumed that the main spar is loaded by lift and drag force.

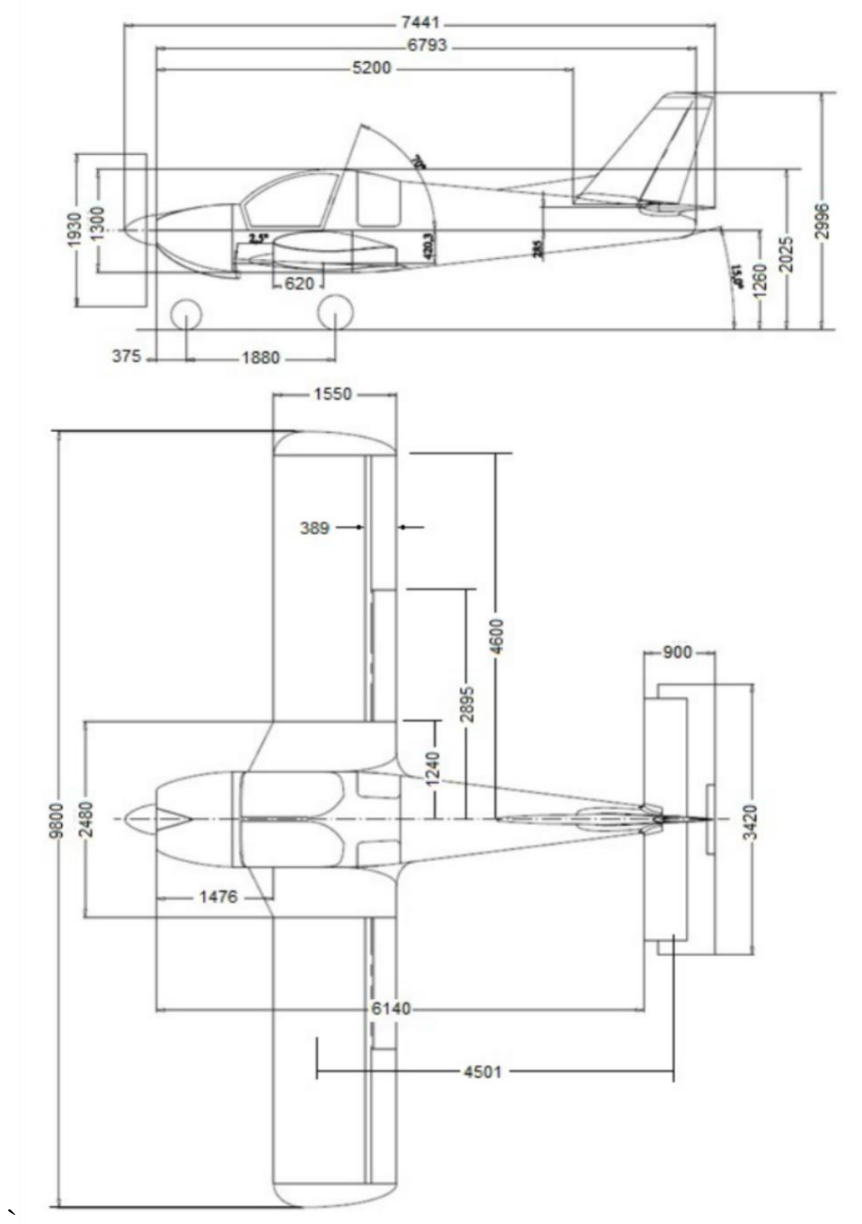


Figure 4.1 Airplane geometry (all dimensions in mm)

Geometrical data necessary for calculation are given in the

Figure 4.1.

4.1.1 Input data

Loads in a vertical direction are calculated from the local distribution defined as:

$$dZ_{(y)} = dZL_{(y)} - n \cdot g \cdot \bar{m} \cdot d_y \quad (4.1)$$

$Z(y)$ is the local upward force, $L(y)$ is the local lift force, \bar{m} is the mass of the wing per unit span:

$$\bar{m} = \frac{m}{(b - 2y_{wstart})/2} \quad (4.2)$$

$$\bar{m} = 13.85 \text{ kg/m}$$

Local torsion moment about the aerodynamic centre is calculated by

$$M_{T(y)} = M_{a(y)} - n \cdot g \cdot \bar{m} \cdot (t_{cg} - \bar{c}_w/4) \quad (4.3)$$

$MT(Y)$ is the local torsion moment; $Ma(Y)$ is the aerodynamic moment about the aerodynamic centre.

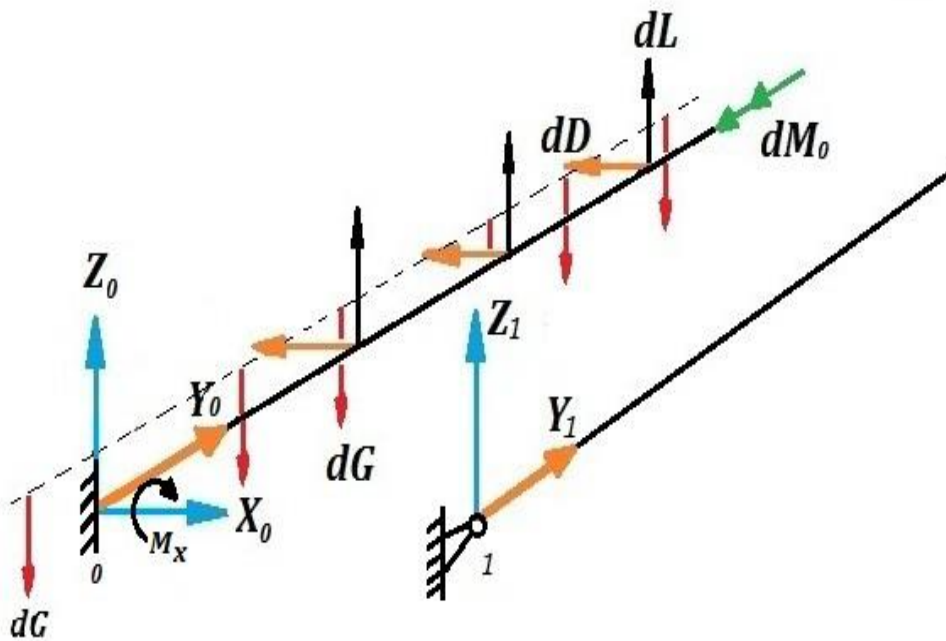


Figure 4.2 Loads and reactions

4.1.2 Load cases

According to EASA [50] CS 23.333(d), CS 23.349(b), CS 23.345, CS 23.455(a) (ii) and CS 23.455, the load cases specified in the Table 4.1 are identified.

Table 4.1 Load cases data

EASA CS23.	Load case	Speed (m/s)	n	Deflection		
				δ_F (°)	δ_A (°)	δ_H (°)
333 d	A	67.12	6.0	0.0	0.0	-
	D	107.22	6.0	0.0	0.0	-
	E	107.22	-3.0	0.0	0.0	-
	G	46.65	-3.0	0.0	0.0	-
349 b	AA+	67.12	4.0	0.0	15.0	-
	AA-	67.12	4.0	0.0	-23.0	-
	DA+	107.22	4.0	0.0	5.0	-
	DA-	107.22	4.0	0.0	-7.7	-
345	AF	33.5	2.0	30	0.0	-
455 a	AFA+	33.5	2.0	30	15.0	-
	AFA-	33.5	2.0	30	-23.0	-
	DFA+	49.14	2.0	30	5.0	-
	DFA-	49.14	2.0	30	-7.7	-
455	AH	67.12	1.0	0.0	0.0	-
	AH+	67.12	1.0	0.0	0.0	30.0
	AH-	67.12	1.0	0.0	0.0	-20.0

Deflections of the horizontal tail are calculated later in this section since it depends on the airplane's lift to maintain trim of the airplane. Necessary lift of the horizontal tail calculated from:

$$C_{LH} = \frac{q}{q_H} \cdot \frac{S}{S_H} \left(C_L \cdot \frac{x_{cg}}{r_H} + \frac{C_{MWF} \cdot \bar{c}}{r_H} \right) \quad (4.4)$$

Necessary deflection of the horizontal tail is calculated from:

$$C_{LH} = \frac{\partial C_{LH}}{\partial \alpha} \left(\alpha_H - \frac{\partial \alpha_H}{\partial \delta_H} \cdot \delta_H \right) = \frac{\partial C_{LH}}{\partial \alpha_H} \cdot \frac{\partial \alpha_H}{\partial \alpha} \left(\alpha_H - \frac{\partial \alpha_H}{\partial \delta_H} \cdot \delta_H \right) \quad (4.5)$$

Derivative $\partial \alpha_H / \partial \delta_H$ is calculated by:

$$\frac{\partial \alpha_H}{\partial \delta_H} = -\lambda_H + k \left[\left(\frac{\partial \alpha}{\partial \delta_H} \right)_{k=1} + \lambda_H \right] \quad (4.6)$$

$$\left. \frac{\partial \alpha_H}{\partial \delta_H} \right|_{K=1} = -\frac{2}{\pi} \left(\sqrt{\lambda_H(1-\lambda_H)} + \arcsin \sqrt{\lambda_H} \right) \quad (4.7)$$

So:

$$\left. \frac{\partial \alpha_H}{\partial \delta_H} \right|_{K=1} = 1 \quad (4.8)$$

$$\frac{\partial \alpha_H}{\partial \delta_H} = -1 \quad (4.9)$$

Gradient $\partial \alpha_H / \partial \alpha$ is calculated as $\partial \alpha_H / \partial \alpha = (1 - \varepsilon_\alpha)$

$$\frac{\partial \alpha_H}{\partial \alpha} = (1 - \varepsilon_\alpha) \quad (4.10)$$

$$\varepsilon_\alpha = 4.44 \cdot (K_\Lambda \cdot K_H)^{1.19} \quad (4.11)$$

$$K_\Lambda = \frac{1}{AR} - \frac{1}{1 + AR^{1.7}} \quad (4.12)$$

$$K_H = \frac{1 - \left| \frac{b_H}{b} \right|}{\sqrt[3]{\frac{2r_H}{b}}} \quad (4.13)$$

Where: K_Λ , K_λ , and K_H are wing aspect ratio factor, taper ratio factor, and horizontal tail location factor.

After substitution in Equ's 4.11, 4.12 and 4.13 we get:

$$K_\Lambda = 0.116$$

$$K_H = 0.067$$

$$\varepsilon_\alpha = 0.2124$$

Necessary deflection of the elevator is:

$$\delta_H = \frac{1}{\frac{\partial \alpha_H}{\partial \delta_H}} \cdot \left[\alpha - \alpha_W - \alpha_n - \frac{C_{LH}}{\frac{\partial C_{LH}}{\partial \alpha_H} \cdot (1 - \epsilon_\alpha)} \right] \quad (4.14)$$

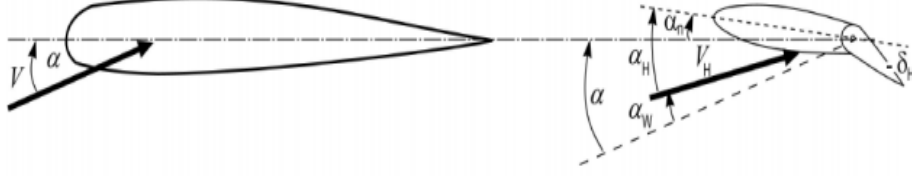


Figure 4.3 Definition of horizontal tail angle of attack

Based on the previous figure:

$$\alpha_H = \alpha - \alpha_W - \alpha_n \quad (4.15)$$

α_n is the mounting angle of the horizontal tail, α_W is induced angle from the wing in the tail region (downwash angle), which can be approximately calculated as:

$$\alpha_W \approx \left(2 + \frac{1}{4\xi^2} \right) \cdot \frac{C_{LW}}{\pi \cdot AR} \quad (4.16)$$

$$\alpha_W = \left(2 + \frac{b_F^2}{4r^2H} \right) \cdot \frac{C_{LW}}{\pi \cdot AR} \quad (4.17)$$

$$\alpha_W = 0.1016 \cdot C_{LW} \quad (4.18)$$

By substituting values of α , α_W and α_n in Eq 3.15, we get α_H

Where $\alpha_n = 0$

$$\alpha_H = \left(\frac{C_{LW}}{a_0} + \alpha_0 \right) \cdot 1.016 \cdot C_{LW} \quad (4.19)$$

Where α_0 is wing zero-lift angle of attack in radian, a_0 is the wing lift curve slope in 1/radian. Note: the zero-lift angle of attack, the moment coefficient, and the wing slope are changed when flaps are used.

$$\delta_H = -(\alpha_H - 0.3359) \cdot C_{LH} \quad (4.20)$$

$$C_{LW} = \frac{(r_H - x_{cg}) \cdot C_L - C_{M0} \cdot \bar{c}}{r_H} \quad (4.21)$$

$$C_L = \frac{C_{LW} \cdot r_H + C_{M0} \cdot \bar{c}}{r_H - x_{cg}} \quad (4.22)$$

After adding the increment due to flap and aileron deflections to the moment, wing lift, and angle of attack equations, we get the new following equations:

$$C_{LH} = \frac{q}{q_H} \cdot \frac{S_W}{S_H} \cdot \left(C_L \cdot \frac{x_{cg}}{r_H} + \frac{\left(C_{M0} + \frac{S_F}{S_W} \cdot \frac{\partial C_m}{\partial \delta_F} \cdot \delta_F + \frac{S_A}{S} \cdot \frac{\partial C_m}{\partial \delta_A} \cdot \delta_A \right) \cdot \bar{c}}{r_H} \right) \quad (4.23)$$

$$C_{LW} = \frac{(r_H - x_{cg}) \cdot C_L - \left(C_{M0} + \frac{S_F}{S_W} \cdot \frac{\partial C_m}{\partial \delta_F} \cdot \delta_F + \frac{S_A}{S_W} \cdot \frac{\partial C_m}{\partial \delta_A} \cdot \delta_A \right) \cdot \bar{c}}{r_H} \quad (4.24)$$

$$\alpha = \frac{C_{LW}}{\frac{\partial C_L}{\partial \alpha}} + \alpha_0 + \left(\frac{S_F}{S_W} \cdot \frac{\partial \alpha}{\partial \delta_F} \cdot \delta_F + \frac{S_A}{S_W} \cdot \frac{\partial \alpha}{\partial \delta_A} \cdot \delta_A \right) \quad (4.25)$$

4.1.3 Deflection of Elevator to Balance Airplane

Eight characteristic weights of the airplane are chosen to calculate required aerodynamic coefficients for stationary flight (for all cases in

Table 4.1. Wing lift coefficient, deflection of the elevator, and other parameters are computed from equations extracted from the previous paragraph; only the lift coefficient of the aircraft calculated by the equation below:

$$C_L = \frac{2 \cdot n \cdot m \cdot g}{\rho V^2 S} \quad (4.26)$$

4.1.4 Summary of Aerodynamic Parameters

The result of calculations shows that the maximum bending moment occurred at full fuel weight what mean it's the proper fuel weight. Tables from Table 4.2 to Table 4.5 show the result of calculations for case A, D, E and G. the results of other cases are in appendix C

Table 4.2 Aerodynamic Parameters at Envelope Point A ($\delta_F = 0^\circ$, $\delta_A = 0^\circ$, $n = 6.0$, $V = 66.87 \text{ m/s}$)

No.	Mass (kg)	x_{cg} (m)	C_L	C_{LH}	C_{LW}	α_H ($^\circ$)	δ_H ($^\circ$)	α ($^\circ$)
1	687.4	-0.024	0.9728	-0.1499	1.0007	4.136	-7.022	9.87
2	687.4	-0.016	0.9728	-0.1407	0.9990	4.125	-6.832	9.85
3	727.4	0.049	1.0294	-0.0618	1.0409	4.407	-5.596	10.37
4	827.4	0.068	1.1780	-0.0264	1.1829	5.364	-5.873	12.14
5	932.4	0.063	1.3195	-0.0241	1.3240	6.315	-6.780	13.90
6	932.4	0.045	1.3195	-0.0511	1.3290	6.349	-7.333	13.96
7	892.4	-0.005	1.2629	-0.1300	1.2871	6.067	-8.569	13.44
8	792.4	-0.019	1.1143	-0.1476	1.1418	5.087	-7.929	11.63

Table 4.3 Aerodynamic Parameters at Envelope Point D ($\delta_F = 0^\circ$, $\delta_A = 0^\circ$, $n = 6.0$, $V = 107.22 \text{ m/s}$)

No.	Mass (kg)	x_{cg} (m)	C_L	C_{LH}	C_{LW}	α_H ($^\circ$)	δ_H ($^\circ$)	α ($^\circ$)
1	687.4	-0.024	0.37829	-0.1332	0.40312	0.10746	-2.67	2.45
2	687.4	-0.016	0.37829	-0.1295	0.40244	0.10293	-2.60	2.45
3	727.4	0.049	0.40031	-0.0989	0.41874	0.21276	-2.12	2.65
4	827.4	0.068	0.45809	-0.0851	0.47396	0.58501	-2.22	3.34
5	932.4	0.063	0.51312	-0.0842	0.52882	0.95485	-2.58	4.03
6	932.4	0.045	0.51312	-0.0947	0.53078	0.96804	-2.79	4.06
7	892.4	-0.005	0.49111	-0.1254	0.51449	0.85821	-3.27	3.85
8	792.4	-0.019	0.43332	-0.1323	0.45798	0.47731	-3.02	3.14

Table 4.4 Aerodynamic Parameters at Envelope Point E ($\delta_F = 0^\circ$, $\delta_A = 0^\circ$, $n = -3.0$, $V = 107.22 \text{ m/s}$)

No.	Mass (kg)	x_{cg} (m)	C_L	C_{LH}	C_{LW}	α_H ($^\circ$)	δ_H ($^\circ$)	α ($^\circ$)
1	687.4	-0.024	-0.1891	0.1278	-0.2130	-4.05	6.51	-5.29
2	687.4	-0.016	-0.1891	0.1260	-0.2126	-4.04	6.47	-5.28
3	727.4	0.049	-0.2002	0.1107	-0.2208	-4.10	6.23	-5.38
4	827.4	0.068	-0.2290	0.1038	-0.2484	-4.28	6.28	-5.73
5	932.4	0.063	-0.2566	0.1034	-0.2758	-4.47	6.46	-6.08
6	932.4	0.045	-0.2566	0.1086	-0.2768	-4.48	6.57	-6.09
7	892.4	-0.005	-0.2456	0.1239	-0.2687	-4.42	6.81	-5.99
8	792.4	-0.019	-0.2167	0.1274	-0.2404	-4.23	6.68	-5.63

Table 4.5 Aerodynamic Parameters at Envelope Point G ($\delta_F = 0^\circ$, $\delta_A = 0^\circ$, $n = -3.0$, $V = 42.25 \text{ m/s}$)

No.	Mass (kg)	x_{cg} (m)	C_L	C_{LH}	C_{LW}	α_H ($^\circ$)	δ_H ($^\circ$)	α ($^\circ$)
1	687.4	-0.024	-0.974	0.1500	-1.0019	-9.36	12.25	-15.20
2	687.4	-0.016	-0.974	0.1407	-1.0002	-9.35	12.06	-15.18
3	727.4	0.049	-1.0306	0.0617	-1.0421	-9.64	10.82	-15.70
4	827.4	0.068	-1.1794	0.0263	-1.1843	-10.59	11.10	-17.49
5	932.4	0.063	-1.3211	0.0240	-1.3256	-11.55	12.01	-19.26
6	932.4	0.045	-1.3211	0.0510	-1.3306	-11.58	12.56	-19.33
7	892.4	-0.005	-1.2644	0.1300	-1.2887	-11.30	13.80	-18.80
8	792.4	-0.019	-1.1157	0.1477	-1.1432	-10.32	13.16	-16.97

Table 4.6 Table 4.16 shown in Appendix C.

- Table 4.6 Aerodynamic Parameters at Envelope Point AA+ ($\delta_F = 0^\circ$, $\delta_A = 15^\circ$, $n = 4.0$, $V = 66.87m/s$)
Table 4.7 Aerodynamic Parameters at Envelope Point AA- ($\delta_F = 0^\circ$, $\delta_A = -23^\circ$, $n = 4.0$, $V = 66.87m/s$)
Table 4.8 Aerodynamic Parameters at Envelope Point DA+ ($\delta_F = 0^\circ$, $\delta_A = 5.0^\circ$, $n = 4.0$, $V = 107.22m/s$)
Table 4.9 Aerodynamic Parameters at Envelope Point DA- ($\delta_F = 0^\circ$, $\delta_A = -7.7^\circ$, $n = 4.0$, $V = 107.22m/s$)
Table 4.10 Aerodynamic Parameters at Envelope Point AF ($\delta_F = 30^\circ$, $\delta_A = 0.0^\circ$, $n = 2.0$, $V = 33.5m/s$)
Table 4.11 Aerodynamic Parameters at Envelope Point AFA+ ($\delta_F = 30^\circ$, $\delta_A = 15^\circ$, $n = 2.0$, $V = 33.5m/s$)
Table 4.12 Aerodynamic Parameters at Envelope Point AFA- ($\delta_F = 30^\circ$, $\delta_A = -23^\circ$, $n = 2.0$, $V = 33.5m/s$)
Table 4.13 Aerodynamic Parameters at Envelope Point DFA+ ($\delta_F = 30^\circ$, $\delta_A = 5.0^\circ$, $n = 2.0$, $V = 49.14m/s$)
Table 4.14 Aerodynamic Parameters at Envelope Point DFA- ($\delta_F = 30^\circ$, $\delta_A = -7.7^\circ$, $n = 2.0$, $V = 49.14m/s$)
Table 4.15 Aerodynamic Parameters at Envelope Point AH ($\delta_F = 0^\circ$, $\delta_A = 0.0^\circ$, $n = 1.0$, $V = 66.87m/s$)
Table 4.16 Aerodynamic Parameters at Envelope Point DH ($\delta_F = 0^\circ$, $\delta_A = 0.0^\circ$, $n = 1.0$, $V = 102.22m/s$)

4.2 Reactions of Supports (Internal forces and moments):

Reactions are shown in

Figure 4.2. Necessary wing geometric data are:

$x_{S0} = 0.619 m$ main spar position

$x_{S1} = 0.116 m$ front spar position

$t_{CG} = 0.769 m$ empty wing center of gravity position

$x_{FCg} = 0.370 m$ fuel center of gravity position

4.3 Characteristic point coordinates

Point "0": $(x_0, y_0, z_0) \equiv (0,0,0)$

Point "1": $(x_1, y_1, z_1) \equiv (x_{S0} - x_{S1}, 0, 0) = (0.619 - 0.116, 0, 0) \approx (0.503, 0, 0)$

Wing c.g.:

$$(x_{Gw}, y_{Gw}, z_{Gw}) \equiv (-(t_{CG} - x_{S0}), y_{Gw}, 0) = \left(-(t_{CG} - x_{S1}), \frac{b/2 - 2.48}{2}, 0 \right) \approx (0.15, 1.83, 0)$$

Fuel c.g.:

$$(x_{GF}, y_{GF}, z_{GF}) \equiv (x_{S0} - x_{FCg}, y_{GF}, 0) = (0.619 - 0.370, 0.811, 0) \approx (0.249, 0.811, 0)$$

Vector position of the characteristic points for "0" is given as:

$$\begin{aligned} \vec{r}_i &= 0.503\hat{i} + 0\hat{j} + 0\hat{k} \\ \vec{r}_{GW} &= -0.15\hat{i} + 1.83\hat{j} + 0\hat{k} \\ \vec{r}_{GF} &= 0.249\hat{i} + 0.811\hat{j} + 0\hat{k} \end{aligned} \quad (4.27)$$

4.4 Equilibrium of forces:

$$\sum \vec{F} = \vec{F}_0 + \vec{F}_1 + \vec{L} + \vec{D} + \vec{G} = 0 \quad (4.28)$$

Where \vec{F}_0 , \vec{F}_1 , \vec{L} , \vec{D} and \vec{G} are lift, drag and gravity force

$$\vec{F}_0 = X_0\hat{i} + Y_0\hat{j} + Z_0\hat{k} \quad (4.29)$$

$$\vec{F}_1 = Y_1 \hat{j} + Z_1 \hat{k} \quad (4.30)$$

Where \vec{F}_0 , \vec{F}_1 , \vec{L} , \vec{D} and \vec{G} are lift, drag and gravity force

Or in component form:

$$\sum F_i = X_0 - D = 0 \quad (4.31)$$

$$\Rightarrow X_0 = D$$

$$\sum F_j = Y_0 - Y_1 = 0 \quad (4.32)$$

$$\sum F_k = Z_0 + Z_1 + L - G = 0 \quad (4.33)$$

\Rightarrow

$$Z_0 + Z_1 = G - L \quad (4.34)$$

4.5 External forces

4.5.1 Lift force

The lift vector found by the equation below:

$$\vec{L} = q \cdot \hat{k} \int_{y_{wstart}}^{b/2} C_l(y) c(y) dy \quad (4.35)$$

4.5.2 Drag force

Drag force has consisted of friction drag and induced drag.

$$\vec{D} = -D \hat{i} = -\hat{i} \int_{y_{wstart}}^{b/2} d_i(y) dy - \hat{i} C_{D0} q (S/2) \quad (4.36)$$

Where:

y_{wstart} is the distance of the wing connection point from the centre of the aircraft. (Note: the wing is not adjacent to the fuselage), S : is the wing area (the wing area divided by 2 because we calculated for semi wing), $d_i(y)$: induced drag at position y and is calculated as:

$$d_i(y) = \rho \cdot V_\infty \cdot \alpha_i(y) \cdot \Gamma(y) \quad (4.37)$$

$$d\vec{D} = d_i(y) \cdot dy(-\hat{i}) \quad (4.38)$$

Anderson's method (NACA report 572) [51] express $\alpha(\theta)$ & $\Gamma(\theta)$ as:

$$\alpha_i(\theta) = \sum_{n=1}^N nA_n \frac{\sin(n\theta)}{\sin \theta} \quad (4.39)$$

$$\Gamma(\theta) = 2bV_\infty \sum_{m=1}^N A_m \sin(m\theta) \quad (4.40)$$

Where: $y = -(b/2) \cdot \cos \theta$, $dy = (b/2) \cdot \sin \theta$.

Circulation Coefficients A_i : are determined by a small program (see appendix) which implements Anderson's method (NACA report 572) [51].

θ : Transformed span-wise coordinates (polar) (Glauert method) We used a small Matlab program to calculate the induced drag coefficient. Friction and form drag coefficient (see appendix):

$$C_{D0} = k_i C_f S_{wet} / S_W \quad (4.41)$$

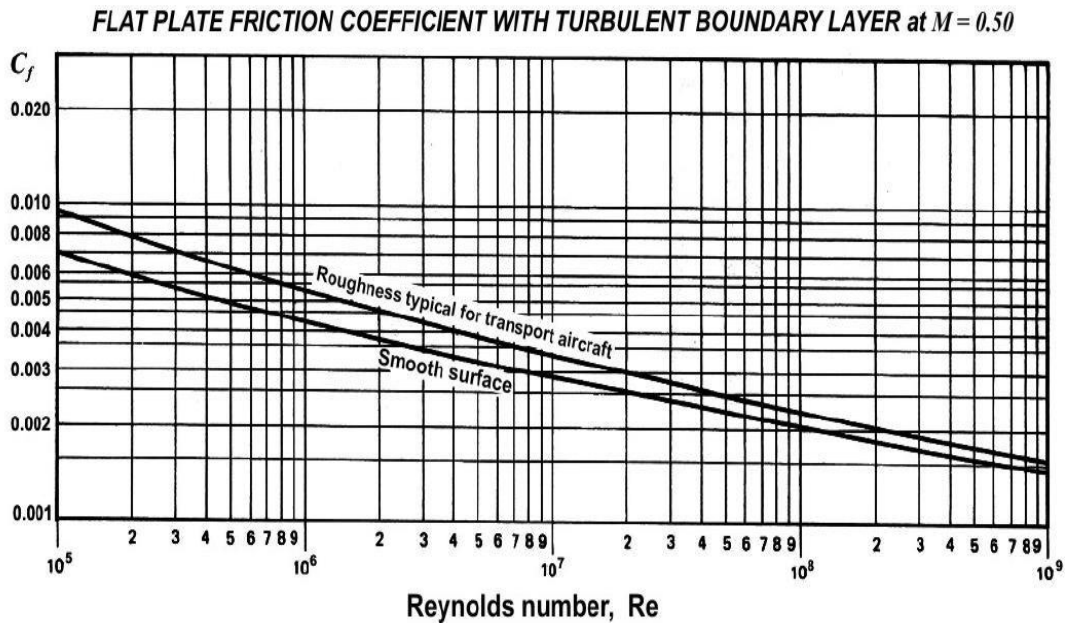


Figure 4.4 Friction Coefficient

Where:

$C_f = 0.0038$ friction coefficient calculated from Figure 4.4 corresponding to Reynold number. It's clear that C_f decreases with increasing the speed, but we deal here with the cruising speed, and we use the same value for other calculations to avoid reducing C_f . Because of certain irregularities in the wing surface due to exposed rivets, skin overlap, etc., the friction coefficient is increased by 10% to 20%, so to be on the safe side, the correction factor 1.2 is applied, and $C_f = 0.0038 \cdot 1.2 = 0.0456$.

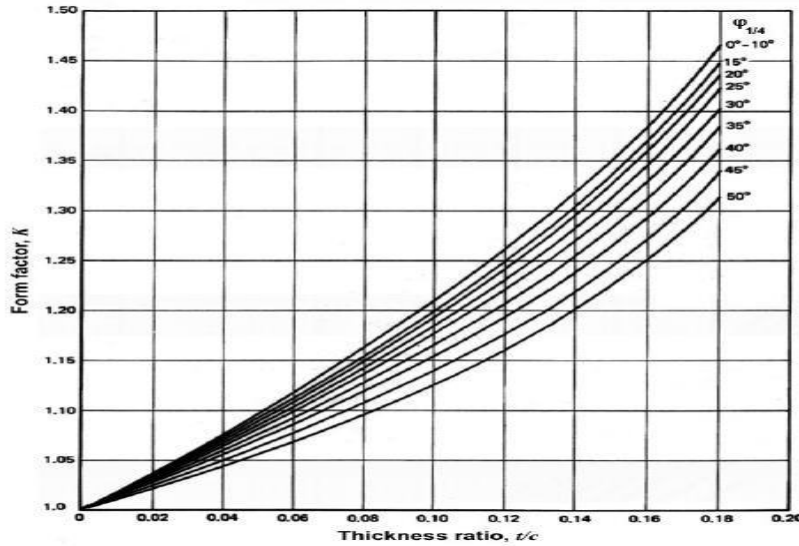


Figure 4.5 Form Factor

$K_i = 1.35$ form coefficient found from Figure 4.5, which is constant since it depends on thickness ratio and sweepback angle.

$S_{wet} = 23.146 \text{ m}$, wetted area of the wing (projected exposed area of the wing S_{exp} multiplied by 1.02 because of curvature of the wing airfoil and duplicated because of the upper and lower surface). By adding the friction coefficient to the induced, we will get the total drag coefficient.

4.5.3 Gravity force

$$\vec{G} = -\vec{G}\hat{k} \quad (4.42)$$

The wing is subjected to its weight and the inertial weight of fuel in fuel tanks. Weight of the wing and fuel contributes to gravity load as:

$$\vec{G} = \vec{G}_F + \vec{G}_w \quad (4.43)$$

$$\vec{G} = -n(m_F + m_w) \cdot g\hat{k} \quad (4.44)$$

Where n : load factor, g : earth gravity acceleration ($g = 9.81 \text{ m/s}^2$), m_F : mass of fuel ($m_F=100/2=50 \text{ kg}$), m_w : mass of the half empty wing ($m_w = 49.702 \text{ kg}$).

4.6 Design fuel load

According to EASA CS 23.343 [50]. If fuel is carried in the wings, the maximum allowable weight of the airplane without any fuel in the wing tank(s) must be established as “maximum zero wings fuel weight” if it is less than the maximum weight.

The maximum zero wings fuel weight (MZFW) doesn't mean the maximum takeoff weight (MTOW) minus full fuel. This definition is incorrect. The MZFW intends to design the wing for the condition where airplane weight is maximum, but the wing fuel tanks are only partially full. Because the fuel load alleviates wing bending loads, using the proper fuel load to determine MZFW is important.

To determine the proper weight of the fuel that gives the maximum bending moment, we increase the fuel weight from zero to full tank, and we calculated the corresponding bending moment for

each case. The calculations show that the maximum bending moment occurred at total fuel weight, which means it's the proper fuel weight.

Table 4.17 to Table 4.20 show the result of calculations for cases A, D, E, and G.

The used gravity force equation:

$$G_{w+F} = g \cdot (m_w + x \cdot m_F) \quad (4.45)$$

$$G_{w+F} = 9.81 \cdot (49.702 + x \cdot 50) \quad 0 \leq x \leq 1 \quad (4.46)$$

thus:

$$\vec{G} = -n \cdot 9.81 \cdot (49.702 + x \cdot 50) \hat{k} \quad (4.47)$$

Table 4.17 Fuel Weight Effect Case A

No.	Fuel	C_{Lw}	C_D	$L(N)$	$D(N)$	$G-L(N)$	$M_{Ex}(Nm)$	$M_{Ey}(Nm)$
1	0.0	1.0007	0.06128	15545.44	951.91	-12619.98	18793.20	-2055.73
2	0.0	0.9990	0.06108	15518.57	948.81	-12593.11	18751.47	-2050.17
3	0.0	1.0409	0.06548	16169.38	1017.16	-13243.92	19762.38	-2184.70
4	0.0	1.1829	0.08188	18375.19	1271.91	-15449.73	23188.66	-2640.64
4.2	10.0	1.2111	0.08588	18813.41	1334.05	-15299.35	23392.00	-2584.66
4.4	20.0	1.2393	0.08988	19251.63	1396.18	-15148.97	23595.34	-2528.67
4.6	30.0	1.2675	0.09388	19689.86	1458.32	-14998.60	23798.68	-2472.69
4.8	40.0	1.2958	0.09788	20128.08	1520.45	-14848.22	24002.02	-2416.71
5	50.0	1.3240	0.10018	20566.79	1556.18	-14698.33	24206.12	-2360.83
6	50.0	1.3290	0.10098	20644.93	1568.61	-14776.47	24327.49	-2376.99
7	50.0	1.2871	0.09518	19994.12	1478.51	-14125.66	23316.59	-2242.46
8	50.0	1.1418	0.07698	17737.04	1195.79	-11868.58	19810.65	-1775.92

Table 4.18 Fuel Weight Effect Case D

No.	Fuel	C_{Lw}	C_D	$L(N)$	$D(N)$	$G-L(N)$	M_{Ex}	$M_{Ey}(Nm)$
1	0.0	0.4031	0.01790	16102.80	715.03	-13177.34	19658.95	337.76
2	0.0	0.4024	0.01790	16075.94	715.03	-13150.48	19617.23	343.31
3	0.0	0.4187	0.01857	16726.75	741.79	-13801.29	20628.13	208.79
4	0.0	0.4740	0.02116	18932.55	845.25	-16007.09	24054.41	-247.15
4.2	10.0	0.4849	0.02186	19370.77	873.21	-15856.71	24257.75	-191.17
4.4	20.0	0.4959	0.02256	19809.00	901.18	-15706.34	24461.09	-135.19
4.6	30.0	0.5069	0.02326	20247.22	929.14	-15555.96	24664.43	-79.21
4.8	40.0	0.5178	0.02396	20685.44	957.10	-15405.58	24867.77	-23.23
5	50.0	0.5288	0.02408	21124.15	961.77	-15255.69	25071.87	32.65
6	50.0	0.5308	0.02416	21202.30	965.25	-15333.84	25193.25	16.50
7	50.0	0.5145	0.02331	20551.49	931.06	-14683.03	24182.34	151.02
8	50.0	0.4580	0.02040	18294.40	814.97	-12425.94	20676.40	617.56

Table 4.19 Fuel Weight Effect Case E

No.	Fuel	C_{Lw}	C_D	$L (N)$	$D (N)$	$G-L (N)$	M_{Ex}	$M_{Ey}(Nm)$
1	0.0	-0.21297	0.01087	-8507.41	434.09	7044.68	-10537.80	6082.92
2	0.0	-0.21264	0.01085	-8493.98	433.56	7031.25	-10516.94	6080.14
3	0.0	-0.22078	0.01101	-8819.39	439.73	7356.66	-11022.39	6147.40
4	0.0	-0.24839	0.01155	-9922.29	461.44	8459.56	-12735.53	6375.37
4.2	10.0	-0.25388	0.01168	-10141.40	466.49	8384.37	-12837.20	6347.38
4.4	20.0	-0.25936	0.01181	-10360.51	471.60	8309.18	-12938.87	6319.39
4.6	30.0	-0.26485	0.01193	-10579.62	476.71	8233.99	-13040.54	6291.40
4.8	40.0	-0.27034	0.01206	-10798.73	481.83	8158.80	-13142.21	6263.41
5	50.0	-0.27583	0.01219	-11018.09	487.02	8083.86	-13244.26	6235.47
6	50.0	-0.27680	0.01221	-11057.16	487.78	8122.93	-13304.95	6243.55
7	50.0	-0.26866	0.01201	-10731.76	479.58	7797.53	-12799.50	6176.28
8	50.0	-0.24041	0.01139	-9603.21	454.92	6668.98	-11046.53	5943.01

Table 4.20 Fuel Weight Effect Case G

No.	Fuel kg	C_{Lw}	C_D	$L (N)$	$D (N)$	$G-L (N)$	$M_{Ex} (Nm)$	$M_{Ey} (Nm)$
1	0.0	-1.00193	0.06023	-7576.36	455.47	6113.63	-9091.59	2562.53
2	0.0	-1.00020	0.05999	-7563.27	453.64	6100.54	-9071.26	2559.82
3	0.0	-1.04215	0.06451	-7880.46	487.78	6417.73	-9563.96	2625.38
4	0.0	-1.18432	0.08140	-8955.53	615.49	7492.80	-11233.86	2847.60
4.2	10.0	-1.21257	0.08518	-9169.11	644.14	7412.08	-11326.95	2818.47
4.4	20.0	-1.24081	0.08897	-9382.69	672.75	7331.36	-11420.03	2789.33
4.6	30.0	-1.26906	0.09275	-9596.28	701.37	7250.65	-11513.11	2760.20
4.8	40.0	-1.29730	0.09654	-9809.86	729.98	7169.93	-11606.19	2731.07
5	50.0	-1.32558	0.10032	-10023.68	758.62	7089.45	-11699.64	2701.98
6	50.0	-1.33061	0.10108	-10061.76	764.33	7127.53	-11758.80	2709.86
7	50.0	-1.28867	0.09523	-9744.57	720.08	6810.34	-11266.10	2644.29
8	50.0	-1.14319	0.07631	-8644.51	577.07	5710.28	-9557.37	2416.91

4.7 External Moments

4.7.1 Moment due to Lift force:

Moment due to lifting force about point “0” is calculated by:

$$\vec{M}_{OL} \equiv \int_{y_{Wstart}}^{b/2} \vec{r}(y) \times d\vec{L} \quad (4.48)$$

Where:

$$d\vec{L} = C_l(y) \cdot q \cdot C(y) \cdot dy \hat{k} \quad (4.49)$$

Product $c(y) \cdot dy$ represents elementary wing area ds , Dynamic pressure is defined as $q = 0.5 \cdot \rho \cdot V^2$, $C_l(y)$ is local lift coefficient at position y , b is the wing span, and vector $r(y)$ is given as:

$$\vec{r}(y) = x_S \hat{i} + y_S \hat{j} + z_S \hat{k} \quad (4.50)$$

Where: x_S distance of the centre of pressure from the main spar (point 0):

$$x_S = x_{S0} - x_{cp} \quad (4.51)$$

$$x_S = 0.619 - x_{cp} \quad (4.52)$$

$$x_{cp} = \left[\left(\frac{x}{c} \right)_{ac} - \frac{C_{MAC}}{C_L} \right] \cdot c \quad (4.53)$$

$$x_S = x_{S0} - \left[\left(\frac{x}{c} \right)_{ac} - \frac{C_{MAC}}{C_L} \right] \cdot c \quad (4.54)$$

$$x_S = 0.619 - \left[0.266 - \frac{C_{MAC}}{C_L} \right] \cdot c \quad (4.55)$$

Where:

$$Z_S = 0$$

Since we have a constant chord so: $C_l(y) = \bar{c}_a = 1.55 \text{ m}$. The integral will be:

$$\vec{M}_{OL} \equiv q \cdot c \cdot \int_{y_{Wstart}}^{b/2} (x_S \hat{i} + y_S \hat{j} + z_S \hat{k}) \times C_l(y) \hat{k} \cdot dy \quad (4.56)$$

$$\vec{M}_{OL} \equiv -q \cdot \bar{c}_a \cdot x_S \hat{j} \int_{y_{Wstart}}^{b/2} C_l(y) \cdot dy + q \cdot \bar{c}_a \cdot y_S \hat{i} \int_{y_{Wstart}}^{b/2} C_l(y) \cdot y dy + 0 \quad (4.57)$$

$$\vec{M}_{OL} \equiv -(x_S \cdot L_{(y_{Wstart})}) \cdot \hat{j} + M_{L(y_{Wstart})} \cdot \hat{i} \quad (4.58)$$

Note: the moment sign is by the right-hand rule.

4.7.2 Moment due to Drag force:

As mentioned, the drag force has consisted of friction drag and induced drag. Friction drag acts approximately in the middle of the wing exposed to airflow, while induced drag distribution depends on induced velocity distribution and intensity of the circulation.

$$\vec{M}_{OD} \equiv \int_{y_{Wstart}}^{b/2} \vec{r} \cdot (y \times d\vec{D}) \quad (4.59)$$

$$\vec{M}_{OD} = \int_{y_{Wstart}}^{b/2} (x_S \hat{i} + y_S \hat{j} + z_S \hat{k}) \times (d_i + q \cdot C_{D0} \cdot c(y)) \cdot dy \cdot (-\hat{i}) \quad (4.60)$$

Since the drag approximately acts on the same level as point “0”, $z_s = 0$ and the equation will be:
induced velocity distribution and intensity of the circulation.
Since the drag approximately acts on the same level as point “0”, so $z_s=0$ and the equation will be:

$$\vec{M}_{OD} = \hat{k} \int_{y_{Wstart}}^{b/2} y_S \cdot d_i \cdot dy + \hat{k} \int_{y_{Wstart}}^{b/2} y_S \cdot q \cdot C_{D0} \cdot c(y) \cdot dy \quad (4.61)$$

$$\vec{M}_{OD} = \hat{k} \cdot (M_{Di} + M_{D0}) \quad (4.62)$$

$$\vec{M}_{OD} = \hat{k} \cdot M_D \quad (4.63)$$

The procedures of calculation of friction and induced drag are mentioned in drag force calculation. We suppose that the total resultant drag force act at the middle of the wing exposed to airflow for approximation.

4.7.3 Moment due to Gravity forces:

Moment due to gravity force about “0” is calculated by the following equation:

$$\vec{M}_{OG} \equiv \vec{r}_{GW} \times (n \cdot m_w \cdot g) \cdot (-\hat{k}) + \vec{r}_{GF} \cdot (n \cdot m_F \cdot g) \cdot (-\hat{k}) \quad (4.64)$$

4.7.4 Equilibrium of Moments:

Equilibrium of moments requires that moment of the external forces and reaction forces about any point is equal to zero. We take point “0” to calculate the equilibrium of moments so:

$$\sum \vec{M}_E 0 = \vec{r}_1 \times (Y_1 \hat{j} + Z_1 \hat{k}) + M_x \hat{i} + \vec{M}_{0L} + \vec{M}_{0D} + \vec{M}_{0G} + \vec{M} = \quad (4.65)$$

Or

$$(r_{1y}Z_1 - r_{1z}Y_1) \cdot \hat{i} - (r_{1x}Z_1 - r_{1z}0) \cdot \hat{j} + (r_{1x}Y_1 - r_{1y}0) \hat{k} + M_x \hat{i} = -\vec{M}_E \quad (4.66)$$

On the left-hand side of this equation are unknown reactions y_l and z_l , while on the right – hand side is pitching moment and moments due to lifting, drag and weight of the wing segment (as mentioned, no need for pitching moment if we deal with the centre of pressure). To shorten the expressions, we gave the external moments the name M_E .

After sorting and combining moments and forces equations (with corresponding numbers), we get the following system of equations:

$$X_0 = D \quad (4.67)$$

$$Y_0 + Y_1 = 0 \quad (4.68)$$

$$Z_0 + Z_1 = G - L \quad (4.69)$$

$$M_x = -M_{Ex} \quad (4.70)$$

$$0.503Z_1 = M_{Ey} \quad (4.71)$$

$$0.503Y_1 = -M_{Ez} \quad (4.72)$$

Where:

$$\vec{M}_{EX} = ML_{(Ystart)} - n \cdot g(m_w \cdot y_{Gw} + m_F \cdot y_{GF}) \quad (4.73)$$

$$\vec{M}_{Ey} = -(X_s \cdot L_{(Ystart)} + n \cdot g(m_w \cdot x_{Gw} + m_F \cdot x_{GF} + q \cdot \bar{c}_a \int_{y_{Wstart}}^{b/2} C_m(y) \cdot c(y) \cdot dy) \quad (4.74)$$

Again we deal with the centre of pressure so that the equation will be:

$$\vec{M}_{Ey} = -(X_s \cdot L_{(Ystart)}) + n \cdot g(m_w \cdot x_{Gw} + m_F \cdot x_{GF}) \quad (4.75)$$

$$\vec{M}_{EZ} = M_{Di} + M_{D0} = M_D \quad (4.76)$$

4.7.5 Load Distribution over Wing

For the load cases given in

Table 4.1 with deflection of command surfaces and corresponding angles of attack of the wing, the wing's load distribution was calculated using a small program. All eight cases are to be considered

for different masses of the airplane. The load distribution over the wing is used to determine the load on ribs to use in the structural dimensioning and testing. Reactions for symmetrical load cases are identical on right-hand and left-hand semi-wing.

For unsymmetrical load cases such as AA+ and AA- reactions on the right-hand semi-wing for loading case AA+ are equal to the reactions to the left-hand semi-wing for the loading case AA- and vice versa. Only reactions on left-hand side semi-wing loads are calculated; it is also assumed that $C_n = C_l$ since angles of attack for the most intensive loads is smaller than 14° .

Semi-wing's support reactions for load cases given in Table 4.21.

Table 4.21 Support Reactions at case A, at point A, ($\delta_F = 0^\circ$, $\delta_A = 0^\circ$, $n = 6.0$, $V = 67.12 \text{ m/s}$)

No	$m \text{ (kg)}$	$\alpha \text{ (}^\circ\text{)}$	$\delta_H \text{ (}^\circ\text{)}$	$X_0 \text{ (N)}$	$Y_0 \text{ (N)}$	$Z_0 \text{ (N)}$	$Y_l \text{ (N)}$	$Z_l \text{ (N)}$	$M_x \text{ (Nm)}$
1	687.4	9.87	-7.02	951.91	4636.555	-8533.04	-4636.56	-4086.93	-18793.20
2	687.4	9.85	-6.83	948.81	4621.423	-8517.22	-4621.42	-4075.89	-18751.47
3	727.4	10.37	-5.60	1017.16	4954.335	-8900.59	-4954.33	-4343.33	-19762.38
4	827.4	12.14	-5.87	1271.91	6195.188	-10199.95	-6195.19	-5249.77	-23188.66
5	932.4	13.90	-6.78	1556.18	7579.799	-10004.83	-7579.80	-4693.51	-24206.12
6	932.4	13.96	-7.33	1568.61	7640.328	-10050.86	-7640.33	-4725.62	-24327.49
7	892.4	13.44	-8.57	1478.51	7201.49	-9667.49	-7201.49	-4458.18	-23316.59
8	792.4	11.63	-7.93	1195.79	5824.445	-8337.92	-5824.45	-3530.66	-19810.65

Table 4.22 Support Reactions at case D, at point D, ($\delta_F = 0^\circ$, $\delta_A = 0^\circ$, $n = 6.0$, $V = 107.22 \text{ m/s}$)

No	$m \text{ (kg)}$	$\alpha \text{ (}^\circ\text{)}$	$\delta_H \text{ (}^\circ\text{)}$	$X_0 \text{ (N)}$	$Y_0 \text{ (N)}$	$Z_0 \text{ (N)}$	$Y_l \text{ (N)}$	$Z_l \text{ (N)}$	$M_x \text{ (Nm)}$
1	687.4	2.45	-2.67	715.03	3482.74	-13848.82	-3482.74	671.48	-19658.95
2	687.4	2.45	-2.60	715.03	3482.74	-13833.00	-3482.74	682.52	-19617.23
3	727.4	2.65	-2.12	741.79	3613.10	-14216.37	-3613.10	415.08	-20628.13
4	827.4	3.34	-2.22	845.25	4117.03	-15515.73	-4117.03	-491.36	-24054.41
5	932.4	4.03	-2.58	961.77	4684.58	-15320.60	-4684.58	64.91	-25071.87
6	932.4	4.06	-2.79	965.25	4701.51	-15366.63	-4701.51	32.80	-25193.25
7	892.4	3.85	-3.27	931.06	4534.96	-14983.26	-4534.96	300.24	-24182.34
8	792.4	3.14	-3.02	814.97	3969.55	-13653.69	-3969.55	1227.75	-20676.40

Table 4.23 Support Reactions at case E, at point E, ($\delta_F = 0^\circ$, $\delta_A = 0^\circ$, $n = -3.0$, $V = 107.22 \text{ m/s}$)

No	$m \text{ (kg)}$	$\alpha \text{ (}^\circ\text{)}$	$\delta_H \text{ (}^\circ\text{)}$	$X_0 \text{ (N)}$	$Y_0 \text{ (N)}$	$Z_0 \text{ (N)}$	$Y_l \text{ (N)}$	$Z_l \text{ (N)}$	$M_x \text{ (Nm)}$
1	687.4	-4.71	1.48	434.09	2114.36	-5048.59	-2114.36	12093.27	10537.80
2	687.4	-4.71	1.45	433.56	2111.75	-5056.50	-2111.75	12087.75	10516.94
3	727.4	-4.81	1.21	439.73	2141.84	-4864.82	-2141.84	12221.47	11022.39
4	827.4	-5.16	1.26	461.44	2247.57	-4215.14	-2247.57	12674.69	12735.53
5	932.4	-5.50	1.44	487.02	2372.16	-4312.70	-2372.16	12396.56	13244.26

6	932.4	-5.51	1.54	487.78	2375.85	-4289.68	-2375.85	12412.61	13304.95
7	892.4	-5.41	1.78	479.58	2335.94	-4481.37	-2335.94	12278.89	12799.50
8	792.4	-5.06	1.66	454.92	2215.81	-5146.15	-2215.81	11815.14	11046.53

Table 4.24 Support Reactions at case G, at point G, ($\delta_F = 0^\circ$, $\delta_A = 0^\circ$, $n = -3.0$, $V = 46.65m/s$)

No	m (kg)	α ($^\circ$)	δ_H ($^\circ$)	X_0 (N)	Y_0 (N)	Z_0 (N)	Y_1 (N)	Z_1 (N)	M_x (Nm)
1	687.4	-14.62	7.23	455.47	2218.47	1019.14	-2218.47	5094.48	9091.59
2	687.4	-14.60	7.04	453.64	2209.59	1011.43	-2209.59	5089.11	9071.26
3	727.4	-15.13	5.80	487.78	2375.88	1198.28	-2375.88	5219.45	9563.96
4	827.4	-16.91	6.08	615.49	2997.93	1831.57	-2997.93	5661.23	11233.86
5	932.4	-18.69	6.99	758.62	3695.05	1717.71	-3695.05	5371.74	11699.64
6	932.4	-18.75	7.54	764.33	3722.87	1740.15	-3722.87	5387.39	11758.80
7	892.4	-18.23	8.78	720.08	3507.37	1553.30	-3507.37	5257.04	11266.10
8	792.4	-16.40	8.14	577.07	2810.76	905.29	-2810.76	4804.99	9557.37

4.7.6 Overview of Maximum Loading Cases

From the results of all loading cases given in the previous section, it is concluded that in each case, the most of the highest value of Z reactions are in number 4, and the other reaction loads are higher in number 6. An overview of reactions is given in

Table 4.25 below. The maximum reactions are found in cases A. 6, D. 4, D. 6, E. 4 and E. 6, so these loading cases have to be used to dimension structural elements.

The maximum positive and negative bending moment are found in case D. 6 and case E. 6. We used the bending moment of case D. 6 for dimensioning and testing of the wing (main spar). The maximum torsion moment found in case E. 4, so this case also should be tested in the structural test. For the structural test, we will test case D. 6 for maximum bending moment and case E.4 for maximum torsion moment about the main spar (chapter 7).

Table 4.25 Maximum Loading Cases

Load case	X_0 (N)	Y_0 (N)	Z_0 (N)	Y_1 (N)	Z_1 (N)	M_x (Nm)	M_y (Nm)
A. 4	1271.91	6195.19	-10199.95	-6195.19	-5249.77	-23188.66	-2640.64
A. 6	1568.61	7640.33	-10050.86	-7640.33	-4725.62	-24327.49	-2376.99
D. 4	845.25	4117.03	-15515.73	-4117.03	-0491.36	-24054.41	-247.15
D. 6	965.25	4701.51	-15366.63	-4701.51	0032.80	-25193.25	16.50
D. 8	814.97	3969.55	-13653.69	-3969.55	1227.75	-20676.40	617.56
E. 4	461.44	2247.57	-4215.14	-2247.57	12674.69	12735.53	6375.37
E. 6	487.78	2375.85	-4289.68	-2375.85	12412.61	13304.95	6243.55
E. 8	454.92	2215.81	-5146.15	-2215.81	11815.14	11046.53	5943.01

G. 4	615.49	2997.93	1831.57	-2997.93	5661.23	11233.86	2847.60
G. 6	758.62	3695.05	1717.71	-3695.05	5371.74	11699.64	2701.98

4.8 Fittings Analysis

In the fitting analysis, we use the critical forces and moments summarized in

Table 4.25.

We have a double shear type of lug in the front spar and multiple shears or finger type in the main spar in the fitting. See Figure 4.6. The female lug attached to the wing's spar. The used material is steel 1.6604.6. According to EASA CS 23.619 and CS 23.625 [50](a), the safety factor must be multiplied by a specific factor known as a fitting factor, which is equal to 1.5, so the fitting safety factor will be:

$$F_s = 1.5 \cdot 1.15 = 1.725$$

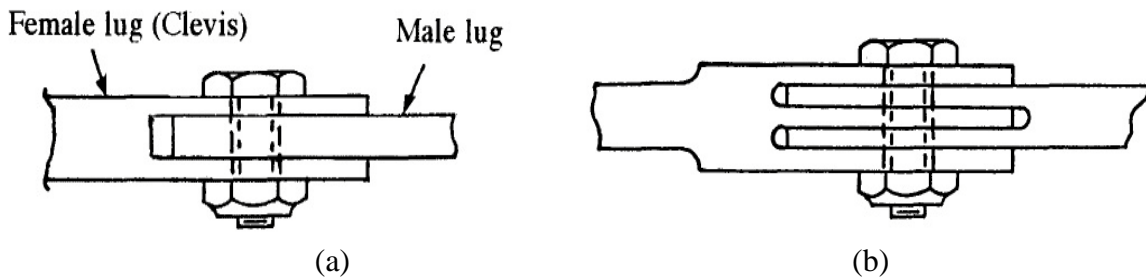


Figure 4.6 (a) Double Shear; (b) Multiple Shear or Finger Type

4.9 Main Spar

The reactions used for lug analysis of the main spar are taken from Table 4.26. Also, we added the force caused by the moment about the x -axis to the Y_0 reactions. The value of the X_0 reaction is so small compared with the value of Y_0 and Z_0 reactions, so we ignored it.

The value of Y_0 before adding the force due to moment about x is $Y_0 = 4701.51N$, and divided over two because there are two connection points in the fitting of the main spar (Figure 4.7), the force due to moment is:

$$Y_{OM} = \frac{M_x}{Z_{spar}} \quad (4.77)$$

$$Y_{OM} = 125966.25 N$$

So:

$$Y_0 = \frac{y_0}{2}$$

$$Y_0 = 2350.755N$$

Where: $Z_{spar} = 0.2 \text{ m}$ and $M_x = 25193.25 \text{ Nm}$.

$$Y_0(\text{Tension}) = Y_{0M} + Y_0 \quad 125966.25$$

$$Y_0(\text{Compression}) = Y_{0M} - Y_0 \quad 123615.495$$

Table 4.26 The reaction used for the lug analysis

Case	Z_0 (N)	Y_0 (N) Tension	Y_0 (N) Compression
D. 4	-15515.7	----	----
D. 6	----	123615.48	128316.99

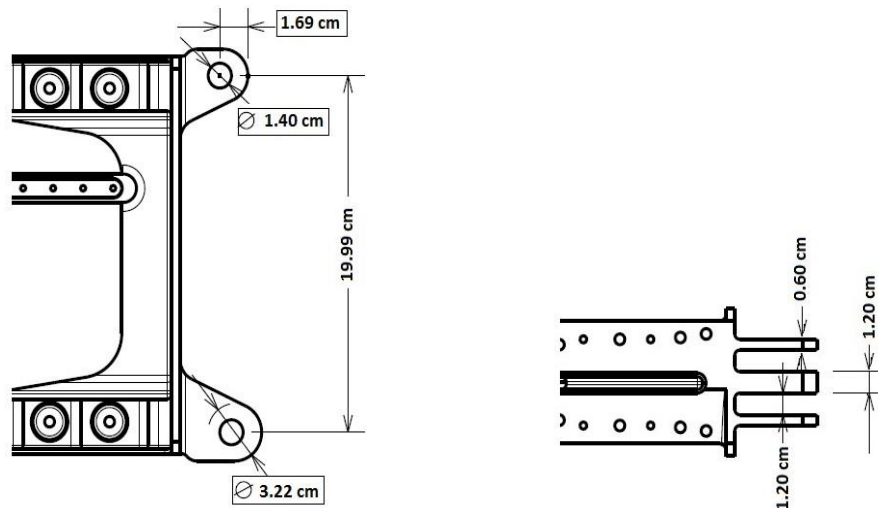


Figure 4.7 Connections Points in the Fitting of Main Spar

This value-added to Y_0 of the upper connection point (Y_0 compression) and subtracted from the lower one (Y_0 tension). Also, the value divided by 4 for one lug.

4.9.1 Applied Load Cases

We have two applied load cases in our fitting loading, namely, Case I: axial load and Case II: Transverse load see Figure 4.8.

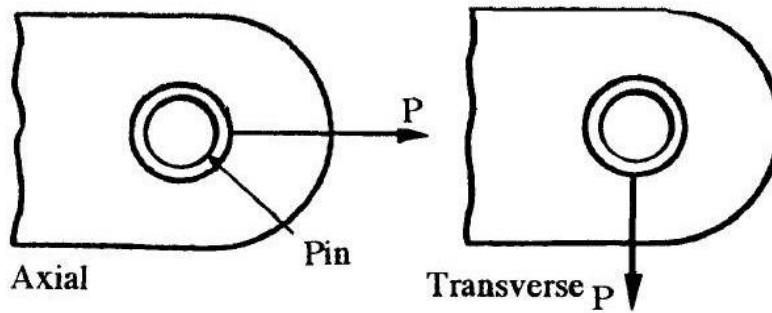


Figure 4.8 Applied load cases for axial and transverse

4.9.2 Axial load analysis

The lug failure modes for this load case are shown in Figure 4.9.

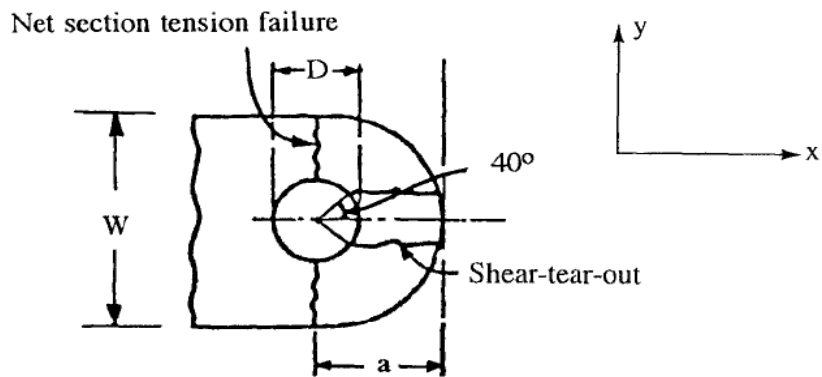


Figure 4.9 Lug tension and shear-tear out failures

For our Lug: $W = 3.22 \text{ cm}$, $D = 1.4 \text{ cm}$, $a = 1.69 \text{ cm}$.

a) Tension failure:

The following equation gives the tension load:

$$P_{tux} = K_t \cdot F_{tux} \cdot A_t \quad (4.78)$$

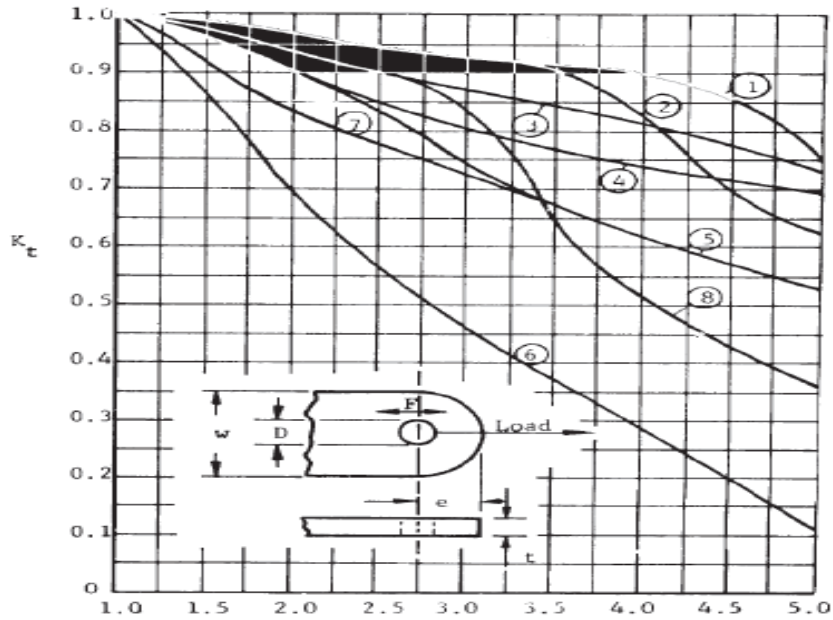


Figure 4.10. Axial Loading

Where:

P_{tux} : Ultimate load for tension failure

K_t : Net tension efficiency factor is taken from

Figure 4.10. $K_t = 0.90$ [52].

F_{tux} : Ultimate tensile stress of the lug material in the x-direction. and for steel, 1.6604.6

$$F_{tux} = 1300 \text{ Mpa} = 1300 \cdot 10^6 \text{ N/m}^2$$

A_t : Minimum net section for tension

$$A_t = (W - D) \cdot t = 1.092 \text{ cm}^2 = 1.092 \cdot 10^{-4} \text{ m}^2$$

t : lug thickness = 0.6 cm

So:

$$P_{tux} = K_t \cdot F_{tux} \cdot A_t \quad (4.79)$$

$$P_{tux} = 127764 \text{ N}$$

The Margin of Safety (MS):

$$MS = \frac{P_{tux}}{F_{s.f} \cdot P} - 1 \quad (4.80)$$

$$MS = 1.40 \text{ ok}$$

Where: $P = Z_o / 4$.

b) Shear-Bearing failure

It consists of shear tear-out of the lug along with a (40°) the angle on both sides of the pin (Figure 4.9), and bearing failure involves the crushing of the lug by the pin bearing. Both of them are critical in tension load.

The following equation gives the ultimate load:

$$P_{bru} = K_{br} \cdot F_{tux} \cdot A_{br} \quad (4.81)$$

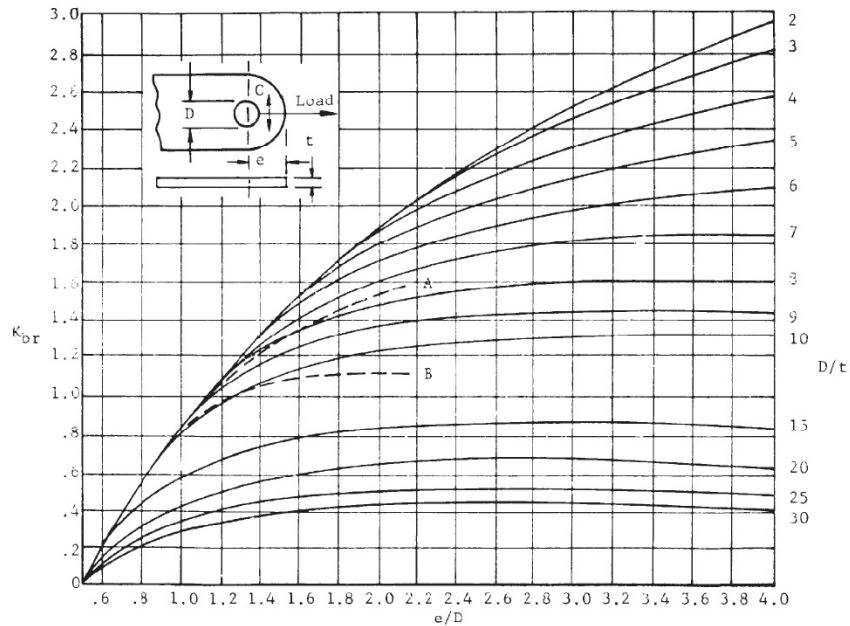


Figure 4.11 Axial Loading

Where:

P_{bru} : Ultimate load for shear tear-out and bearing failure

K_{br} : shear bearing efficiency factor is taken from the Figure 4.11 [52] at $a/D = 1.21$ and $D/t = 2.33$ (t : thickness of one lug = 0.6 cm), so: $K_{br} = 1.55$

F_{tux} : Ultimate tensile stress of the lug material in x -direction. For steel $1.6604.6$:

$F_{tux} = 1300 \text{ Mpa} = 1300 \cdot 10^6 \text{ N/m}^2$

A_{br} : projected bearing area $A_{br} = D \cdot t = 0.84 \text{ cm}^2 = 0.84 \cdot 10^{-4} \text{ m}^2$.

So

$$P_{bru} = K_{br} \cdot F_{tux} \cdot A_{br} = 125580 \text{ N}$$

The Margin of Safety (MS):

$$MS = \frac{P_{bru}}{F_{tyy} \cdot P_{tr}} - 1 \quad (4.82)$$

$$MS = 1.36 \text{ ok}$$

c) Pin-shear-off failure

Pin single shear-off failure is given by

$$P_{ps} = F_{su} \cdot A_p \quad (4.83)$$

Where:

P_{ps} : Ultimate load for pin shear-off failure

F_{su} : Ultimate shear stress of the pin material (steel $1.4534.6$) (For steel, ultimate shear stress is 0.75 of ultimate tensile stress) $\sigma_t = 1500 \times 10^6 \text{ N}$

$$F_{su} = 0.75 \cdot \sigma_t = 1125 \cdot 10^6 N/m^2$$

$P_{p,s}$: Pin cross-section area

$$A_p: \text{Pin cross-section area } A_p = \frac{\pi D^2}{4} = 1.54 \text{ cm}^2 = 1.54 \times 10^{-4} \text{ m}^2$$

So:

$$P_{p,s} = \sigma_t \cdot A_p \quad (4.84)$$

$$P_{p,s} = 173250 \text{ N}$$

The Margin of Safety (MS):

$$MS = \frac{P_{p,s}}{1.725 \cdot P} - 1 \quad (4.85)$$

$$MS = 2.25 \text{ ok}$$

Where: $P = Y_0/4$ case D6, $Y_0 = 2350.755 \text{ N}$

$$P = \frac{Y_0}{4}$$

$$P = 587.68875 \text{ N}$$

d) Pin bending failure

If the pin used in the lug is too small, the pin can bend enough to precipitate failure in the lug. Since a weak or smaller pin can cause an inner lug (t_2) to fail at a smaller load, larger pins (ample MS) are always recommended.

The moment arm is given by (Figure 4.12):

$$b = \frac{t_1}{2} + \delta + \gamma \cdot \left(\frac{t_2}{4}\right) \quad (4.86)$$

$\delta = 0.05 \text{ cm}$ is a gap (lug chamfer or use flange bushings) as shown in Figure 4.12

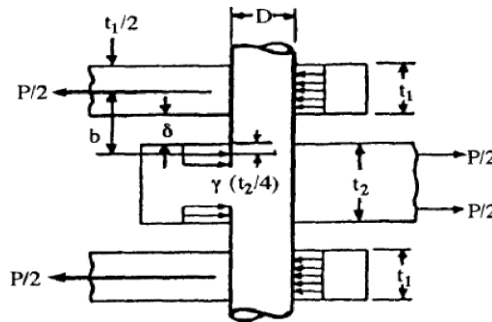


Figure 4.12 Pin Moment Arm for Determination of Bending Moment

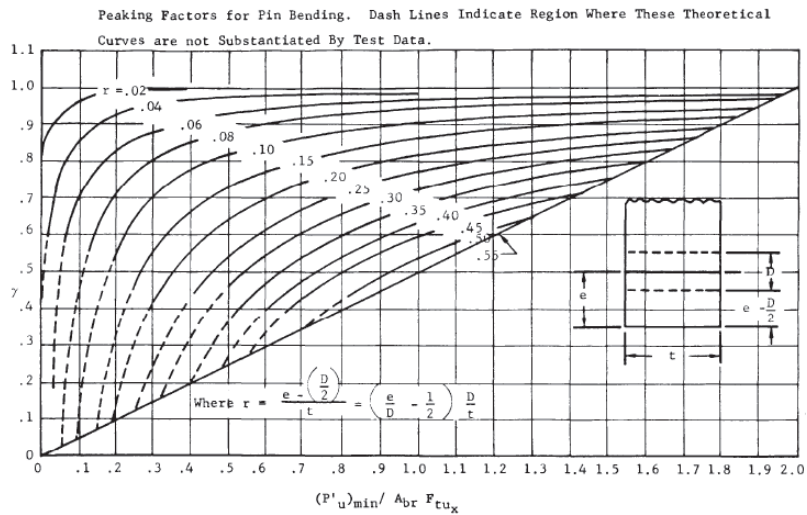


Figure 4.13 Peaking Factor for Pin Bending

$\gamma = 0.25$ is reduction factor (only applies to the inner lug) is taken from

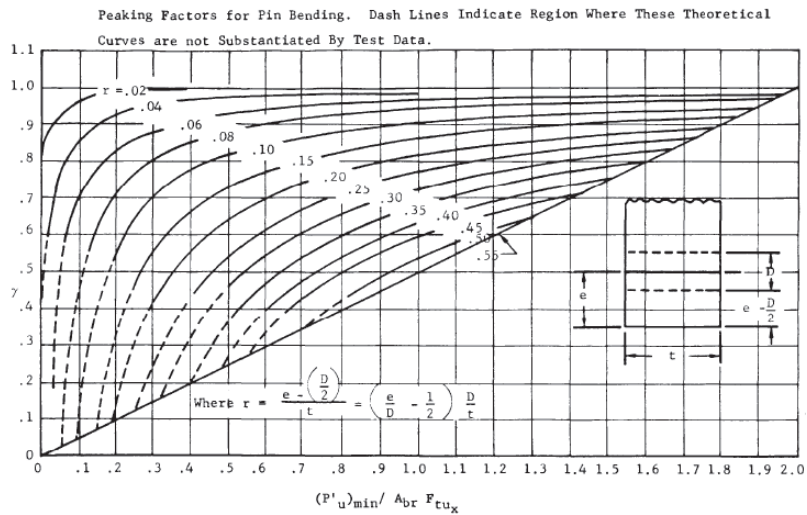


Figure 4.13 [52]. To calculate the reduction factor, we needed to calculate: $r = \frac{a-D/2}{t_2}$ and

$$\frac{(P_u)_{\min}}{A_{br} \cdot F_{tu_x}} = \frac{P_{bru}}{2 \cdot A_{br} \cdot F_{tu_x}}$$

A_{br} : the new area was calculated by using the thickness of the female lug. (P_{min}): The smaller of P_{bru} and P_{tu} for the inner lug (same as for outer lug).

So, the moment arm is ($t_1 = 0.6 \text{ cm}$, $t_2 = 1.2 \text{ cm}$) $b = \frac{t_1}{2} + \delta + \gamma \cdot \left(\frac{t_2}{4} \right) = 0.425 \text{ cm}$, and the pin bending moment ($P = Y_0 / 4$ case (D6)) is:

$$P = \frac{Y_0}{4}$$

$$P = 587.68875 \text{ N}$$

$$M = \frac{P}{2} \cdot b = 68.17 \text{ Nm}$$

Note: we used the compression force (Y_0 compression) because it gives the maximum bending moment.

Given the ultimate tensile stress of the pin material, for Ultimate bending moment, assume the ultimate bending moment is the moment that produces tension stress at the surface of the pin (tension part) equal to the ultimate tensile stress of the material, then

$$M_u = \frac{\sigma_t \cdot \pi \cdot r^4}{4 \cdot r} = \frac{\sigma_t \cdot \pi \cdot r^3}{4} \quad (4.87)$$

$$M_u = 2035.75 \text{ Nm}$$

The Margin of Safety (MS):

$$MS = \frac{M_u}{F_{s,f} \cdot M} - 1 \quad (4.88)$$

$$MS = 16.31 \text{ ok}$$

4.9.3 Transverse load analysis

The lug failure modes for the transverse load case are shown in Figure 4.14 type I below.

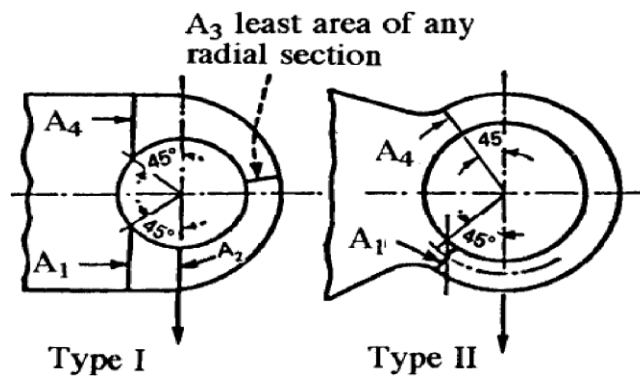


Figure 4.14 Failure mode of transverse load

The critical transverse load of our lug is found in case D. 4 (

Table 4.25), and since we have two connection points, the value is divided over two, and there are four lugs in one connection (the central lug represent two lugs).

a) The ultimate load

The ultimate load is obtained by:

$$P_{tru} = K_{tru} \cdot A_{br} \cdot F_{tuy} \quad (4.89)$$

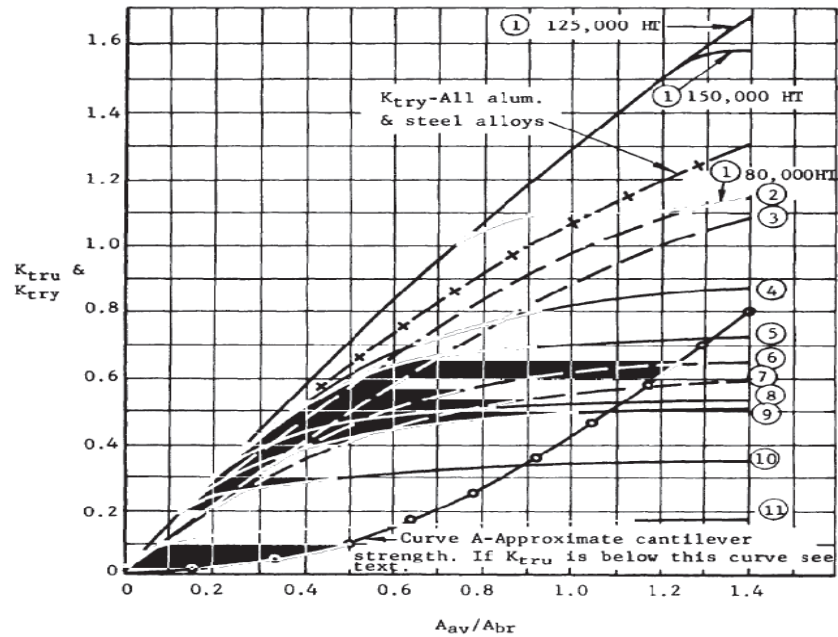


Figure 4.15 Transverse Loading Kt

Where:

P_{tru} : Ultimate transverse load

$K_{tru} = 1.06$ Efficiency factor for transverse load, calculated based on Figure 4.15 [52]

A_{br} : Projected bearing area $A_{br} = 0.84 \times 10^{-4} m^2$

F_{tuy} : Ultimate tensile stress of lug material in y -direction (Approximately equal to the ultimate tensile in x direction) $K_{tuy} = 1300 \times 10^6 N/m^2$

So, the ultimate load is:

$$P_{tru} = 115752N$$

b) The yield load

The yield load is given by:

$$P_y = K_{try} \cdot A_{br} \cdot F_{tuy} \quad (4.90)$$

Where:

P_y : Yield transverse load

$K_{try} = 0.91$: Efficiency factor for transverse yield load calculated based on [52]

A_{br} : Projected bearing area $A_{br} = 0.84 \times 10^{-4} m^2$

F_{tuy} : Tensile yield stress of lug material in y -direction

The Tensile yield is approximately=0.89 of the ultimate tensile stress from high strength steel, so $F_{tuy} = 0.89 \cdot 1300 \times 10^6 = 1157 \times 10^6 N/m$.

The Margin of Safety (MS):

$$MS = \frac{P_{tru}}{F_{s,f} \cdot P_{tr}} - 1 \quad (4.91)$$

$$MS = 33.6 \text{ Large}$$

CHAPTER 5
NUMERICAL CRACK PROPAGATION ANALYSIS

5 NUMERICAL CRACK PROPAGATION ANALYSIS

5.1 Introduction

In this chapter, numerical analyses of the damaged wing-fuselage attachment lug were conducted by XFEM and improved FEM. So a summary of these methods and their implementation in corresponding software packages are given at the beginning.

5.2 Finite element method (FEM)

The evaluation of Stress Intensity Factor (SIF) for various types of crack positions and geometries in the finite element method is widely used to evaluate Stress Intensity Factor (SIF) for several types of crack positions geometries. Some procedures usually use extrapolation procedures based on point matching techniques with nodal displacements due to their application in many crack configurations. An example of this type of technique is the displacement extrapolation method (DEM).

The number of elements depends on the distributed nodes around the crack tip, which can be set by the user, as shown in Figure 5.1. The stresses are computed from the displacement solutions that are the primary output of the FE programs [53]. Souiyah et al. employed this method to predict the crack propagations directions, calculate the Stress Intensity Factors (SIFs), and then validated the predicted SIF and cracked path with the corresponding numerical and analytical results obtained by other researchers. The comparison showed that the program could demonstrate the SIF evaluation and the crack path direction satisfactorily [54].

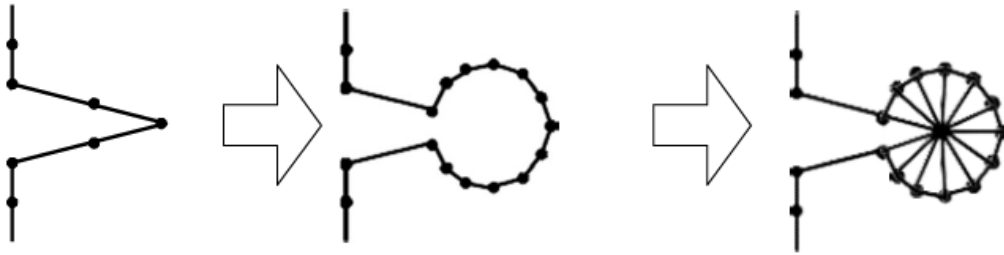


Figure 5.1 The cut and patch procedure of generating singular elements around a crack tip

One of the best-known numerical approaches is the adaptive re-meshing technique based on the finite element method. The literature [55], Table 4.2 to Table 4.5 aimed by Ricardo Branco et al. to provide an overview of adaptive remeshing technique proposals developed to evaluate the crack shape progression and fatigue life. In [56], [57] the SIF of an aluminium plate with central crack was computed by A. Gopichand et al., using the virtual crack closure technique (VCCT). Compared with empirical values and displacement extrapolation method values, the values obtained were compared with empirical values and found to be in order.

In [58] (displacement distribution, stress distribution, weight function method, J-integral, interaction integral) were applied to calculate and compare KI values by using the FE software ABAQUS. The selected methods were applied on the benchmark model: the compact tension specimen, and the results were compared. Based on this comparison, it was concluded that:

(1) The J-integral method and the interaction integral implemented thru ABAQUS provide consistent K values with the one calculated by ASTM. So it is established that those are appropriate methods to determine accurate K values for both 2D and 3D cracks.

(2) The displacement and stress extrapolation method deliver consistent results with acceptable accuracy. Once the stress and displacement distributions are available, mentioned methods can be used for a SIF calculation. KI values were lower than those with J-integral or interaction integral and similar to the surface values (lower constraint).

(3) The 3D model provides more accurate results than 2D models.

(4) With J-integral, it is not possible to separate KI, KII and KIII. However, this disadvantage can be resolved by using the integral interaction method. The interaction integral was the most consistent method. In the literature [59], [57] two different crack growth criteria and the crack trajectory prediction for various applications were compared using the maximum circumferential stress criterion and the strain energy density criterion. For each example, the angle of direction at each crack increment length and the final crack propagation path was determined. The displacement extrapolation method was used to determine the stress intensity factors under mode I and mixed-mode loading. Numerical calculations made by the finite element methods showed that this technique could correctly describe the stress and deformations field near the crack tip. The two criteria gave good results on the crack propagation path, and the results between them were very close.

5.2.1 The effect of the mesh

The two criteria gave good results on the crack propagation path, and the results between them were very close. In finite element analysis, mesh size is the critical issue. Because it directly affects the accuracy, computing time and efforts needed for creating the finite element models. The accuracy of the result obtained is determined by the mesh element size [60]. Shashikant T. More and Dr. R. S. Bindu [57], [61] presented a study of the effects of the mesh element size on the accuracy of the numerically obtained results. The guidelines for choosing the appropriate mesh strategy in finite element modelling were based on these results. The analyses were conducted by using Femap and NX-Nastran. It was found that for static analysis, which assumes steady loading and response conditions, the model discretized into elements of size 40 mm to obtain satisfying results, consuming fewer computer resources and computing time. For buckling analysis, the FE model, which was meshed between 30 and 50 mm, gave optimal accuracy and efficiency. Three element types and eight-element sizes were used to compare the accuracy of modal analysis by Weibing Liu et al. As curve and surface boundary of a higher-order element can accurately approach structure boundary, calculation accuracy under hexahedral 36 elements was higher than tetrahedral element.

Meanwhile, the calculation accuracy of modal analysis can be improved by increasing the number of nodes. In that case, the order of algebraic equations obtained by the discrete differential equation is increased. After mesh type was selected, the calculation accuracy of modal analysis could also be increased by changing element size. But when mesh size was changed to a point or a place, the changes of calculation accuracy became stable. There is no significance for improving the calculation of modal analysis by changing the mesh element size continuous [62].

5.3 Extended Finite Element Method (XFEM)

5.3.1 Introduction

The requirement of re-meshing the discontinuous of crack's domain is the notable restriction of FEM, which represents a significant issue for modelling the crack propagation in complex geometry. To mitigate the difficulties of computational crack propagation in FEM, Belytschko and Black [63] suggested the extended finite element method (XFEM). This method can resolve the problem of FEM by enriching in the proximity of the crack and simulate the domain re-meshing. This method is based on the partition of unity and also provides using higher-order elements or particular finite elements without significant changes in the formulation. It has been widely acknowledged that this method since it uses the assumptions of linear elastic fracture mechanics (LEFM), simplifies the fracture growth modelling.

Since its introduction in ,1999 many new upgrades and applications have been proposed in the scientific literature [57], [64].

Compared to the finite element method, the XFEM provides many improvements in the numerical modelling of fracture propagation. In the FEM, the crack model must follow mesh element edges, while crack geometry in the XFEM does not need not be aligned with the mesh element edges, which is significant flexibility. This capability has been illustrated in Figure 5.2, [65], [36], [57].

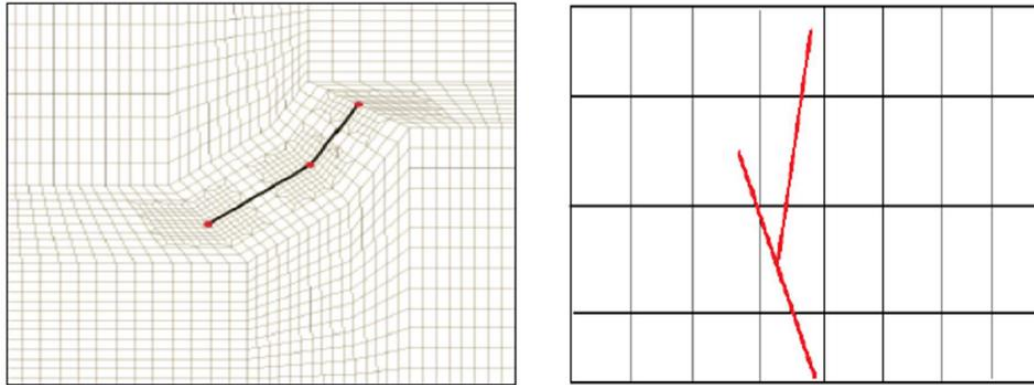


Figure 5.2 Comparison of a crack path in FEM (left) and XFEM (right)

The extended finite element method (XFEM) is also known in the literature as a generalized finite element method (GFEM) or partition of unity method. (PUM) is a numerical procedure that upgrades the traditional finite element method (FEM) by extending the solution space for solutions to differential equations with discontinuous functions. The extended finite element method was designed to solve the problems with localized features that could not be efficiently resolved by mesh refinement.

A key advantage of XFEM is that the finite element mesh does not need to be updated to track the crack path in such problems. This method has more general use in solving problems with singularities, material interfaces. With the regular meshing of microstructural features such as voids, a localized advantage can be described by an appropriate set of basic functions [66].

The extended finite element method (XFEM) has proved to be a competent mathematical tool that enables a local enrichment of approximation spaces. The partition of the unity concept recognizes the enrichment. This concept gives an approximate solution with well-known non-smooth characteristics in small parts with computational domains, i.e. discontinuities and singularities near the crack tip. Standard numerical methods such as a finite element or finite volume often exhibit poor accuracy for crack growth simulation problems. The XFEM offers significant advantages by enabling optimal convergence for these applications [67], [57].

The XFEM is based on the enrichment of the FE model by adding extra degrees of freedom added to the nodes of the elements cut by the crack. In this way, crack is included in the numerical model without modifying the domain discretization, because the mesh is generated completely independent of the fracture. Therefore, only a single mesh is needed for any fracture length and orientation. In addition, nodes surrounding the crack tip are enriched with functions that reproduce the asymptotic crack tip behaviour. This enables the modelling of the crack within the fracture-tip element and increases the accuracy in calculating the stress intensity factors [65], [57].

5.3.2 Partition of unity

Partition of unity is a set R of continuous functions from X to the interval $[0,1]$ such that for every point, $x \in X$,

- there is a neighbourhood of x where all but one finite number of the functions $of R$ are 0,

- the sum of all the function values at x is 1, $\sum_{i=1}^n f_i(x) = 1$.

Partitions of unity are helpful because they often allow extending local constructions to the whole space. They are also important for interpolation of data, signal processing, and the theory of spline functions. An example of partition of unity for 4 functions is illustrated in Figure 5.3 [65].

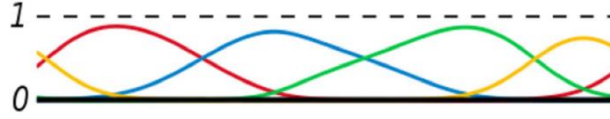


Figure 5.3 Partition of unity of a circle with four functions

If this condition is verified, any point x in X has only finite i with $f_i(x) \neq 0$. It can be shown that the sum in Equation does not have to be identically unity to work; for any function $\phi(x)$, it is verified that

$$\sum_{i=1}^n f_i(x)\phi(x) = \phi(x) \quad (5.1)$$

It can also be shown that the partition of unity property is satisfied by the set of finite element shape functions N_j , i.e.

$$\sum_{j=1}^m N_j(x) = 1 \quad (5.2)$$

By improving a finite element approximation, the enrichment procedure may be applied. In other words, the accuracy of the solution can be enhanced by including the analytical solution of the problem in the finite element formulation. For example, in fracture mechanics problems, if the analytical fracture tip solution can be added to the framework of the finite element discretization, predicting fracture tip fields may be improved and cause an increase in the number of degrees of freedom.

The partition of unity finite element method (PUFEM) [68] using the concept of enrichment functions along with the partition of unity property, can help to obtain the following approximation of the displacement within a finite element.

$$u^h(x) = \sum_{j=1}^m N_j(x)(u_i + \sum_{i=1}^n p_i(x)a_{ji}) \quad (5.3)$$

where, $p_i(x)$ is the enrichment functions and a_{ji} is the additional unknowns or degrees of freedom associated with the enriched solution. m and n are the total numbers of nodes of finite elements and the number of enrichment functions p_i .

Based on the discussion above, for an enriched node χ_k Equation (5.3) [69].

$$u^h(x_k) = (u_k + \sum_{i=1}^n p_i(x_k)a_{ji}) \quad (5.4)$$

Which is not a possible solution. To overcome this problem and satisfy interpolation at the nodal point, i.e. $u^h(x_{ki}) = u_i$, a slightly modified expression for the enriched displacement field was proposed as:

$$u^h(x) = \sum_{j=1}^m N_j(x) [u_j + \sum_{i=1}^n (p_i(x) - p_i(x_j)) a_{ji}] \quad (5.5)$$

A significant improvement in finite element discretization is provided by the generalized finite element method (GFEM), which represent a major improvement in finite element discretization, in which two separate shape functions are used for the ordinary and the enriched part of the finite element approximation [70] [57], where:

$$u^h(x) = \sum_{j=1}^m N_j(x) u_j + \sum_{j=1}^m \bar{N}_j(x) \sum_{i=1}^n p_i(x) a_{ji} \quad (5.6)$$

Where $\bar{N}_j(x)$ are the shape functions associated with the enrichment basis function $p_i(x)$. For a reason which explained in the previous section, equation.

$$u^h(x) = \sum_{j=1}^m N_j(x) u_j + \sum_{j=1}^m \bar{N}_j(x) \sum_{i=1}^n p_i(x) a_{ji} \quad (5.7)$$

should be modified as follows:

$$u^h(x) = \sum_{j=1}^m N_j(x) u_j + \sum_{j=1}^m \bar{N}_j(x) \left[\sum_{i=1}^n (p_i(x) - p_i(x_j)) a_{ji} \right] \quad (5.8)$$

5.3.3 Enrichment functions

In two-dimensional problems, crack growth modelling is characterized using two different types of enrichment functions:

5.3.4 The Heaviside function

For the elements wholly cut by the crack, The Heaviside function $H(x)$ is applied for enrichment. The splitting of the element by the fracture results in a jump in the displacement field, and the Heaviside function provides a simple mathematical approach to model this kind of behaviour. For a continuous curve Γ , representing a fracture within the deformable body Ω , we can consider a point $x(x, y)$ in Ω (Figure 5.4). The objective is to determine the position of this point concerning the fracture location. If the closest point belonging to Γ is $\bar{x}(\bar{x}, \bar{y})$ and the outward normal vector to Γ in \bar{x} is n , the Heaviside function might be defined as follows:

$$H(x, y) = \begin{cases} 1 & \text{for } (x - \bar{x}) \cdot n > 0 \\ -1 & \text{for } (x - \bar{x}) \cdot n < 0 \end{cases} \quad (5.9)$$

This function introduces the discontinuity across the fracture faces.

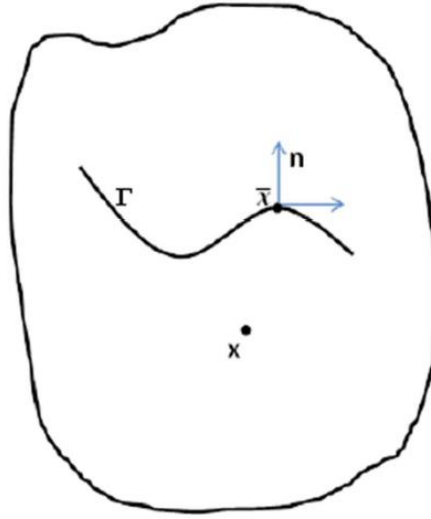


Figure 5.4 Evaluation of Heaviside function

5.3.5 Asymptotic near-tip field functions

For those elements that are not wholly fractured and containing crack tip, the Heaviside function cannot be used to approximate the displacement field in the entire element. For the crack tip, the enrichment functions originally introduced by Fleming [57], [71] for use in the element free Galerkin method. They were later used in XFEM formulation by Belytschko. These four functions describe the crack tip displacement field. The first function is discontinuous at the fracture tip.

$$[F_\alpha(r, \theta), \alpha = 1] = \begin{cases} \sqrt{r} \sin \frac{\theta}{2} \\ \sqrt{r} \cos \frac{\theta}{2} \\ \sqrt{r} \sin \frac{\theta}{2} \sin \theta \\ \sqrt{r} \cos \frac{\theta}{2} \sin \theta \end{cases} \quad (5.10)$$

In this formulation r, θ are polar coordinates defined at the fracture tip. The above functions can simulate the asymptotic mode I and mode II displacement fields in LEFM, representing the near-tip singular behaviour in strains and stresses. These functions significantly improve the accuracy of the calculation of KI and KII, [72] [57].

Four different additional degrees of freedom in each direction for each node are added to the finite element formulation using the enrichment functions. The term $\sqrt{r} \sin \frac{\theta}{2}$ discontinuous and therefore can represent the discontinuous behaviour at the fracture tip. The remaining three functions are used to enhance the approximation of the near crack tip. Figure 5.5 shows a part of a mesh with four-node bilinear types of elements. The circled nodes are the nodes of elements wholly cut by the fracture

and therefore enriched with Heaviside function. The nodes with the green square are containing fracture tip and are enriched by the fracture tip particular function mentioned in the equation:

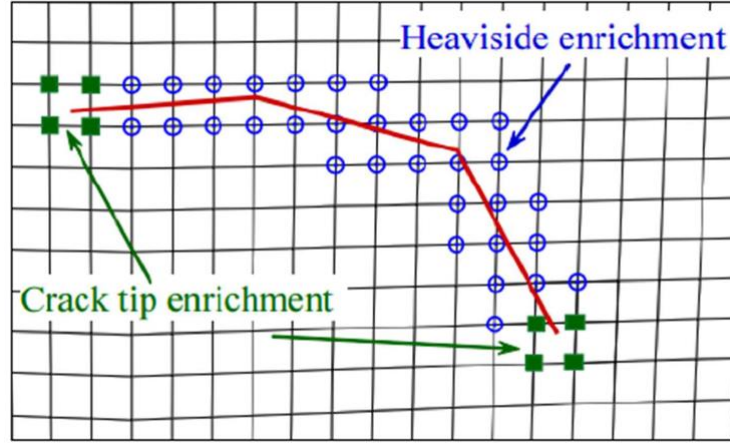


Figure 5.5 The Enriched nodes in extended finite element method. [73]

Based on what discussed about the enrichment functions, the following expression for the XFEM approximation might be formulated:

$$u^h = u_{FEM}(x) + u_{Enr}(x) \quad (5.11)$$

$$u_{xfem} = \sum_{i \in I} N_i(x) u_i + \sum_{j \in J} N_{ij}(x) [H(x)] a_j + \sum_{k \in K_I} [N_k(x) \sum_{l=1}^4 b_k^{II} F_l^I(x)] + \sum_{k \in K_{II}} [N_k(x) \sum_{l=1}^4 b_k^{III} F_l^{II}(x)] \quad (5.12)$$

where, J is the set of nodes whose elements is completely cut by the crack and therefore enriched with the Heaviside function (x), K_I and K_{II} are the sets of nodes containing the fracture tips 1 and 2, and crack tip enrichment functions are: $F_l^I(x)$ and F_l^{II} . u_i are the standard degrees of freedom, and a_j , b_k^{II} , b_k^{III} are the vectors of additional nodal degrees of freedom for modelling fracture faces and the two crack tips, respectively.

5.3.6 Level set method for modelling discontinuities

In some cases, numerical simulations include moving objects, such as curves and surfaces on a fixed grid. This kind of modelling and tracking is difficult and requires a complex mathematical procedure. The Level Set Method (LSM) is a numerical technique that can help to solve these difficulties. The critical point in this method is to represent the moving object as a zero level set function. To fully characterize a fracture, two different level set functions are defined:

1. A normal function, $\phi(x)$
2. A tangential function, $\psi(x)$.

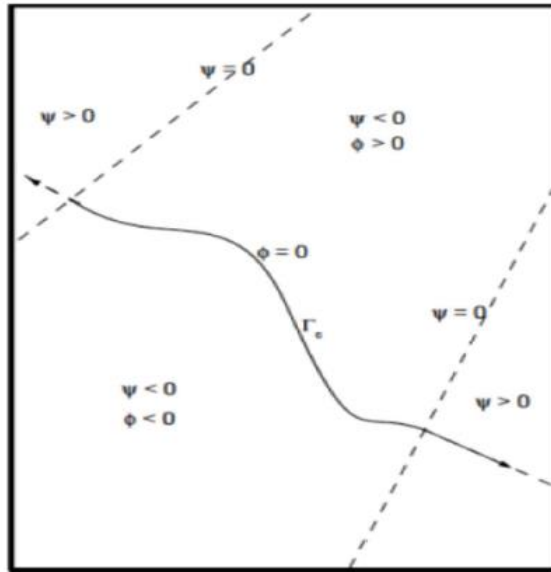


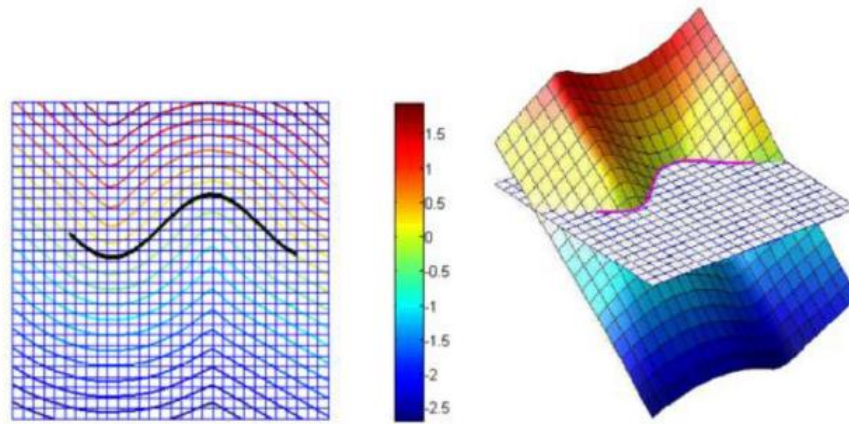
Figure 5.6 Construction of level set functions normal function for $\phi(x)$ and tangential function, $\psi(x)$

For evaluating the signed distance functions, assume Γ_c be the crack surface (shown in Figure 5.6) and x the point we want to evaluate the $\phi(x)$ function. The normal level set function can be defined as:

$$\phi = (\bar{x} - \chi) \cdot n \quad (5.13)$$

Where \bar{x} and n are defined previously.

In Figure 5.7, the plot of the normal signed function $\phi(x)$ for a fracture is illustrated. The tangential level set function $\psi(x)$ is computed by finding the minimum signed distance to the normal at the fracture tip.



(a) 2D contour of $\psi(x)$

(b) 3D contour of $\psi(x)$

Figure 5.7 Picture of normal level set function of $\psi(x)$ for (a) 2D contour of $\psi(x)$ and (b) 3D contour of $\psi(x)$

In case of an interior fracture, two different functions can be applied. However, a unique tangential level set function can be defined as:

$$\psi(x) = \max(\psi_1(x), \psi_2) \quad (5.14)$$

In conclusion, referring to Figure 5.6, it may be written as follows:

$$\begin{cases} \text{for } \chi \in \Gamma_{cr} & \phi(x = 0) \quad \text{and } \psi(x \leq 0) \\ \text{for } \chi \in \Gamma_{tip} & \phi(x = 0) \quad \text{and } \psi(x = 0) \end{cases} \quad (5.15)$$

Where indicates the fracture tips location.

5.3.7 Numerical integration and convergence

The Gauss quadrature has been used for polynomial integrands. For non-polynomial ones, this method may reduce the accuracy of results. Introducing a fracture in the finite element discretization changes displacements and stresses into non-linear fields, which the Gauss quadrature cannot integrate.

A-triangulation procedure was proposed [74] in which elements edges align with the fracture faces. This approach is illustrated in Figure 5.8). Within these sub-elements, the standard Gauss integration procedure can be used.

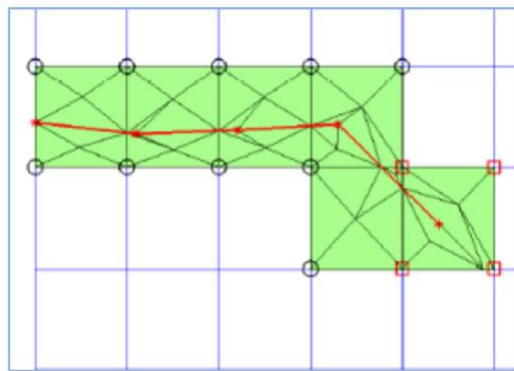


Figure 5.8 Sub-triangulation of elements cut by a fracture

Therefore, for elements containing the fracture tip, including the singular stress field, this procedure might be inaccurate if Gauss points of sub-triangles are too close at the fracture tip.

Fracture modelling with the standard finite element method is performed by remeshing the domain so that elements boundaries match the fracture geometry. But newly created elements have to be well conditioned and not badly shaped. Accordingly, remeshing procedure is a complicated and computationally costly operation. On the other hand, since the sub-triangulation is performed only for integration purposes, no additional degrees of freedom are added to the system and sub-triangles are not forced to be well-shaped.

An alternative method based on eliminating quadrature sub-elements has been proposed [75], [57].

In such an approach, discontinuous non-differentiable functions are replaced with equivalent polynomial functions. So, consequently, the Gauss quadrature can be carried out over the whole element.

The XFEM method provides more accurate results than the FEM one when there is a discontinuity in the domain. But, it cannot improve the convergence rate due to the presence of the singularity, and the convergence is lower than expected by using the FEM method in smooth problems. Several methods have been proposed during the last decades to achieve an optimal rate of convergence, e.g. XFEM with a fixed enrichment area, high-order XFEM [76] as a modified construction of blending elements.

5.3.8 XFEM implementation in ABAQUS

The first formulation of the XFEM goes back to 1999, and therefore, there is a shortage of commercial software that has been using such a method. The enormous improvements provided by the XFEM have made many attempts to include XFEM in multi-purpose commercial FEM software. Among the commercial software, the most famous ones are LS-DYNA and Abaqus and ANSYS.

Other software, including ASTER and Morfeo, which have included this capability XFEM module, was introduced in Abaqus in 2009 with the Abaqus 6.9 release [77]. The XFEM implementation in Abaqus/Standard is based on the phantom nodes method [76] in which phantom nodes are superposed to the real ones to reproduce the presence of the discontinuity.

Abaqus's crack surfaces and tips are identified with a numerical procedure based on the Level Set Method. Once the mesh discretization has been created, each node of the finite element grid is characterized with three coordinates for the global coordinate system and two additional parameters, called PHILSM and PSILSM. These parameters are nonzero only for the enriched elements, and they might be easily interpreted as the nodal coordinates of the enriched nodes in a coordinate system centred at the fracture tip and whose axes are, respectively, tangent and normal to the fracture surfaces at the fracture tip [77] [57].

5.3.9 Improved Finite Element Method

By applying the Unstructured Mesh Method (UMM), FEM has been improved by enabling the change of the finite element mesh just in the immediate vicinity of the crack, which significantly simplifies the modelling of crack growth. Implementing UMM, ANSYS Mechanical has introduced the Separating Morphing and Adaptive Re-meshing Technology (SMART) for crack growth simulation [78], [79].

This technology automatically updates the mesh at each solution step but only near the crack, so the SIFs solutions are computed for every new position of the propagating crack front. This feature implies applying one specific element type and patch conforming tetrameshing method, a restriction made using the software itself. The simulation of crack growth is done thru the crack increment. The minimum crack increment is 0.25 times the average element size along the crack front, and the maximum crack increment is 1.5 times the average element size along the crack front.

So, selecting the average element size along the crack front is of paramount importance, which implies that the successful application of SMART highly depends on the mesh definition of the crack which propagation is to be simulated. Although new, this improved FEM has been successfully applied in several studies [80], [81], [82].

The integral interaction method, calculating SIFs for opening mode along the crack front in ANSYS, uses area integration for 2D problems and volume integration for 3D problems. The interaction integral I is defined as [69]:

$$I = \frac{-\int_V q_{i,j} (\sigma_{kl} \varepsilon_{kl}^{aux} \delta_{ij} - \sigma_{kj}^{aux} u_{ki} - \sigma_{kj} u_{ki}^{aux}) dV}{\int_s \delta q_n ds} \quad (5.16)$$

Where:

$\sigma_{ij}, \varepsilon_{ij}, u_i$ are stress, strain and displacement respectively

$\sigma_{ij}^{aux}, \varepsilon_{ij}^{aux}, u_i^{aux}$ are stress, strain and displacement of the auxiliary field respectively

q_i is crack-extension vector.

Here, the interaction integral I is associated with the stress intensity factors as:

$$I = \frac{2}{E^*} (K_1 K_1^{aux} + K_2 K_2^{aux}) + \frac{1}{\mu} K_3 K_3^{aux} \quad (5.17)$$

Where K_i ($i=1,2,3$) is mode I, II, and III SIFs modes; K_i^{aux} ($i=1,2,3$) are mode I, II, and III SIFs auxiliary modes; $E^* = E$ for plane stress; $E^* = \frac{E}{1-\nu^2}$ for plane strain and E , ν , μ are Young's modulus, Poisson's ratio and shear modulus, respectively.

5.3.10 Finite Element Analysis of the Wing-fuselage Attachment Lug

In this research, a pin-loaded attachment lug, whose resistance to external forces occurring during the flight was analyzed, is shown in Figure 5.9 with all dimensions [83].

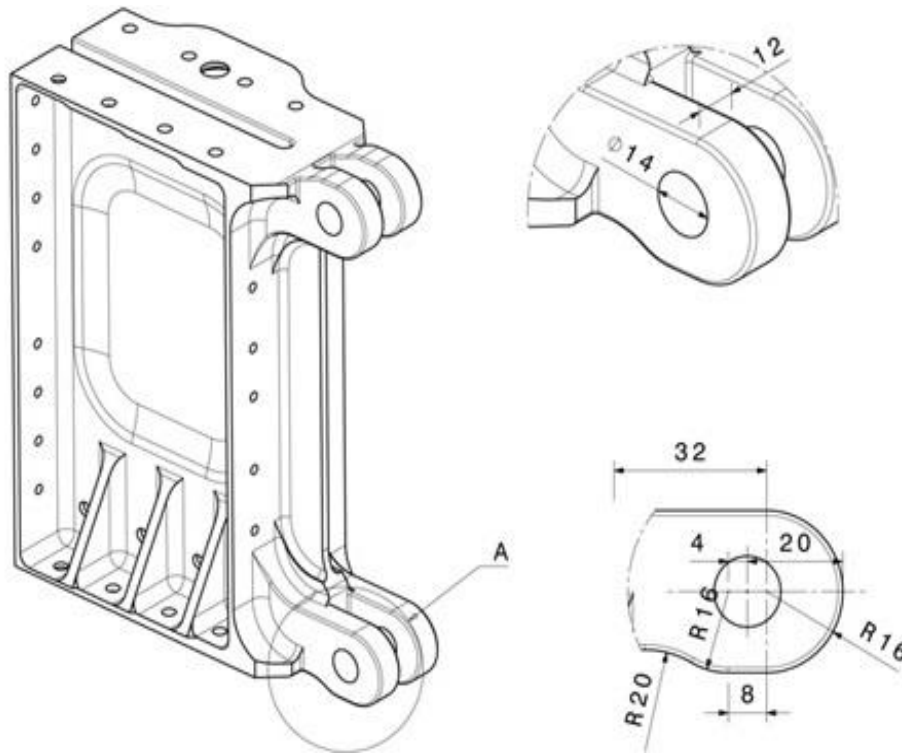


Figure 5.9 The dimensions of wing-fuselage attachment lugs used in the analysis

The lug is part of the assembly developed in CATIA v5 during the design of the light aerobatic aircraft Safat 03, and firstly the whole assembly was exported to MSC Patran/Nastran for classical finite element analysis (FEA). The highest stresses in the wing-fuselage attachment were identified around lug holes

Figure 5.10b. A magnified view of one of the lugs

Figure 5.10a, provides insight into the values of Von Mises stresses in the zone around the hole: the stress ranges from 725 MPa to 886 MPa, and these values were obtained in the case when the attachment was subjected to maximum expected external forces (load factor was $n=6$ indicating the flight

case with a g-force of 6g). The wing-fuselage attachment material was steel with an adopted Young modulus of 206,000 MPa, and the Poisson's ratio is 0.3 [83].

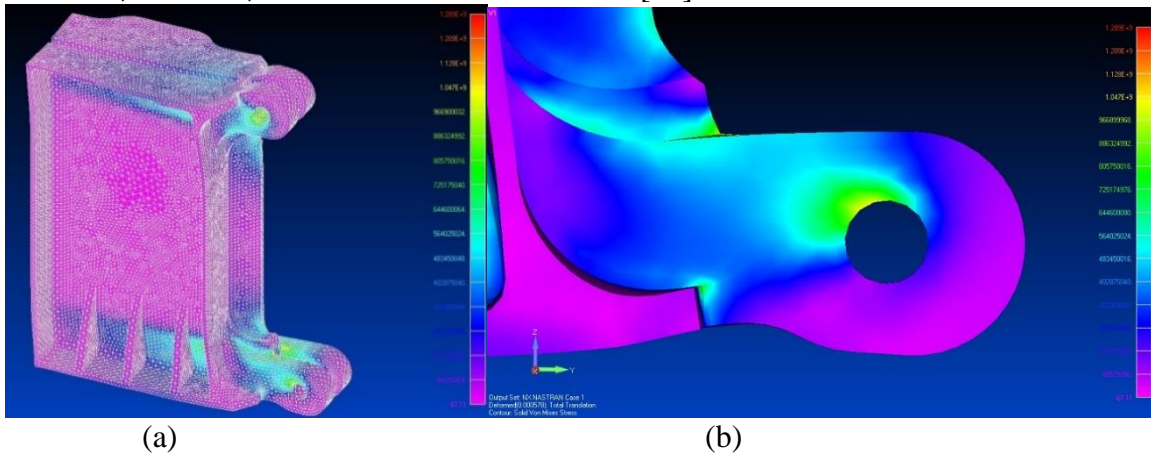


Figure 5.10 The stress distribution (a) in wing-fuselage attachment, (b) around the lower lug hole

The detailed analysis of loads to which light aircraft is exposed during the flight has shown that the total maximum axial force transferred to lug by pin would be $P_{ax,max} = 208,830.7$ N, whereas the maximum transverse force would be $P_{tr,max} = 20,177.3$ N. Considering that the wing-fuselage attachment has a pair of lugs with the exact dimensions and of the same shape Figure 5.9, the values of forces acting on each lug should be equal to one-half of the above values, i.e. $P_{ax,max} = 104,415.35$ N and $P_{tr,max} = 10,088.65$ N. The resultant force (Figure 5.11) will then be $P_{ob,max} = 104,901.6$ N, and the angle α will take the value $\alpha = 5,52^\circ$. Taking into account that $P_{ob,max}$ is significantly greater than $P_{tr,max}$, and that it only slightly deviates from the horizontal component, it was decided that to simplify the numerical model – only the axial component should be used in the analysis of the possible crack growth from the lug hole. However, its magnitude was adopted as $P_{ax} = 104,901.6$ N [83].

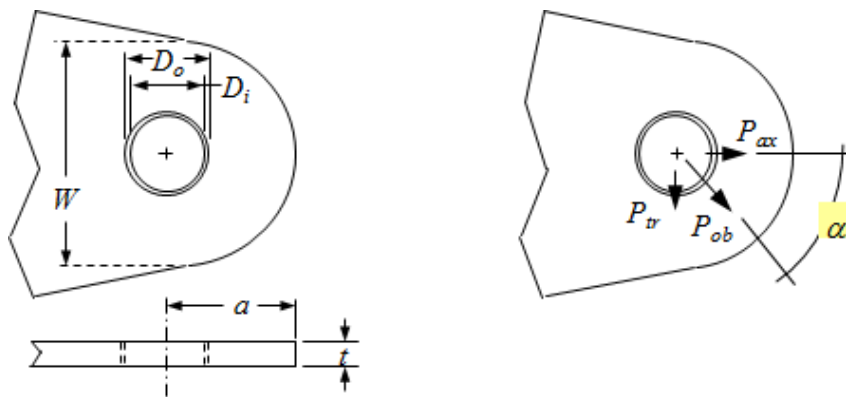


Figure 5.11. The lug dimensions and forces necessary for evaluation of $\sigma_{t,max}$

Light-sport aircraft regulations [84] suggest that maximum allowed tensile stress $\sigma_{t,max}$ along the axial direction of pin-loaded attachment lug can be calculated using the following formula:

$$\sigma_{t,max} = \frac{P_{ax}}{(W - D_0) \cdot t \cdot K_{ax}} \quad (5.18)$$

where K_{ax} represents the axial tension failure factor which can be determined – for selected material and W/D_0 ratio – from the diagrams in [85], while W , D_0 and t are shown in Figure 5.11. In the case of the lug analyzed here $W/D_0 = 32/14 = 2.286$ and the material is steel, thus the value of K_{ax} is approximately 0.583, and taking into account that $t = 12$ mm and $P_{ax} = 104,901.6$ N, using previous equation, the maximum calculated stress in the axial direction is approximately $\sigma_{t,max} = 833$ MPa . This value falls within the range of stresses around lug hole obtained in FEA (725 MPa to 886 MPa), hence $P_{ax} = 104,901.6$ N can be adopted as the external load for the crack growth simulation to assess the number of cycles of such high stress that will lead to complete failure of damaged pin-loaded attachment lug.

5.3.11 XFEM analysis of the crack growth in the lug

The lug model used in XFEM simulation Figure 5.12 was obtained in CATIA v5 by “cutting off” the wing-fuselage attachment model. After that, it was imported to Abaqus and the previously calculated load $P_{ax} = 104,901.6$ N was applied in the red zone (Figure 5.12), as well as the adequate boundary conditions. It was then assumed that due to very high stress, both the corner crack and through crack might appear in the lug, i.e., a possibility of damage presence that does not spread throughout the lug's possibility of the appearance of damage through the whole thickness. The idea was to compare the growth of the corner crack with the growth of the through crack, both located at the same position, and then to assess the risk of losing the integrity of wing-fuselage attachment once the crack has occurred [83].

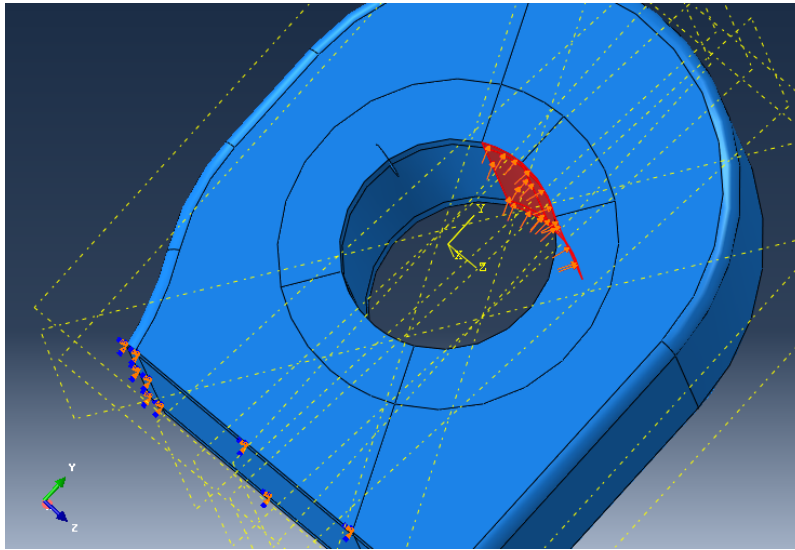


Figure 5.12 The lug model used for XFEM analysis of crack growth

For that purpose two different finite element meshes were used: one made of linear hexahedral elements of type C3D8R (Figure 5.13) and the other made of quadratic tetrahedral elements of type C3D10 (Figure 5.14). Meshes with the different number of nodes and elements have been used in the research to analyze the influence of mesh density to values of cycles obtained, and in thesis two significantly different meshes will be presented: hexahedral with 221,708 nodes and 111,023 elements, and tetrahedral with 1,121,350 nodes and 695,350 elements. It will be shown that both produce more or less the same results [83].

5.3.12 XFEM simulation of the corner crack growth

In first two XFEM simulations, with two different element types, a penny-shaped corner crack was generated using a circular surface with a radius of 2 mm.

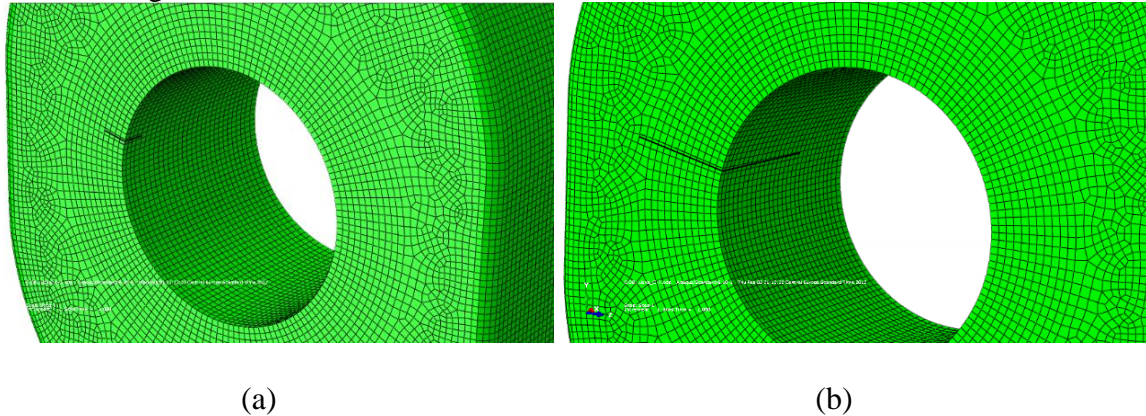


Figure 5.13 (a) Initial penny-shaped crack in hexahedral mesh, and (b) crack after 6th step of propagation

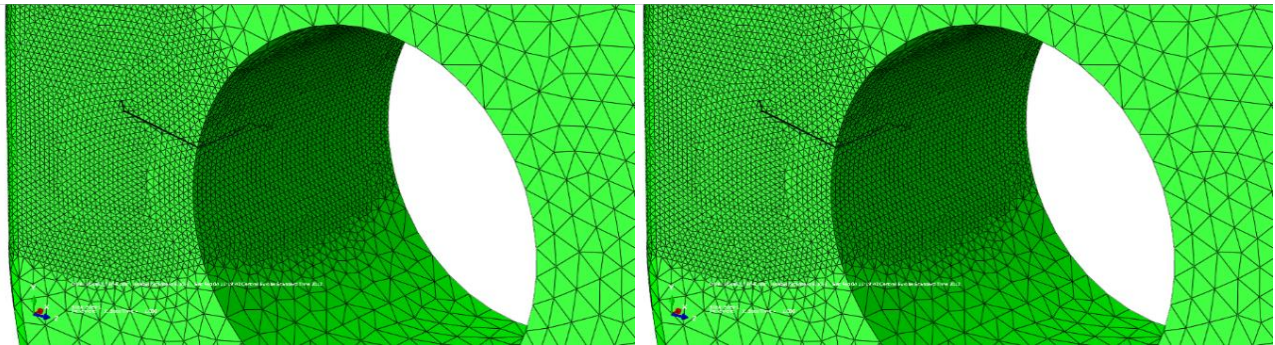


Figure 5.14 (a) Initial penny-shaped crack in tetrahedral mesh, and (b) crack after 6th step of propagation

In a case of hexahedral mesh, crack growth was forced to be in a single plane, i.e. newly formed crack fronts remained in the plane of initial penny-shaped crack, while in a case of tetrahedral mesh crack growth was not limited to a single plane, allowing the new fronts to be generated in the most probable directions determined by the calculated values of kink angle. All the stress intensity factors (SIFs) calculations have been done with the help of the software add-in named *Morfeo/Crack for Abaqus* [79], which allows the user to choose whether the growth will be simulated in a single plane or not.

After six steps of propagation and SIFs calculations, with maximum increment of 1 mm per step, both cracks – in hexahedral and tetrahedral mesh – reached the depth of 8 mm (as can be seen in Figure 5.13b and Figure 5.14b). Cracks' propagation was then terminated. Some of the nodes on the crack fronts negative values of stress intensity factor were calculated, indicating that crack growth stopped in a certain direction(s). This can be clearly seen in Table 5.1 and Table 5.2 [83] in, which values of equivalent stress intensity factors K_{eq} and Mode I stress intensity factors K_I for two meshes are given. In both cases in 7th step negative values of K_I occurred ($K_I = -33.38 \text{ MPa mm}^{0.5}$ and $K_I = -9.23 \text{ MPa mm}^{0.5}$ respectively) even if the shapes of cracks were not the same: crack forced to grow in a single plane kept the regular circular shape (Figure 5.13b), while the crack that “freely” propagated got irregular shape (Figure 5.14b) [83].

Table 5.1 SIF values calculated for corner crack growth in the lug model with hexahedral mesh

			Penny shape edge crack (hexahedral elements)					
			Equivalent SIF K_{eq} (MPa mm ^{0.5})			Mode I SIF K_I (MPa mm ^{0.5})		
Step	Crack depth (mm)	No. of nodes on the front	Max	Min	Mean value	Max	Min	Mean value
1	2	14	1281.64	1119.81	1203.12	1282.92	1117.88	1203.04
2	3	22	1620.84	1266.39	1395.40	1605.83	1093.75	1323.43
3	4	30	1813.83	1420.85	1560.34	1806.29	1415.71	1552.45
4	5	38	1990.86	1496.79	1667.47	1983.72	1498.86	1668.65
5	6	46	2139.00	1588.09	1781.63	2138.81	1585.82	1777.70
6	7	53	2246.24	1696.40	1872.15	2244.99	1693.98	1873.75
7	8	58	2353.80	1799.61	1956.56	2342.47	-33.38	1707.04

Table 5.2 SIF values calculated for corner crack growth in the lug model with tetrahedral mesh

			Penny shape edge crack (tetrahedral elements)					
			Equivalent SIF K_{eq} (MPa mm ^{0.5})			Mode I SIF K_I (MPa mm ^{0.5})		
Step	Crack depth (mm)	No. of nodes on the front	Max	Min	Mean value	Max	Min	Mean value
1	2	40	1299.94	1044.84	1155.38	1306.22	1039.67	1153.84
2	3	53	1929.91	1208.76	1382.53	2447.42	1203.42	1433.43
3	4	67	1682.04	1298.76	1481.61	3243.83	1303.75	1603.01
4	5	81	1932.62	1161.30	1563.13	1823.81	1081.39	1487.99
5	6	120	1866.75	670.82	1354.84	1545.87	473.17	1218.96
6	7	91	1630.91	349.70	1087.30	1723.08	90.87	857.08
7	8	87	1746.87	512.43	1132.67	1932.71	-9.23	987.56

The other SIFs values presented in Table 5.1 and Table 5.2 will be discussed later.

Along with the SIFs calculations, *Morfeo/Crack for Abaqus* employs Paris law to determine the number of applied load cycles that will grow crack to a certain length. In this case, the stress ratio $R = -1$ was adopted (since during the flight wing load varies from tensile to compressive), while Paris coefficient $n = 2.26$ and $C = 7.526 \cdot 10^{-11}$ were taken from fatigue tests [69], [86] with the steel used for manufacturing the wing-fuselage attachment showed in Figure 5.9. Results of the integration of the Paris function are shown in the graph in Figure 5.15. It shows the change of crack depth with the number of applied load cycles for both free growth and in-the-plane crack propagation. The maximum number of cycles $N = 701$ (for crack depth 8 mm) was obtained with mesh consisting of hexahedral elements, whereas the number of cycles needed to grow the initial crack to the same depth with tetrahedral elements was $N = 632$. Obviously, slightly greater number of cycles was obtained with hexahedral elements, but difference is less than 10% suggesting that both free and in-the-plane propagation results in similar

fatigue life assessments, regardless of the final crack shape (regular or irregular), element type, mesh density and SIF deviations (visible in Table 5.1 and Table 5.2 [83]).

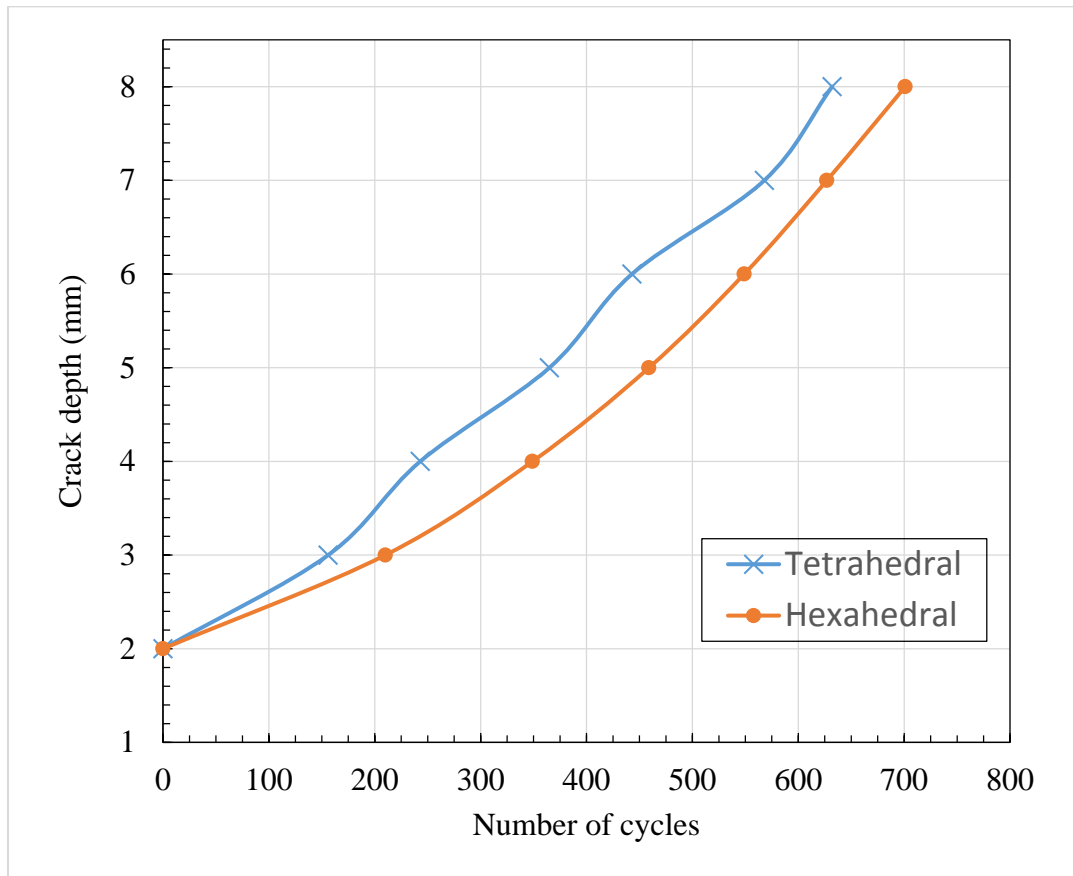
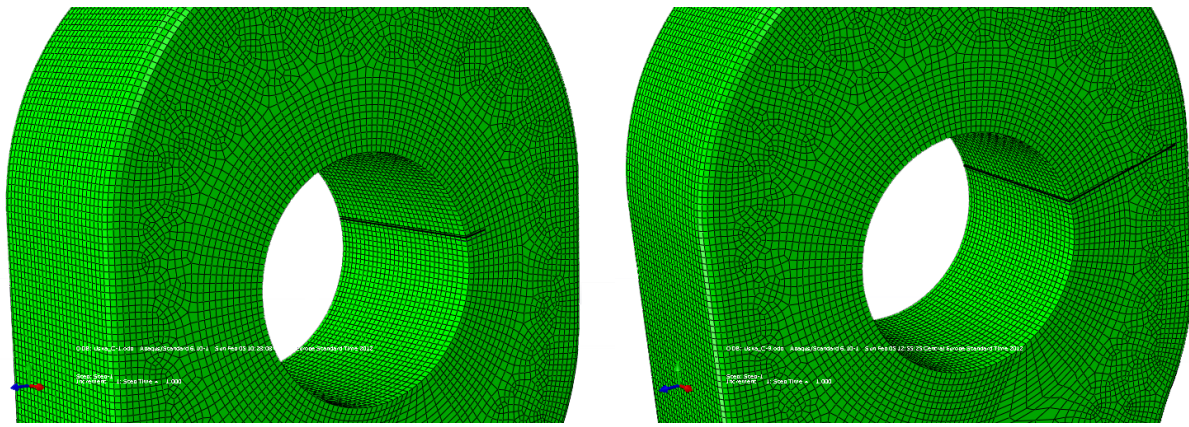


Figure 5.15. Number of cycles vs crack depth for hexahedral and tetrahedral mesh

5.3.13 XFEM simulation of the through crack growth

Considering the observed “behavior” of the corner crack, which propagated more or less in the same manner in both meshes and “produced” approximately the same number of cycles, it was decided to perform a XFEM simulation with the through the crack in FE model with hexahedral mesh only (Figure 5.16). The reason why this model was selected prior to the model with tetrahedral mesh was simple: a higher number of nodes in tetrahedral mesh produced longer calculation time considerably in XFEM based analyses of corner cracks’ growths without producing significantly different results. Thus, there was a belief that the number of cycles obtained with tetrahedral mesh would not be substantially different from the values obtained with less dense hexahedral mesh [83].

The growth simulation of through crack was performed using both approaches, free and in-the-plane propagation, and the results of in-the-plane growth are presented here.



(a)

(b)

Figure 5.16 (a) Initial through crack, and (b) through crack after 9th step of propagation

The total number of propagation steps was nine, and since the initial crack depth was 1.25 mm, a growth increment of 0.75 mm produced the final crack depth of 7.25 mm (Figure 5.16). As can be seen in Figure 5.16b through crack almost reached the outer surface of the lug.

Table 5.3 SIF values calculated for through crack growth in the lug model with hexahedral mesh

Step	Crack depth (mm)	No. of nodes on the front	Through crack					
			Equivalent SIF K_{eq} (MPa mm ^{0.5})			Mode I SIF K_I (MPa mm ^{0.5})		
			Max	Min	Mean value	Max	Min	Mean value
1	1.25	58	2020.73	1878.97	1975.73	2019.43	1876.97	1974.27
2	2.00	60	2245.33	2182.45	2224.09	2244.20	2180.66	2222.10
3	2.75	58	2380.99	2345.09	2371.53	2378.64	2320.31	2360.68
4	3.50	58	2486.80	2440.17	2457.58	2449.92	1971.08	2316.70
5	4.25	61	2762.26	2413.78	2516.19	2734.97	2360.57	2481.08
6	5.00	63	2776.20	2609.50	2674.60	2776.03	2288.89	2614.89
7	5.75	58	2918.78	2702.31	2818.05	2885.23	2696.31	2790.51
8	6.50	58	3145.00	2965.41	3052.80	3114.52	301.08	2598.67
9	7.25	67	3532.27	2142.87	3084.65	3642.05	1301.12	2762.92

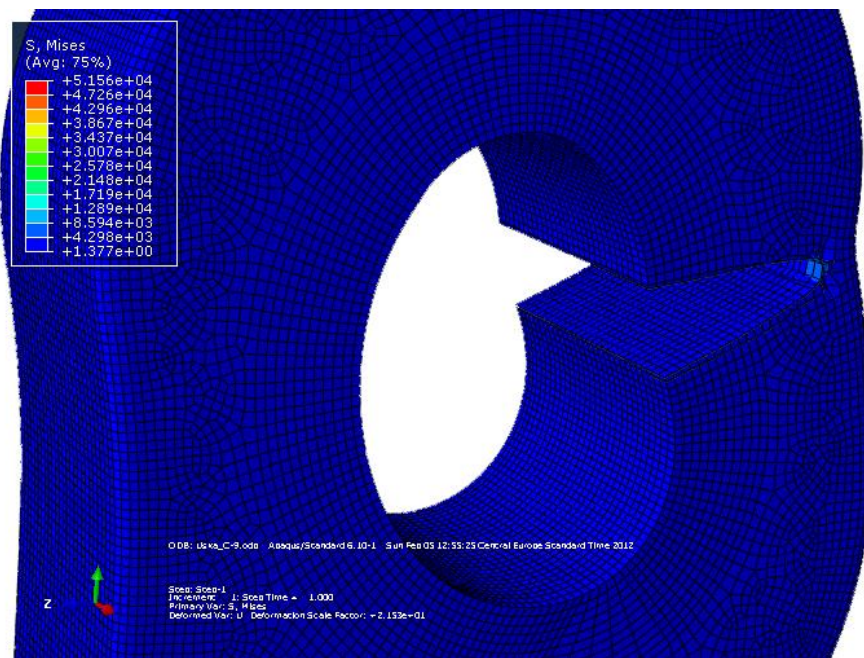


Figure 5.17 Von Mises stresses after 9th step of through crack growth

The SIFs values presented in Table 5.3 were used to calculate the number of cycles to the final depth, assuming the same Paris coefficients as for the corner crack. In Figure 5.17 enlarged FE model of cracked lug after 9th step of crack propagation can be seen, as well as the stress distribution. This stress distribution was used later for comparisons as expected (high values were detected in the vicinity of the crack front) [83].

5.3.14 Improved FEM analysis of the crack propagation in the lug

Since the wing-fuselage attachment must be designed according to the safe-life approach, its experimental analysis is not required by Federal Aviation Administration (FAA). In the case of lighter aircraft structures, there is a requirement to evaluate the innovative design numerical analyses since they are used for obtaining the stresses or number of cycles. However, it can be problematic because of the lack of experimental data.

In this case, traditional FEM was used to evaluate the number of cycles obtained by XFEM in Abaqus. Then the same geometry was analyzed in Ansys Workbench v 19.2, where tetrahedral mesh with element type SOLID187 was created. This type of analysis could only be conducted with tetrahedral mesh (mandatory by Ansys)). The simulation is based on the use of the Unstructured Mesh Method (UMM) that creates tetrahedral mesh for crack fronts, achieving the same high-fidelity results as a simulation run with “the ideal” hexahedral mesh configuration [20]. Separating Morphing and Adaptive Remeshing Technology (SMART) has been introduced by Ansys, which enables automatic re-meshing during the crack growth simulation.

So, unlike the XFEM method implemented in Abaqus, where there is no re-meshing during the simulation, mesh around the crack front in Ansys changes and adapts with every growth step to better capture the field values around the crack front nodes.

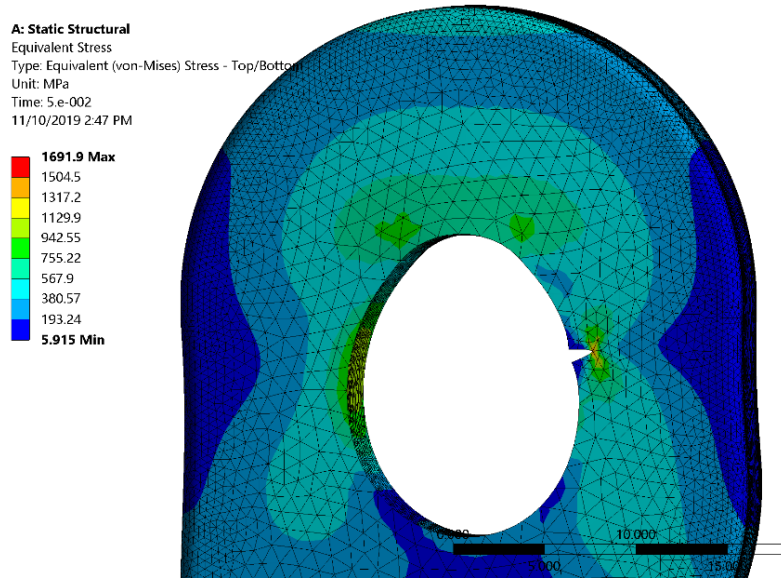


Figure 5.18 Von Mises stresses after “opening” of through crack in Ansys simulation

The same load and boundary conditions previously used in Abaqus were applied to the FE model in Ansys. Automated crack growth was defined with the same values of Paris coefficients used in XFEM based analysis. Figure 5.18 shows the initial mesh and Von Mises stresses (linear elastic analysis) after crack “opening”.

The equivalent stress distribution was compared to the distribution obtained in Abaqus, and no significant difference was found confirming that FEM and XFEM model were equivalents. The extreme stress values were not considered since they represented singularities.

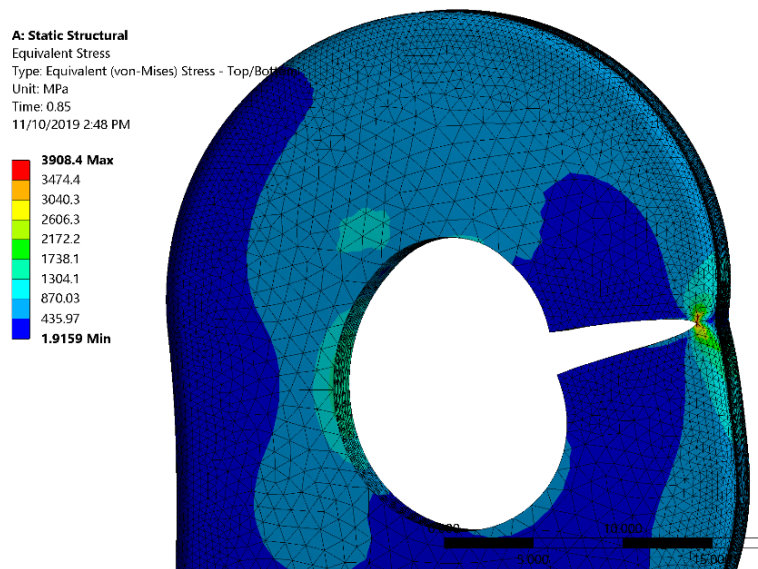


Figure 5.19 Von Mises stresses and the crack shape at the end of propagation (magnified view)

Then, the crack was propagated in Ansys until it reached the same depth as in Abaqus. The shape of the crack is shown in Figure 5.19, and obtained stress distribution was compared to the stress distribution (Figure 5.17) obtained in Abaqus. Once more, good agreement of the results was found, and

since Ansys has incorporated procedure for the calculation of the number of cycles using Paris law, crack length vs the number of cycles graph was made. The figure shows the comparison of the mean K_I values calculated in Abaqus (XFEM) and Ansys (FEM), while graphs in Figure show the comparison of the obtained number of cycles of applied load obtained using FEM and XFEM approach [83].

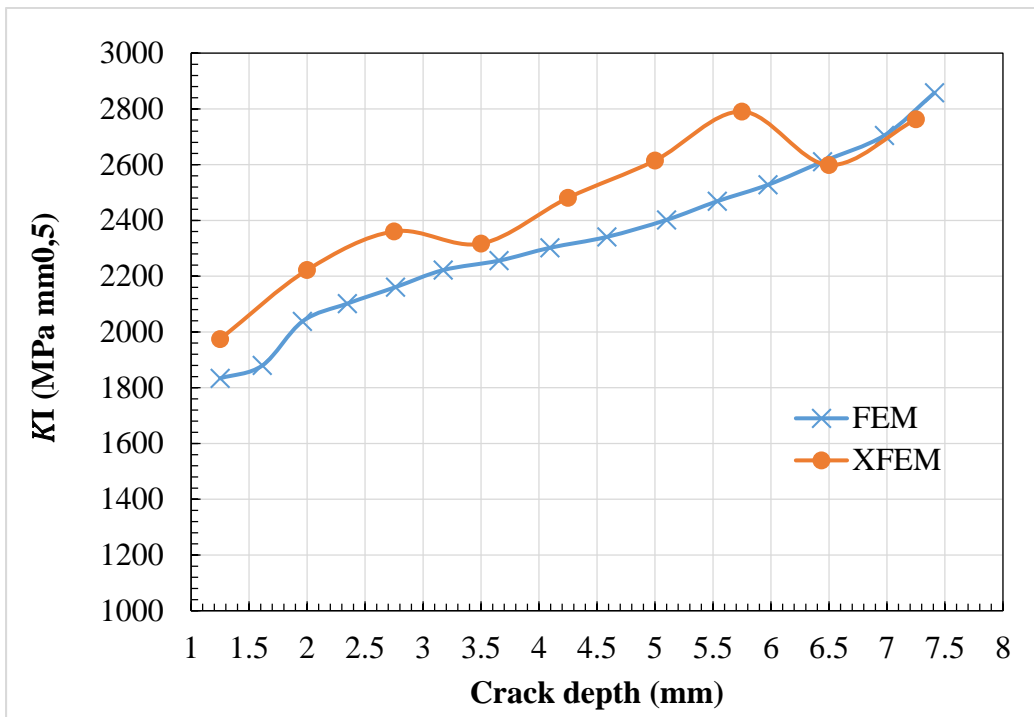


Figure 5.20 The mean K_I values calculated for the through crack growth using XFEM and FEM

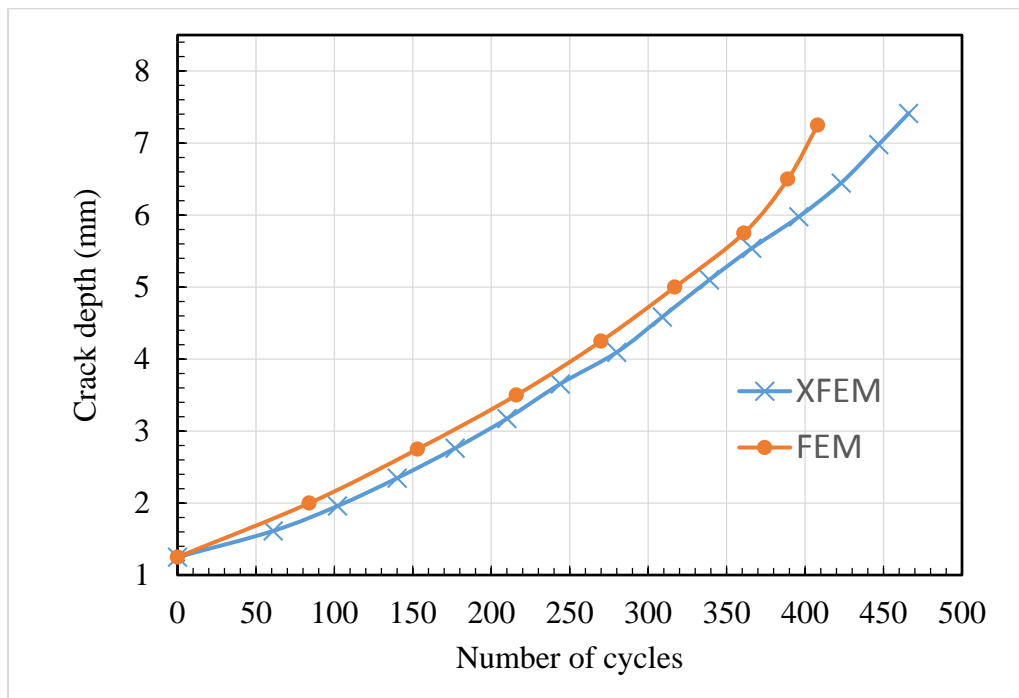


Figure 5.21 Crack depth vs number of cycles graphs obtained using XFEM and FEM

CHAPTER 6
EXPERIMENTAL VERIFICATION of
NUMERICALLY OBTAINED LOAD

6 EXPERIMENTAL VERIFICATION of NUMERICALLY OBTAINED LOAD

From the financial point of view of such a project that involves the development and manufacturing of the light aerobatic aircraft wing, it is expensive to build several prototypes just to validate the wing concept and all wing attachments and connections. On the other hand, it is impossible to obtain the license to fly without testing a prototype since civil aviation authorities require testing. In the previous Chapter, numerical simulations of wing behavior have been presented, and obtained results (deformations and stresses) allow us to predict the specific reactions of the designed wing under specific loading conditions. Numerical modelling is not expensive (compared to prototype manufacturing and full-scale wing testing), but the accuracy of the FE model has to be evaluated and confirmed before a variety of different numerical simulations can be done. Thus, a comparison with the experimental values is the only way to validate the quality of the numerical model if the deformation of the wing tip obtained in the experiment is close to the wing tip deformation obtained in FE analysis under the same load. In that case, we can claim that deformations and stresses numerically evaluated in the wing areas not covered in the experiment (since they are not easily accessible, for instance) can be accepted as accurate within a reasonable margin of error. Prototype of the wing used in experiments presented in Figure 6.1

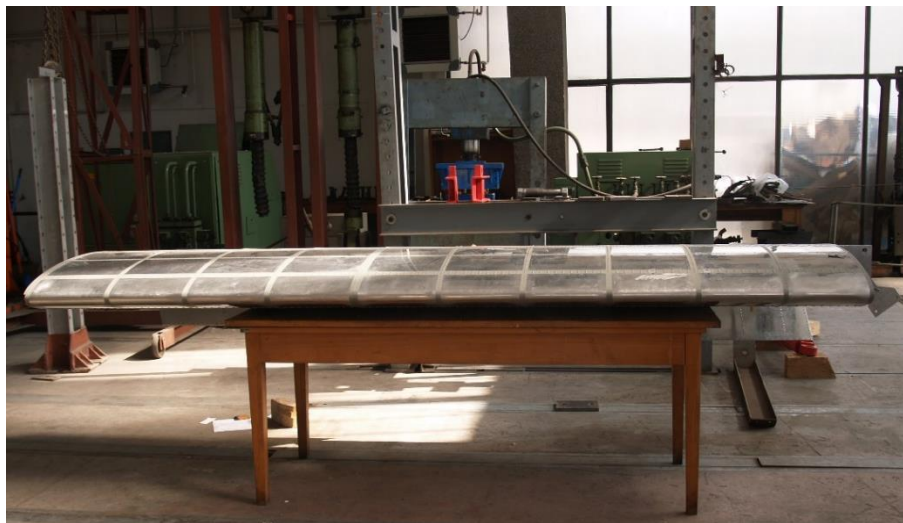


Figure 6.1 Prototype of the wing used in experiments

Therefore, a single set of wings (Figure 6.1 and Figure 6.2) has been manufactured to validate the mechanical behavior under different loading conditions and to evaluate the numerical results presented in the previous Chapter. As shown in Figure 6.2, the wing prototype has a completely functional aileron and flap, while Figure 6.3 shows the shape of rib number 11. All elements of the wing prototype have been manufactured using aluminium alloy 2024-T3, except the wing-fuselage attachment (the material was high-quality steel). The numerical model of the wing showed in the previous Chapter was made according to the original wing drawings used for prototype manufacturing, too: so, the difference between the actual wing and the 3D model is slight if we neglect a number of small features (holes, cut-outs, brackets...) with no considerable influence on the load-carrying capabilities of the wing.



Figure 6.2 Completely functional flap and aileron

The primary structure of the wing that supports the bending load is the spar. The spar is connected to the fuselage through wing-fuselage attachment, which consists of two components: one of them is part of the spar, the other is part of the main fuselage frame (bulkhead). They both have two pairs of lugs, and to connect them; pins are used (Figure 6.3). To reduce experimental costs, the part of the wing-fuselage attachment that belongs to the bulkhead was not manufactured (due to the complexity of its shape), and a simple thick steel plate with holes (Figure 6.3 and Figure 6.4) was used instead. The steel plate has two pairs of lugs that fit the lugs of the spar, while the holes on the other side are used to attach the wing to steel I-beams in the laboratory (test bench, Figure 6.5), thus holding the wing in a horizontal position during tests. The auxiliary spar and the smaller steel plate (visible in Figure 6.3 and Figure 6.4) were also used to connect the wing to steel I-beams (Figure 6.5).



Figure 6.3 Rib number 11 and pins (circled) used to connect the central spar to steel plate

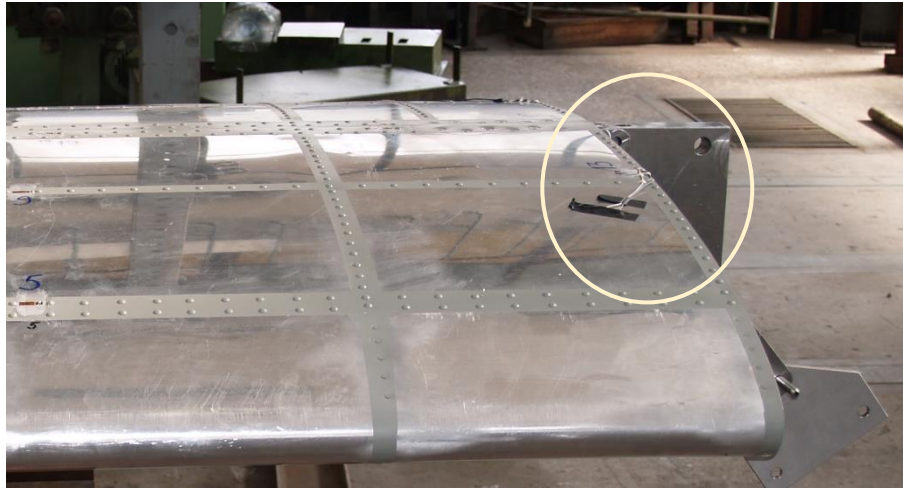


Figure 6.4 Steel plate (circled) with holes used to fix the wing and hold it in a horizontal position



Figure 6.5 Test bench consisting of 6 I-beams carries the wing prototype during experiments

To measure displacements and strains under predefined loads. A metrology system was installed to correlate the numerical simulation values with the tests' results. As mentioned above, the main goal was to compare the displacements (deflections) measured in different zones of the wing prototype with the ones obtained numerically. Displacements were measured at 10 positions, while the strain was measured at 26 separate locations. In total, 36 strain gauges have been glued to the wing on both upper and lower surface (Figure 6.6 and Figure 6.7). The force transducer was also used to measure the applied load. For data acquisition, the QuantumX data acquisition system produced by HBM was used. Several 4-channel universal amplifiers were utilized, and collected signals were processed using Catman software from HBM. Catman allows visualization of sensor data, stores data in a binary format, analyses data during the tests, and generates output in different forms (including MS Excel files, Figure 6.8) which can be used for further data processing.

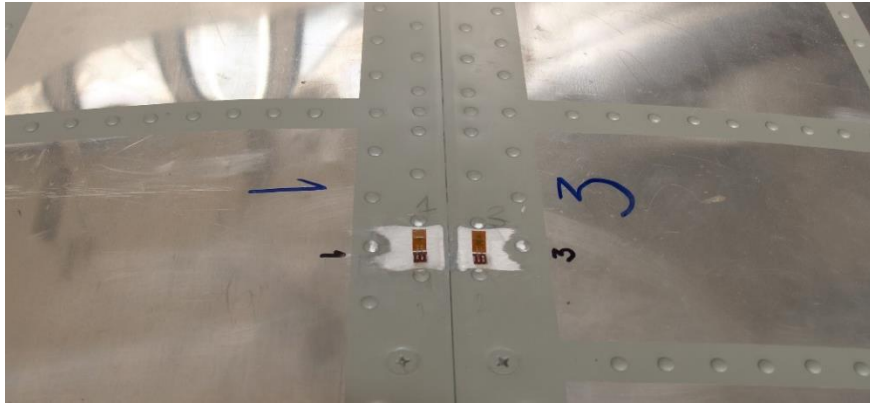


Figure 6.6 Strain gauges used to monitor deflections and strains on the upper surface of the wing

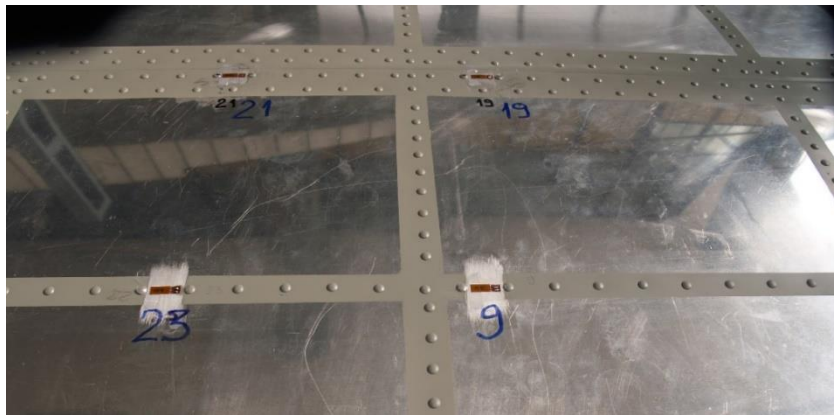


Figure 6.7 Strain gauges used to monitor deflections and strains on the lower surface of the wing

M	N	O	P	Q	R	S	T	U	V	W	
HBM_CATMAN_DATAFILE_31											
#####											
18:13											
CHANNELS: 38											
SEPARATOR: 9											
MAXLINES: 18											
t1	t2	t3	t4	t5	t6	t7	t8	t9	t10	t11	t12
um/m	um/m	um/m	um/m	um/m	um/m	um/m	um/m	um/m	um/m	um/m	um/r
11/10/2012	11/10/2012	11/10/2012	11/10/2012	11/10/2012	11/10/2012	11/10/2012	11/10/2012	11/10/2012	11/10/2012	11/10/2012	11/10/2012
dt =10 ms	dt =10 ms	dt =10 ms	dt =10 ms	dt =10 ms	dt =10 ms	dt =10 ms	dt =10 ms	dt =10 ms	dt =10 ms	dt =10 ms	dt =10 ms
3	-1	4	1	2	1	3	1	3	1	2	
-293	270	-224	107	-26	50	-64	50	-108	95	-53	
-611	565	-406	216	-67	66	-170	95	-220	183	-88	
-933	808	-600	335	-171	44	-172	147	-417	272	-95	
-1074	930	-713	400	-304	-3	-204	170	-478	308	-88	
-1196	1030	-804	469	-295	-49	-164	191	-559	343	-68	
-1254	1065	-825	502	-283	-75	-122	201	-588	359	-46	
-1307	1102	-843	534	-279	-115	-103	209	-615	372	-23	
-1354	1146	-859	570	-276	-169	-88	217	-640	386	0	
-1390	1169	-865	590	-271	-246	-74	221	-659	392	31	
-1393	1167	-866	589	-270	-246	-73	222	-660	393	35	
-988	691	-489	287	-247	-171	-146	129	-455	239	-34	
-825	524	-372	193	-206	-139	-130	100	-381	185	-49	

Figure 6.8 Data from Catman software exported to MS Excel

6.1 Test setup

As mentioned above, the central spar was connected by two pins to a thick steel plate, fixed to the test bench through threaded bolts. This configuration was designed to create infinitely rigid conditions in the wing root, providing conservative test results from the point of view of actual conditions during the flight. More than 20 different loading conditions (cases) were used in wing prototype tests over the period of one month; here, experimental results for the critical loading condition (case D, $n=6$, no fuel considered) will be presented.

The test principle was this: once we calculate loads along wingspan for any case defined by regulations, we introduce them to wing prototype using whiffle-tree configuration (Figure 6.9). The decision to use a whiffle-tree was made because we needed to apply different loads along the wingspan to simulate the nearly parabolic distribution of aerodynamic forces in combination with inertial forces. Since we had a single hydraulic jack (Figure 6.10) to introduce the load, the choice of spreaders and link rods (stirrups) seemed to be the only solution (the alternative approach was to use bags with sand).

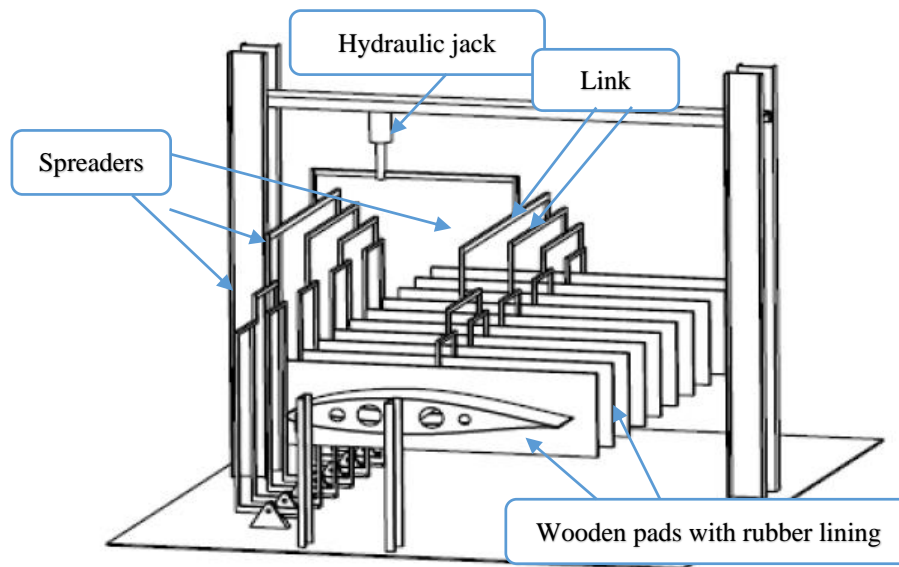


Figure 6.9 Scheme of the whiffle-tree for wing structure testing

The choice of spreader location allows us to introduce the forces produced by the winglet (the winglet was not attached to the wing during experiments). Stirrups' locations and spreaders' lengths must be determined carefully to impose the load in the experiment that will be close to the load obtained in calculations. It is important that the connecting link rods are normal to the central spar when the load factor reaches $6g$. As a reminder, more than 20 tests were carried out on the test bench and the setting was made to suit all the tests. However, spreader lengths and stirrups positions had to be determined by considering deflections of the wing when the applied load is equivalent to flight conditions with an acceleration $6g$. The spreaders have been balanced by considering stirrups weight to avoid inducing extra loading to the wing. To protect the wing structure from damage and ensure that the designed load was applied along the wing chord. Wooden pads with rubber lining have been used. The wooden pads consist of two separated parts to provide easy assembling and disassembling.



Figure 6.10 Hydraulic jack (with force transducer) used to apply loads on the wing

It was decided to apply loads using the whiffle-tree on the ribs' positions along the wingspan. As a result, the whiffle-tree shown in Figure 6.11 was designed in Catia v5 software. But the determination of stirrups' locations and spreaders' lengths turned out to be a challenging task.

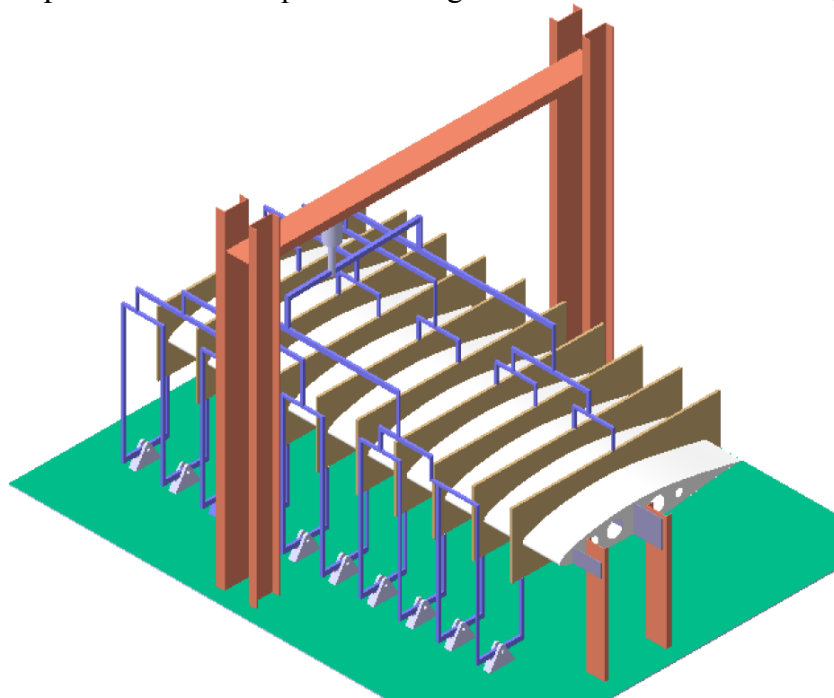


Figure 6.11 Designed whiffle-tree system for wing structure testing (CATIA drawing)

6.2 Determination of loads for critical case D and whiffle-tree system dimensions

Determining the chord-wise and span-wise distribution of the resultant load, the magnitude of the applied loads, as well as the method of applying those loads on the wing are important steps in the structural test. Here we suppose that the y-axis goes through the central (main) spar. The moment of external load about the y-axis for each wing segment is calculated using the relation:

$$M_{y_{seg}} = -\left(x_s \cdot L_{y_{seg}}\right) + n \cdot g \cdot \left(m_{w_{seg}} \cdot x_{GW} + m_{F_{seg}} \cdot x_{GF}\right) \quad (6.1)$$

Chord-wise position of the resultant load from the main spar is now calculated using:

$$x_{T_{seg}} = \frac{M_{y_{seg}}}{L_{T_{seg}}} = \frac{-\left(x_s \cdot L_{y_{seg}}\right) + n \cdot g \cdot \left(m_{w_{seg}} \cdot x_{GW} + m_{F_{seg}} \cdot x_{GF}\right)}{L_{y_{seg}} - n \cdot g \cdot \left(m_{w_{seg}} + m_{F_{seg}}\right)} \quad (6.2)$$

Here, x_s is the distance of the centre of pressure x_{C_p} from the central spar

$$x_s = x_{s_0} - x_{C_p} = 0.619 - x_{C_p} \quad (6.3)$$

where:

$$x_{C_p} = \left[\left(\frac{x}{c}\right)_{ac} - \frac{C_{MAC}}{C_{LW}} \right] \cdot c \quad (6.4)$$

In the case D (n=6) $C_{LW} = 0.5308$ and $C_{MAC} = -0.0663$, thus the load distribution (lift force minus inertial force) and the moment distribution along the span and chord-wise position of the resultant load from the central spar are given in Table 6.1 (the fuel is not considered):

Table 6.1 Load and moment distribution along the span for case D, n=6 (without fuel)

y (m)	L (N)	W (N)	L-W (N)	M (Nm)
4.90	0	0	0	0
4.87	25.64	23.98	1.66	0.02
4.82	105.14	63.94	41.20	0.81
4.75	276.54	119.90	156.64	7.60
4.66	566.26	191.83	374.43	32.57
4.54	994.12	287.75	706.37	92.67
4.40	1573.89	399.65	1174.24	218.2
4.2	2313.9	527.5	1786.37	446.4
4.1	3217.95	671.42	2546.53	824.73
3.86	4285.91	831.28	3454.63	1406.47
3.64	5514.57	1007.13	4507.44	2249.96
3.4	6898.12	1198.96	5699.16	3411.12
3.15	8428.68	1398.79	7029.89	4972.24
2.88	10096.74	1614.6	8482.14	6987.14
2.6	11891.42	1838.4	10053.02	9515
2.3	13800.82	2078.2	11722.62	12606.06
1.99	15812.15	2325.98	13486.17	16319.11
1.68	17397.77	2573.77	14824.00	20726.77
1.35	19086.23	2837.54	16248.69	25800.87
1.24	21202.3	2925.46	18276.84	27580.02

The load and the moment distribution along the span are given in Figure 6.12 and Figure 6.13.

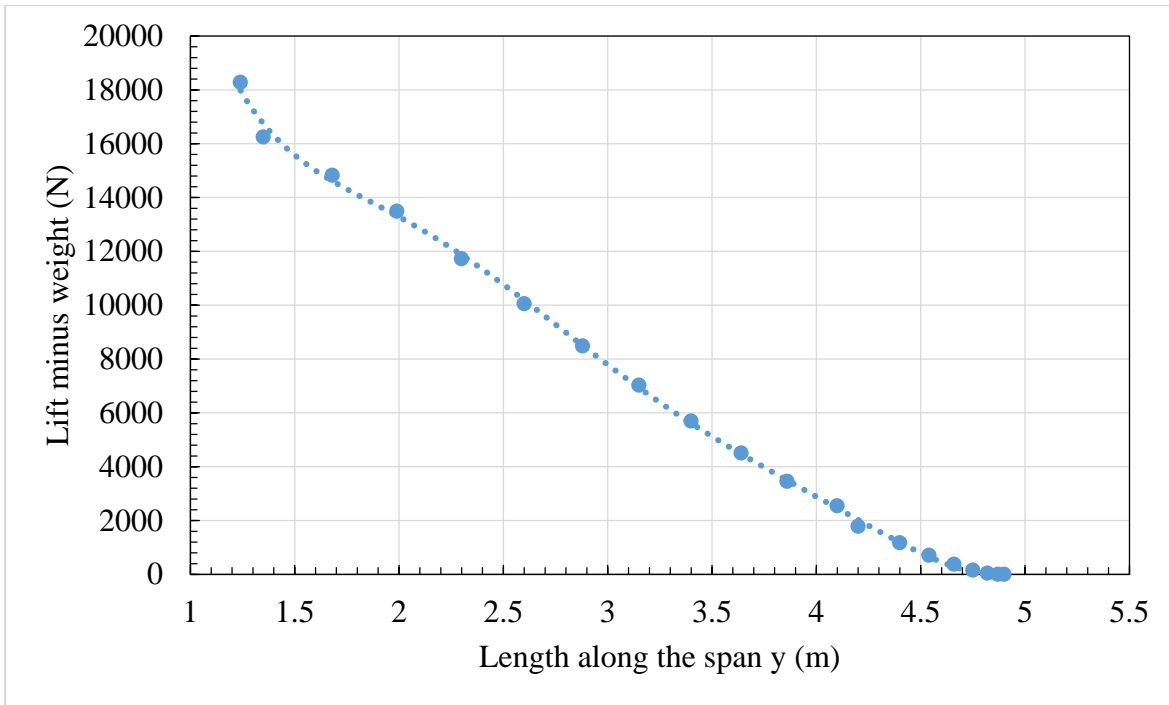


Figure 6.12 Load ($L - W$) distribution along the span

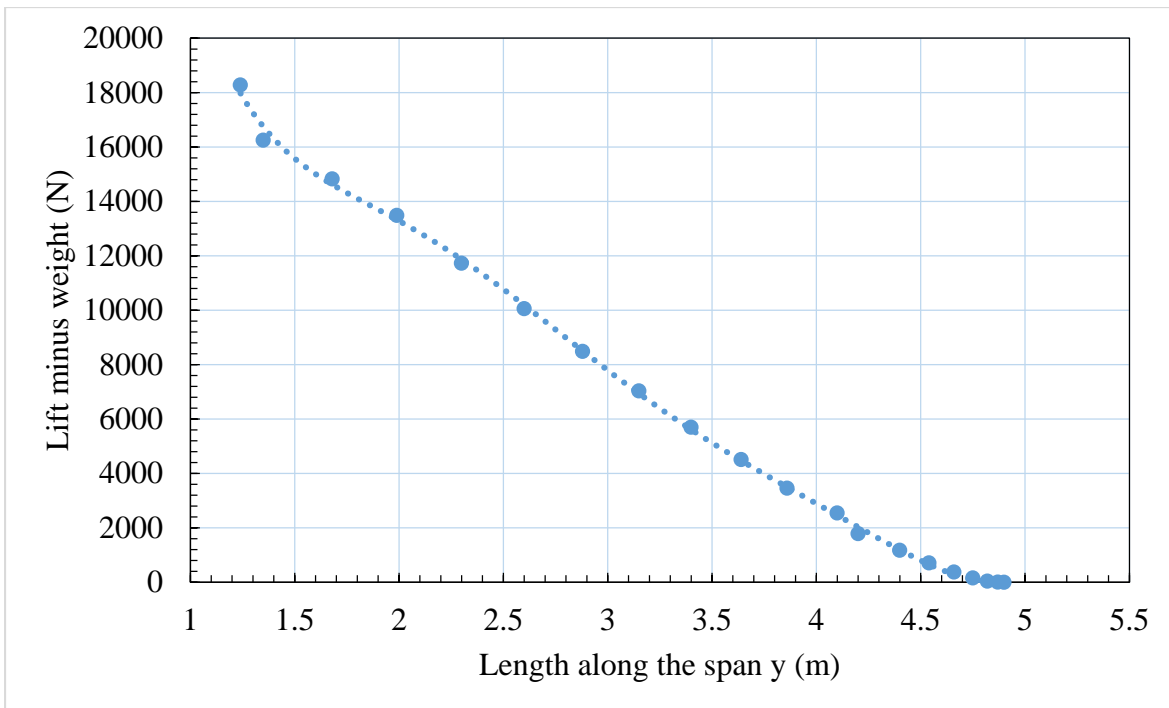


Figure 6.13 Moment distribution along the span

Since the first rib of the wing prototype is at position $y = 4.54 \text{ m}$, and rib number 10 is at position $y = 1.566 \text{ m}$ (measured from the x -axis), values of $L - W$ and M had to be recalculated for the ribs' positions (let us not forget that decision was made to apply loads on the ribs in the experiment). For

that purpose, polynomial interpolation was used, and values calculated at rib positions are given in Table 2. Obtained values fit well to original graphs, as can be seen for moment values at ribs shown in Figure 6.14 Moment calculated at ribs' positions (orange squares) vs moment distribution.

Table 6.2 Calculated loads and moments at ribs.

Rib No.	y (m)	L-W (N)	Moment (Nm)
1	4.54	706.37	92.67
2	4.206	1669.38	482.42
3	3.872	3474.64	1340.09
4	3.535	5033.16	2729.79
5	3.200	6728.67	4651.38
6	2.865	8517.27	7129.60
7	2.543	10312.08	10053.12
8	2.217	12192.68	13570.28
9	1.891	14125.21	17664.78
10	1.566	15433.47	22337.97

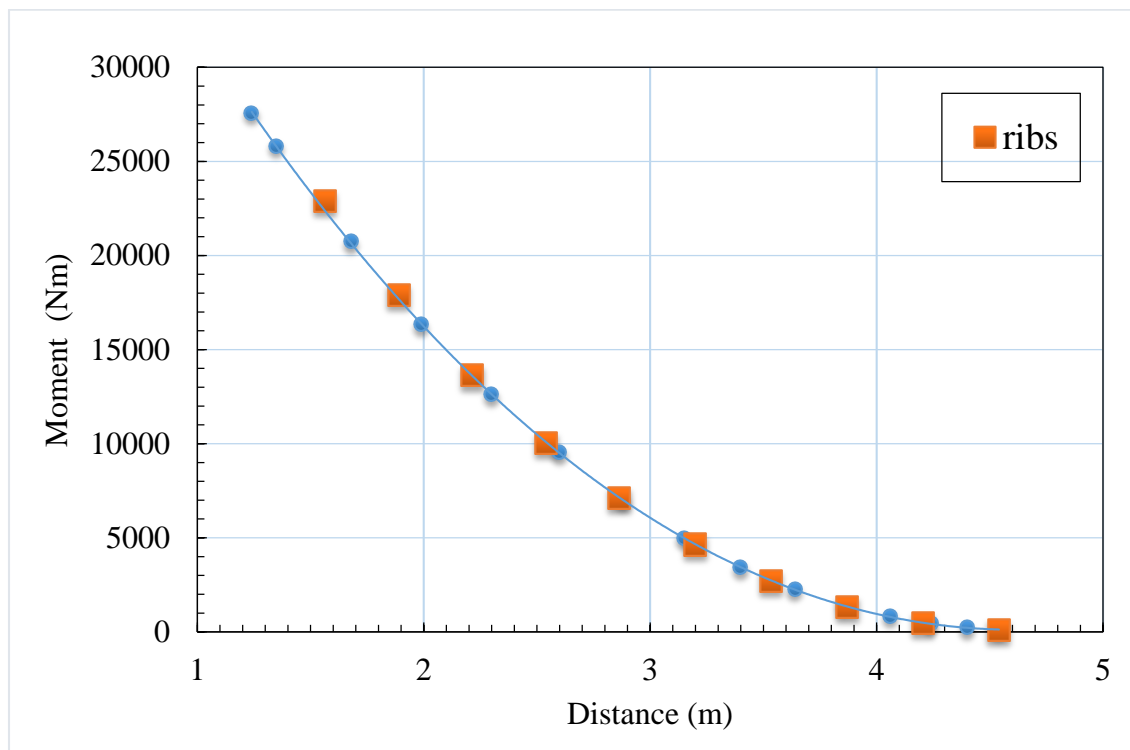


Figure 6.14 Moment calculated at ribs' positions (orange squares) vs moment distribution

As mentioned above, the ribs are supported with wooden pads, and through them, the loads will be applied. To define the lengths of all stirrups and spreaders, as well as their exact positions in whiffle-tree that will provide the application of precise loads on ribs. The static equilibrium equations must be used. Since the whiffle-tree shown in Figure 6.11 is complex for hand calculations, we decided to use the Ms Excel file *Whiffletree.xlsm* available for free download at the website [87]. Figure 6.15 shows the screenshot of the main sheet of the *Whiffletree.xlsm* file. Using the macro integrated into this Excel file, we obtained the whiffle-tree dimensions, forces, and moments shown in Figure 6.16 Forces, moments, and dimensions of the whiffle-tree and Table 6.3.

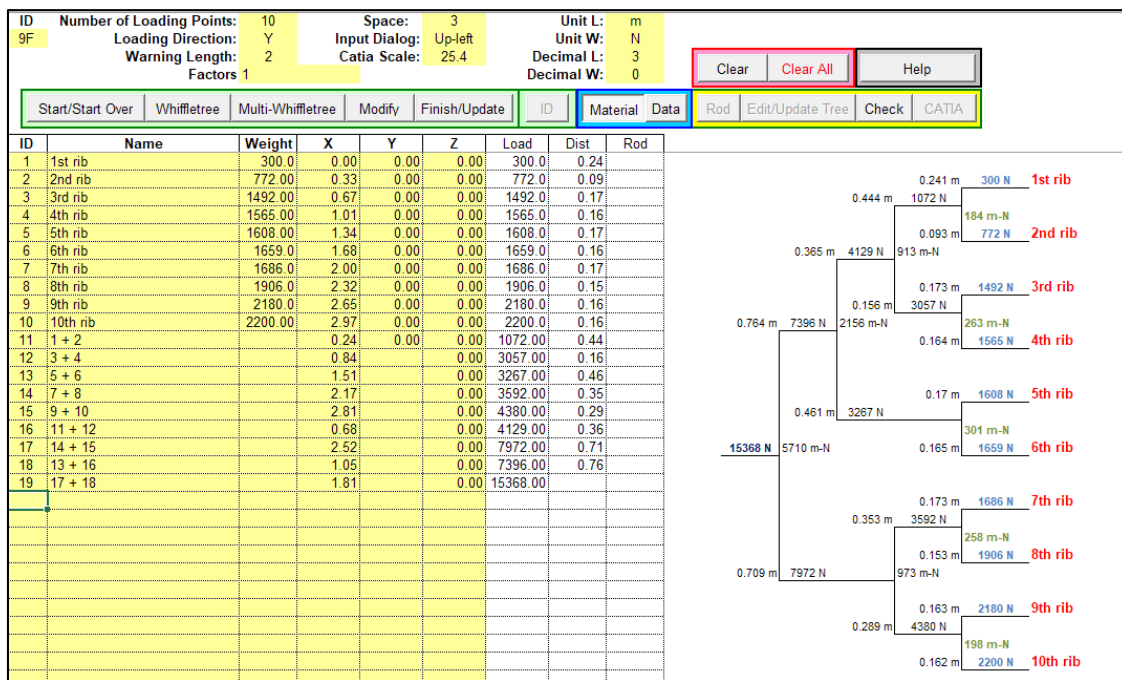


Figure 6.15 Screenshot of MS Excel file used to design the whiffle-tree

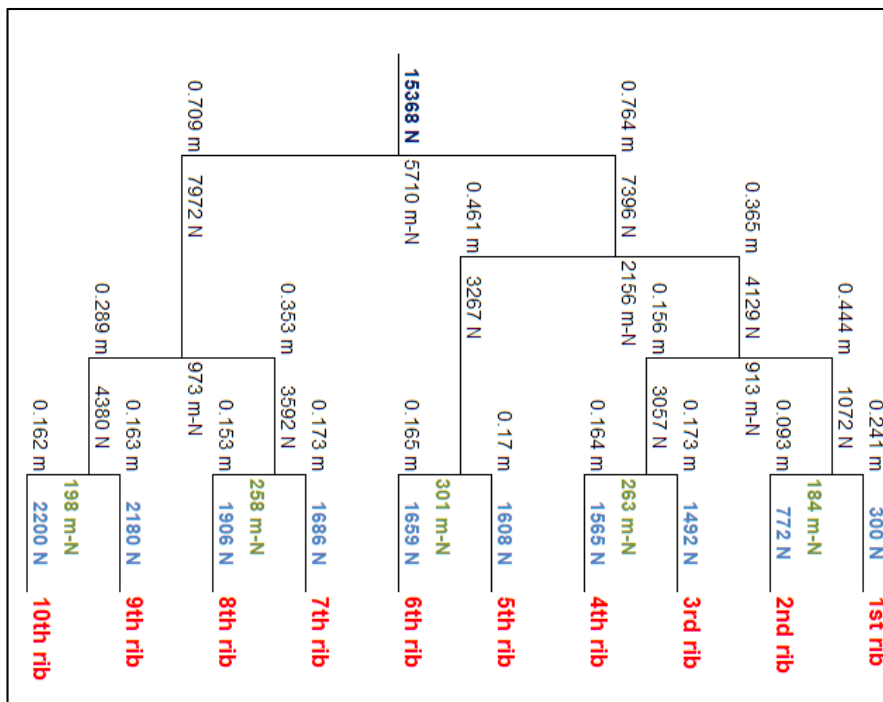


Figure 6.16 Forces, moments, and dimensions of the whiffle-tree

Table 6.3 Force and moment at each rib for the whiffle-tree configuration shown in Figure 6.16
Forces, moments, and dimensions of the whiffle-tree.

Rib No.	y (m)	Force (N)	Moment (Nm)
1	4.54	300	96
2	4.206	772	454.048

3	3.872	1492	1310.424
4	3.535	1565	2701.897
5	3.200	1608	4623.792
6	2.865	1659	7101.452
7	2.543	1686	10025.856
8	2.217	1906	13607.944
9	1.891	2180	17900.712
10	1.566	2200	22895.312
	Total Force (N)	15368	

Comparing the values of moments and forces calculated for the designed whiffle-tree Table 6.3 with values in Table 6.2, it can be seen that the total force of 15368 N that will be introduced by a hydraulic jack is very close to the calculated value of force at tenth rib 15433.47 N (the eleventh rib is at the position of support,

Figure 6.17. At the same time, moment 22895.312 Nm at tenth rib (Table 6.3) is somehow greater than moment 22337.97 Nm (see

Table 6.2 Calculated loads and moments at ribs), but the difference is about 2.5 %. This was considered acceptable, and the design of the whiffle-tree shown in Figure 6.16 was adopted. After that, the test assembly was completed with the manufactured whiffle-tree shown in Figure 6.18 and Figure 6.19.



Figure 6.17 Whiffle-tree is not introducing the force on the 11th rib



Figure 6.18 Test assembly for the light aerobatic aircraft wing



Figure 6.19 Test assembly for the light aerobatic aircraft wing (view from the other side)

6.3 Wing test loading and obtained displacements at the wing tip

European Aviation Safety Agency’s specifications for light aerobatic aircraft define two types of loading that must be applied to the wing structure during testing:

- *Loading No 1*: Load must rise up to the limit load (6g) in steps, adding 10% of the load in each step, with a pause of 3 s between steps. Once a 6g load is achieved, slow unloading is conducted.
- *Loading No 2*: A destructive test is carried out with loading rise until the limit load (6g) as described above, and after that, the incremental increase of load is applied until wing failure.

Following these instructions, the load introduced by the hydraulic jack was incrementally increased during the test until the maximum force of 15787 N (as measured by force transducer) was achieved (see Table 6.4 Values of forces and displacements measured at 10 wing locations). Since the force was introduced in too many steps, in Table 6.4 only 15 steps of loading (and unloading) are presented.

Table 6.4 Values of forces and displacements measured at 10 wing locations

F	W1	W2	W3	W4	W5	W6	W7	W8	W9	W10
kN	mm									
-0.048	-0.215	-0.171	-0.11	-0.069	-0.029	-0.099	-0.146	-0.099	-0.056	-0.029
3.557	47.38	38.797	26.707	18.196	8.799	24.861	40.916	27.885	18.841	9.966
7.002	70.564	57.771	39.625	26.77	12.937	36.447	59.901	39.882	26.561	13.731
10.493	90.557	74.108	50.65	34.116	16.471	46.088	75.19	49.483	32.728	16.598
12.272	102.06	83.564	57.035	38.484	18.557	51.637	84.046	55.133	36.335	18.314
14.027	118.25	97.127	66.243	44.802	21.535	60.087	98.041	64.002	42.056	21.239
14.921	125.65	103.31	70.395	47.629	22.892	63.560	103.45	67.74	44.554	22.44
15.787	133.43	109.72	74.747	50.652	24.371	67.382	109.27	71.828	47.308	23.753
12.426	131.16	108.11	74.025	50.475	24.449	67.149	109.67	72.567	48.357	24.718
10.483	122.32	100.87	69.269	47.269	22.937	63.208	103.63	68.582	45.853	23.643
7.522	108.07	89.027	61.425	41.958	20.413	56.470	93.409	61.964	41.671	21.782
6.796	104.46	86.054	59.453	40.617	19.771	54.769	90.797	60.306	40.596	21.302
3.492	85.181	70.316	48.913	33.477	16.316	45.461	76.085	50.931	34.621	18.505
-0.009	44.319	36.588	25.535	17.693	8.65	23.741	39.371	27.574	19.228	10.45
-0.617	26.958	22.245	15.677	10.979	5.364	14.758	24.801	17.279	12.12	6.792

Table 6.4 Values of forces and displacements measured at 10 wing locations shows displacements measured by 10 strain gauges on the wing for each applied force and processed by Catman software. Since the deformation at the wing tip for case D was numerically evaluated and presented in the previous chapter, we will extract results from two sensors S10 and S11, positioned at the wingtip (one was on the upper surface of the wing, the other on the lower). Values collected from the sensor S10 are represented in column W2 of Table 4, while values from the sensor S11 are represented in column W7 of Table 6.4. Extracted values are shown in Table 6.5, while Figure 6.20 shows changes of displacement with the change of force, as measured by sensors S10 and S11.

Table 6.5 Values of forces and displacement measured by sensors S10 and S11

F	S10	S11
<i>kN</i>	<i>mm</i>	<i>mm</i>
-0.048	-0.171	-0.146
3.557	38.797	40.916
7.002	57.771	59.901
10.493	74.108	75.19
12.272	83.564	84.046
14.027	97.127	98.041
14.921	103.311	103.456
15.787	109.723	109.271
12.426	108.112	109.679
10.483	100.874	103.636
7.522	89.027	93.409
6.796	86.054	90.797
3.492	70.316	76.085
-0.009	36.588	39.371
-0.617	22.245	24.801

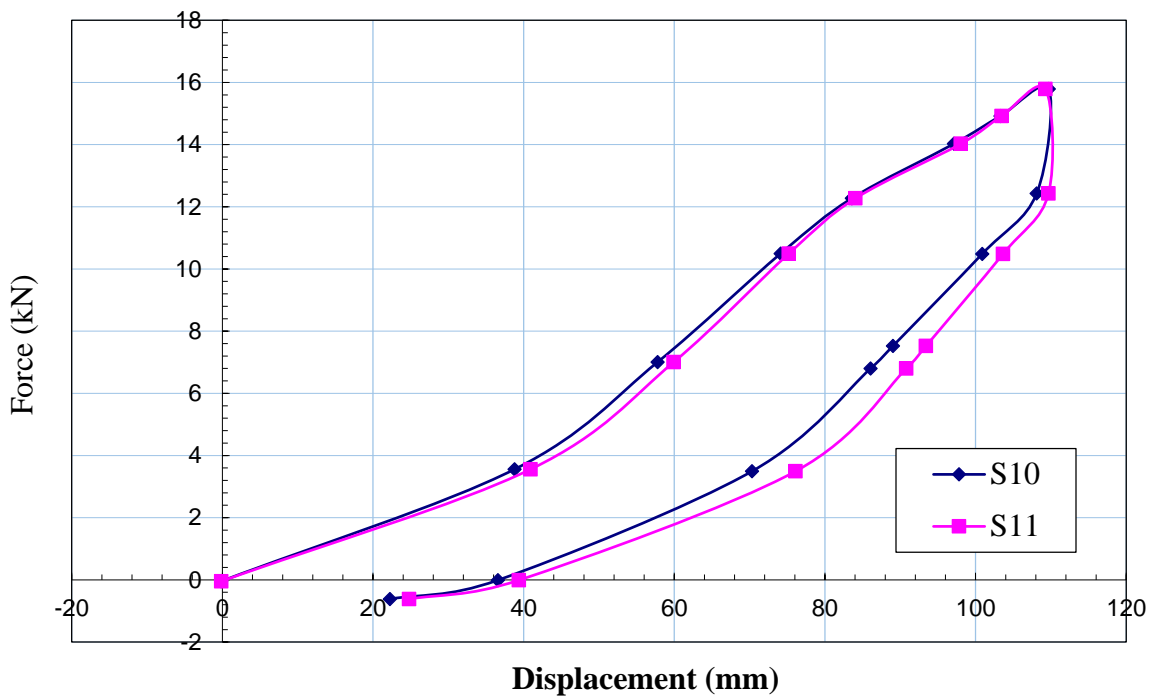


Figure 6.20 Graph of displacements at the wingtip

The test showed a good correspondence of the force-displacement curve until the limit load.

CHAPTER 7
OPTIMIZATION of THE WING-FUSELAGE
ATTACHMENT LUG

7 OPTIMIZATION of THE WING-FUSELAGE ATTACHMENT LUG

In the previous chapter, it has been established that under the specified load, the initial crack in the attachment lug is propagating rather quickly, so in this chapter, the focus will be on the optimization of the attachment lug's geometry. To be more specific, the effect of the crucial geometrical parameters on the crack's growth rate will be analyzed. Also, an improved geometry that is more fatigue resistant will be suggested. It has to be noted that one of the easiest ways to extend the fatigue life is the selection of the material, in this case, steel that is more fatigue resistant. But, the wing-fuselage attachment assembly made of this kind of steel would significantly increase the costs of the design and the production of the aircraft. So, it was decided that the material of the attachment lug remain the same, while its geometry will be redesigned.

The initial geometry dimensions of the attachment lug, needed for the optimization, are given in the previous chapter. The new finite element mesh was generated (Figure 7.1), with an average element mesh size of 1.7mm. This average element mesh size will be used throughout the optimization to avoid the influence of the mesh density on the optimization results (the number of cycles to catastrophic failure). All other input parameters (boundary conditions, load value and material) are identical to those used in the previous chapter. The SIFs values after the first crack propagation step are shown in Figure 7.2, where it can be seen that $K_{I\ max} = 1880.0\ MPa\sqrt{mm}$, and also that the most values of K_I along the crack front are between 1850 and $1880.0\ MPa\sqrt{mm}$. However, mentioned maximum value of $K_{I\ max}$ will be used afterward as the main optimization criterion, i.e. the goal is to achieve that the $K_{I\ max}$ after first propagation step be reduced under prescribed value ($K_{I\ max} < 1400\ MPa\sqrt{mm}$), if possible.

The SIF values just before the fracture of the attachment lug are shown in Figure 7.3, where it can be seen that the crack has grown for an additional 7.37 mm, regarding its initial size. In Figure 7.4, the diagram of the crack growth as a function of the number of cycles is presented. The maximum number of cycles $N_{\max}=515$ (calculated for $R=-1$, as before) is slightly higher than the one obtained in the previous chapter. The reason for this is that with every new calculation, the software generates a new finite element mesh around the crack front, so some results discrepancies will always be present. In any case, the results obtained here will be used for comparison with the values that will be obtained after attachment lug geometry's optimization. The initial mass of the attachment lug is 87 grams.

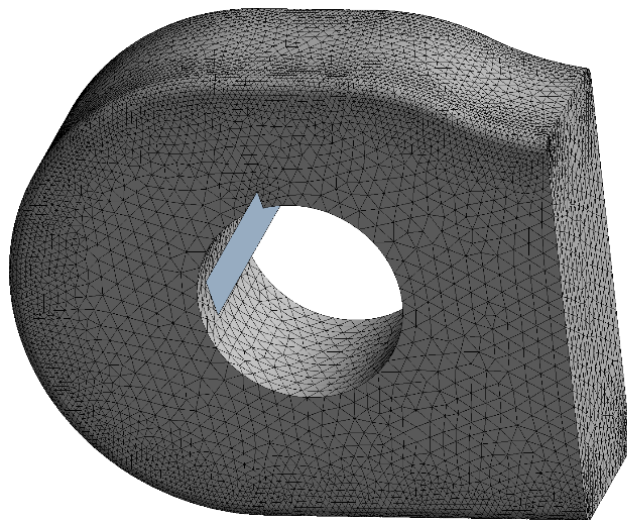


Figure 7.1 Finite element mesh used in optimization

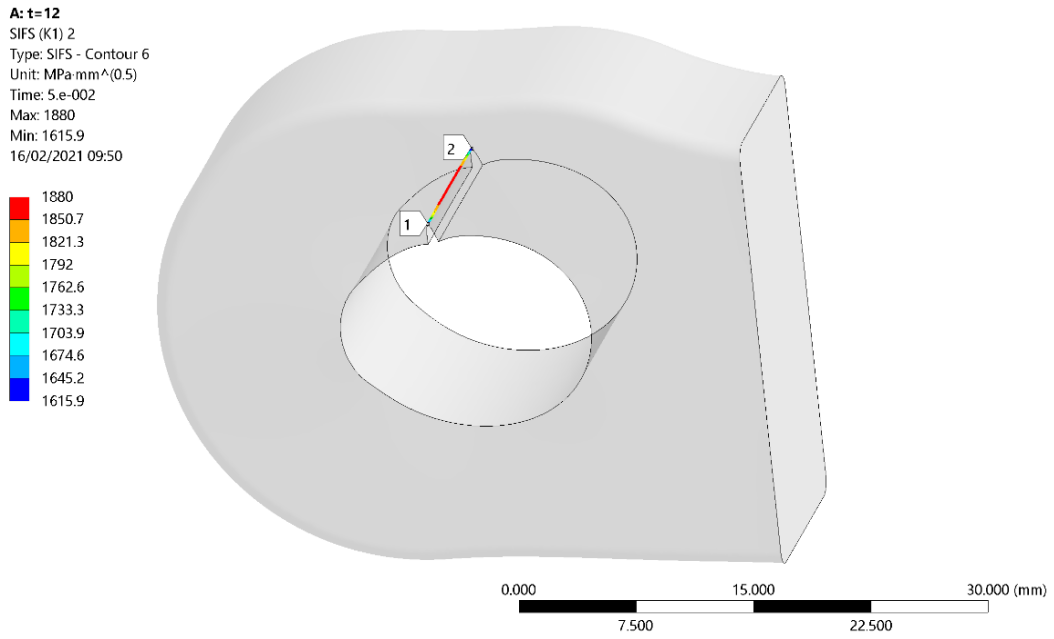


Figure 7.2 SIF values along crack front after 1st step of propagation (original lug)

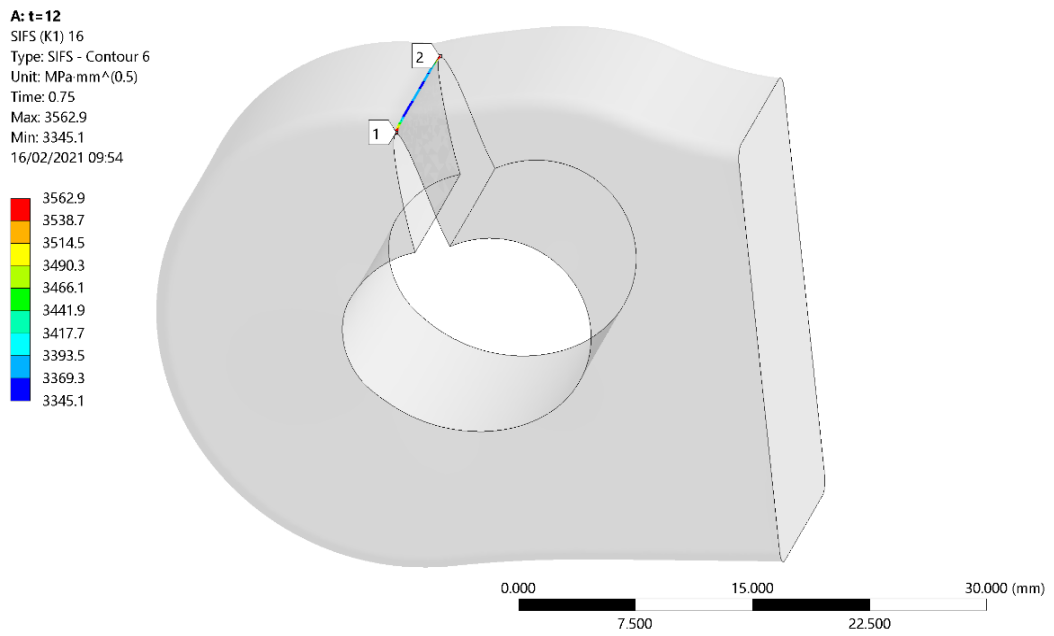


Figure 7.3 SIF values after 15th step of propagation (total crack extension 7.37 mm)

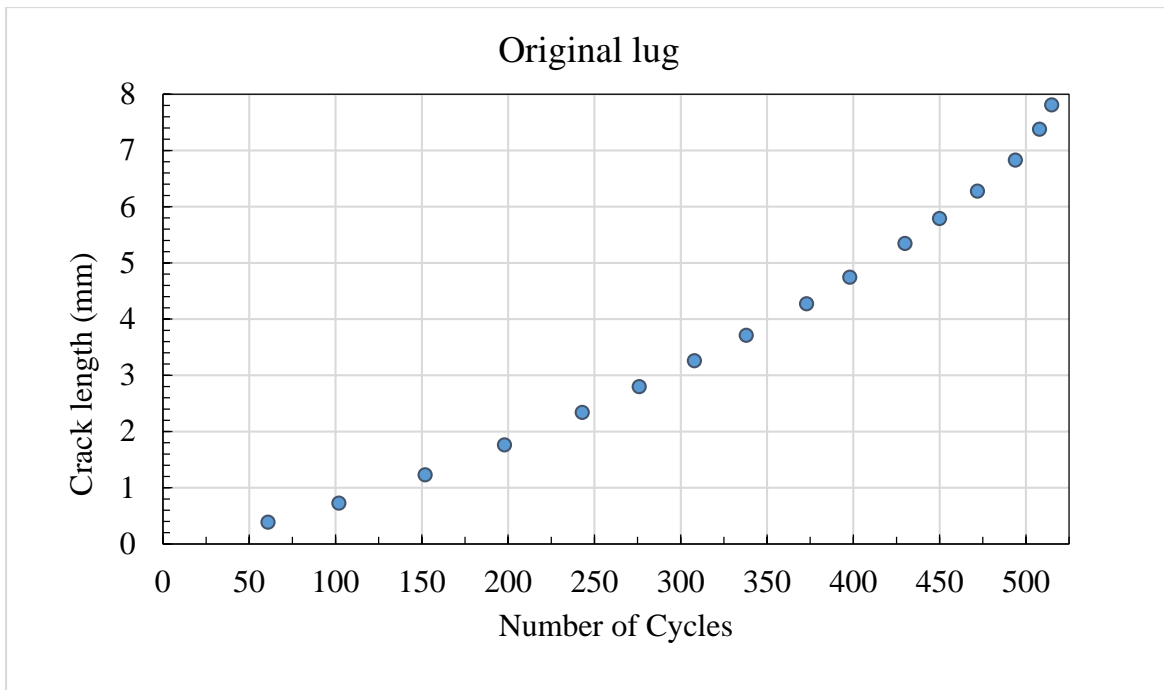


Figure 7.4 Crack length vs Number of cycles for original lug ($N_{max}=515$)

7.1 Model number 1: Original lug with increased thickness

It is known that the fatigue life of any supporting structure will be longer if its thickness is increased. This is why it was decided to first analyse the effect of the lug thickness increase without the change of other geometrical parameters. It can be seen in Figure 7.5 that the lug thickness was changing by adding the material in the normal direction to the coloured surface. This adding was conducted in steps of 1.25mm. For all newly obtained thicknesses the $K_{I_{max}}$ was calculated and for the $t=17\text{mm}$ (see Table 7.1) the $K_{I_{max}}$ was lower than $1400 \text{ MPa}\sqrt{\text{mm}}$ for the first time. The mass of the luge with this thickness value is 123 grams, which represents an increase of 41.3%.

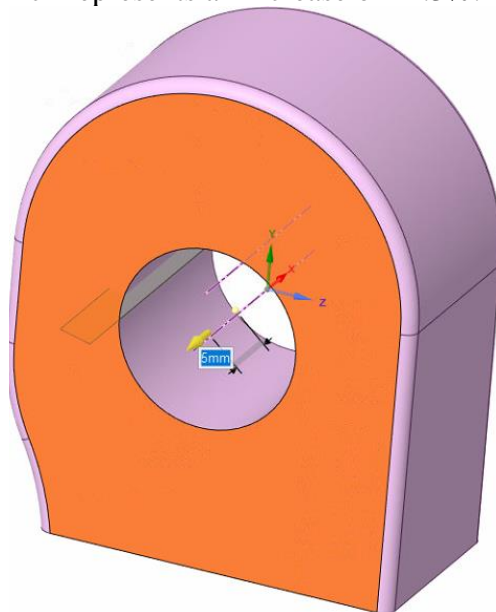


Figure 7.5 Thickness of lug was varied by adding material perpendicularly to the highlighted face

Table 7.1 Values of maximum SIFs after crack opening for different thicknesses

Added thickness (mm)	Total thickness (mm)	$K_{I\ max}$ (MPa mm ^{0.5})
0	12.00	1880.0
1.25	13.25	1789.6
2.50	14.50	1631.8
3.75	15.75	1499.5
5.00	17.00	1391.2

After the first propagation step and the step just before the fracture of the attachment lug with a thickness of 17mm, the SIF values are shown in

Figure 7.6 and Figure 7.7. It is noticeable that the start and the end values of $K_{I\ max}$ are significantly lower than the $K_{I\ max}$ for the attachment lug with the initial thickness of 12mm, but at the price of the significant increase in its mass. The change of $K_{I\ max}$ in function of lug's thickness is represented in Figure 7.8. In Figure 7.9, the diagram of the crack growth as a function of the number of applied load cycles for R=-1 is presented.

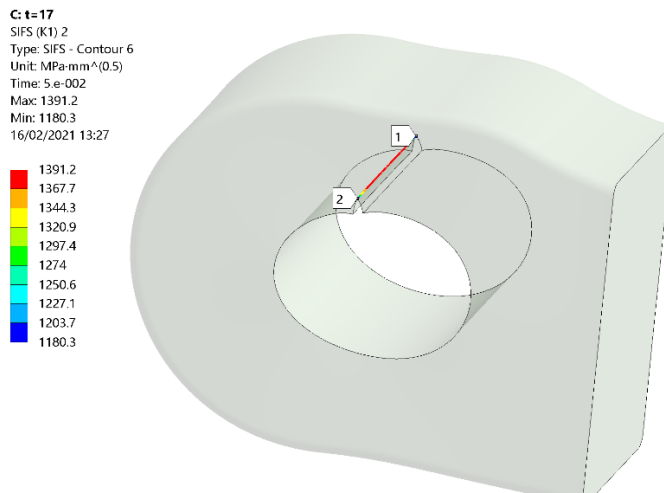


Figure 7.6 Stress intensity factor (SIF) values along crack front after 1st step of propagation

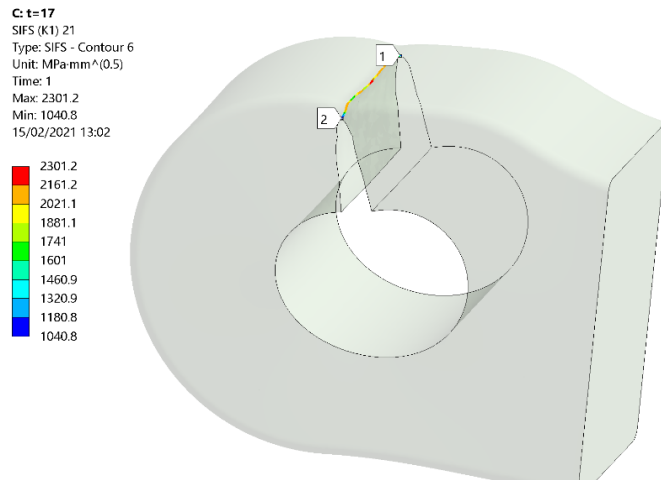


Figure 7.7 SIF values after 20th step of propagation (total crack extension 6.84 mm)

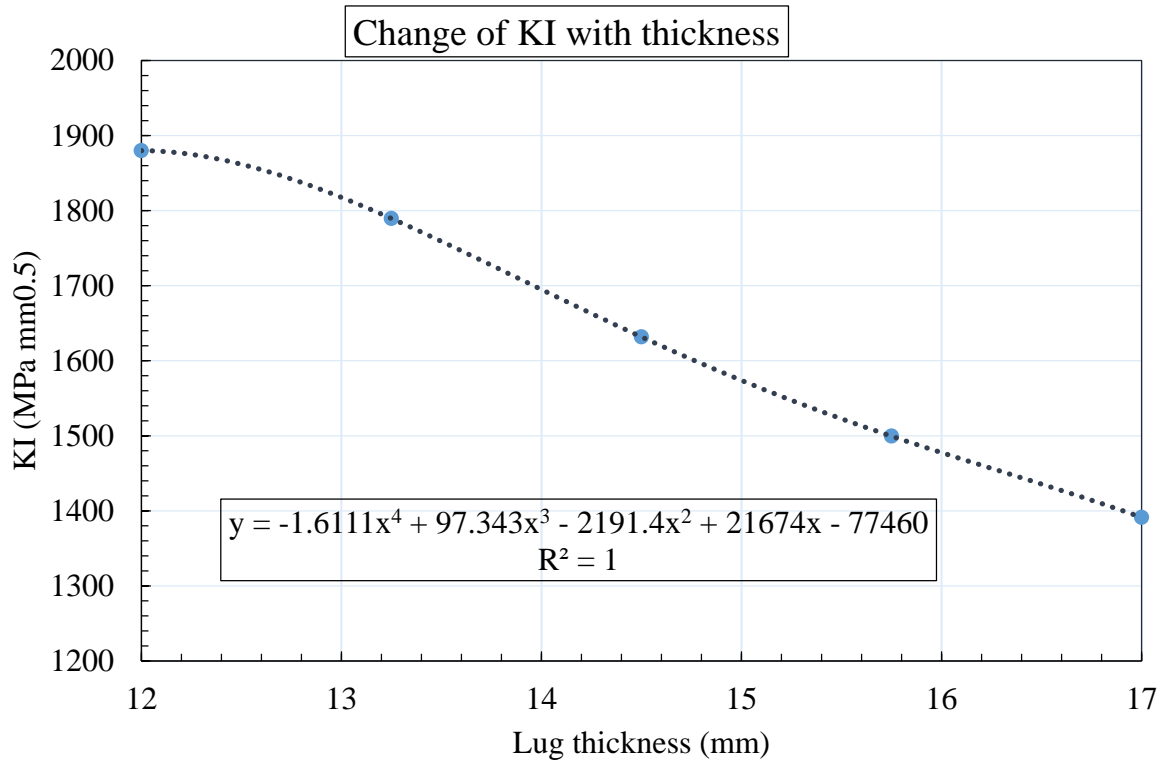


Figure 7.8 Maximum K_I after crack opening for different lug thicknesses

The determination coefficient of the trend line $r^2 = 1$, is presented in Figure 7.8 Maximum K_I after crack opening for different lug thicknesses Fig. 8. Its equation is:

$$K_{I \max} = -1.6111t^4 + 97.343t^3 - 2191.4t^2 + 21674t - 77460 \quad (7.1)$$

With this equation, the value of $K_{I \max}$ for a given value of thickness in mm can be calculated with high accuracy. However, with thickness increase, the mass of the lug is increasing too, so it was decided to keep the lug's thickness value of 17mm, because this thickness provides the double fatigue life, regarding the initial lug's thickness (compare Figure 7.4 and Figure 7.9).

Since the relation between lug's thickness and the $K_{I \max}$ value at the beginning of crack propagation is established, and since it is almost certain that the thickness has the dominating influence on the lug's fatigue life, it was logical to assume that with the variation of other geometrical parameters, the lug's fatigue life can be increased to be higher than initial 515 cycles, while decreasing the mass of 123 grams (obtained for thickness of 17mm).

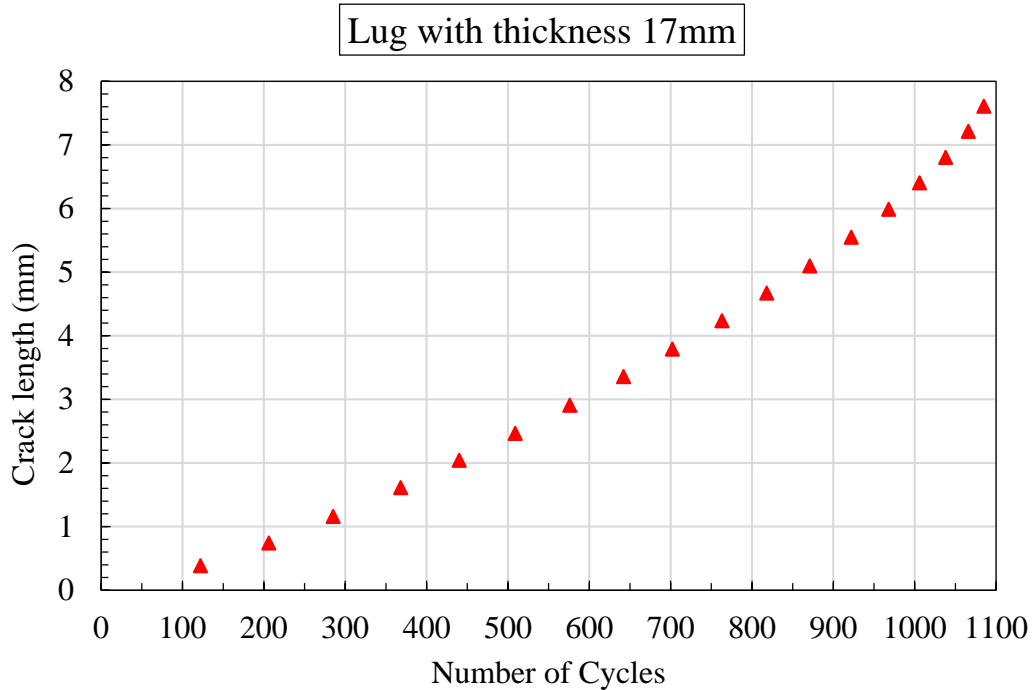


Figure 7.9 Crack length vs Number of cycles for lug with thickness 17mm ($N_{max}=1085$)

7.2 Model number 2: Two-parameter optimization of lug

It was decided to conduct optimization with two input optimization parameters: the lug's thickness and the rounding radius (highlighted surfaces in Figure 7.10). In the *Design Exploration* module of *Ansys Workbench*, the total number of $3^2 = 9$ combinations of thickness values and rounding radii were generated and the $K_{I\ max}$ value for first crack propagation step was calculated by finite element method for each combination (Figure 7.11).

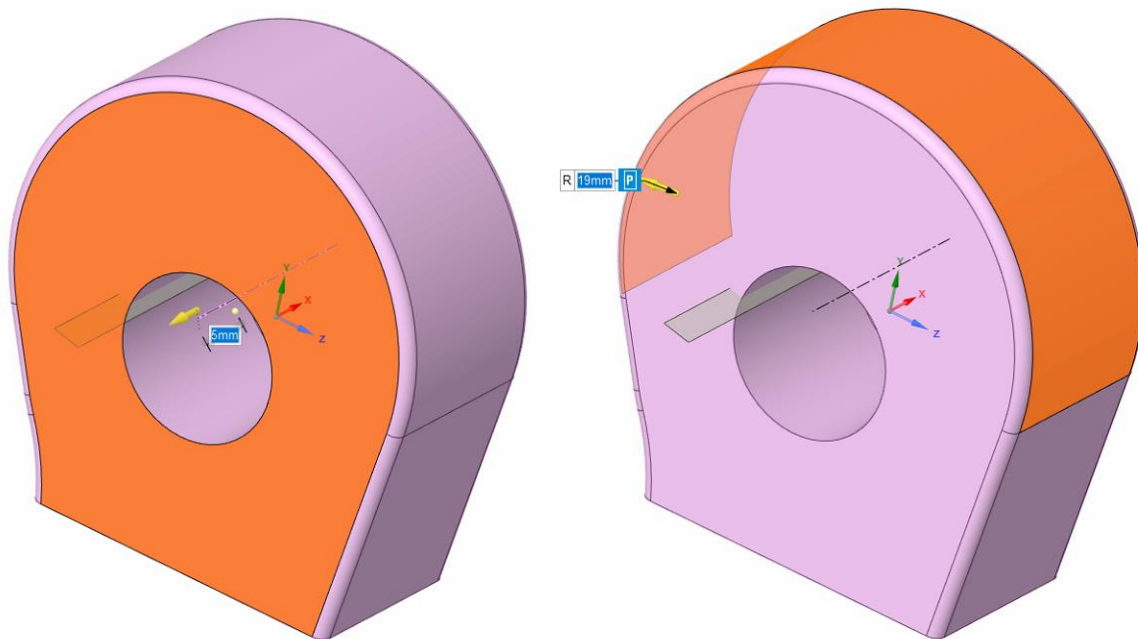


Figure 7.10 Thickness of lug was varied along with the radius of the surface (highlighted)

Table of Outline A2: Design Points of Design of Experiments					
	A	B	C	D	E
1	Name	P3 - radius (mm)	P5 - thickness (mm)	P4 - SIFS (K1) Maximum (MPa mm ^{0.5})	P6 - SYS-3\PartBody Mass (kg)
2	1	14.5	0	2119.8	0.078385
3	2	10	0	2844.3	0.058793
4	3	19	0	1785.7	0.10789
5	4	14.5	-5	3648.5	0.045599
6	5	14.5	5	1479.5	0.11117
7	6	10	-5	4947.2	0.034186
8	7	19	-5	3059.4	0.06279
9	8	10	5	1989.4	0.083401
10	9 DP 2	19	5	1250	0.15299

Figure 7.11 Maximum K_I (column D) and lug mass (column E) after crack opening

The table presented in Figure 7.11 shows that the decrease of the lug's thickness (the values of -5 in the C column) gives a very high $K_{I\max}$ values, while, only with the increase of rounding radius (B column) the significant decrease in $K_{I\max}$ values occurs. The lug's mass in the E column varies from 58 grams to 153 grams, and the only combination of $r = 19\text{mm}$ and $t = 17\text{mm}$ gives $K_{I\max}$ values lower than $1400\text{MPa}\sqrt{\text{mm}}$ (to be more specific $K_{I\max} = 1250\text{MPa}\sqrt{\text{mm}}$). (It has to be mentioned that the software generates only manufacturable values, i.e. the accuracy of only one decimal place was required.) The previous statement is illustrated in Figure 7.12, as it is clearly seen that only an increase of thickness and radius leads to a decrease of $K_{I\max}$.

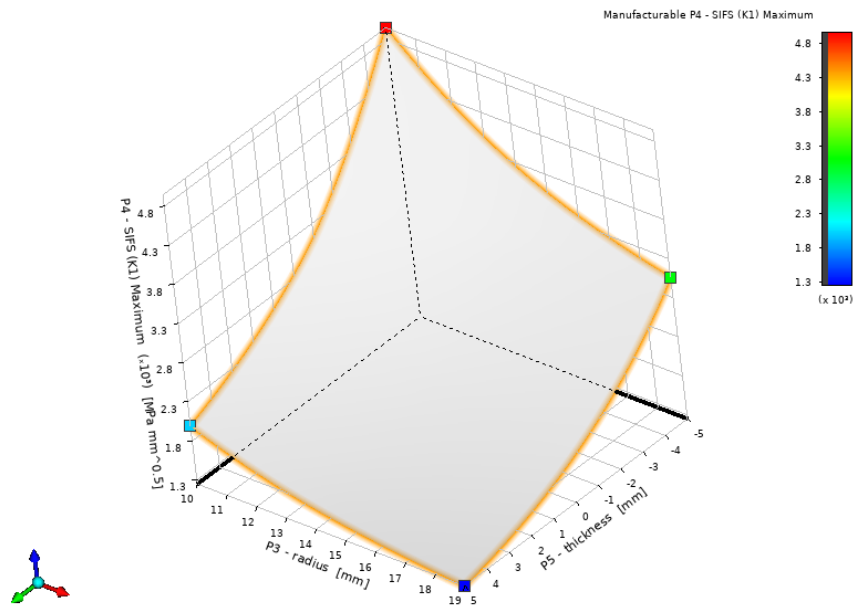


Figure 7.12 Response surface for different thicknesses and radii of lug

The SIF values along the crack front for lug's thickness of 17mm and rounding radius of 19mm are presented in Figure 7.13. The maximum value of $1256.8\text{MPa}\sqrt{\text{mm}}$ is slightly higher than one in the table in Figure 7.11 because of the earlier mentioned reason (different node numbers in mesh around the crack front in two computations with the same geometry), but it is convincingly the minimum $K_{I\max}$ value, regarding two previous lug models. The lug's mass, however, is significantly increased for 75.8%

(from 87 grams to 153 grams), so it became obvious that additional parameters should be included in the optimization in order to achieve mass reduction and fatigue life prolongation.

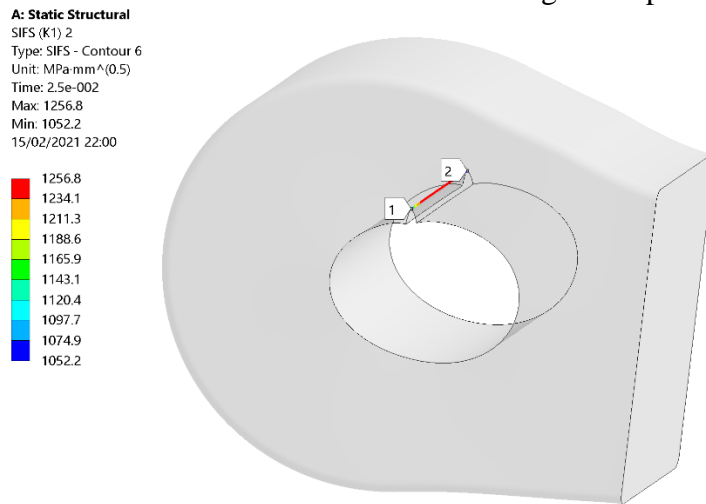


Figure 7.13 SIF values along crack front after 1st step of propagation

The SIF values when a crack reaches the extension of 6.75mm are shown in Figure 7.14, in which is also visible that there is still a lot of space for its further growth, unlike in two previous lug's geometries where after reaching approximately 7mm, in the very next step complete fracture of the lug occurred. This was possible thanks to the increased rounding radius, which provides additional space for crack growth, and the fatigue life prolongation, accordingly. By comparing the $K_{I\ max}$ values in Figure 7.14 with values in Figure 7.7 and Figure 7.3, it can be seen that this value is minimal for the case presented in Figure 7.14. With further crack growth the crack gains appearance displayed in Figure 7.15, just before the fracture. In Figure 7.16, the diagram of the crack growth as a function of the number of cycles to complete fracture for R=-1, is presented, with the highest fatigue life obtained in this analysis: $N_{max}=1933$.

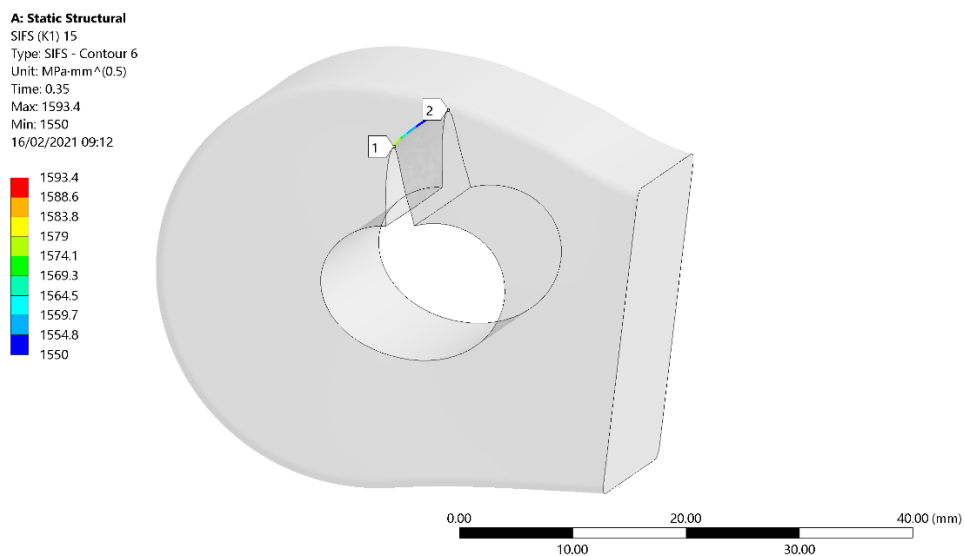


Figure 7.14 SIF values after 14th step of propagation (total crack extension 6.75 mm)

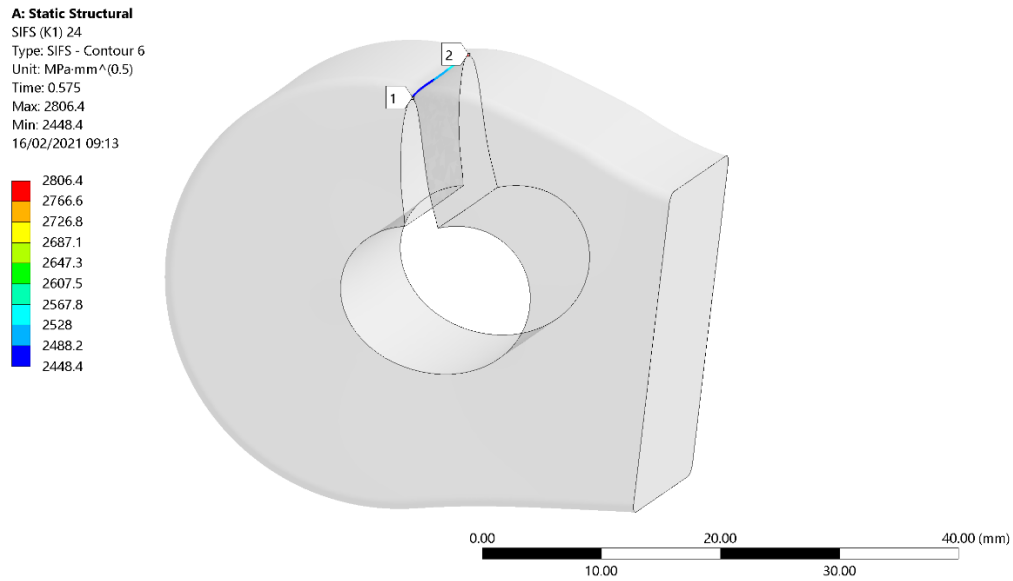


Figure 7.15 SIF values after 23rd step of propagation (total crack extension 10.89 mm)

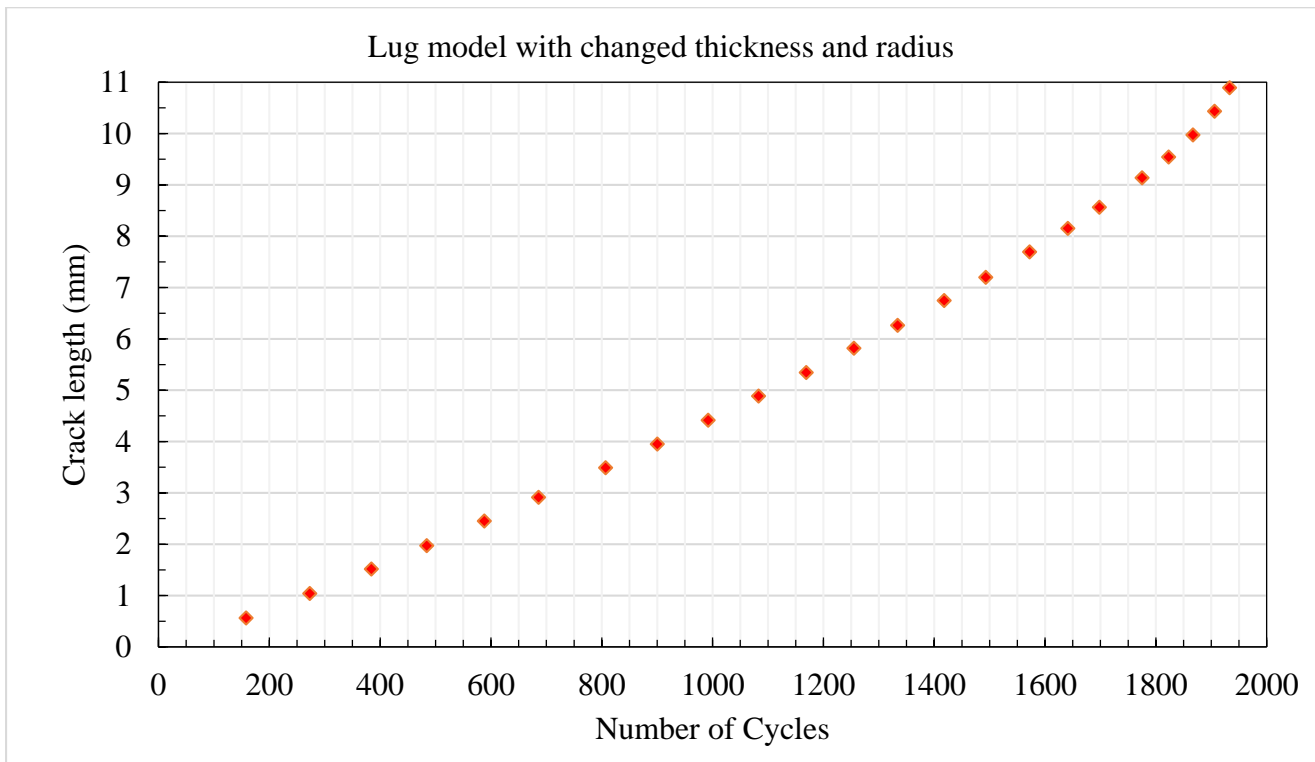


Figure 7.16 Crack length vs Number of cycles for lug with $t=17\text{mm}$ and $r=19\text{mm}$ ($N_{\text{max}}=1933$)

7.3 Model number 3: Three-parameter optimization of lug

Optimization model 3 had three geometrical input optimization parameters: the lug's thickness (Figure 7.17), the rounding radius and the radius of a pin hole (Figure 7.18). Besides them, one “non-geometrical” input parameter was also selected: the initial position of the crack with respect to the surface

of the pin hole (Figure 7.19). This was necessary because in this case, with geometrical parameters varying, the size of the pin hole is changing, too. So, in order to keep the same initial size of the crack, the crack edge in the shape of the rectangle has to be “attached” to the newly generated pin hole surface (Figure 7.19).

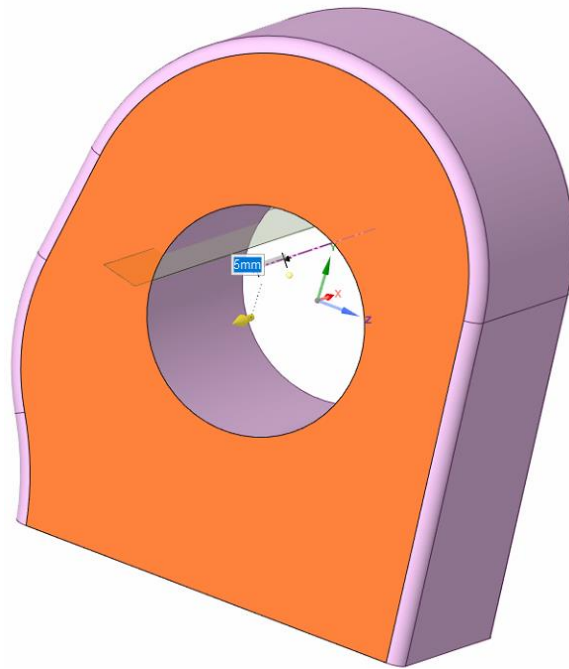


Figure 7.17 Thickness was varied by adding/removing material perpendicularly to the highlighted face

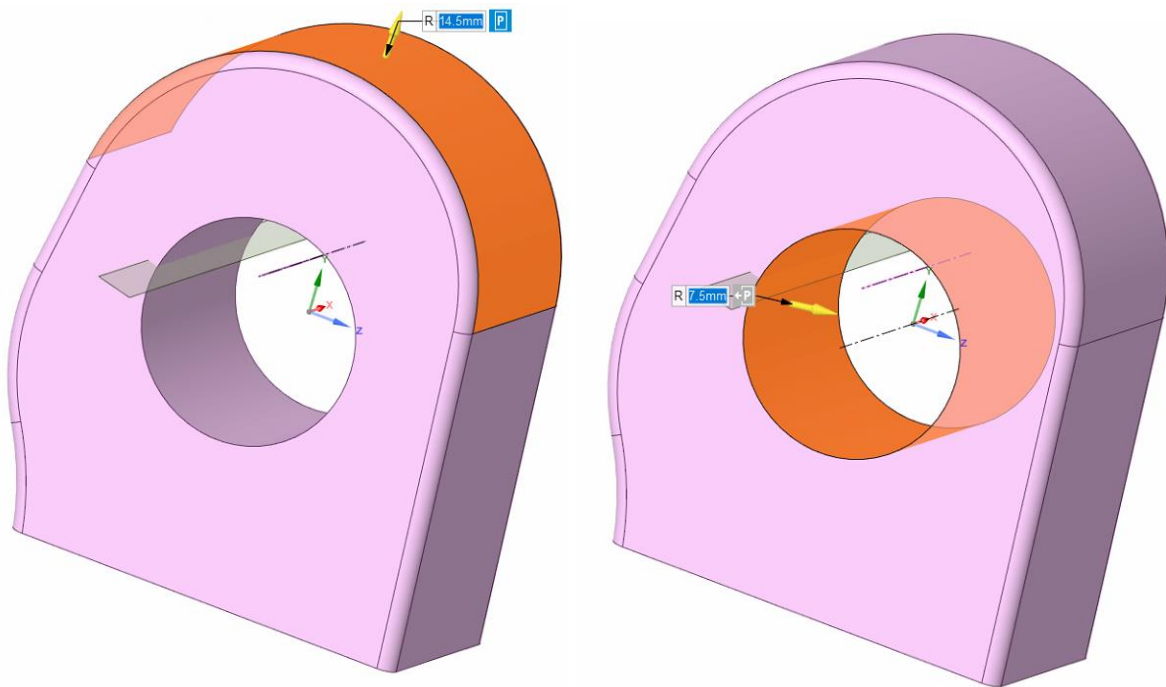


Figure 7.18 Radii of highlighted surfaces were varied

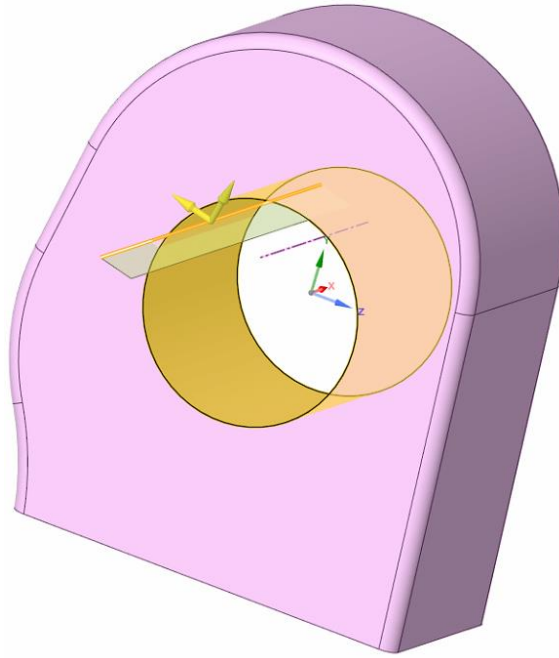


Figure 7.19 Initial crack position was kept constant with respect to the yellow surface

In the *Design Exploration* module of *Ansys Workbench*, the total number of $3^3 = 27$ combinations of thickness values and two radii were generated and the $K_{I\ max}$ value for the first crack propagation step, was calculated by finite element method for each combination (Figure 7.20). Some of those combinations gave very high $K_{I\ max}$ values or mass values, so they were eliminated from further calculations. In the end the number of the combinations, i.e. Design points (DP) was diminished to 14. As a representative combination DP 27 was selected (Figure 7.20), because this combination gave the $K_{I\ max} = 1267.6\ MPa\sqrt{mm}$ in the first step of crack propagation (Figure 7.21) and the lug's mass of 108 grams.

Table of Design Points					
	A	B	C	D	E
1	Name	P3 - radius	P5 - thickness	P7 - radius 2	P8 - Parameter 1
2	Units	mm	mm	mm	
3	DP 1	16.94	1.82	7	0
4	DP 2	19	5	7	0
5	DP 6	11.331	-3.521	9.2605	0.01479
6	DP 7	11.331	-3.521	9.2605	0.08521
7	DP 10	17.669	-3.521	9.2605	0.01479
8	DP 11	17.669	-3.521	9.2605	0.08521
9	DP 13	14.5	0	5	0.05
10	DP 17	14.5	0	10	0.05
11	DP 21	11.331	3.521	9.2605	0.01479
12	DP 22	11.331	3.521	9.2605	0.08521
13	DP 25	17.669	3.521	9.2605	0.01479
14	DP 26	17.669	3.521	9.2605	0.08521
15	DP 27	14.5	5	7.5	0.05
16	DP 28 (Current)	19	0	7.5	0.05
*					

Figure 7.20 Generated design points with selected parameters ($r_1=14.5\text{mm}$, $r_2=7.5\text{mm}$, $t=17\text{mm}$)

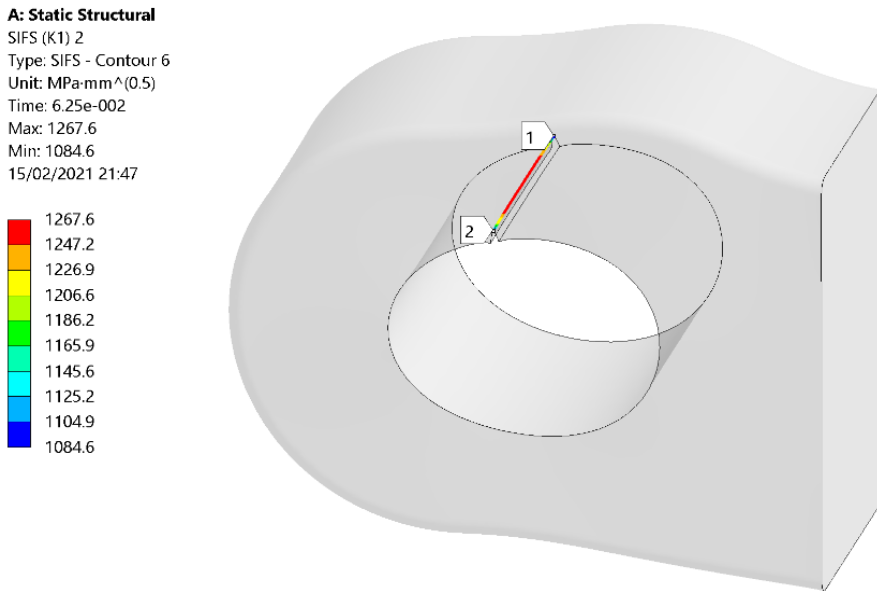


Figure 7.21 SIF values along crack front after 1st step of propagation

Although the first value of $K_{I\ max}$ was promising that the fatigue life of model 3 would be comparable to the fatigue life obtained for model 2 (because the difference of the start values of $K_{I\ max}$ was almost negligible), the crack under the applied load grew relatively fast and reached maximum extension (Figure 7.22) after $N_{\max}=786$ load cycles for $R=-1$ (Figure 7.23). It was obvious that the lack of the growth space (which existed in model 2), disabled the prolongation of fatigue life to at least 1000 cycles, but compared to the initial shape of the lug, model 3 has for 52,6% longer fatigue life, while the mass is increased for 24.1%.

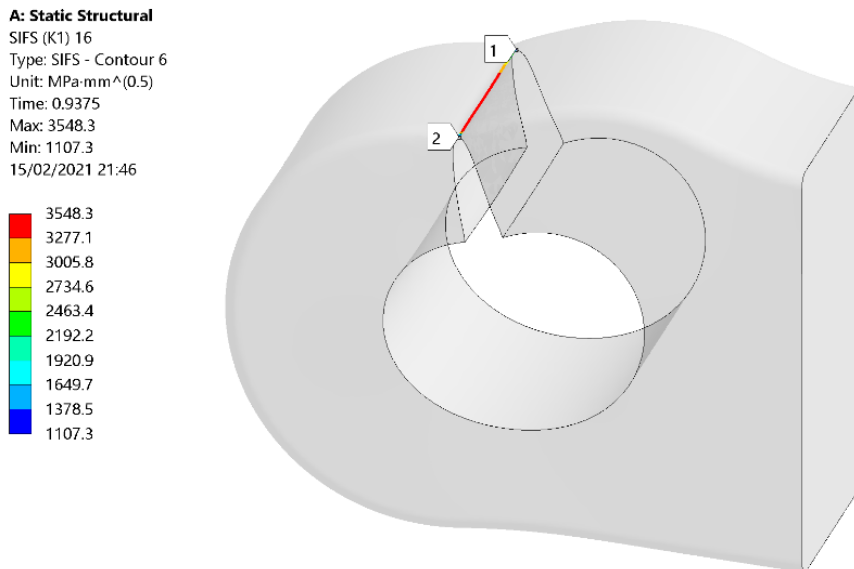


Figure 7.22 SIF values after 15th step of propagation (total crack extension 7.03 mm)

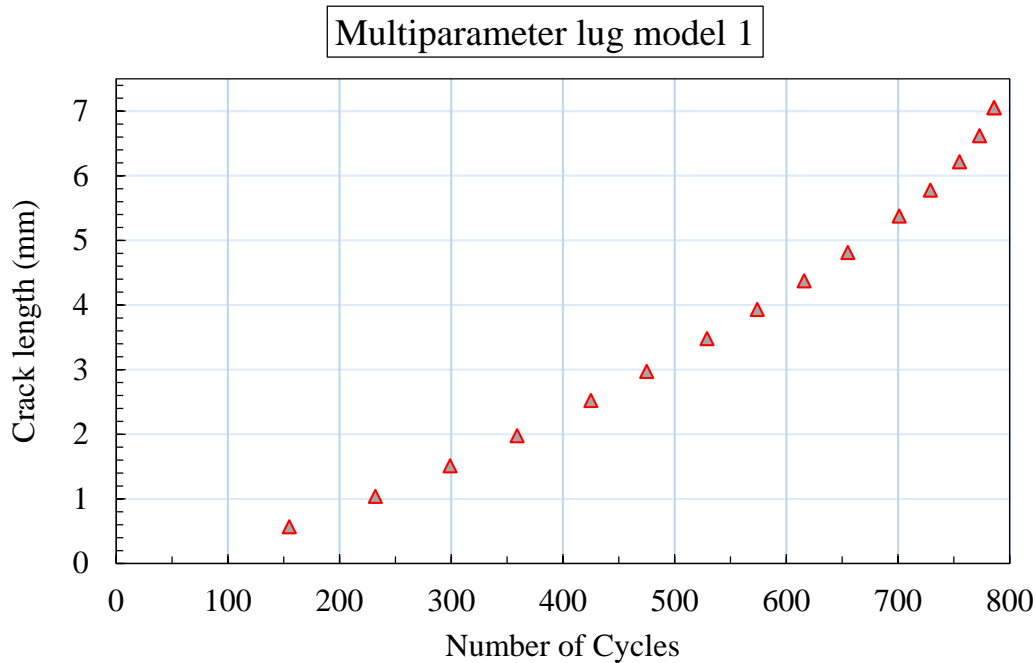


Figure 7.23 Crack length vs Number of cycles for three-parameter lug model 1 ($N_{max}=786$)

7.4 Model number 4: Different combination of three parameters

Optimization model 4, as model 3, has the same three input optimization parameters (the lug's thickness, the rounding radius and radius of a pin hole), but in this case, based on the table presented in Figure 7.24, other parameter values were selected. In this case, the initial lug's thickness of 12mm was kept (in the C column, the added value is 0), but the rounding radius was increased to 19mm (similar to model 2). As for model 3, the pin hole radius, in this case, was 7.5mm. For this lug, the mass was 105 grams and SIF values after the first crack propagation step are presented in Figure 7.25, and they are over $1400 MPa\sqrt{mm}$. The SIF values after crack extension of 7.09mm are given in Figure 7.26.

Table of Design Points					
	A	B	C	D	E
1	Name	P3 - radius	P5 - thickness	P7 - radius 2	P8 - Parameter 1
2	Units	mm	mm	mm	
3	DP 1	16.94	1.82	7	0
4	DP 2	19	5	7	0
5	DP 6	11.331	-3.521	9.2605	0.01479
6	DP 7	11.331	-3.521	9.2605	0.08521
7	DP 10	17.669	-3.521	9.2605	0.01479
8	DP 11	17.669	-3.521	9.2605	0.08521
9	DP 13	14.5	0	5	0.05
10	DP 17	14.5	0	10	0.05
11	DP 21	11.331	3.521	9.2605	0.01479
12	DP 22	11.331	3.521	9.2605	0.08521
13	DP 25	17.669	3.521	9.2605	0.01479
14	DP 26	17.669	3.521	9.2605	0.08521
15	DP 27	14.5	5	7.5	0.05
16	DP 28 (Current)	19	0	7.5	0.05
*					

Figure 7.24 Generated design points with selected parameters ($r_1=19\text{mm}$, $r_2=7.5\text{mm}$, $t=12\text{mm}$)

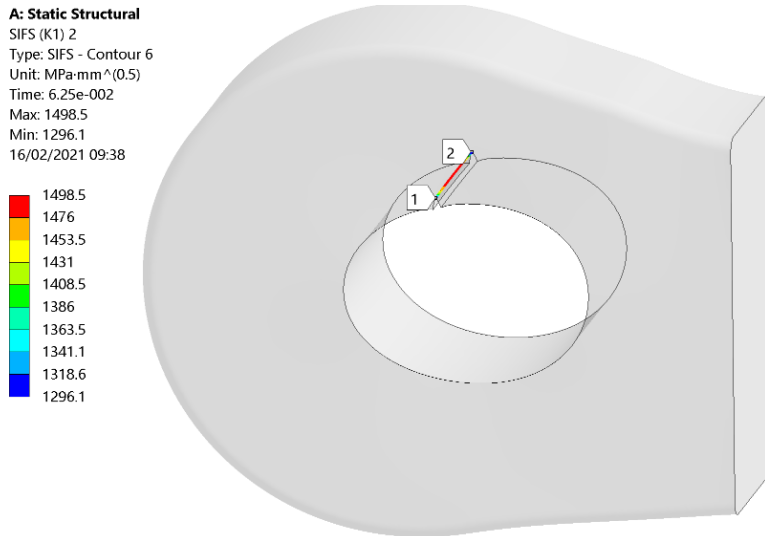


Figure 7.25 SIF values along crack front after 1st step of propagation

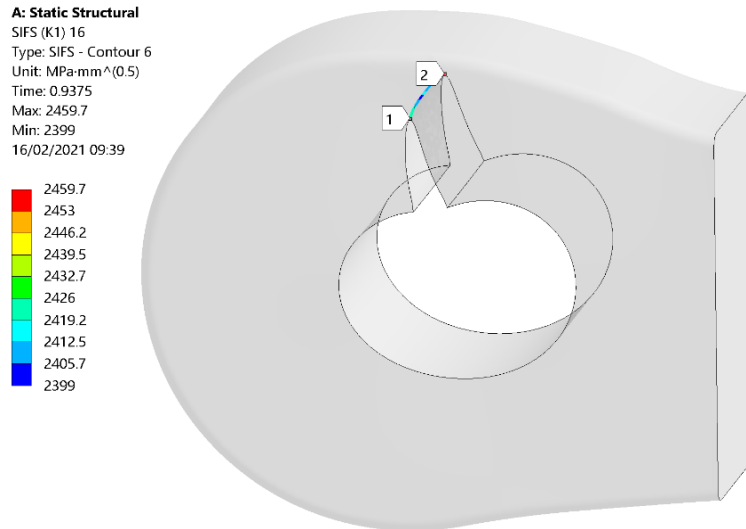


Figure 7.26 SIF values after 15th step of propagation (total crack extension 7.09 mm)

In Figure 7.26, it can be seen that in this lug model, the additional growth space exists (similar as for model 2), but maximum SIF values are significantly higher here than the SIF values for model 2 given in Figure 7.14 ($2450 \text{ MPa}\sqrt{\text{mm}}$ versus $1590 \text{ MPa}\sqrt{\text{mm}}$) which is the consequence of lesser lug's thickness in this model. This is the reason why the obtained number of cycles ($N_{\text{max}}=824$, Figure 7.27) is significantly lower than for model 2, though the final length of the crack just before fracture is almost the same as in model 2.

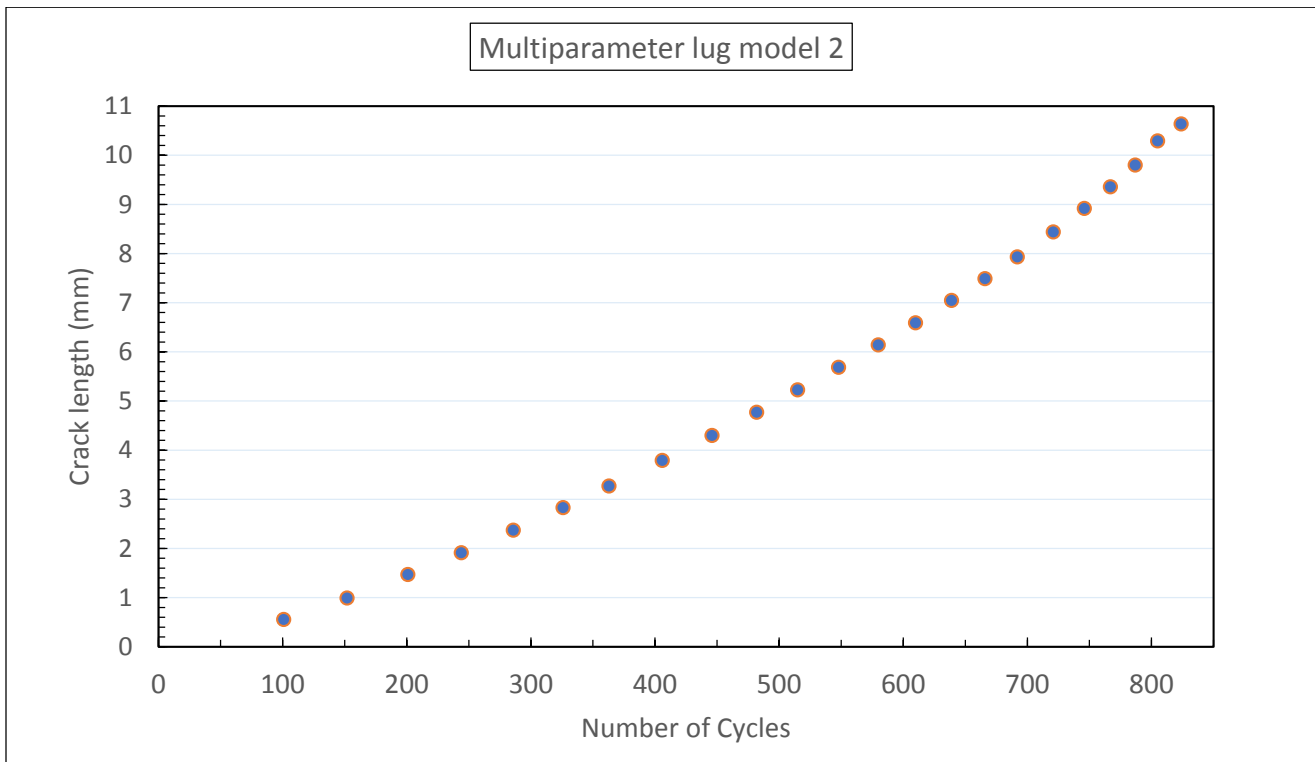


Figure 7.27 Crack length vs Number of cycles for three-parameter lug model 2 ($N_{\max}=824$)

7.5 Comparison of results

Figure 7.28 and Table 7.2 the complete results of all conducted analyses are presented. The number of cycles for all 5 models is given comparatively (the initial lug and 4 models, which are the optimisation product with different parameters). In some models, the crack length reached almost 11mm before fracture, but in

Figure 7.28, only the lengths up to 7mm are shown for easier comparison.

The longest fatigue life, without a doubt, was obtained for model 2 (M2: Two-parameter optimization), where the number of cycles was increased 3.75 times with respect to this number for the initial lug, but at the cost of a mass increase of 75.9% (Table 7.2). Considering that wing-fuselage attachment has two lugs per pin, its mass would be increased for $4 \times (153g - 87g) = 264g$, which in absolute numbers is not much, but in light aircraft design and production, every gram counts. On the other hand, model M4 has a mass increase of only 20.7% (a wing-fuselage attachment of $4 \times (105g - 87g) = 72g$) and provides for 60% longer fatigue life comparing to the initial lug's, so it seems that this model is more acceptable than M2. Of course, if the safety of the aircraft is in the first place, then the advantage has model m2, because, with approximately 2000 cycles of ultimate loading, it enables that potential crack could be spotted in time during the inspection and thus catastrophic failures could be prevented.

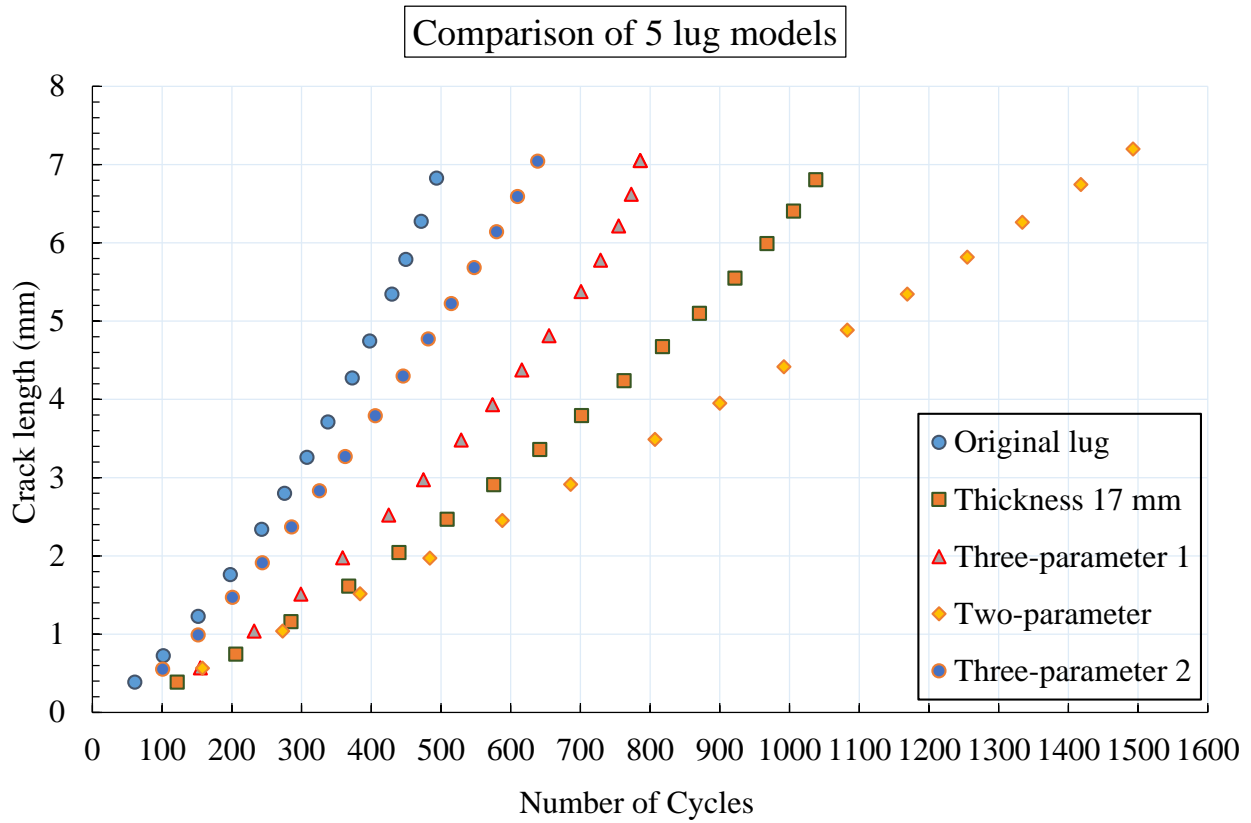


Figure 7.28 Crack length vs Number of cycles for all five lug models (max extension 7mm)

Table 7.2 Comparison of properties for five lug models

	Mass (grams)	Initial $K_{I\ max}$ (MPa mm ^{0.5})	Total number of cycles
Original lug	87	1880.0	515
M1: Lug 17 mm	123 (+41.4%)	1391.2	1085 (+110.7%)
M2: Two-parameter	153 (+75.9%)	1256.8	1933 (+275.4%)
M3: Three-parameter 1	108 (+24.1%)	1267.6	786 (+52.6%)
M4: Three-parameter 2	105 (+0.7%)	1498.5	824 (+60.0%)

CHAPTER 8
DISCUSSION and CONCLUSION

8 CONCLUSION

Before repeating the most important findings of the research presented here and drawing final conclusions, it must be emphasized that work on this thesis was a part of wider research which included specialists in different areas (aerodynamics, flight mechanics, aeroelasticity, manufacturing, etc.) Since the evaluation of stresses and deformations of the wing (consequently its fatigue life, too) depends on results these specialists obtained in their work, their results were used as input data in some chapters of this thesis, while in some cases necessary data were obtained independently from their calculations. These calculations are usually very detailed and consist of a large number of output data; that is the reason why only the most important were presented in this thesis. Otherwise, if all data would have been presented, the thesis would have more than 500 pages. Also, the conclusions which were the result of research presented in some chapters have been presented in those chapters; as a consequence, here the most important of them will be repeated briefly.

As showed in the thesis, the wing structure of the light aircraft was analyzed first and it was shown that it satisfies strength requirements according to standards CS23. Magnitudes and distribution of loads have been considered in detail and distribution of pressure loading was done according to the requirements of CS23. The inertial loading was modeled too, and all displacements (translations and rotations) are relatively small, which shows that structure has enough stiffness. Detailed analysis of the state of stresses, deformations, and strength of wing structure regarding the magnitude of limit loads shows the stresses at structural elements do not exceed the elastic limit. Experimental verification of analytical/numerical results was carried out on the full-scale wing and it was shown that the difference between deformations was satisfactory low.

Then, the behavior and fatigue life of the damaged wing-fuselage attachment lug were analyzed. Due to the high loads attachment carries and its high impact on the overall aircraft integrity, the crack occurrence in it is not allowed. Still, some recent events in commercial aviation indicate that damages might occur quite unexpectedly. The cracking issues of some wing-fuselage attachments had led many airlines to check their airplanes, and as result 50 jets have been grounded worldwide in 2019, causing a significant profit loss.

Thus, two types of the crack in the lug – the corner crack and through the crack – were analyzed using XFEM in the case of the maximum allowed load. Based on the SIF values obtained in simulations of the penny shaped corner crack growth it can be concluded that the damage propagates rapidly and that it takes a small number of cycles to reach the critical depth. In the case of through initial crack, the number of cycles is even smaller. The number of cycles for through crack was confirmed in classical FEM simulations carried out in Ansys Workbench. It was shown that differences in calculated mean values of stress intensity factors of mode I (SIF K_I) are not significant (XFEM based results are somewhat higher). It should be again pointed out that the cycles obtained in numerical simulations were evaluated on the basis of the action of the maximum allowed axial force (load factor $n=6$) and that in the case of significantly smaller force ($n=1$) the number of cycles would be much higher. However, considering that the purpose of the light aerobatic aircraft is doing aerobatics, the use of maximum load was justified.

It is important to mention again that SIFs calculated can provide a wider picture of the possible crack paths once the damage was initiated and that finite element mesh type might influence results, but not dramatically. For example, SIF calculated for penny-shaped crack growth in the hexahedral mesh of lug showed significant oscillation along with the nodes on the newly formed crack fronts. The difference of about 25% indicated that crack was not growing uniformly; moreover, values in few nodes became negative signaling that three-dimensional crack can no longer propagate in some directions. This is important information for designers because knowing the directions in which cracks growth is highly unlikely might lead designers to define the optimized structure (from

the fatigue point of view) early in the design process. It was also shown that mode I is dominant meaning that cracks in the lug mostly grow in a single plane.

In the case of tetrahedral mesh SIF values through steps were on average smaller than values obtained with hexahedral mesh, which can be explained by the fact that more nodes were generated around the crack front, and the fact that propagation was not restricted to a single plane: directions in which the crack has grown were determined by the calculated kink angle. This is why its final shape is irregular, in contrast to the almost circular shape obtained in the hexahedral mesh. Negative values of K_I also occurred at some nodes suggesting that three-dimensional crack propagation in some directions wasn't possible. The crack didn't reach the same length in two perpendicular directions which offers a clue about the direction in which the corner damage on the real lug will most likely grow faster: the crack path along the thickness (vertical direction) is longer than the path in a radial direction. This is an important finding because in periodic inspections portion of the crack in the radial direction is visible, while the portion in the vertical direction cannot be seen due to the presence of the pin. Thus, if a small crack exists in the radial direction, it is highly likely that its length in the vertical direction is greater.

Though differences in SIF values are obvious, obtained number of cycles for both meshes was similar (difference was 9.8%). However, the difference of the order of magnitude 10% might be significant when number of cycles is measured in millions, and further research will focus on determination of the influence of the mesh quality on estimated fatigue life. Nevertheless, it was shown that XFEM based analyses could be very useful, not only for SIF values calculation, but also for three-dimensional cracks' paths predictions in complex geometries.

After analyzing possible crack paths and influences of the mesh type on SIF values, in the last phase of the research, the focus was on the optimization of the attachment lug's geometry. Several strategies for the fatigue life extension were followed, including the easiest: to replace the material used in the design with other, fatigue resistant material. But, since the use of more fatigue-resistant material increases costs significantly, geometry redesign was selected as an alternative approach.

- To redesign the wing-fuselage attachment lug for the purpose of obtaining longer fatigue life with damage, the following assumptions were taken into account:
- The average element mesh size was fixed throughout the optimization to avoid the influence of the mesh density on results (the number of cycles to catastrophic failure),
- Boundary conditions, load value, and material property were kept constant, and Certain SIF value $K_{(I \max)}$ was used as the main criterion for redesign i.e. the goal was to achieve $K_{(I \max)}$ after the first propagation step.

The initial mass of the attachment lug was 87 grams, and four different models were used in the study, with the respect to three different design parameters: the lug's thickness, the rounding radius, and the radius of a pinhole. In model 1, the lug thickness was changing by adding the material in the normal direction to the surface. Using predefined criterion ($K_{(I \max)}$ value in the first step) as the goal, the mass of the lug with a new thickness value reached 123 grams, which represents an increase of 41.3%. In model 2, two parameters were changed simultaneously, the lug's thickness and the rounding radius, and the required criterion was satisfied with the lug's mass of 153 grams, which was an increase in mass by 75.8% (from 87 grams to 153 grams). It became obvious that additional parameters should be included in the redesign in order to achieve mass reduction and fatigue life prolongation. So, model 3 had three geometrical input optimization parameters: the lug's thickness, the rounding radius, and the radius of a pin. Besides them, one "non-geometrical" input parameter was also selected: the initial position of the crack with respect to the surface of the pinhole. This was necessary because in this case, with geometrical parameters varying, the size of the pinhole was changing, too.

Achieving the required goal in model 3 led to mass of the lug equal to 108 grams. Compared to the initial shape of the lug, model 3 had approximately 52,6% longer fatigue life, while the mass was increased by 24.1%. Optimization model 4, as model 3, had the same three input redesign parameters (the lug's thickness, the rounding radius and radius of a pin hole), but the initial lug's thickness was kept constant, and with increased rounding radius (similar to model 2) obtained mass was 105 grams. Since geometry changed significantly, the additional space for crack growth exists in model 4, but maximum SIF values are significantly higher here than the SIF values for model 2 which is the consequence of lesser lug's thickness in this model.

To conclude, the longest fatigue life was obtained for model 2 where the number of cycles was increased 3.75 times with respect to the number for the initial lug, but at the cost of a mass increase of 75.9%. Considering that wing-fuselage attachment has two lugs per pin, its mass would be increased by 264 grams. On the other hand, model 4 has a mass increase of only 20.7% (or 72 grams) and provides around 60% longer fatigue life than the initial lug's, and it looks more acceptable than model 2. However, if the safety of the aircraft is the priority, then model 2 is preferable since it can sustain approximately 2000 cycles of ultimate loading when damaged, providing the opportunity of the crack being spotted during the inspection thus reducing the possibility of catastrophic failure.

References

- [1] "Business Insider," [Online]. Available: <https://www.businessinsider.com/boeing-737ng-pickle-fork-crack-lion-air-2019-11..>
- [2] [Online]. Available: <https://www.theguardian.com/business/2019/nov/06/boeing-737-cracks-ryanair-grounds-three-planes-due-to-cracking-between-wing-and-fuselage>.
- [3] S. Barter, P. K. Sharp and G. Clark, "The failure of an F/A-18 trailing edge flap hinge," *Engineering Failure Analysis*, vol. 1, no. 4, pp. 255-266, 1994.
- [4] R. Rigby and M. H. Aliabadi, "Stress intensity factors for cracks at attachment lugs," *Engineering Failure Analysis*, vol. 4, no. 2, pp. 133-146, 1997.
- [5] C. R. F. Azevedo, E. Hippert Jr, G. Spera and P. Gerardi, "Aircraft landing gear failure: fracture of the outer cylinder lug," *Engineering Failure Analysis*, vol. 9, no. 1, pp. 1-15, 2002.
- [6] J.-H. Kim, S.-B. Lee and S.-G. Hong, "Fatigue crack growth behavior of Al7050-T7451 attachment lugs under flight spectrum variation," *Theoretical and applied fracture mechanics*, vol. 40, no. 2, pp. 135-144, 2003.
- [7] K. Maksimović, V. Nikolić and S. Maksimović, "Efficient computation method in fatigue life estimation of damaged structural components," *Facta universitatis-series: Mechanics, Automatic Control and Robotics*, vol. 4, no. 16, pp. 101-114, 2004.
- [8] L. Witek, "Failure analysis of the wing-fuselage connector of an agricultural aircraft," *Engineering Failure Analysis*, vol. 13, no. 4, pp. 572-581, 2006.
- [9] A. LANCIOTTI, F. Nigro and C. Polese, "Fatigue crack propagation in the wing to fuselage connection of the new trainer aircraft M346," *Fatigue & Fracture of Engineering Materials & Structures*, vol. 29, no. 12, pp. 1000-1009, 2006.
- [10] X. Huang and T. Moan, "Improved modeling of the effect of R-ratio on crack growth rate," *International Journal of fatigue*, vol. 29, no. 4, pp. 591-602, 2007.
- [11] L. Allegrucci, M. Amura, F. Bagnoli and M. Bernabei, "Fatigue fracture of a aircraft canopy lever reverse," *Engineering Failure Analysis*, vol. 16, no. 1, pp. 391-401, 2009.
- [12] L. M. Wu, Y. T. He, H. W. Zhang, R. H. Cui, J. Q. Du and H. Ding, "Study on fatigue crack growth model of attachment lug subjected to oblique pin-load," in *Advanced Materials Research*, 2011.
- [13] N. Antoni and F. Gaisne, "Analytical modelling for static stress analysis of pin-loaded lugs with bush fitting," *Applied Mathematical Modelling*, vol. 35, no. 1, pp. 1-21, 2011.
- [14] S. Mikheevskiy, G. Glinka and D. Algera, "Analysis of fatigue crack growth in an attachment lug based on the weight function technique and the UniGrow fatigue crack growth model," *International journal of fatigue*, vol. 42, pp. 88-94, 2012.
- [15] S. Boljanović, S. Maksimović and A. Carpinteri, "Fatigue life evaluation of damaged aircraft lugs," *Scientific Technical Review*, vol. 63, no. 4, pp. 3-9, 2013.
- [16] K. Mookaiya, S. Balaji and S. R. Balakrishan, "Crack Growth Analysis In Aircraft Wing Lug Section And Fatigue Life Estimation," *International Journal of Engineering Research and Technology (IJERT)*, vol. 2, no. 6, pp. 2018-2023, 2013.
- [17] M. Naderi and N. Iyyer, "Fatigue life prediction of cracked attachment lugs using XFEM," *International Journal of Fatigue*, vol. 77, pp. 186-193, 2015.
- [18] S. Boljanović and S. Maksimović, "Fatigue damage analysis of wing-fuselage attachment lug," *Procedia Structural Integrity*, vol. 5, pp. 801-808, 2017.

- [19] M. D. R. M. Abraham J Pulickal, "Design Structural Analysis and Fatigue Calculation of Wing Fuselage Lug Attachment of a Transport Aircraft," vol. 4, no. 8, 2017.
- [20] T. A. M.H. Sumanth, "Comparative analysis of aircraft wing fuselage lug attachment bracket," *International Journal for Technological Research in Engineering*, vol. 5, no. 11, pp. 4422-4429, 2018.
- [21] A. Sedmak, "Computational fracture mechanics: An overview from early efforts to recent achievements," *Fatigue & Fracture of Engineering Materials & Structures*, vol. 41, no. 12, pp. 2438-2474, 2018.
- [22] K. Nasri, M. Abbadi, M. Zenasni, M. Ghammouri and Z. Azari, "Double crack growth analysis in the presence of a bi-material interface using XFEM and FEM modelling," *Engineering Fracture Mechanics*, vol. 132, pp. 189-199, 2014.
- [23] L. Marsavina, D. M. Constantinescu, E. Linul, F. A. Stuparu and D. A. Apostol, "Experimental and numerical crack paths in PUR foams," *Engineering Fracture Mechanics*, vol. 167, pp. 68-83, 2016.
- [24] A. Bergara, J. I. Dorado, A. Martin-Meizoso and J. M. Martínez-Esnaola, "Fatigue crack propagation in complex stress fields: Experiments and numerical simulations using the Extended Finite Element Method (XFEM)," *International Journal of Fatigue*, vol. 103, pp. 112-121, 2017.
- [25] E. Rakipovski, A. Grbovic, G. Kastratovic and N. Vidanovic, "Application of extended finite element method for fatigue life predictions of multiple site damage in aircraft structure," *STRUCTURAL INTEGRITY AND LIFE-INTEGRITET I VEK KONSTRUKCIJA*, vol. 15, no. 1, pp. 3-6, 2015.
- [26] A. Grbović, A. Sedmak, G. Kastratović, D. Petrašinić, N. Vidanović and A. Sghayer, "Effect of laser beam welded reinforcement on integral skin panel fatigue life," *Engineering Failure Analysis*, vol. 101, pp. 383-393, 2019.
- [27] A. Grbović, G. Kastratović, A. Sedmak, I. Balać and M. D. Popović, "Fatigue crack paths in light aircraft wing spars," *International Journal of Fatigue*, vol. 123, pp. 96-104, 2019.
- [28] J. C. Sobotka, Y.-D. Lee, R. C. McClung and J. W. Cardinal, "Stress-Intensity Factor Solutions for Tapered Lugs with Oblique Pin Loads," in *International Committee on Aeronautical Fatigue*, 2019.
- [29] K. Shridhar, B. S. Suresh and M. M. Kumar, "Fatigue Analysis of Wing-Fuselage Lug section of a Transport Aircraft," *Procedia Structural Integrity*, vol. 14, pp. 375-383, 2019.
- [30] N. K. Simha, F. D. Fischer, G. X. Shan, C. R. Chen and O. Kolednik, "J-integral and crack driving force in elastic-plastic materials," 2008.
- [31] J. Schijve, *Fatigue of structures and materials*, Springer., 2008.
- [32] S. P. Timoshenko and J. N. Goodier, "Theory of elasticity, 3rd article ed," New York: McGraw-Hill, 1987.
- [33] G. R. Irwin, "Analysis of stresses and strains near the end of a crack transversing a plate," *Trans. ASME, Ser. E, J. Appl. Mech.*, vol. 24, pp. 361-364, 1957.
- [34] H. A. Richard and M. Sander, *Fatigue Crack Growth*, Springer, 2016.
- [35] N. Recho, *Fracture mechanics and crack growth*, John Wiley & Sons, 2012.
- [36] A. M. S. Sghayer, "Fatigue life assessment of damaged integral skin-stringer panels," 2018.
- [37] A. Almarnaess, "Fatigue handbook: offshore steel structures," 1985.
- [38] W. A. J. Albert, "Uber Treibseile am Harz. Archiv fur Mineralogie, Geognosie," *Bergbau und Huttenkunde*, vol. 10, p. 215, 1837.

- [39] W. J. M. Rankine, A manual of applied mechanics, Charles Griffin and Company, 1872.
- [40] H. W. Hayden, W. G. Moffatt and J. Wulff, *The structure and properties of materials, Vol. 3, 1965*, John Wiley and Sons Inc., New York). Google Scholar.
- [41] "J.A. Ewing, Classic historic discovery of role of microscopic cracks in fatigue of metals, Philosophical Transactions of the Royal Society, 1903".
- [42] A. A. GRIFFITH, "The phenomenon of rupture and flow in solids," *Phil. Trans. Royal Soc. London, A*, vol. 221, pp. 163-198, 1920.
- [43] P. C. Paris, M. P. Gomez and W. E. Anderson, "A rational analytic theory of fatigue, *The Trend, Engineering*, no. 13, p. 9, 1961.
- [44] J. Schijve, "Fatigue of Structures and Materials," 2009.
- [45] A. P. Parker, *Fracture mechanics: by HL Ewalds and RJH Wanhill, Edward Arnold, London, 1984. ISBN 0-7131-3515-8, 304 pages, illustrated, paperback, £ 13.50*, Elsevier, 1989.
- [46] P. Paris and F. Erdogan, "A critical analysis of crack propagation laws," 1963.
- [47] E. Wolf, "Fatigue crack closure under cyclic tension," *Engineering fracture mechanics*, vol. 2, no. 1, pp. 37-45, 1970.
- [48] T. L. Anderson, "Fracture mechanics-Fundamentals and applications," *STIA*, vol. 92, p. 40200, 1991.
- [49] W. H. Munse, "Grover,'" *La Motte, " Fatigue of Welded Steel Structures," Welding Research Council, New York, 1964.*
- [50] E. A. S. Agency, "Certification Specifications for Normal, Utility, Aerobatic, and Commuter Category Aeroplanes-CS-23," 2012.
- [51] "National advisory committee for aeronautics: report No. 572. Determination of the characteristics of tapered wings," 1937.
- [52] "ANALYSIS & DESIGN OF COMPOSITE & METALLIC FLIGHT VEHICLE STRUCTURES - ABBOTT - 2019 - THIRD EDITION | Mendeley".
- [53] M. Souiyah, A. Alshoaibi, A. Muchtar and A. K. Ariffin, "Stress intensity factor evaluation for crack emanating from circular-hole using finite element method," *International review of mechanical engineering*, vol. 2, no. 4, 2008.
- [54] M. Souiyah, A. Muchtar, A. Alshoaibi and A. K. Ariffin, "Finite element analysis of the crack propagation for solid materials," *American Journal of Applied Sciences*, vol. 6, no. 7, p. 1396, 2009.
- [55] R. Branco, F. V. Antunes and J. D. Costa, "A review on 3D-FE adaptive remeshing techniques for crack growth modelling," *Engineering Fracture Mechanics*, vol. 141, pp. 170-195, 2015.
- [56] A. Gopichand, M. S. Kumar and A. Sharma, "Computation of Stress Intensity Factor of Cracked Aluminium Plate Using Virtual Crack Closure Technique," *International Journal of Engineering Research and Applications*, vol. 2, no. 6, pp. 460-465, 2012.
- [57] K. A. Eldwaib, "Optimization of integral wing spar based on estimated fatigue life," Univerzitet u Beogradu, 2018.
- [58] G. Qian, V. F. González-Albuixech, M. Niffenegger and E. Giner, "Comparison of KI calculation methods," *Engineering Fracture Mechanics*, vol. 156, pp. 52-67, 2016.
- [59] A. Boulenuar, N. Benseddiq, M. Mazari and N. Benamara, "FE model for linear-elastic mixed mode loading: estimation of SIFs and crack propagation," *Journal of Theoretical and Applied Mechanics*, vol. 52, 2014.

- [60] A. Dutt, "Effect of mesh size on finite element analysis of beam," *International Journal of Mechanical Engineering*, vol. 2, no. 12, pp. 8-10, 2015.
- [61] S. T. More and R. S. Bindu, "Effect of mesh size on finite element analysis of plate structure," *Int. J. Eng. Sci. Innovative Technol*, vol. 4, no. 3, pp. 181-185, 2015.
- [62] W. B. Liu, M. Gheni and L. Yu, "Effect of mesh size of finite element analysis in modal analysis for periodic symmetric struts support," in *Key Engineering Materials*, 2011.
- [63] T. Belytschko and T. Black, "Elastic crack growth in finite elements with minimal remeshing," *International journal for numerical methods in engineering*, vol. 45, no. 5, pp. 601-620, 1999.
- [64] H. N. Moghaddam, A. Keyhani and I. Aghayan, "Modelling of crack propagation in layered structures using extended finite element method," *Civil Engineering Journal*, vol. 2, no. 5, pp. 180-188, 2016.
- [65] J. Sepehri, "Application of extended Application of extended finite element method (XFEM) to simulate simulate hydraulic fracture propagation from oriented perforations.," 2014..
- [66] D. Datta, "Introduction to eXtended Finite Element (XFEM)," *Erasmus MSc in Computational Mechanics, Ecole Centrale de Nantes*, 2013.
- [67] V. Kumar, I. V. Singh and B. Mishra, "XFEM, crack growth examination of cryo-rolled (CR) 6082 Al alloys," *Int. J. Emerg. Technol. Adv. Eng*, vol. 4, no. 1, pp. 264-271, 2014.
- [68] J. M. Melenk and I. Babuška, "The partition of unity finite element method: basic theory and applications," in *Research Report/Seminar für Angewandte Mathematik*, 1996.
- [69] "SMART Fracture Whitepaper | Ansys," [Online]. Available: <https://www.ansys.com/resource-library/white-paper/smart-fracture>.
- [70] T. Strouboulis, K. Copps and I. Babuška, "The generalized finite element method," *Computer methods in applied mechanics and engineering*, vol. 190, no. 32-33, pp. 4081-4193, 2001.
- [71] M. Fleming, Y. A. Chu, B. Moran and T. Belytschko, "Enriched element-free Galerkin methods for crack tip fields," *International journal for numerical methods in engineering*, vol. 40, no. 8, pp. 1483-1504, 1997.
- [72] N. Moës, J. Dolbow and T. Belytschko, "A finite element method for crack growth without remeshing," *International journal for numerical methods in engineering*, vol. 46, no. 1, pp. 131-150, 1999.
- [73] E. Giner, N. Sukumar, J. E. Tarancón and F. J. Fuenmayor, "An Abaqus implementation of the extended finite element method," *Engineering fracture mechanics*, vol. 76, no. 3, pp. 347-368, 2009.
- [74] J. E. Dolbow, "An extended finite element method with discontinuous enrichment for applied mechanics.," 2000.
- [75] G. Ventura, "On the elimination of quadrature subcells for discontinuous functions in the extended finite-element method," *International Journal for Numerical Methods in Engineering*, vol. 66, no. 5, pp. 761-795, 2006.
- [76] J. Song, P. M. A. Areias and T. Belytschko, "A method for dynamic crack and shear band propagation with phantom nodes," *International Journal for Numerical Methods in Engineering*, vol. 67, no. 6, pp. 868-893, 2006.
- [77] D. Systemes, "Abaqus 6.9 Overview," *Last Modified*, 2009.
- [78] D. Đukić, A. Grbović, G. Kastratović, N. Vidanović and A. Sedmak, "Stress intensity factors numerical calculations for two penny shaped cracks in the elastic solid," 2020.
- [79] "<https://www.ansys.com/resource-library/white-paper/smart-fracture>," [Online].

- [80] B. Aleksić, A. Grbović, L. Milović, A. Hemer and V. Aleksić, "Numerical simulation of fatigue crack propagation: A case study of defected steam pipeline," 2019.
- [81] A. Grbović, N. Mirkov and B. Rašuo, "Numerical Simulation of Crack Propagation in Seven-Wire Strand".
- [82] N. Mitrovic, M. Milosevic and G. Mladenovic, "Computational and Experimental Approaches in Materials Science and Engineering".
- [83] A. Solob, A. Grbović, Ž. Božić and S. A. Sedmak, "XFEM based analysis of fatigue crack growth in damaged wing-fuselage attachment lug," 2020.
- [84] "Light-Sport Aircraft," [Online]. Available: https://www.faa.gov/aircraft/gen_av/light_sport/.
- [85] "Bombardier Strength Manual," in *Chapter 03: Joints & Fittings, Section 04: Lug and Pin Analysis*, pp. 7-11.
- [86] A. Grbović, "Investigation of fatigue life in superalloys structural components.," Faculty of Mechanical Engineering, University of Belgrade, Serbia, 2012.
- [87] "www.3dwhiffletree.com | Mendeley".
- [88] J. G. Rosengarten, The American Philosophical Society, 1743-1903, American Philosophical Society, 1903.
- [89] Q.-Z. Xiao and B. L. Karihaloo, "Improving the accuracy of XFEM crack tip fields using higher order quadrature and statically admissible stress recovery," *International Journal for Numerical Methods in Engineering*, vol. 66, no. 9, pp. 1378-1410, 2006.
- [90] "Cenaero Simulation technologies for Aeronautics," [Online]. Available: <http://www.cenaero.be/>.
- [91] N. Mitrovic, M. Milosevic and G. Mladenovic, Computational and Experimental Approaches in Materials Science and Engineering: Proceedings of the International Conference of Experimental and Numerical Investigations and New Technologies, CNNTech 2019, vol. 90, Springer Nature, 2019.
- [92] "Boeing's latest crisis is growing after an airline found cracks on two 737 planes that weren't due for inspection yet," [Online]. Available: <https://www.businessinsider.com/boeing-737ng-pickle-fork-crack-lion-air-2019-11>.

APPENDICES

Appendix A

Program WING_LOADING

```
DIMENSION Y(48),C(48),CLA(48),Q(48),QT(48),QM(48),CL(48),CCZ(48)
CHARACTER AAA*20,BBB*20
AAA="Lift (N)= "
BBB="Speed (m/s)=  "
WRITE(*,*)AAA
READ(*,*) RZ
WRITE(*,*)
WRITE(*,*)BBB
READ(*,*)V
OPEN(UNIT=6,FILE="Chords.txt")
OPEN(UNIT=7,FILE="Loads.txt")
RO=1.225          ! Density
DIP=0.5*RO*(V**2) ! Dynamic pressure
BE = 4.75        ! One half of effective wing span
S=15.03          ! Wing area
CZ=RZ/(DIP*S)    ! Lift coefficient
PI=3.14159
CEL=4.0*S/(2.0*BE*PI)
! Calculation of wing chords
DO 22 I=1,48
Y(I)=0.1*(I-1)
IF(Y(I).GE.1.24)GOTO 10
C(I)=1.796*(1.0-(Y(I)/1.24))+1.55*(Y(I)/1.24)
GOTO 20
10 C(I)=1.55
! Chords of equivalent elliptic wing
20 CL(I)=CEL*SQRT(1.0-(Y(I)*Y(I))/(4.75**2))
! Schrenk's chords for distribution of aerodynamic load
22 CLA(I)=0.5*(C(I)+CL(I))
! Aerodynamic loading (forces) in cross-sections of wing
DO 30 I=1,48
30 Q(I)=0.1*CLA(I)*(RZ/S)
! Transversal forces
QQ=0.0
DO 40 I=47,1,-1
QQ=QQ+Q(I+1)
40 QT(I)=QQ
! Bending moments
DO 60 I=1,47
QFM=0.0
DO 50 J=I+1,48
50 QM(I)=QFM+0.1*Q(J)*(J-I)
60 CONTINUE
! Printing the results
```

```

WRITE(6,65)RZ,V
65  FORMAT("Lift (N) =",F10.3," Speed (m/s)= ",F10.2)
WRITE(6,66)RO,DIP
66  FORMAT("Density (kg/m^3)=",F10.3," Dyn. pres.(N/m^2) =",F15.3)
WRITE(6,67)CZ
67  FORMAT("Wing lift coefficient = ",F10.3)
WRITE(*,*)
DO 70 I=1,48
!   Position, chord, chord of elliptic wing, Schrenk's chord
CCZ(I)=Q(I)/(0.1*DIP*C(I))
70  WRITE(6,75)Y(I),C(I),CL(I),CLA(I),CCZ(I)
75  FORMAT(5F15.4)
CLOSE(6)
!   Position, Force, Shear force, Bending moment
DO 80 I=1,48
80  WRITE(7,85)Y(I),Q(I),QT(I),QM(I)
85  FORMAT(4F15.4)
CLOSE(7)
STOP
END

```

Table 3.7 Load cases

	<i>Case: A_023</i>			<i>Case: A_028</i>		
<i>Y (m)</i>	<i>q (N/m)</i>	<i>FT (N)</i>	<i>MF (Nm)</i>	<i>q (N/m)</i>	<i>FT (N)</i>	<i>MF (Nm)</i>
0.000	7066.725	28023.346	61340.898	6947.933	27552.275	60309.770
0.100	7029.104	27670.010	58573.918	6910.945	27204.879	57589.285
0.200	6989.827	26967.100	55877.191	6872.328	26513.785	54937.895
0.300	6948.888	26268.117	53250.375	6832.078	25826.553	52355.258
0.400	6906.284	25573.229	50693.063	6790.189	25143.346	49840.914
0.500	6862.007	24882.600	48204.813	6746.656	24464.326	47394.492
0.600	6816.045	24196.398	45785.172	6701.467	23789.660	45015.520
0.700	6768.387	23514.793	43433.688	6654.610	23119.514	42703.570
0.800	6719.017	22837.955	41149.891	6606.070	22454.053	40458.164
0.900	6667.918	22166.053	38933.293	6555.831	21793.445	38278.813
1.000	6615.070	21499.262	36783.367	6503.871	21137.861	36165.027
1.100	6560.450	20837.754	34699.582	6450.169	20487.475	34116.281
1.200	6504.031	20181.709	32681.416	6394.698	19842.457	32132.043
1.300	6467.858	19531.307	30728.281	6359.133	19202.986	30211.740
1.400	6444.542	18884.521	28839.830	6336.209	18567.072	28355.031
1.500	6419.329	18240.066	27015.822	6311.419	17933.451	26561.689
1.600	6392.175	17598.133	25256.012	6284.723	17302.309	24831.459
1.700	6363.039	16958.916	23560.119	6256.076	16673.836	23164.068
1.800	6331.867	16322.611	21927.861	6225.428	16048.228	21559.252
1.900	6298.606	15689.425	20358.918	6192.727	15425.685	20016.682
2.000	6263.194	15059.564	18852.961	6157.910	14806.412	18536.041
2.100	6225.563	14433.245	17409.633	6120.911	14190.621	17116.977
2.200	6185.636	13810.688	16028.564	6081.655	13578.530	15759.127
2.300	6143.330	13192.125	14709.354	6040.060	12970.365	14462.088

2.400	6098.550	12577.792	13451.572	5996.034	12366.359	13225.453
2.500	6051.194	11967.937	12254.782	5949.473	11766.756	12048.777
2.600	6001.143	11362.817	11118.497	5900.263	11171.809	10931.594
2.700	5948.266	10762.703	10042.229	5848.275	10581.782	9873.419
2.800	5892.413	10167.877	9025.441	5793.361	9996.955	8873.725
2.900	5833.417	9578.636	8067.576	5735.357	9417.619	7931.960
3.000	5771.086	8995.294	7168.049	5674.074	8844.083	7047.553
3.100	5705.199	8418.186	6326.228	5609.295	8276.676	6219.884
3.200	5635.503	7847.666	5541.463	5540.770	7715.747	5448.311
3.300	5561.699	7284.116	4813.051	5468.207	7161.669	4732.144
3.400	5483.440	6727.946	4140.256	5391.264	6614.849	4070.658
3.500	5400.312	6179.602	3522.297	5309.532	6075.722	3463.087
3.600	5311.816	5639.570	2958.339	5222.524	5544.769	2908.609
3.700	5217.345	5108.389	2447.500	5129.642	5022.517	2406.358
3.800	5116.143	4586.654	1988.835	5030.140	4509.552	1955.403
3.900	5007.250	4075.040	1581.331	4923.079	4006.538	1554.749
4.000	4889.423	3574.315	1223.900	4807.232	3514.230	1203.326
4.100	4760.988	3085.373	915.363	4680.956	3033.507	899.976
4.200	4619.601	2609.274	654.435	4541.945	2565.412	643.433
4.300	4461.807	2147.314	439.703	4386.804	2111.217	432.312
4.400	4282.099	1701.133	269.590	4210.117	1672.537	265.058
4.500	4070.638	1272.923	142.298	4002.211	1251.525	139.906
4.600	3806.045	865.859	55.712	3742.065	851.304	54.776
4.700	3415.241	485.255	7.186	3357.831	477.098	7.066
4.750	2874.612	143.731	0.000	2826.290	141.314	0.000

<i>Y (m)</i>	<i>Case: D_023</i>			<i>Case: D_028</i>		
	<i>q (N/m)</i>	<i>FT (N)</i>	<i>MF (Nm)</i>	<i>q (N/m)</i>	<i>FT (N)</i>	<i>MF (Nm)</i>
0.000	7252.969	28761.908	62957.566	7134.177	28290.822	61926.410
0.100	7214.357	28399.260	60117.633	7096.197	27934.113	59133.000
0.200	7174.044	27677.824	57349.848	7056.544	27224.494	56410.555
0.300	7132.027	26960.420	54653.805	7015.215	26518.840	53758.664
0.400	7088.300	26247.217	52029.086	6972.205	25817.318	51176.922
0.500	7042.856	25538.387	49475.242	6927.504	25120.098	48664.922
0.600	6995.682	24834.102	46991.844	6881.104	24427.348	46222.176
0.700	6946.769	24134.533	44578.410	6832.991	23739.238	43848.270
0.800	6896.098	23439.855	42234.402	6783.150	23055.939	41542.660
0.900	6843.652	22750.246	39959.379	6731.563	22377.625	39304.902
1.000	6789.411	22065.881	37752.785	6678.211	21704.469	37134.453
1.100	6733.352	21386.939	35614.090	6623.069	21036.648	35030.789
1.200	6675.445	20713.604	33542.738	6566.111	20374.342	32993.359
1.300	6638.319	20046.059	31538.133	6529.594	19717.730	31021.584
1.400	6614.389	19382.227	29599.908	6506.055	19064.771	29115.107
1.500	6588.511	18720.787	27727.834	6480.601	18414.166	27273.691
1.600	6560.642	18061.936	25921.639	6453.188	17766.105	25497.082
1.700	6530.737	17405.871	24181.053	6423.773	17120.787	23785.000

1.800	6498.744	16752.797	22505.770	6392.305	16478.410	22137.158
1.900	6464.606	16102.922	20895.479	6358.726	15839.181	20553.242
2.000	6428.261	15456.461	19349.828	6322.976	15203.308	19032.910
2.100	6389.638	14813.635	17868.469	6284.985	14571.010	17575.811
2.200	6348.659	14174.671	16451.000	6244.677	13942.511	16181.557
2.300	6305.238	13539.805	15097.021	6201.968	13318.043	14849.753
2.400	6259.278	12909.281	13806.094	6156.761	12697.846	13579.971
2.500	6210.674	12283.354	12577.758	6108.952	12082.170	12371.752
2.600	6159.303	11662.286	11411.525	6058.423	11471.274	11224.623
2.700	6105.033	11046.355	10306.893	6005.042	10865.432	10138.082
2.800	6047.708	10435.853	9263.310	5948.656	10264.928	9111.589
2.900	5987.157	9831.082	8280.197	5889.097	9670.063	8144.582
3.000	5923.184	9232.366	7356.963	5826.171	9081.153	7236.467
3.100	5855.561	8640.048	6492.957	5759.655	8498.536	6386.612
3.200	5784.027	8054.492	5687.508	5689.293	7922.571	5594.356
3.300	5708.278	7476.089	4939.900	5614.785	7353.642	4858.992
3.400	5627.957	6905.262	4249.373	5535.780	6792.163	4179.775
3.500	5542.638	6342.466	3615.127	5451.857	6238.585	3555.917
3.600	5451.810	5788.202	3036.306	5362.517	5693.399	2986.576
3.700	5354.849	5243.021	2512.005	5267.145	5157.148	2470.862
3.800	5250.979	4707.536	2041.251	5164.976	4630.434	2007.819
3.900	5139.217	4182.438	1623.007	5055.044	4113.936	1596.425
4.000	5018.285	3668.516	1256.156	4936.093	3608.431	1235.582
4.100	4886.464	3166.688	939.487	4806.431	3114.822	924.100
4.200	4741.351	2678.042	671.682	4663.694	2634.179	660.681
4.300	4579.398	2203.906	451.292	4504.395	2167.810	443.900
4.400	4394.954	1745.967	276.695	4322.971	1717.370	272.163
4.500	4177.920	1306.471	146.048	4109.492	1285.073	143.656
4.600	3906.353	888.679	57.180	3842.373	874.124	56.244
4.700	3505.250	498.044	7.376	3447.840	489.886	7.255
4.750	2950.373	147.519	0.000	2902.050	145.103	0.000

<i>Y (m)</i>	<i>Case: E_023</i>			<i>Case: E_028</i>		
	<i>q (N/m)</i>	<i>FT (N)</i>	<i>MF (Nm)</i>	<i>q (N/m)</i>	<i>FT (N)</i>	<i>MF (Nm)</i>
0.000	3779.315	14987.009	32805.383	3753.143	14883.220	32578.203
0.100	3759.195	14798.043	31325.574	3733.162	14695.563	31108.641
0.200	3738.189	14422.123	29883.369	3712.302	14322.246	29676.422
0.300	3716.295	14048.304	28478.539	3690.559	13951.016	28281.318
0.400	3693.510	13676.674	27110.871	3667.932	13581.960	26923.125
0.500	3669.831	13307.323	25780.139	3644.417	13215.167	25601.609
0.600	3645.250	12940.340	24486.100	3620.006	12850.726	24316.533
0.700	3619.762	12575.814	23228.521	3594.695	12488.725	23067.662
0.800	3593.359	12213.838	22007.137	3568.475	12129.255	21854.734
0.900	3566.031	11854.502	20821.684	3541.336	11772.407	20677.496
1.000	3537.768	11497.898	19671.898	3513.268	11418.273	19535.668
1.100	3508.557	11144.122	18557.486	3484.260	11066.946	18428.977

1.200	3478.384	10793.267	17478.160	3454.295	10718.521	17357.123
1.300	3459.038	10445.429	16433.617	3435.084	10373.091	16319.813
1.400	3446.569	10099.524	15423.666	3422.701	10029.582	15316.856
1.500	3433.084	9754.867	14448.178	3409.310	9687.312	14348.122
1.600	3418.563	9411.559	13507.023	3394.889	9346.381	13413.481
1.700	3402.980	9069.702	12600.055	3379.414	9006.892	12512.797
1.800	3386.310	8729.404	11727.109	3362.859	8668.950	11645.901
1.900	3368.521	8390.773	10888.034	3345.194	8332.664	10812.634
2.000	3349.583	8053.921	10082.644	3326.387	7998.145	10012.821
2.100	3329.457	7718.962	9310.746	3306.400	7665.506	9246.268
2.200	3308.104	7386.017	8572.145	3285.195	7334.866	8512.783
2.300	3285.479	7055.206	7866.626	3262.727	7006.346	7812.148
2.400	3261.531	6726.658	7193.959	3238.944	6680.074	7144.141
2.500	3236.204	6400.505	6553.909	3213.793	6356.179	6508.523
2.600	3209.437	6076.884	5946.220	3187.211	6034.800	5905.042
2.700	3181.158	5755.940	5370.626	3159.128	5716.079	5333.435
2.800	3151.288	5437.825	4826.845	3129.465	5400.166	4793.418
2.900	3119.736	5122.696	4314.574	3098.132	5087.220	4284.695
3.000	3086.402	4810.722	3833.503	3065.028	4777.407	3806.955
3.100	3051.165	4502.082	3383.294	3030.035	4470.904	3359.864
3.200	3013.891	4196.965	2963.598	2993.020	4167.900	2943.074
3.300	2974.420	3895.576	2574.041	2953.822	3868.599	2556.215
3.400	2932.567	3598.134	2214.227	2912.259	3573.216	2198.893
3.500	2888.110	3304.877	1883.739	2868.109	3281.990	1870.694
3.600	2840.782	3016.066	1582.132	2821.109	2995.179	1571.176
3.700	2790.259	2731.988	1308.934	2770.936	2713.069	1299.869
3.800	2736.135	2452.962	1063.638	2717.187	2435.975	1056.272
3.900	2677.899	2179.349	845.702	2659.354	2164.256	839.846
4.000	2614.885	1911.559	654.547	2596.776	1898.321	650.014
4.100	2546.197	1650.070	489.540	2528.564	1638.643	486.150
4.200	2470.582	1395.451	349.994	2453.473	1385.787	347.571
4.300	2386.193	1148.392	235.155	2369.669	1140.440	233.527
4.400	2290.085	909.773	144.178	2274.226	903.473	143.180
4.500	2176.995	680.765	76.102	2161.919	676.050	75.575
4.600	2035.489	463.065	29.795	2021.393	459.858	29.589
4.700	1826.486	259.516	3.843	1813.837	257.719	3.817
4.750	1537.355	76.868	0.000	1526.708	76.335	0.000

<i>Y (m)</i>	<i>Case:G_023</i>			<i>Case: G_028</i>		
	<i>q (N/m)</i>	<i>FT (N)</i>	<i>MF (Nm)</i>	<i>q (N/m)</i>	<i>FT (N)</i>	<i>MF (Nm)</i>
0.000	3593.052	14248.374	31188.576	3566.900	14144.665	30961.568
0.100	3573.924	14068.722	29781.703	3547.911	13966.320	29564.934
0.200	3553.953	13711.329	28410.574	3528.085	13611.529	28203.783
0.300	3533.138	13355.934	27074.975	3507.422	13258.721	26877.912
0.400	3511.476	13002.620	25774.711	3485.918	12907.979	25587.109
0.500	3488.964	12651.473	24509.572	3463.569	12559.387	24331.180

0.600	3465.594	12302.576	23279.316	3440.370	12213.030	23109.869
0.700	3441.363	11956.017	22083.711	3416.315	11868.993	21922.979
0.800	3416.261	11611.880	20922.518	3391.396	11527.361	20770.232
0.900	3390.280	11270.254	19795.498	3365.604	11188.222	19651.414
1.000	3363.410	10931.226	18702.367	3338.929	10851.661	18566.246
1.100	3335.638	10594.885	17642.887	3311.360	10517.769	17514.469
1.200	3306.952	10261.321	16616.752	3282.882	10186.633	16495.807
1.300	3288.560	9930.626	15623.688	3264.624	9858.345	15509.971
1.400	3276.705	9601.770	14663.514	3252.855	9531.882	14556.785
1.500	3263.885	9274.099	13736.102	3240.129	9206.597	13636.125
1.600	3250.080	8947.710	12841.331	3226.424	8882.584	12747.867
1.700	3235.265	8622.702	11979.063	3211.717	8559.941	11891.871
1.800	3219.416	8299.176	11149.143	3195.983	8238.770	11067.993
1.900	3202.505	7977.234	10351.420	3179.195	7919.171	10276.078
2.000	3184.500	7656.983	9585.722	3161.321	7601.252	9515.950
2.100	3165.366	7338.533	8851.868	3142.326	7285.120	8787.439
2.200	3145.065	7021.997	8149.669	3122.173	6970.888	8090.352
2.300	3123.555	6707.490	7478.921	3100.820	6658.670	7424.486
2.400	3100.787	6395.135	6839.406	3078.218	6348.588	6789.625
2.500	3076.709	6085.056	6230.901	3054.314	6040.767	6185.550
2.600	3051.260	5777.385	5653.162	3029.052	5735.335	5612.015
2.700	3024.375	5472.259	5105.938-	3002.362	5432.430	5068.772
2.800	2995.977	5169.822	4588.955	2974.171	5132.193	4555.553
2.900	2965.981	4870.224	4101.932	2944.393	4834.776	4072.075
3.000	2934.289	4573.626	3644.569	2912.931	4540.337	3618.042
3.100	2900.789	4280.197	3216.549	2879.675	4249.044	3193.137
3.200	2865.352	3990.118	2817.538	2844.496	3961.076	2797.030
3.300	2827.827	3703.583	2447.180	2807.244	3676.626	2429.368
3.400	2788.036	3420.801	2105.099	2767.743	3395.902	2089.777
3.500	2745.770	3141.997	1790.900	2725.785	3119.128	1777.864
3.600	2700.775	2867.420	1504.157	2681.117	2846.549	1493.209
3.700	2652.741	2597.343	1244.423	2633.433	2578.438	1235.365
3.800	2601.285	2332.068	1011.216	2582.351	2315.094	1003.856
3.900	2545.919	2071.940	804.022	2527.389	2056.859	798.170
4.000	2486.010	1817.348	622.288	2467.916	1804.120	617.758
4.100	2420.708	1568.747	465.413	2403.088	1557.329	462.026
4.200	2348.820	1326.676	332.745	2331.724	1317.020	330.323
4.300	2268.590	1091.794	223.566	2252.078	1083.847	221.938
4.400	2177.219	864.935	137.072	2161.371	858.640	136.074
4.500	2069.702	647.213	72.351	2054.637	642.503	71.824
4.600	1935.170	440.243	28.327	1921.085	437.039	28.120
4.700	1736.468	246.726	3.654	1723.829	244.930	3.627
4.750	1461.587	73.079	0.000	1450.948	72.547	0.000

Appendix B

```
PROGRAM WING_FORCES
DIMENSION XA(26),XR(26),CZR(11),YY(11),FR(11),PA(26),DDX(27),
# DX(25),FEC(26)
OPEN(UNIT=4,FILE="Input Data D_0.23.txt")
OPEN(UNIT=5,FILE="CXYFr D_0.23.txt")
OPEN(UNIT=6,FILE="Force Node D_0.23.txt")
OPEN(UNIT=7,FILE="Output D_0.23.txt")
READ(4,*)RHO
READ(4,*)V
READ(4,*)DY
READ(4,*)Ca
READ(4,*)RHO1
READ(4,*)V1

!*****
!Ca=1.55           ! Wing Chord (m)
!DY=0.32          ! - Distance between Ribs (m)
!V=107.06         ! - Speed (m/sec)
!RHO=1.225        ! - density (kg/m^3)
Pd=RHO*V**2/2.0   ! - dynamic pressure (N/m^2)
FAK=Pd*DY*Ca

!*****
READ(5,*)NC
DO 10 I=1,26
READ(5,*)XA(I)
10  XR(I)=XA(I)/ Ca
DO 12 I=1,25
12  DX(I)=XA(I+1)-XA(I)
DO 14 I=2,25
14  DDX(I)=0.5*(DX(I-1)+DX(I))
DDX(1)=0.5*DX(1)
DDX(26)=0.5*DX(25)
DDX(27)=0.4
READ(5,*)NP
DO 15 I=1,11
READ(5,*)YY(I),FR(I)
15  CZR(I)=FR(I)/FAK   ! - Lift coefficient
CMD=-0.066           ! - Moment coefficient
TLK=0.258            ! -ratio of cord of aileron or flap to total cord
BE=0.0               ! - angle of deflection of aileron or flap (radians)
V1=107.6             ! - Speed (m/sec)
RHO1=1.1225          ! - density (kg/m^3)
Pd1=RHO1*V1*V1/2.0  ! - dynamic pressure
BE=BE*3.14/180.     ! - angle (rad)
DO 100 J=1,11
CZ=CZR(J)
```

```

WRITE(6,117)
117 FORMAT("_____")
WRITE(6,16)J,YY(J)
16 FORMAT(/,"Case D023 - Rib: ",I3," y = ",F8.3)
WRITE(6,*)
DO 60 I=1,26
X=XR(I)
TET=ACOS(1.0-2.0*X)
FI=ACOS(2.0*TLK-1.0)
! Functions fz i fm
IF(X.GE.0.03)THEN
FZ=0.716/TAN(TET/2.0)
FM=5.8*SIN(TET)-3.26/TAN(TET/2.0)
ELSE
FZ=4.07
FM=-17.43*(1.-X/0.03)-16.56*(X/0.03)
END IF
! Function fb
IF(X.GE.0.03)GOTO 20
!*****
TETB=ACOS(0.94)
FB=1.3*LOG10((1.0-COS(TET+FI))/(1.0-COS(TET-FI)))+
# (0.024-1.273*SIN(FI))/TAN(TETB/2.0)
GOTO 50
20 IF(X.GT.0.985-TLK.AND.X.LT.1.015-TLK)GOTO 30
FB=1.3*LOG10((1.0-COS(TET+FI))/(1.0-COS(TET-FI)))+
# (0.024-1.273*SIN(FI))/TAN(TET/2.0)
GOTO 50
!*****
30 X1=0.985-TLK
X2=1.015-TLK
TET1=ACOS(1.0-2*X1)
TET2=ACOS(1.0-2*X2)
FB1=1.3*LOG10((1.0-COS(TET1+FI))/(1.0-COS(TET1-FI)))+
# (0.024-1.273*SIN(FI))/TAN(TET1/2.0)
FB2=1.3*LOG10((1.0-COS(TET2+FI))/(1.0-COS(TET2-FI)))+
# (0.024-1.273*SIN(FI))/TAN(TET2/2.0)
FB=FB1*(1.0-(X-X1)/(X2-X1))+FB2*(X-X1)/(X2-X1)
50 PA(I)=Pd1*(CZ*FZ+CMD*FM+BE*FB)
60 CONTINUE
DO 70 I=1,26
70 FEC(I)=PA(I)*DDX(I)*DY
FREZ=0.0
REZM=0.0
DO 80 I=1,26
FREZ=FREZ+FEC(I)
80 REZM=REZM+FEC(I)*XA(I)
!*****
WRITE(6,85)

```

```

85 FORMAT(8X,' XA(m)      FEC(N)   PA(N./m^2) ',/)

DO 90 I=1,26
90  WRITE(6,65)XA(I),FEC(I),PA(I)
65  FORMAT(3F15.3)
100 CONTINUE
    WRITE(7,*)"Distribution of forces and pressure"
    WRITE(7,*)
    WRITE(7,105)Ca
105  FORMAT("  Wing Chord(m)    Ca  =",F10.3)
    WRITE(7,106)V
106  FORMAT("  Speed (m/s)      V  =",F10.3)
    WRITE(7,110)RHO
110  FORMAT("  Density (kg/m^3)  RHO =",F10.4)
    WRITE(7,111)Pd
111  FORMAT("  Dyn. pres.(N/m^2)  Pd =",F10.4)
    WRITE(7,115)V1
115  FORMAT("  Speed (m/s)      V1 =",F10.3)
    WRITE(7,116)RHO1
116  FORMAT("  Dyn. pres.(N/m^2)  RHO1 =",F10.4)
    WRITE(7,112)Pd1
112  FORMAT("  Dyn. pres.(N/m^2)  Pd =",F10.4)
    WRITE(7,113)FAK
113  FORMAT("  Force. (m)      FAK  =",F10.4)
    CLOSE(4)
    CLOSE(5)
    CLOSE(6)
    CLOSE(7)
    STOP
    END

```

Results PROGRAM WING_FORCES

Table 3.5 Load distribution of forces and pressure case D0.23

<i>Case D023 - Rib:1 y =1.240</i>			
<i>Rib</i>	<i>X (m)</i>	<i>Fz (N)</i>	<i>p (N/m²)</i>
1	0.000	109.295	25299.693
2	0.027	284.943	25083.045
3	0.071	279.855	19652.740
4	0.116	224.744	14631.761
5	0.167	187.757	11504.725
6	0.218	154.672	9477.436
7	0.269	130.718	8009.709
8	0.320	113.303	6875.150

9	0.372	96.044	5943.311
10	0.421	82.554	5211.774
11	0.471	72.454	4574.140
12	0.520	63.866	4031.958
13	0.570	56.736	3546.001
14	0.620	47.856	3115.594
15	0.666	41.079	2760.689
16	0.713	36.200	2432.807
17	0.759	31.866	2141.502
18	0.806	27.833	1 870.507
19	0.852	27.620	1628.538
20	0.912	25.586	1343.814
21	0.971	18.737	1094.439
22	1.019	12.110	911.898
23	1.054	8.969	789.514
24	1.090	7.748	672.600
25	1.126	5.419	564.434
26	1.150	1.909	497.046

Case D023 - Rib:2 y =1.596			
Rib	X (m)	Fz (N)	p (N/m²)
1	0.000	106.770	24715.313
2	0.027	278.305	24498.664
3	0.071	273.173	19183.529
4	0.116	219.192	14270.302
5	0.167	182.929	11208.878
6	0.218	150.525	9223.316
7	0.269	127.057	7785.366
8	0.320	109.981	6673.603
9	0.372	93.088	5760.368
10	0.421	79.888	5043.421
11	0.471	69.990	4418.538
12	0.520	61.574	3887.271

13	0.570	54.579	3411.201
14	0.620	45.922	2989.684
15	0.666	39.317	2642.248
16	0.713	34.543	2321.420
17	0.759	30.304	2036.552
18	0.806	26.363	1771.735
19	0.852	26.042	1535.487
20	0.912	23.949	1257.828
21	0.971	17.378	1015.053
22	1.019	11.124	837.686
23	1.054	8.168	718.990
24	1.090	6.979	605.814
25	1.126	4.813	501.349
26	1.150	1.676	436.415

<i>Case D023 - Rib:3 y =1.922</i>			
<i>Rib</i>	<i>X (m)</i>	<i>Fz (N)</i>	<i>p (N/m²)</i>
1	0.000	101.041	23389.025
2	0.027	263.238	23172.379
3	0.071	258.009	18118.625
4	0.116	206.591	13449.947
5	0.167	171.971	10537.436
6	0.218	141.112	8646.577
7	0.269	118.748	7276.206
8	0.320	102.442	6216.164
9	0.372	86.378	5345.168
10	0.421	73.836	4661.334
11	0.471	64.396	4065.390
12	0.520	56.373	3558.894

13	0.570	49.684	3105.264
14	0.620	41.532	2703.924
15	0.666	35.317	2373.438
16	0.713	30.781	2068.622
17	0.759	26.760	1798.362
18	0.806	23.028	1547.567
19	0.852	22.460	1324.302
20	0.912	20.233	1062.678
21	0.971	14.293	834.882
22	1.019	8.888	669.257
23	1.054	6.349	558.933
24	1.090	5.233	454.242
25	1.126	3.438	358.173
26	1.150	1.147	298.809

<i>Case D023 - Rib:4 y =2.247</i>			
<i>Rib</i>	<i>X (m)</i>	<i>Fz (N)</i>	<i>p (N/m²)</i>
1	0.000	99.441	23018.789
2	0.027	259.032	22802.141
3	0.071	253.776	17821.352
4	0.116	203.074	13220.942
5	0.167	168.912	10350.000
6	0.218	138.485	8485.578
7	0.269	116.428	7134.072
8	0.320	100.338	6088.468
9	0.372	84.505	5229.264
10	0.421	72.146	4554.673
11	0.471	62.834	3966.808
12	0.520	54.921	3467.226

13	0.570	48.318	3019.861
14	0.620	40.307	2624.153
15	0.666	34.200	2298.399
16	0.713	29.731	1998.053
17	0.759	25.770	1731.871
18	0.806	22.097	1484.989
19	0.852	21.460	1265.349
20	0.912	19.196	1008.201
21	0.971	13.432	784.587
22	1.019	8.263	622.240
23	1.054	5.842	514.252
24	1.090	4.745	411.929
25	1.126	3.055	318.205
26	1.150	1.000	260.396

<i>Case D023 - Rib:5 y =2.573</i>			
<i>Rib</i>	<i>X (m)</i>	<i>Fz (N)</i>	<i>p (N/m²)</i>
1	0.000	97.609	22594.715
2	0.027	254.215	22378.068
3	0.071	248.927	17480.855
4	0.116	199.045	12958.639
5	0.167	165.408	10135.310
6	0.218	135.475	8301.169
7	0.269	113.771	6971.271
8	0.320	97.928	5942.204
9	0.372	82.360	5096.506
10	0.421	70.211	4432.503
11	0.471	61.046	3853.891
12	0.520	53.258	3362.229

13	0.570	46.753	2922.039
14	0.620	38.904	2532.782
15	0.666	32.921	2212.448
16	0.713	28.528	1917.222
17	0.759	24.637	1655.711
18	0.806	21.030	1413.312
19	0.852	20.315	1197.823
20	0.912	18.008	945.803
21	0.971	12.446	726.978
22	1.019	7.548	568.385
23	1.054	5.261	463.074
24	1.090	4.187	363.465
25	1.126	2.615	272.425
26	1.150	0.831	216.398

Case D023 - Rib:6 y =2.895			
Rib	X (m)	Fz (N)	p (N/m²)
1	0.000	97.726	22621.777
2	0.027	254.522	22405.129
3	0.071	249.237	17502.582
4	0.116	199.302	12975.377
5	0.167	165.632	10149.010
6	0.218	135.667	8312.937
7	0.269	113.941	6981.660
8	0.320	98.081	5951.538
9	0.372	82.496	5104.978
10	0.421	70.334	4440.299
11	0.471	61.160	3861.097
12	0.520	53.364	3368.930

13	0.570	46.853	2928.282
14	0.620	38.993	2538.613
15	0.666	33.003	2217.933
16	0.713	28.605	1922.380
17	0.759	24.709	1660.571
18	0.806	21.098	1417.886
19	0.852	20.388	1202.132
20	0.912	18.084	949.784
21	0.971	12.509	730.654
22	1.019	7.594	571.822
23	1.054	5.298	466.340
24	1.090	4.223	366.558
25	1.126	2.643	275.347
26	1.150	0.842	219.205

<i>Case D023 - Rib:7 y =3.230</i>			
<i>Rib</i>	<i>X (m)</i>	<i>Fz (N)</i>	<i>p (N/m²)</i>
1	0.000	95.152	22025.904
2	0.027	247.753	21809.258
3	0.071	242.424	17024.145
4	0.116	193.641	12606.810
5	0.167	160.709	9847.346
6	0.218	131.438	8053.820
7	0.269	110.207	6752.905
8	0.320	94.694	5746.020
9	0.372	79.482	4918.438
10	0.421	67.615	4268.636
11	0.471	58.647	3702.435
12	0.520	51.027	3221.397

13	0.570	44.653	2790.831
14	0.620	37.021	2410.227
15	0.666	31.206	2097.163
16	0.713	26.915	1808.803
17	0.759	23.117	1553.557
18	0.806	19.600	1317.172
10	0.852	18.779	1107.251
20	0.912	16.415	862.108
21	0.971	11.123	649.707
22	1.019	6.589	496.151
23	1.054	4.481	394.430
24	1.090	3.438	298.459
25	1.126	2.026	211.021
26	1.150	0.604	157.382

Case D023 - Rib:8 y =3.565			
Rib	X (m)	Fz (N)	p (N/m²)
1	0.000	91.823	21255.223
2	0.027	238.998	21038.574
3	0.071	233.612	16405.346
4	0.116	186.319	12130.115
5	0.167	154.341	9457.182
6	0.218	125.969	7718.686
7	0.269	105.379	6457.041
8	0.320	90.314	5480.210
9	0.372	75.583	4677.172
10	0.421	64.098	4046.612
11	0.471	55.396	3497.227
12	0.520	48.004	3030.583

13	0.570	41.809	2613.056
14	0.620	34.471	2244.177
15	0.666	28.882	1940.962
16	0.713	24.729	1661.906
17	0.759	21.057	1415.149
18	0.806	17.661	1186.912
19	0.852	16.698	984.535
20	0.912	14.255	748.709
21	0.971	9.331	545.013
22	1.019	5.289	398.280
23	1.054	3.424	301.423
24	1.090	2.424	210.383
25	1.126	1.227	127.824
26	1.150	0.297	77.421

Case D023 - Rib:9 y =3.899			
Rib	X (m)	Fz (N)	p (N/m²)
1	0.000	89.781	20782.664
2	0.027	233.630	20566.016
3	0.071	228.209	16025.918
4	0.116	181.829	11837.821
5	0.167	150.437	9217.944
6	0.218	122.615	7513.192
7	0.269	102.418	6275.626
8	0.320	87.628	5317.223
9	0.372	73.192	4529.235
10	0.421	61.942	3910.474
11	0.471	53.403	3371.400
12	0.520	46.151	2913.581

13	0.570	40.065	2504.050
14	0.620	32.907	2142.360
15	0.666	27.456	1845.184
16	0.713	23.389	1571.834
17	0.759	19.795	1330.281
18	0.806	16.473	1107.040
19	0.852	15.422	909.289
20	0.912	12.932	679.177
21	0.971	8.232	480.817
22	1.019	4.492	338.268
23	1.054	2.776	244.394
24	1.090	1.801	156.377
25	1.126	0.737	76.810
26	1.150	0.109	28.392

<i>Case D023 - Rib: 10 y =4.235</i>			
<i>Rib</i>	<i>X (m)</i>	<i>Fz (N)</i>	<i>p (N/m²)</i>
1	0.000	73.109	16923.316
2	0.027	189.788	16706.668
3	0.071	184.083	12927.162
4	0.116	145.162	9450.681
5	0.167	118.550	7264.122
6	0.218	95.226	5834.944
7	0.269	78.239	4794.026
8	0.320	65.691	3986.125
9	0.372	53.668	3321.050
10	0.421	44.331	2798.644
11	0.471	37.125	2343.779
12	0.520	31.015	1958.040

13	0.570	25.821	1613.808
14	0.620	20.134	1310.830
15	0.666	15.817	1062.978
16	0.713	12.443	836.219
17	0.759	9.481	637.175
18	0.806	6.766	454.734
19	0.852	4.999	294.763
20	0.912	2.119	111.311
21	0.971	0.744	43.461
22	1.019	0.216	12.841
23	1.054	-0.215	-12.356
24	1.090	-0.328	-18.684
25	1.126	-0.326	-18.816
26	1.150	-0.429	-24.026

<i>Case D023 - Rib:11 y =4.560</i>			
Rib	X (m)	Fz (N)	p (N/m²)
1	0.000	92.316	21369.416
2	0.027	240.295	21152.768
3	0.071	234.918	16497.035
4	0.116	187.403	12200.748
5	0.167	155.285	9514.993
6	0.218	126.779	7768.343
7	0.269	106.094	6500.880
8	0.320	90.963	5519.595
9	0.372	76.161	4712.921
10	0.421	64.619	4079.510
11	0.471	55.878	3527.633
12	0.520	48.452	3058.856
13	0.570	42.230	2639.397
14	0.620	34.848	2268.781
15	0.666	29.226	1964.107
16	0.713	25.053	1683.672
17	0.759	21.363	1435.657
18	0.806	17.948	1206.212
19	0.852	17.006	1002.718
20	0.912	14.575	765.512
21	0.971	9.596	560.525

22	1.019	5.482	412.781
23	1.054	3.581	315.204
24	1.090	2.574	223.433
25	1.126	1.345	140.151
26	1.150	0.343	89.269

Table 3.6 Load distribution of forces and pressure case E0.23.

Case E023 - Rib: 1 $y = 1.240$			
Rib	X (m)	Fz (N)	p (N/m²)
1	0.000	72.416	16762.863
2	0.027	187.965	16546.215
3	0.071	182.248	12798.330
4	0.116	143.638	9351.435
5	0.167	117.225	7182.891
6	0.218	94.088	5765.170
7	0.269	77.233	4732.428
8	0.320	64.779	3930.784
9	0.372	52.856	3270.819
10	0.421	43.598	2752.419
11	0.471	36.449	2301.056
12	0.520	30.386	1918.313
13	0.570	25.229	1576.796
14	0.620	19.603	1276.259
15	0.666	15.333	1030.457
16	0.713	11.988	805.636
17	0.759	9.052	608.359
18	0.806	6.363	427.614
19	0.852	4.566	269.214
20	0.912	1.670	87.702
21	0.971	-1.117	-65.258
22	1.019	-2.287	-172.217
23	1.054	-2.735	-240.720
24	1.090	-3.491	-303.021
25	1.126	-3.429	-357.137
26	1.150	-1.493	-388.673

Case E023 - Rib: 2 $y = 1.596$			
Rib	X (m)	Fz (N)	p (N/m²)
1	0.000	71.101	16458.564
2	0.027	184.508	16241.917
3	0.071	178.769	12554.003
4	0.116	140.747	9163.216
5	0.167	114.711	7028.838
6	0.218	91.928	5632.845
7	0.269	75.327	4615.609
8	0.320	63.050	3825.831
9	0.372	51.317	3175.558

10	0.421	42.210	2664.755
11	0.471	35.165	2220.031
12	0.520	29.193	1842.971
13	0.570	24.106	1506.603
14	0.620	18.596	1210.695
15	0.666	14.415	968.783
16	0.713	11.125	747.635
17	0.759	8.239	553.710
18	0.806	5.598	376.182
19	0.852	3.744	220.760
20	0.912	0.817	42.928
21	0.971	-1.825	-106.596
22	1.019	-2.800	-210.861
23	1.054	-3.152	-277.443
24	1.090	-3.891	-337.797
25	1.126	-3.744	-389.987
26	1.150	-1.614	-420.245

Case E023 - Rib: 3 $y = 1.922$			
Rib	X (m)	F_z (N)	p (N/m²)
1	0.000	68.115	15767.404
2	0.027	176.657	15550.756
3	0.071	170.867	11999.055
4	0.116	134.180	8735.708
5	0.167	109.000	6678.932
6	0.218	87.023	5332.292
7	0.269	70.996	4350.273
8	0.320	59.121	3587.448
9	0.372	47.820	2959.187
10	0.421	39.056	2465.640
11	0.471	32.250	2035.997
12	0.520	26.482	1671.846
13	0.570	21.555	1347.172
14	0.620	16.309	1061.778
15	0.666	12.331	828.699
16	0.713	9.165	615.895
17	0.759	6.392	429.583
18	0.806	3.859	259.362
19	0.852	1.878	110.706
20	0.912	-1.119	-58.770
21	0.971	-3.432	-200.488
22	1.019	-3.966	-298.633
23	1.054	-4.099	-360.853
24	1.090	-4.801	-416.785
25	1.126	-4.460	-464.599
26	1.150	-1.889	-491.955

Case E023 - Rib: 4 $y = 2.247$			
Rib	X(m)	Fz(N)	p(N/m²)
1	0.000	67.282	15574.558
2	0.027	174.466	15357.909
3	0.071	168.662	11844.214
4	0.116	132.348	8616.426
5	0.167	107.407	6581.302
6	0.218	85.654	5248.432
7	0.269	69.788	4276.239
8	0.320	58.025	3520.935
9	0.372	46.845	2898.815
10	0.421	38.176	2410.083
11	0.471	31.437	1984.648
12	0.520	25.726	1624.099
13	0.570	20.843	1302.688
14	0.620	15.671	1020.228
15	0.666	11.749	789.614
16	0.713	8.618	579.138
17	0.759	5.877	394.950
18	0.806	3.374	226.767
19	0.852	1.357	79.999
20	0.912	-1.659	-87.145
21	0.971	-3.881	-226.685
22	1.019	-4.291	-323.123
23	1.054	-4.364	-384.126
24	1.090	-5.055	-438.825
25	1.126	-4.660	-485.418
26	1.150	-1.966	-511.963

Case E023 - Rib: 5 $y = 2.573$			
Rib	X (m)	Fz (N)	p (N/m²)
1	0.000	66.327	15353.511
2	0.027	171.955	15136.862
3	0.071	166.134	11666.730
4	0.116	130.248	8479.700
5	0.167	105.581	6469.395
6	0.218	84.086	5152.309
7	0.269	68.403	4191.379
8	0.320	56.769	3444.695
9	0.372	45.727	2829.615
10	0.421	37.167	2346.402
11	0.471	30.505	1925.790
12	0.520	24.859	1569.369
13	0.570	20.027	1251.698
14	0.620	14.939	972.601

15	0.666	11.083	744.812
16	0.713	7.991	537.005
17	0.759	5.286	355.251
18	0.806	2.818	189.405
19	0.852	0.760	44.802
20	0.912	-2.279	-119.670
21	0.971	-4.395	-256.714
22	1.019	-4.664	-351.195
23	1.054	-4.667	-410.802
24	1.090	-5.346	-464.087
25	1.126	-4.889	-509.280
26	1.150	-2.054	-534.898

Case E023 - Rib: 6 $y = 2.895$			
Rib	X (m)	Fz (N)	p (N/m²)
1	0.000	66.552	15405.560
2	0.027	172.546	15188.911
3	0.071	166.729	11708.521
4	0.116	130.743	8511.895
5	0.167	106.011	6495.746
6	0.218	84.455	5174.942
7	0.269	68.729	4211.361
8	0.320	57.064	3462.647
9	0.372	45.990	2845.910
10	0.421	37.405	2361.397
11	0.471	30.724	1939.649
12	0.520	25.063	1582.256
13	0.570	20.219	1263.705
14	0.620	15.111	983.816
15	0.666	11.240	755.361
16	0.713	8.138	546.925
17	0.759	5.425	364.599
18	0.806	2.949	198.203
19	0.852	0.900	53.090
20	0.912	-2.133	-112.012
21	0.971	-4.274	-249.643
22	1.019	-4.576	-344.585
23	1.054	-4.595	-404.521
24	1.090	-5.278	-458.138
25	1.126	-4.835	-503.661
26	1.150	-2.033	-529.497

Case E023 - Rib: 7 $y = 3.230$			
Rib	X (m)	Fz (N)	p (N/m²)
1	0.000	65.012	15049.129
2	0.027	168.497	14832.481
3	0.071	162.654	11422.336

4	0.116	127.356	8291.431
5	0.167	103.066	6315.300
6	0.218	81.926	5019.948
7	0.269	66.496	4074.528
8	0.320	55.038	3339.713
9	0.372	44.187	2734.328
10	0.421	35.778	2258.714
11	0.471	29.221	1844.743
12	0.520	23.665	1494.007
13	0.570	18.904	1181.486
14	0.620	13.932	907.020
15	0.666	10.165	683.121
16	0.713	7.127	478.988
17	0.759	4.473	300.587
18	0.806	2.053	137.959
19	0.852	-0.062	-3.665
20	0.912	-3.131	-164.457
21	0.971	-5.103	-298.063
22	1.019	-5.177	-389.849
23	1.054	-5.084	-447.535
24	1.090	-5.747	-498.873
25	1.126	-5.205	-542.139
26	1.150	-2.175	-566.478

Case E023 - Rib: 8 y = 3.565			
Rib	X (m)	Fz (N)	p (N/m²)
1	0.000	63.183	14625.672
2	0.027	163.687	14409.023
3	0.071	157.812	11082.332
4	0.116	123.333	8029.507
5	0.167	99.567	6100.921
6	0.218	78.920	4835.806
7	0.269	63.843	3911.963
8	0.320	52.632	3193.662
9	0.372	42.044	2601.762
10	0.421	33.846	2136.721
11	0.471	27.435	1731.990
12	0.520	22.004	1389.163
13	0.570	17.341	1083.807
14	0.620	12.530	815.782
15	0.666	8.888	597.295
16	0.713	5.926	398.274
17	0.759	3.341	224.538
18	0.806	0.988	66.386
19	0.852	-1.206	-71.092
20	0.912	-4.318	-226.765
21	0.971	-6.088	-355.588

22	1.019	-5.891	-443.625
23	1.054	-5.665	-498.638
24	1.090	-6.305	-547.267
25	1.126	-5.643	-587.852
26	1.150	-2.344	-610.413

Case E023 - Rib: 9 y = 3.899			
Rib	X (m)	Fz (N)	p (N/m²)
1	0.000	62.248	14409.342
2	0.027	161.229	14192.693
3	0.071	155.339	10908.636
4	0.116	121.278	7895.699
5	0.167	97.780	5991.403
6	0.218	77.385	4741.734
7	0.269	62.488	3828.914
8	0.320	51.402	3119.049
9	0.372	40.950	2534.039
10	0.421	32.858	2074.399
11	0.471	26.522	1674.388
12	0.520	21.156	1335.601
13	0.570	16.542	1033.906
14	0.620	11.814	769.172
15	0.666	8.235	553.449
16	0.713	5.313	357.040
17	0.759	2.763	185.687
18	0.806	0.444	29.822
19	0.852	-1.790	-105.539
20	0.912	-4.924	-258.595
21	0.971	-6.591	-384.976
22	1.019	-6.256	-471.097
23	1.054	-5.961	-524.745
24	1.090	-6.589	-571.990
25	1.126	-5.868	-611.205
26	1.150	-2.430	-632.858

Case E023 - Rib: 10 y = 4.235			
Rib	X (m)	Fz (N)	p (N/m²)
1	0.000	53.561	12398.343
2	0.027	138.384	12181.695
3	0.071	132.346	9293.961
4	0.116	102.172	6651.827
5	0.167	81.165	4973.320
6	0.218	63.113	3867.245
7	0.269	49.889	3056.894
8	0.320	39.971	2425.451
9	0.372	30.777	1904.487
10	0.421	23.682	1495.055

11	0.471	18.041	1138.924
12	0.520	13.269	837.695
13	0.570	9.120	570.025
14	0.620	5.159	335.884
15	0.666	2.170	145.863
16	0.713	-0.391	-26.268
17	0.759	-2.611	-175.472
18	0.806	-4.614	-310.076
19	0.852	-7.221	-425.751
20	0.912	-10.558	-554.494
21	0.971	-11.268	-658.163
22	1.019	-9.648	-726.479
23	1.054	-8.718	-767.435
24	1.090	-9.237	-801.814
25	1.126	-7.952	-828.297
26	1.150	-3.231	-841.504

<i>Case E023 - Rib: 11 y = 4.560</i>			
<i>Rib</i>	<i>X (m)</i>	<i>Fz (N)</i>	<i>p (N/m²)</i>
1	0.000	63.569	14715.066
2	0.027	164.702	14498.418
3	0.071	158.835	11154.109
4	0.116	124.183	8084.801
5	0.167	100.306	6146.178
6	0.218	79.555	4874.680
7	0.269	64.403	3946.281
8	0.320	53.140	3224.494
9	0.372	42.497	2629.748
10	0.421	34.254	2162.474
11	0.471	27.812	1755.793
12	0.520	22.355	1411.296
13	0.570	17.671	1104.427
14	0.620	12.826	835.043
15	0.666	9.157	615.413
16	0.713	6.180	415.313
17	0.759	3.580	240.592
18	0.806	1.213	81.496
19	0.852	-0.964	-56.858
20	0.912	-4.067	-213.611
21	0.971	-5.880	-343.444

22	1.019	-5.741	-432.272
23	1.054	-5.542	-487.850
24	1.090	-6.187	-537.050
25	1.126	-5.551	-578.202
26	1.150	-2.308	-601.138

Appendix C

Table 4.6 Table 4.16 shown in Appendix C.

Table 4.6 Aerodynamic Parameters at Envelope Point AA+ ($\delta_F = 0^\circ$, $\delta_A = 15^\circ$, $n = 4.0$, $V = 66.87m/s$)

<i>No.</i>	<i>Mass (kg)</i>	<i>x_{cg} (m)</i>	<i>C_L</i>	<i>C_{LH}</i>	<i>C_{LW}</i>	<i>α_H (°)</i>	<i>δ_H (°)</i>	<i>α (°)</i>
1	687.4	-0.024	0.6485	-0.2227	0.6901	2.04	-6.33	3.34
2	687.4	-0.016	0.6485	-0.2166	0.6889	2.03	-6.20	3.33
3	727.4	0.049	0.6863	-0.1640	0.7168	2.22	-5.38	3.68
4	827.4	0.068	0.7853	-0.1404	0.8115	2.86	-5.56	4.87
5	932.4	0.063	0.8797	-0.1389	0.9056	3.49	-6.17	6.05
6	932.4	0.045	0.8797	-0.1568	0.9089	3.52	-6.54	6.09
7	892.4	-0.005	0.8419	-0.2095	0.8810	3.33	-7.36	5.74
8	792.4	-0.019	0.7429	-0.2212	0.7841	2.68	-6.93	4.53

Table 4.7 Aerodynamic Parameters at Envelope Point AA- ($\delta_F = 0^\circ$, $\delta_A = -23^\circ$, $n = 4.0$, $V = 66.87m/s$)

<i>No.</i>	<i>Mass (kg)</i>	<i>x_{cg} (m)</i>	<i>C_L</i>	<i>C_{LH}</i>	<i>C_{LW}</i>	<i>α_H (°)</i>	<i>δ_H (°)</i>	<i>α (°)</i>
1	687.4	-0.024	0.64853	-0.0151	0.6514	1.78	-2.07	9.73
2	687.4	-0.016	0.64853	-0.0089	0.6502	1.77	-1.95	9.72
3	727.4	0.049	0.68627	0.0437	0.6781	1.96	-1.12	10.07
4	827.4	0.068	0.78533	0.0672	0.7728	2.60	-1.31	11.26
5	932.4	0.063	0.87967	0.0688	0.8669	3.23	-1.91	12.44
6	932.4	0.045	0.87967	0.0508	0.8702	3.26	-2.28	12.48
7	892.4	-0.005	0.84193	-0.0018	0.8423	3.07	-3.10	12.13
8	792.4	-0.019	0.74287	-0.0136	0.7454	2.41	-2.68	10.92

Table 4.8 Aerodynamic Parameters at Envelope Point DA+ ($\delta_F = 0^\circ$, $\delta_A = 5.0^\circ$, $n = 4.0$, $V = 107.22m/s$)

<i>No.</i>	<i>Mass (kg)</i>	<i>x_{cg} (m)</i>	<i>C_L</i>	<i>C_{LH}</i>	<i>C_{LW}</i>	<i>α_H (°)</i>	<i>δ_H (°)</i>	<i>α (°)</i>
1	687.4	-0.024	0.2522	-0.1569	0.28145	-0.71	-2.31	0.02
2	687.4	-0.016	0.2522	-0.1545	0.28100	-0.72	-2.26	0.02
3	727.4	0.049	0.2669	-0.1341	0.29186	-0.64	-1.94	0.15
4	827.4	0.068	0.3054	-0.1249	0.32867	-0.39	-2.01	0.61
5	932.4	0.063	0.3421	-0.1243	0.36525	-0.15	-2.24	1.07
6	932.4	0.045	0.3421	-0.1313	0.36655	-0.14	-2.39	1.09
7	892.4	-0.005	0.3274	-0.1517	0.35569	-0.21	-2.71	0.95
8	792.4	-0.019	0.2889	-0.1563	0.31802	-0.47	-2.54	0.48

Table 4.9 Aerodynamic Parameters at Envelope Point DA- ($\delta_F = 0^\circ$, $\delta_A = -7.7^\circ$, $n = 4.0$, $V = 107.22m/s$)

No.	Mass (kg)	x_{cg} (m)	C_L	C_{LH}	C_{LW}	α_H ($^\circ$)	δ_H ($^\circ$)	α ($^\circ$)
1	687.4	-0.024	0.2522	0.2685	-0.0875	0.76	-2.45	2.16
2	687.4	-0.016	0.2522	0.2681	-0.0851	0.76	-2.40	2.15
3	727.4	0.049	0.2669	0.2789	-0.0647	0.89	-2.14	2.29
4	827.4	0.068	0.3054	0.3157	-0.0555	1.36	-2.42	2.75
5	932.4	0.063	0.3421	0.3523	-0.0549	1.82	-2.87	3.21
6	932.4	0.045	0.3421	0.3536	-0.0619	1.83	-3.02	3.23
7	892.4	-0.005	0.3274	0.3428	-0.0824	1.70	-3.28	3.09
8	792.4	-0.019	0.2889	0.3051	-0.0869	1.22	-2.90	2.62

Table 4.10 Aerodynamic Parameters at Envelope Point AF ($\delta_F = 30^\circ$, $\delta_A = 0.0^\circ$, $n = 2.0$, $V = 33.5m/s$)

No.	Mass (kg)	x_{cg} (m)	C_L	C_{LH}	C_{LW}	α_H ($^\circ$)	δ_H ($^\circ$)	α ($^\circ$)
1	687.4	-0.024	1.2917	-0.3180	1.3510	0.92	-7.04	3.60
2	687.4	-0.016	1.2917	-0.3057	1.3487	0.91	-6.79	3.58
3	727.4	0.049	1.3669	-0.2010	1.4044	1.21	-5.08	4.20
4	827.4	0.068	1.5642	-0.1540	1.5929	2.23	-5.20	6.33
5	932.4	0.063	1.7521	-0.1510	1.7802	3.25	-6.16	8.43
6	932.4	0.045	1.7521	-0.1868	1.7869	3.29	-6.88	8.51
7	892.4	-0.005	1.6769	-0.2916	1.7313	2.99	-8.60	7.88
8	792.4	-0.019	1.4796	-0.3150	1.5384	1.94	-8.00	5.71

Table 4.11 Aerodynamic Parameters at Envelope Point AFA+ ($\delta_F = 30^\circ$, $\delta_A = 15^\circ$, $n = 2.0$, $V = 33.5m/s$)

No.	Mass (kg)	x_{cg} (m)	C_L	C_{LH}	C_{LW}	α_H ($^\circ$)	δ_H ($^\circ$)	α ($^\circ$)
1	687.4	-0.024	1.2917	-0.4000	1.3663	1.00	-8.70	1.06
2	687.4	-0.016	1.2917	-0.3877	1.3640	0.99	-8.45	1.04
3	727.4	0.049	1.3669	-0.2829	1.4196	1.29	-6.74	1.66
4	827.4	0.068	1.5642	-0.2360	1.6082	2.32	-6.86	3.78
5	932.4	0.063	1.7521	-0.2329	1.7955	3.33	-7.82	5.89
6	932.4	0.045	1.7521	-0.2688	1.8022	3.37	-8.54	5.97
7	892.4	-0.005	1.6769	-0.3735	1.7466	3.07	-10.26	5.34
8	792.4	-0.019	1.4796	-0.3969	1.5536	2.02	-9.66	3.17

Table 4.12 Aerodynamic Parameters at Envelope Point AFA- ($\delta_F = 30^\circ$, $\delta_A = -23^\circ$, $n = 2.0$, $V = 33.5m/s$)

<i>No.</i>	<i>Mass (kg)</i>	<i>x_{cg} (m)</i>	<i>C_L</i>	<i>C_{LH}</i>	<i>C_{LW}</i>	<i>α_H (°)</i>	<i>δ_H (°)</i>	<i>α (°)</i>
1	687.4	-0.024	1.29173	-0.1924	1.3276	0.79	-4.50	7.50
2	687.4	-0.016	1.29173	-0.1801	1.3253	0.78	-4.25	7.48
3	727.4	0.049	1.36689	-0.0753	1.3809	1.08	-2.53	8.10
4	827.4	0.068	1.56419	-0.0284	1.5695	2.11	-2.65	10.22
5	932.4	0.063	1.7521	-0.0253	1.7568	3.12	-3.61	12.33
6	932.4	0.045	1.7521	-0.0612	1.7635	3.16	-4.34	12.41
7	892.4	-0.005	1.67694	-0.1659	1.7079	2.86	-6.05	11.78
8	792.4	-0.019	1.47963	-0.1893	1.5149	1.81	-5.46	9.61

Table 4.13 Aerodynamic Parameters at Envelope Point DFA+ ($\delta_F = 30^\circ$, $\delta_A = 5.0^\circ$, $n = 2.0$, $V=49.14m/s$)

<i>No.</i>	<i>Mass (kg)</i>	<i>x_{cg} (m)</i>	<i>C_L</i>	<i>C_{LH}</i>	<i>C_{LW}</i>	<i>α_H (°)</i>	<i>δ_H (°)</i>	<i>α (°)</i>
1	687.4	-0.024	0.6003	-0.3258	0.6611	-2.82	-3.45	-5.06
2	687.4	-0.016	0.6003	-0.3201	0.6600	-6.93	0.77	-5.07
3	727.4	0.049	0.6353	-0.2714	0.6859	-6.96	1.74	-4.78
4	827.4	0.068	0.7270	-0.2496	0.7735	-7.07	2.27	-3.80
5	932.4	0.063	0.8143	-0.2482	0.8606	-7.18	2.41	-2.82
6	932.4	0.045	0.8143	-0.2648	0.8637	-7.19	2.09	-2.78
7	892.4	-0.005	0.7794	-0.3135	0.8378	-7.15	1.12	-3.07
8	792.4	-0.019	0.6877	-0.3244	0.7481	-7.04	0.80	-4.08

Table 4.14 Aerodynamic Parameters at Envelope Point DFA- ($\delta_F = 30^\circ$, $\delta_A = -7.7^\circ$, $n = 2.0$, $V=49.14m/s$)

<i>No.</i>	<i>Mass (kg)</i>	<i>x_{cg} (m)</i>	<i>C_L</i>	<i>C_{LH}</i>	<i>C_{LW}</i>	<i>α_H (°)</i>	<i>δ_H (°)</i>	<i>α (°)</i>
1	687.4	-0.024	0.6003	-0.2565	0.6481	-2.89	-2.04	-2.91
2	687.4	-0.016	0.6003	-0.2507	0.6471	-2.90	-1.93	-2.92
3	727.4	0.049	0.6353	-0.2020	0.6729	-2.76	-1.13	-2.63
4	827.4	0.068	0.7270	-0.1802	0.7606	-2.28	-1.19	-1.64
5	932.4	0.063	0.8143	-0.1788	0.8476	-1.81	-1.63	-0.66
6	932.4	0.045	0.8143	-0.1955	0.8507	-1.79	-1.97	-0.63
7	892.4	-0.005	0.7794	-0.2442	0.8249	-1.93	-2.77	-0.92
8	792.4	-0.019	0.6877	-0.2550	0.7352	-2.42	-2.49	-1.93

Table 4.15 Aerodynamic Parameters at Envelope Point AH ($\delta_F = 0^\circ$, $\delta_A = 0.0^\circ$, $n = 1.0$, $V=66.87m/s$)

<i>No.</i>	<i>Mass (kg)</i>	<i>x_{cg} (m)</i>	<i>C_L</i>	<i>C_{LH}</i>	<i>C_{LW}</i>	<i>α_H (°)</i>	<i>δ_H (°)</i>	<i>α (°)</i>
1	687.4	-0.024	0.1621	-0.1270	0.1858	-1.36	-1.09	-0.28
2	687.4	-0.016	0.1621	-0.1255	0.1855	-1.36	-1.06	-0.28
3	727.4	0.049	0.1716	-0.1124	0.1925	-1.31	-0.85	-0.19
4	827.4	0.068	0.1963	-0.1065	0.2162	-1.15	-0.90	0.11
5	932.4	0.063	0.2199	-0.1061	0.2397	-0.99	-1.05	0.40
6	932.4	0.045	0.2199	-0.1106	0.2405	-0.99	-1.14	0.41
7	892.4	-0.005	0.2105	-0.1237	0.2335	-1.04	-1.35	0.32
8	792.4	-0.019	0.1857	-0.1267	0.2093	-1.20	-1.24	0.02

Table 4.16 Aerodynamic Parameters at Envelope Point DH ($\delta_F = 0^\circ$, $\delta_A = 0.0^\circ$, $n = 1.0$, $V=102.22m/s$)

<i>No.</i>	<i>Mass (kg)</i>	<i>x_{cg} (m)</i>	<i>C_L</i>	<i>C_{LH}</i>	<i>C_{LW}</i>	<i>α_H (°)</i>	<i>δ_H (°)</i>	<i>α (°)</i>
1	687.4	-0.024	0.0630	-0.1243	0.0862	-2.03	-0.36	-1.53
2	687.4	-0.016	0.0630	-0.1237	0.0861	-2.03	-0.35	-1.53
3	727.4	0.049	0.0667	-0.1185	0.0888	-2.01	-0.27	-1.49
4	827.4	0.068	0.0763	-0.1162	0.0980	-1.95	-0.29	-1.38
5	932.4	0.063	0.0855	-0.1161	0.1072	-1.89	-0.35	-1.26
6	932.4	0.045	0.0855	-0.1178	0.1075	-1.89	-0.38	-1.26
7	892.4	-0.005	0.0819	-0.1230	0.1048	-1.90	-0.46	-1.29
8	792.4	-0.019	0.0722	-0.1241	0.0954	-1.97	-0.42	-1.41